Long term stability of silicide based thermoelectric materials and modules

Antoine de Padoue Shyikira

UiA University of Agder

Doctoral Dissertations at the University of Agder 412

Antoine de Padoue Shyikira

Long term stability of silicide based thermoelectric materials and modules

Doctoral Dissertation for the Degree *Philosophiae Doctor (PhD)* at the Faculty of Faculty of Engineering and Science, Specialisation in Engineering Sciences - Renewable Energy

University of Agder

Faculty of Engineering and Science

2023

Doctoral Dissertations at the University of Agder 412
ISSN: 1504-9272
ISBN: 978-82-8427-127-9

Printed by Make!Graphics
Kristiansand

Preface

This doctoral dissertation was conducted at the University of Agder, Grimstad - Norway in the department of Engineering Sciences. The scientific research was supervised by Professor Peter Hugh Middleton and Gunstein Skumedal,Ph.D and was conducted in the period from August 2017 to June 2022. The dissertation was submitted as partial fulfilment of the degree of doctor philosophiae, to the Faculty of Engineering and Science.

Acknowledgments

Life in itself is a challenging experience that requires us to be goal oriented and have motivation, confidence, and determination. A doctoral research fellowship is not so different, but it also requires a high degree of dedication, organization, collaboration and most importantly support from the people around you. It is in that regard, that I would like to show my sincere appreciation to my colleagues, partners, friends, and family for all the support (major or minor) that I received as a Ph.D. research fellow.

I wish to extend my appreciation to my supervisor, Professor Peter Hugh Middleton. Thank you for your encouragement and support, both scientific and moral, but most importantly for introducing and welcoming me to the hobby we now share: creating devices/instruments. Many thanks also go to my co-supervisors Professor Tor Oskar Sætre and Gunstein Skomedal. Thank you, Gunstein, for your mentorship and invaluable guidance, as well as the support and encouragement you unconditionally offered me throughout this period.

I would like to thank my colleagues, namely Gerrit Surup, Johan Olav Brekestad, Thomas Benjamin Ferriday, Anette Heimdal, Ingrid Lande, Odin Kvam, and many more, for the time you took to share your insight and expertise in different situations, helping me to advance. Special thanks go to Naureen Akhtar for your tremendous support; and thank you for being a wonderful friend.

Furthermore, I would like to recognize all the partners in the TESil project for the important discussions we had, they gave me a lot of good suggestions. I would also like to express my appreciation for the Elkem R&D group members, especially Anders Hope Amundsen, for welcoming me in your laboratory facility and providing me with tremendous support.

I am also grateful to have met and made friends along the journey whose energy kept mine in balance and who were more than happy to share a cup of coffee when needed or (why not?) a glass of beer. Thank you Sinziana (Suz), Shaun, Andreas, Basant, Solomon, Madhawa, Merethe, Saeed Rahimi Gorji, Oscar, Immanuel, to name a few.

I was lucky and amazed to sit with the best office mates in the whole world. Thank you Sissel and Lorenzo for the amazing discussions and support we have shared and continue to share. Likewise, many thanks to Haidar and Javad for sharing many life experiences and advices.

As challenging this experience was, I had the moral support of my friends and family, away from the work environment. Many thanks "k'umuryango wa" Isabwe, Titi, Vedaste, and all of my relatives.

Vestine Kamugisha, I cannot find words to thank you for being the best wife, woman and friend I could ask for. Thank you for picking me up whenever I lost courage; thank you for creating a comfortable, relaxing, and welcoming environment in our home. But most importantly, thank you for blessing my life with "Two boys". Gabrio and Declan, thank you for your smiles every time I opened the door: seeing your faces relieved all the pressure of the day and fueled me for the night, when you needed a cup of milk or water.

The list is long, but I hope I have been able to express my thankfulness for the feelings your presence and support gave me in my professional and personal life.

Antoine de Padoue Shyikira

Grimstad, Norway

Abstract

Silicide-based thermoelectric generators are potential candidates for waste heat recovery at temperatures below 500 °C. For the last two decades, the conversion efficiency of modules based on n-type magnesium silicides and p-type higher manganese silicide has improved significantly. However, the conditions in which thermoelectric generators operate (for example, remote areas in the oil, gas, and telecommunication industries, in automobiles, etc.) are harsh (corrosive, for example) and hostile (due to thermal instability). In this project, there was much focus on the stability of the thermoelectric modules, with special interest given to oxidation of the thermoelectric materials and module stability. The thermal oxidation studies were conducted on higher manganese silicide alloys; the studies mainly investigated the effect of the alloys' composition, consolidation techniques and the operational atmosphere's effect on their oxidation potential. Moreover, the choice of matching electrodes and good bonding technology for the module assembly was the ultimate step before finally testing the actual performance and stability of the module over an extended period.

The thorough oxidation studies conducted in this thesis revealed the importance of different production processes for the higher manganese silicide thermoelectric materials on the oxidation robustness of the alloys. The study showed that the purity (fewer impurities) of the raw elements and optimal doping level are among the key factors for the alloys to resist oxidation by growing a protective SiO_2 protective oxide layer. Moreover, it was also shown that powder consolidation by spark plasma sintering produced stronger bulk pellets, and mechanical strength played a key role in passive oxidation.

During the module's contacts design, silver electrodes and solid liquid interdiffusion bonding technology were used. The contact resistance of the assembled modules were measured

using an automated point contact measurement test rig. On the magnesium silicide the specific contact resistance was on average 0.17 $m\Omega cm^2$ with 2.1% standard deviation. The higher manganese silicide's contact interface, on the other hand, the results were dispersed along the bond, where 0.07 $m\Omega cm^2$ was the lowest value and 1.12 $m\Omega cm^2$ the highest (81.3% standard deviation).

Finally, the module stability was investigated by testing the performance of the assembled modules. The tested modules produced up to $7.4 mW/cm^2$ power density at 400 °C and sustained more than 300 thermal cycles. The gradual degradation was found to mainly originate from the mechanical failure of the contact interfaces and oxidation of the n-type magnesium silicide relative to the p-type material. Applying a high-temperature coating did not reduce the degradation rate, which showed that it would be better to encapsulate the modules to count-act the effect of oxidation.

Abstrakt

Silisid-baserte termoelektriske generatorer er potensielle kandidater for spillvarmegjenvinning på temperaturer under 500 °C. Gjennom de siste to tiårene har konverteringseffektiviteten til moduler basert på n-type magnesiumsilisider og p-type mangansilisider blitt betydelig forbedret. Forholdene der termoelektriske generatorer fungerer (for for eksempel fjerntliggende områder i olje-, gass- og telekommunikasjonsindustrien, i biler, etc.) er korrosive og utfordrende (på grunn av termisk ustabilitet). I dette prosjekt, var det mye fokus på stabiliteten til de termoelektriske modulene, med spesiell interesse for oksidasjon av termoelektriske materialer og modulstabilitet. Termiske oksidasjonsstudier ble utført på legeringer med mangansilisider; studiene undersøkte hovedsakelig effekten av legeringenes sammensetning, konsolideringsteknikker og den operasjonelle atmosfærens effekt på deres oksidasjonspotensial. Valget av passende elektroder og god bindingsteknologi for modulsammenstillingen var det ultimate trinnet før ble testet den faktiske ytelsen og stabiliteten over en lengre periode.

De grundige oksidasjonsstudiene utført i denne oppgaven avdekket viktigheten av ulike produksjonsprosesser for høyere mangansilisid termoelektriske materialer på oksidasjonsrobustheten til legeringene. Studien viste at renheten (færre urenheter) av råelementene og optimalt dopingnivå er blant nøkkelfaktorene for at legeringene skall motstå oksidasjon gjennom å skape et beskyttende lag av SiO_2. Det var også vist at pulverkonsolidering ved gnistplasmasintring ga sterkere bulk pellets, hvor mekanisk styrke spilte en nøkkelrolle i passiv oksidasjon.

Under modulens kontaktdesign ble sølvelektroder og fast-flytende interdiffusjon bindeteknologi brukt. Kontaktmotstanden til de sammensatte modulene ble målt ved hjelp av en automatisert punktkontaktmålingstestrigg. På magnesiumsilisid var den spesifikke

kontaktmotstanden i gjennomsnitt 0.17 $m\Omega cm^2$ med 2.1% standardavvik. For de mangan-silisidenes kontaktareal derimot, var resultatene spredt langs bindingen, hvor 0.07 $m\Omega cm^2$ var laveste verdi og 1.12 $m\Omega cm^2$ den høyeste (81.3% standardavvik).

Til slutt ble modulstabiliteten undersøkt ved å teste ytelsen på de sammensatte modulene. De testede modulene produserte opptil 7.4 mW/cm^2 pulvertetthet ved 400 °C og gikk gjennom mer enn 300 termiske sykluser. Den gradvise nedbrytningen ble funnet å hovedsakelig stamme fra mekanisk svikt i kontaktgrensesnittene og oksidasjon av n-typen magnesiumsilisid i forhold til p-type materialet. Påføring av høytemperaturbelegg reduserte ikke nedbrytningshastigheten, noe som viste at det ville være bedre å kapsle inn modulene for å motvirke effekten av oksidasjon.

Publications

The following papers were published in peer-reviewed international conference proceeding and Journals. The papers are listed in the order they were published in and the original copies are attached in the appendix section.

I. **Antoine de Padoue Shyikira**, Gunstein Skomedal, Tor OskarSætre, Peter Hugh Middleton, (2021). "*Performance evaluation and stability of silicide-based thermoelectric modules*". Materialstoday Proceedings - 17th European Thermoelectric Conference. vol. 185, p. 3467-3474. doi.org/10.1016/j.matpr.2020.05.193

II. **Antoine de Padoue Shyikira**, Naureen Akhtar, Gunstein Skomedal, Tor Oskar Sætre, Peter Hugh Middleton, (2021). "*High temperature oxidation of higher manganese silicides*". Corrosion Science vol. 185. doi.org/10.1016/j.corsci.2021.109327

III. **Antoine de Padoue Shyikira**, Naureen Akhtar, Gunstein Skomedal, Peter Hugh Middleton, (2022). "*The effect of Mo and Ge reactive elements on high-temperature oxidation of higher manganese silicide*". Corrosion Science vol. 194.

doi.org/10.1016/j.corsci.2021.109920

The following article will soon be submitted as a journal article and it is summarized as section 5.3 of this dissertation.

Measurement of the contact resistance in silicide-based thermoelectric modules

Contents

Bibliography **99**

List of Figures

List of Tables

Abbreviations

AC alternating current

BM Ball milling

CTE coefficient of thermal expansion

CVD chemical vapour deposition

DC direct current

DMM digital multimeter

DNV GL Det Norske Veritas Germanischer Lloy

DOS density of states

DSC differential scanning calorimeter

EDS energy dispersive X-ray spectroscopy

HFHIS high frequency induction heated sintering

HMS Higher Manganese Silicide

HP Hot-Pressing

HPCVD hybrid-organic chemical vapour deposition

HV Vickers hardness

ICM intermetallic compound

IEA International Energy Agency

IUPAC International union of pure and applied chemistry

IV current–voltage

LM levitation melting

MGS Magnesium Silicide

MOCVD microwave plasma-assiste chemical vapour deposition

Mtoe Million tonnes of oil equivalent

NASA National aeronautics and space administration

PCM point contact measurement

PF Power Factor

PhD, Ph.D philosophiae doctor

PPS pulse plasma sintering

PVD physical vapour deposition

RT room temperature

RTCVD rapid thermal chemical vapour deposition

RTG radioisotopes thermoelectric generator

S/V surface-to-volume

SEM scanning electron microscope

SiNW Silicon nanowires

SLID solid liquid interdiffusion

SPS Spark Plasma Sintering

SSD solid state diffusion

SSS solid state sintering

TAGS Tellurium Silver Germanium and Antimony

TE thermoelectric

TEG thermoelectric generator

TEM thermoelectric material

TESil thermoelectric silicide

TGA thermal gravimetric analysis

TSDR gency for toxic substances and disease registry

TTT time temperature transformation

USA United States of America

USD United states of America dollar

WHP waste heat-to-power

XPS X-ray photoelectron spectroscopy

XRD X-ray diffractometer

Symbols

z thermoelectric figure of merit

zT dimensionless figure of merit

S Seebeck coefficient

V potential difference

T temperature

Π Peltier coefficient

ζ Thomson coefficient

$\dot{q}$ heat per unit volume

I current

J current density

σ electrical conductivity

κ thermal conductivity

R_i internal resistance

τ relaxation time

E_f Fermi energy

k_B Boltzmann constant

e electron charge

m* density of states' effective mass

h Planck's constant

n free-charge carrier volumetric density

$T_{h/c}$ Temperature at the hot or cold sides

E_d energy difference - band gap

N_{eff}^{C} effective density of states in the conduction band

$\kappa_{l,e,b}$ phonon, charge carrier and hole-electron recombination components of the thermal conductivity

C_v bulk heat capacity at constant volume

ν propagation velocity of excitation

Λ phonon mean free path

L Lorentz number

$\sigma_{e/h}$ electrical conductivity when electrons or holes as majority carriers

$S_{e/h}$ Seebeck coefficient when electron/-holes as majority carriers

I electrical current

R electrical resistance

ρ volume density

V_H hole voltage

B magnetic field intensity

q carrier's charge

μ majority carrier mobility

a thermal diffusivity

c_p specific heat capacity

$\dot{Q}$ heat flux

V_{oc} open circuit voltage

V_{cell} cell or unicouple voltage

$S_{n/p}$ Seebeck coefficient of n or p-type semiconductor materials

$R_{contact}$ contact resistance

$A_{n/p}$ cross-section area at the n or p-type semiconductor materials

R_L load resistance

P_{out} output power

η_{max} maximum conversion efficiency

$\dot{\epsilon}_{ss}$ steady-state creep deformation rate

G elastic shear modulus

b Burgers vector

Chapter 1

Introduction

1.1 Energy and waste heat

In his effort to explore the nature of life, I. Asimov [1] associates the phrase "making an effort" with the definition of life. Scientifically, the ability to make an effort is termed "energy". Therefore, energy is a primordial requirement for all living objects. This analogy allows us to understand (without making it an excuse for) the linear growth trend in the global energy demand [2–4], but also to recognise a corresponding parallel negative impact on the climate as result of increased greenhouse gas emissions [4]. Specifically, humankind contributes a fair share to both the need for energy and detrimental actions related to energy production. However, the will to adopt climate change mitigation strategies has increased and such strategies are being put in place. According to the International Energy Agency (IEA) [5], there is commitment to reducing greenhouse gas emissions by 30-55% by 2030, and further support for optimising energy technologies and/or innovating sustainable solutions is key to reducing emissions (see figure 1.1).

Despite a remarkable increase in renewable energy technologies, the power production side accounts for huge losses originating mostly from oil, coal and natural gas inputs. In the United States of America (USA) [6] (see figure1.2), the energy losses accounted for between 45 and 70% (equivalent to around 10 million tonnes of oil equivalent (Mtoe)) originating from both production and consumption, in year 2018. Waste heat in power generation

or industrial processes comes from various sources: the majority originates from exhaust systems (gas or fluid) and heated air from heating systems (high temperature gases) [7]. Waste heat is commonly recovered using waste heat-to-power (WHP) systems that convert the recycled heat into electric power. The most known WHP are Organic Rankine Cycles [8, 9], Kalina Cycle, turbocharger systems, thermoelectric generator (TEG) [10], etc.

Thermoelectric generators recover waste heat by producing electricity from a temperature difference between a hot surface and a heat sink. Thermoelectricity has found success in spacecraft [11] for which radio isotope generator (RTG) provide electricity and heat. Moreover, uses for the technology have been found in industrial applications, the oil and gas industries and communication, especially in remote areas. TEG waste heat recovery has been tested in the automobile industry, mainly by companies such as BMW, Ford, Renault, Honda, etc [12, 13]. Thermoelectricity also has other applications such as in domestic waste heat recovery, micro heat sources (smart watches [14], wearable devices and clothes [15]), the internet of things [16–20],etc. However, the drawback of the technology is a low conversion efficiency (mostly below 5% [21], although it can reach 15% (laboratory scale) [22] for optimal systems) and the thermal instability of the thermoelectric material in harsh environments. Commercially available thermoelectric materials (TEM) are estimated to have around 1/6 of the Carnot efficiency [23]. Most systems of this type have a zT close to 1, deemed not cost effective by the USA Department of Energy [7] since the device would rarely achieve 5% efficiency. The ultimate goal would be to be able to make a TEG system that can achieve a conversion efficiency of 20%, which would be possible if the materials have a figure of merit(zT) of at least 2, which would be equivalent to recovering $29.3 * 10^4$kWh every year.

There have been several materials systems developed for different purposes or applications, mainly in the waste heat sector (high or low temperature). Key production companies include Tecteg [24], Gentherm [25], Alphabet-xprt Energy [26], Ferrotec [27], etc.;they produce mostly skutterudites, Pb-Te and Bi-Te based modules for low to medium temperature waste heat harvesters, and oxides and SiGe based TEGs as high-temperature harvesters. For industrial applications, most industries require materials/systems that have a lifetime of several years and need little maintenance. In addition, the exhaust products (gas, fluid or other hot products) in the industrial sector are corrosive, and their

temperatures are not stable over time; therefore, it is important that the materials in energy harvesting systems are robust and stable over time.

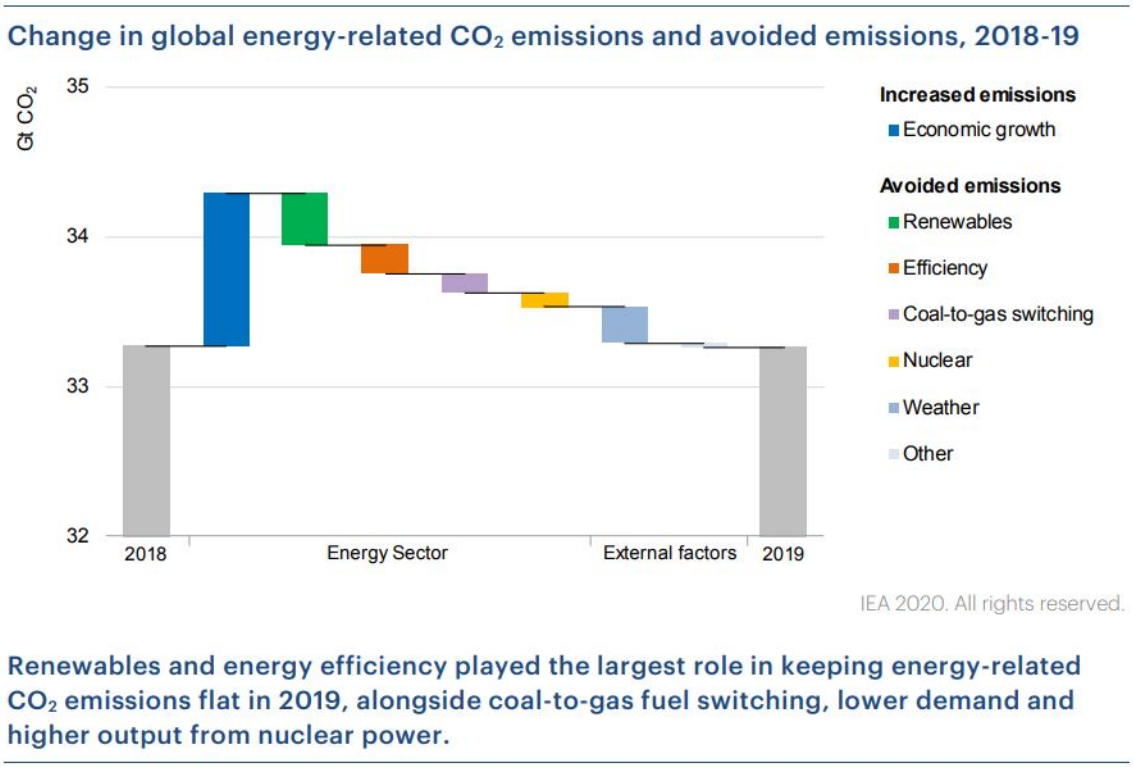

Figure 1.1: Renewables and energy efficiency role to reducing greenhouse gas emissions in 2019 [28]

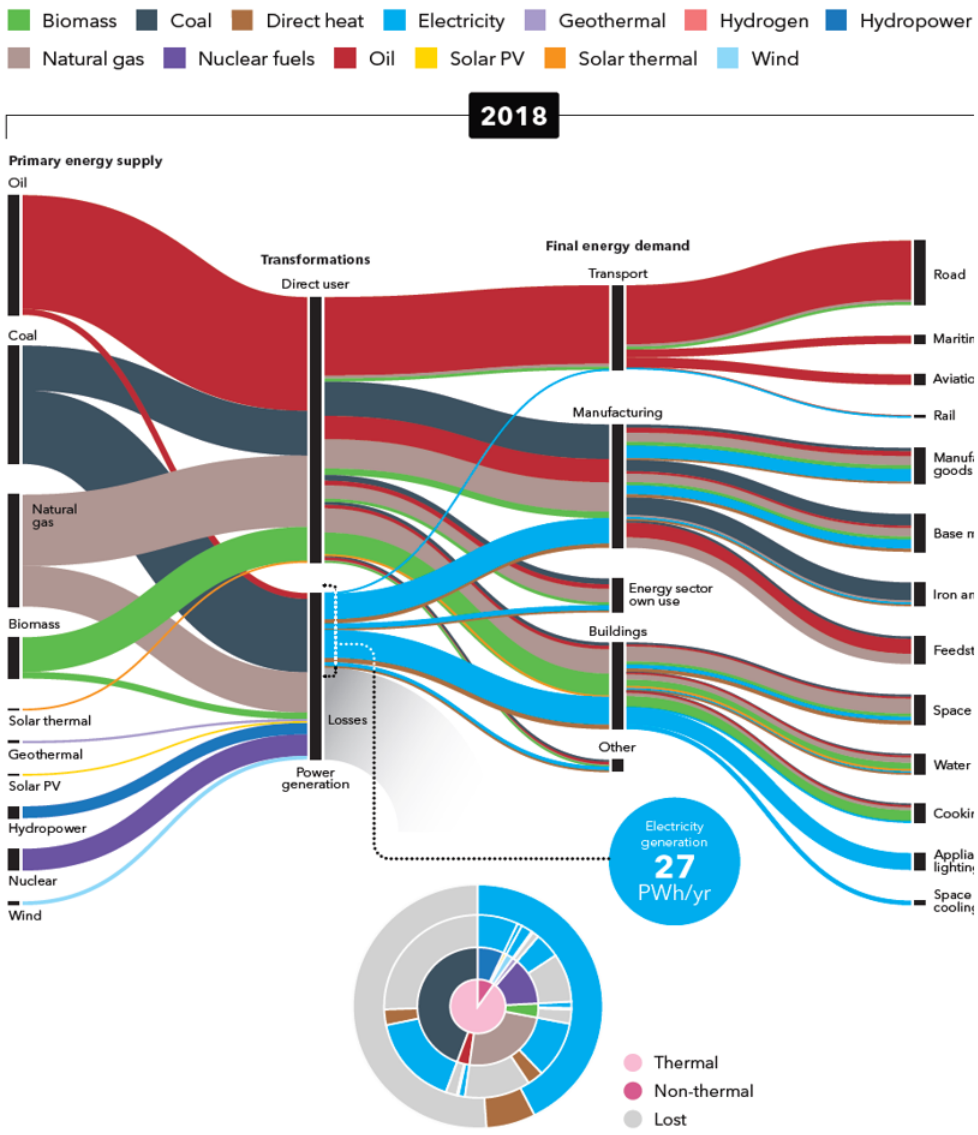

Figure 1.2: USA energy flow: 2018. The concentric pie charts below every flowchart illustrate losses on the power generation side. The inner circle shows the amount and loss type (thermal or non-thermal), the 2nd inner circle shows the input sources, 3rd circle shows the generated electricity and losses associated with each source, finally the outer circle shows the overall output in function of electricity, direct heat and losses for 2018 [6]. Credit: Det Norske Veritas Germanischer Lloyd (DNV GL)

1.2 Scope of the thesis

As briefly discussed in the previous section, thermoelectric power generators are good candidate systems for waste heat recovery in sectors such as transportation and manufac-

turing industries. Though the technology has seen remarkable developments in the last two decades, there are a few major disadvantages that are still holding it back from being competitive on the energy market. These include

- scarcity of raw material resources for industrial mass production and environmental friendliness (e.g. Pb, Hg, and Cd based compounds [29, 30]);
- low conversion efficiency [31,32] compared to other technologies (photo-voltaic modules 20% [33]) ;
- lack of advanced technology for module assembly, instead of pick-and-place;
- lack of structural stability at the materials and module levels;
- and uneffective thermal stability of systems and modules over time.

Silicide-based thermoelectric materials address many of the challenges listed above. The basic chemical elements (Si, Mn, Mg, Fe) and dopants/alloying elements (Sn, Bi, Sb, Ge, Mo, Al, Cr and Re) are relatively non-toxic (almost all do not figure on the US Agency for Toxic Substances and Diseases Registry with the highest scoring 700ppm [30]), cheap, abundant (Si, and Mn), and sustainable. However, the group of materials have got drawback related to finding good n- and p-type couple both with high thermoelectric properties (therefore high "zT"). Through computational screening as done by Løvvik et al. [29], magnesium silicide (Mg_2Si) and higher manganese silicide ($MnSi_{1.75}$) based TEMs, abbreviated as MGS and HMS, respectively, were found to be relatively promising and interesting compounds for thermoelectric applications. MGS have been shown to be, theoretically, a better n-type than a p-type TEM with zT reaching 1.6 at 300K. Similar results have not yet been achieved experimentally, but zT=1.3 at 700K was achieved by improving thermal properties through alloying with tin ($Mg_2Si_{1-x}Sn_x$) [34, 35]. On the other hand, HMS is a good match as a p-type thermoelectric material due to the alloy's thermo-mechanical strength and high resistance to thermal oxidation [36]. Despite all the benefits, including the ease of manufacture, HMS has a disadvantageous zT between 0.3 and 0.5 below 500^0C [36–39].

Several studies have been conducted to improve the thermoelectric properties (Seebeck coefficient and electrical conductivity) while reducing the thermal conductivity of both

HMS [40–45] and MGS [46–50]. By improving the power factor of HMS and introducing heavy atoms (e.g. Re [44, 45, 51], Ru [43]) for phonon scattering purposes, Ghodke S. et.al. [52] achieved an impressive zT of 1.15 at 600^0C marking a step towards to finding a p-type match for MGS. On the other hand, modules' mechanical, environmental, and thermal stability is another capital concern that needs to be addressed. However, little has been reported on the durability of the material and modules.

In response to limited knowledge regarding the stability of silicide-based thermoelectric modules, this project focuses on

- studying the thermal stability in air by investigating the oxidation kinetics and mechanisms of the materials;
- optimizing the interface/bonding layer (composition and bonding parameters) between the electrodes and the TEM;
- evaluating the operation of the developed module by subjecting the module to thermal stresses (thermal cycles) in air and vacuum environments.

1.3 Objectives and research questions

Thermoelectric modules are operated in harsh and varied thermal environments. A good understanding of the materials and module performance in varied conditions is important for optimization, which includes choosing the bonding layer, choosing the best metal electrode and deciding on the module design, thus meeting the application requirements is our main objective.

Based on the main objective, three questions arise:

- What is the operational environment's contribution to TEM degradation (oxidation)?
- How long can TEGs withstand thermal stresses in varied conditions (atmosphere) in the operating temperature range?

- How much do the condition and mode of operation of TEGs affect their life span?

1.4 Thesis outline

This thesis manuscript is split into six chapters as follows:

Chapter 1 describes worldwide energy demand, use and resulting waste, and introduces the benefits of incorporating thermoelectric technology in the world's energy system(s). Finally, it highlights the motivation behind the PhD project and lists its objectives.

Chapter 2 introduces thermoelectric phenomena, electrical and thermal parameters, and conversion efficiency. Moreover, it provides an overview of the TEM (grouped following temperature regimes) and the state of the art in silicide-based TEM, especially HMS and MGS.

Chapter 3 presents a roadmap for testing the stability of thermoelectric modules with an emphasis on bonding technology and testing the long-term stability of the modules.

Chapter 4 describes the methods adopted in this project including sample preparation, thermal oxidation, electroplating, microscopy, and electrical and electronic characterisation techniques.

Chapter 5 summarises the main outcomes of the project as a whole based on the published papers and one scientific article under preparation for publication. The copies of the published papers are appended at the end of this dissertation.

Chapter 6 shows the contribution of the main findings to the study of thermoelectricity and makes recommendations for future projects.

Chapter 2

Thermoelectric materials

2.1 Thermoelectric phenomena

When a temperature gradient is applied to any isolated conductor, an electric potential is generated as a result of the "absolute Seebeck effect" [53, 54]. In 1821, a German physicist, Thomas Johann Seebeck (1770–1831), made use of the theory developed in 1794 by Alessandro Volta by electrically connecting two dissimilar electrical conductors and applying a temperature difference. The energy levels of the materials shifted differently resulting in the generation of a potential difference/voltage across the two unjoined ends of metal A and B (forming a thermocouple) terminals following the "relative Seebeck effect" (see figure 2.1(a) in black path). The instantaneous relationship between temperature gradient and voltage generated by the thermocouple at a given temperature is defined by the Seebeck coefficient as in equation 2.1. The best-known application of the Seebeck temperature-voltage effect is in thermometry where the standard thermocouple converts thermal energy to electrical energy, therefore becoming an accurate thermal sensor.

Contrary to the Seebeck effect, when an electromotive force is applied across the unpaired electrodes terminals, a change in heat occurs at the junctions. The manifestation is called the "Peltier effect", named after Jean Charles Athanase Peltier's discovery in 1834. The heat that evolves at the cold side of the thermocouple is absorbed at the other end of the junction or the hot side (see figure 2.1(a) in red path)); therefore the technology finds

application in refrigeration or heat pumps. The Peltier coefficients at electrode A and B would be expressed as a function of heat transfer (from cold side to hot side) per unit time and inversely proportional to the applied current as in equation 2.2.

In the late 19th century, William Thomson, first Baron Kelvin (1824–1907), found out there was a relationship between the two thermoelectric effects ($\pi = S * T$). This led to a further understanding that if both a temperature gradient and current are applied to a conductor, heat evolves or is released by the conductor, which is known as the "Thomson effect". As shown in figure 2.1(b), if the direction of the applied current opposes the temperature gradient, heat is absorbed, and it is rejected in the opposite case. These thermal effects have both found applications in refrigeration. Although the Thomson effect can be used in both heat exchangers or electricity generation, not many applications have been reported relative to the Peltier and Seebeck based systems.

$$S = \frac{\Delta V}{\Delta T} \tag{2.1}$$

Where S is the Seebeck coefficient[μV/K], ΔV the thermal voltage generated [V], and ΔT the temperature gradient between the hot and cold side [K].

$$\Pi_A - \Pi_B = \frac{\dot{Q}}{I} \tag{2.2}$$

Π_A and Π_B are the Peltier coefficients of electrode A and B respectively, $\dot{Q}$ is the heat absorbed/released by the thermocouple, and I the current through the full circuit.

$$\zeta = \left| \frac{\dot{q}}{J * \Delta T} \right| \tag{2.3}$$

ζ represents the Thomson coefficient[Joule/A*K], $\dot{q}$ the heat generated per unit volume [Joule/m^3], and J the current density[A/m^2].

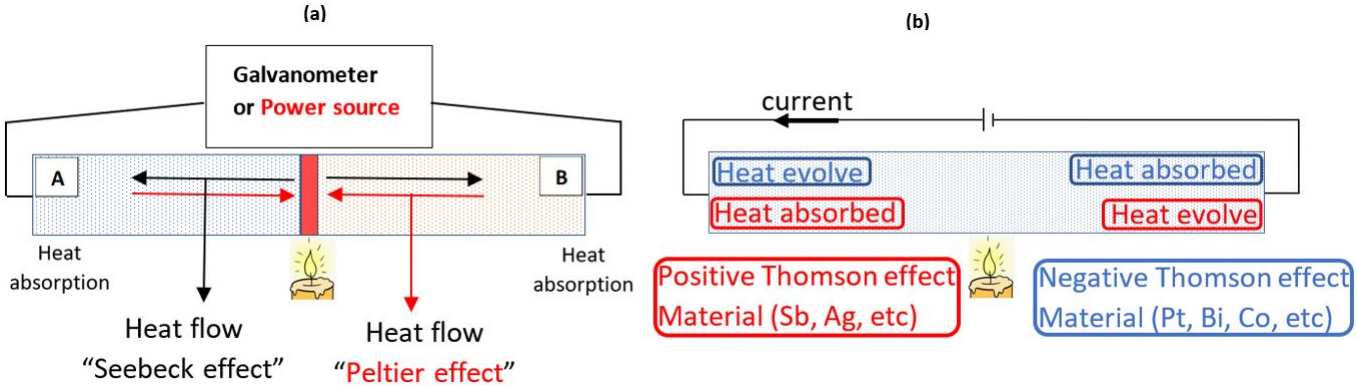

Figure 2.1: Schematic illustration of the (a)Seebeck and Peltier effects, and the (b) Thomson effect.

2.2 Thermoeletric figure of merit and conversion efficiency

The quality of TEMs is determined by a figure of merit "z", which is expressed as the ratio between the materials' generated power factor and thermal conductivity, as in equation 2.4. The power factor ($PF = \sigma S^2$) is the product of the electrical conductivity and the square of the Seebeck coefficient. "z" is expressed in T^{-1} units, but often and conventionally referred to as a dimensionless parameter "zT", T being the absolute temperature, and κ the thermal conductivity.

$$zT = \frac{\sigma S^2}{\kappa} T \tag{2.4}$$

The performance of thermoelectric modules is a resultant of the efficiency of the module equation 2.5. It strongly depends on the temperature gradient between the hot and cold sides of the module and is limited by the Carnot efficiency.

$$\eta_{max} = \frac{T_h - T_c}{T_h} * \frac{\sqrt{1 + z_{p,n}\overline{T}} - 1}{\sqrt{1 + z_{p,n}\overline{T}} + \frac{T_c}{T_h}} \tag{2.5}$$

$$z_{p,n} = \frac{(\sigma_p + \sigma_n)(S_p + S_n)^2}{\kappa_p + \kappa_n} \tag{2.6}$$

where η_{max} is the maximum efficiency of the thermoelectric module, T_h and T_c are the respective hot and cold side temperatures, $z_{p,n}$ is the thermoelectric module's figure of merit (equation 2.6 or z=$S^2_{p,n}/R_i\kappa$) and $\overline{T}$ is the average temperature $(T_h + T_c)/2$.

2.3 Thermoelectric transport properties

Thermoelectric materials are characterised based on their electrical and thermal transport properties. These parameters are combined in one figure of merit as discussed in section 2.2, thanks to Edmund Altenkirch and Abraham F.Ioffe [55]. The thermal-voltage effect or Seebeck effect originates from a thermal diffusion caused by a thermal force acting on particles in a temperature gradient. The transport entropy of each particle leads to the accumulation of electric charges and as a result to an electric field between the hot and cold sides of the TEM [56]. The thermopower generated is denoted by the Seebeck coefficient

(S), while the electrical conductivity [S/m] and the thermal conductivity [W/m*K] are symbolized by σ and κ, respectively, as in equation 2.4.

2.3.1 Seebeck coefficient

The Seebeck coefficient can be expressed as the difference between the average energy of electrons weighted by the relaxation time and the Fermi energy (equation 2.7). Since the Seebeck effect is dependent on several physical processes, voltage related (or diffusive) Seebeck coefficient is most dependent on the diffusion of charge carriers due to thermal gradient [57].

$$S = \mp \frac{1}{eT} \left(\frac{\langle \tau E \rangle}{\langle \tau \rangle} - E_f \right) \tag{2.7}$$

where the angular brackets signify the average energy value of all particles with energy E weighted by the relaxation time τ and the Fermi energy E_f [eV]. Using the Boltzmann statistics, equation 2.7 can be approximated as a function of the density of state mass and inversely proportional to the density of charge carriers as in equation 2.8.

$$S = \frac{8\pi^2 k_B^2}{3eh^2} m^* T \left(\frac{\pi}{3n} \right)^{2/3} \tag{2.8}$$

where k_B is the Boltzmann constant (1.38×10^{-23} [m^2 kg/ sec^2 K]), e is the symbol of the charge carrier [coulomb], here "electron" taken as an example,m^* is the density of states effective mass[kg/m^3], h is the Planck's constant(6.63×10^{-34} [J*sec], n is the free-charge carrier volume density [m^{-3}].

2.3.2 Electrical conductivity

On the other hand, the electrical conductivity (equation 2.9), depends on the charge carrier concentration "n" (equation 2.10) and the charge carrier mobility μ (equation 2.12) derived from the Drude model and the equation 2.9 can be written as $\sigma = n\mu e$ [57].

$$\sigma = \frac{ne^2\tau}{m^*} \tag{2.9}$$

where σ is the electrical conductivity, with n is the free-charge carrier volume density, τ the relaxation time and m^* the density of states effective mass.

2.3.3 Carrier density in doped semiconductors

In intrinsic semiconductors both electrons and holes are charge carriers and $n_e = n_h$ [56, 58]. However, the intrinsic concentration of charge carriers is not sufficient to yield enough current density for practical application for non-degenerate semiconductors [59]. Therefore, the need to add a donor (impurity that can give electrons) or acceptor (impurity that can give holes) to promote one type of majority carrier, electrons or holes, respectively. In doped semiconductors, the carries can be from the dopant ionization or the valence band, therefore the carrier concentration (for example n-type semiconductor so only donors are considered) would be approximated as

$$n_e = 2N_D \left(1 + \sqrt{1 + 4\frac{N_D}{N_{eff}^C} e^{E_d/k_B T}}\right)^{-1} \tag{2.10}$$

$$N_{eff}^C = 2\left(\frac{2\pi m_e^* k_B T}{\hbar}\right)^{3/2} \tag{2.11}$$

where n_e is the charge (electrons) carrier concentration, N_D is the donor or dopant's density [atoms/m^3], $E_d = E_C - E_D$ is the energy difference [eV] between the donor level and the conduction band's closest edge (or the ionization energy of the donor impurity) [eV], N_{eff}^C is the effective density of states in the conduction band, and k_B is the Boltzmann constant.

2.3.4 Mobility and effective mass of charge carriers

The intrinsic mobility of charge carriers is defined as the ratio between the carriers' drift velocity and the magnitude of the electric field applied to the carriers ($\mu = |v|/E$) [60]. Applying Newton's second law to the motion of the charge carriers, the mobility can be expressed by equation 2.12, below.

$$\mu = \frac{e\tau}{m^*} \tag{2.12}$$

The charge of the carriers "e" would be negative for n-type materials, though the mobility is always positive so its absolute value would counteract the charge sign. The density of states (DOS) effective mass of charge carriers (m^*) is also the mass that the carriers seem to have under external excitement or in case of cross-interaction among the carriers

under a certain force (for example: thermal diffusion) [61]. The electron's motion at this level is different from that of a free electron in an intrinsic semiconductor and its mass is expressed as the product of the density of states' mass ($N_v^{2/3}$) and the mass it would have in a single valley (or conduction band minima) along the axes of symmetry within each valley (m_1,m_2 and m_3) [62].

$$m^* = N_v^{2/3} \left(m_1 m_2 m_3\right)^{1/3} \tag{2.13}$$

2.3.5 Thermal conductivity and components

Finally, the thermal conductivity "κ" (equation 2.14) comprises three components, namely the phonon component (κ_l), the charge carrier component (κ_e) and the hole-electron recombination effect component (κ_b). The phonon thermal conductivity or lattice thermal conductivity, formulated as in equation 2.15, is a resultant of the crystal lattice vibration due to thermal diffusion in a material [63].

$$\kappa = \kappa_l + \kappa_e + \kappa_b \tag{2.14}$$

$$\kappa_l = \frac{1}{3} C_v \langle \nu \Lambda \rangle \tag{2.15}$$

where C_v is the bulk heat capacity at constant volume and ν is the propagation velocity of excitation, $\Lambda = \nu\tau$ is the phonon mean free path [distance], and the angle bracket is the average over all modes.

The Wiedemann-Franz law (equation 2.16) states that the electronic thermal conductivity (κ_e) is proportional to the electrical conductivity (of respective majority carriers) at not too low temperature [60]; therefore, as will be discussed later, a good electrical conductor is also a good thermal conductor.

$$\kappa_e = L\sigma T \tag{2.16}$$

where the coefficient of proportionality (L) is the Lorentz number for the free-electron model, though it can also be applied to semiconductors, and T is the absolute temperature.

$$L = \frac{\pi^2 k_B^2}{3e^2} \tag{2.17}$$

with k_B being the Boltzmann constant, and e the electron/hole charge, L is approximated as $2.45 * 10^{-8} W\Omega K^{-2}$, though it varies from material to material.

The final component of the thermal conductivity is κ_b. It is the bipolar thermal conductivity generated by the effect of electron-hole pairs recombination in an intrinsic semiconductor usually due to narrow band-gap in the semiconductors. The latter generates energy in the form of heat at the cold side of the thermoelectric generator and adds the third term of the thermal conductivity parameter expressed in equation 2.18; more details can be found in reference [61].

$$\kappa_b = \frac{\sigma_e \sigma_h}{\sigma_e + \sigma_h}(S_e - S_h)^2 T \tag{2.18}$$

where $\sigma_{e,h}$ are the electrical conductivity of electrons and holes, respectively, and $S_{e,h}$ are the Seebeck coefficients of electrons and holes, respectively. The bipolar effect is negligible in degenerate semiconductors, which is why the bipolar term is often omitted for doped TEM.

2.4 Optimisation of the zT

Achieving an effective TEM requires first and foremost an optimal coefficient of performance (zT) and high mechanical strength. Maximising the zT (equation 2.4), relies on optimising the electronic and thermal transport parameters figure 2.2. Ideally, this means increasing PF equivalent to high σ and S, but at the same time decreasing the thermal conductivity (κ) [64,65]. However, that is not a straightforward operation since, as shown by equation 2.14, the electrical charge carrier is related to thermal conductivity in the denominator of the zT.

Several theoretical studies have been conducted to understand and optimize the zT based on the band structure engineering [57, 59–61, 66–69] and band convergence [70, 71] in TEMs. S, σ and κ_e are all depend on charge carrier diffusion. Based upon theoretical models, section 2.3 presents the three parameters in function of the DOS mass and carrier concentration. Empirically, the m^* is the main parameter to maximise to increase the PF. As reported on different thermoelectric systems (PbTe, PbSe, Mg_2Si,etc) [71] and by equation 2.13 multi-valley band structure would increase S and σ [69]. However, it is important to keep in mind that m^* must be such that the carrier mobility is not too low, therefore allowing for a balance between increased DOS and carrier mobility. Overall,

heavy doping using heavy atoms as a dopant would be a good solution to not only increase the carrier concentration but also reduce the lattice thermal conductivity. Finally, adopting advanced and available grinding technologies such as high-speed planetary ball milling can reduce the powder particle size, promoting/increasing the grain boundaries (which implies increased phonon scattering), therefore reducing the lattice thermal conductivity.

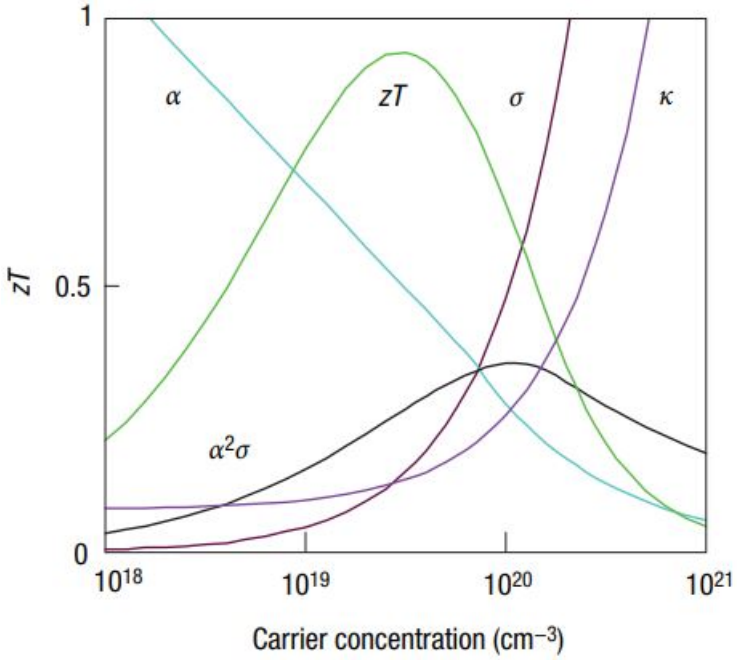

Figure 2.2: A representative diagram of the optimization of zT by tuning the thermal conductivity, the Seebeck effect and electrical conductivity [72]

2.5 Thermoelectric materials

Since Seebeck first discovered thermoelectric materials [73], several other material systems have been investigated targeting distinct areas of application. The types of the state-of-the-art materials that have been studied include inorganic [74] and organic [75] with different physical structures from macro- and nano-sized materials to thick and thin films [76]. Although milestones have been achieved in each category of materials, in this report we will focus on inorganic macro-sized bulk thermoelectric materials. In this section, the materials are divided into three categories based on the temperature range of application and tables 2.1 and 2.2 give a summary of the state-of-the-art materials' electrical and

mechanical characteristics.

2.5.1 Low temperature (RT - 200 °C)

Bismuth telluride has been the leading material at low temperature from near room temperature to around 200 °C, thanks to its low lattice thermal conductivity and low effective mass of carriers (and therefore high carrier mobility) [77]. However, the material system has drawbacks related to bipolar conduction effects stemming from its narrow band gap of 0.14eV [78,79]. The bipolarity effect is partially reduced by alloying with Sb_2Te_3 for p-type BiSbTe-based TEM and with Bi_2Se_3 for n-type BiTeSe-based system [80]. In the 1960s, this material system dominated the thermoelectric cooling industry and it was used in several electric devices [81]. Not long ago, they were found to have good thermoelectric properties near room temperature in power generation mode. The research conducted was mainly to optimize majority carrier concentration in the range of 2-4x$10^{19}$$cm^{-3}$. Several approaches were employed, among them, dopant inclusion; Yu Pan et al. [82] and Chen Lidong et al. [74] reviewed a number of preferred donors (e.g. Ga [78]) and acceptors (e.g. Pb, Sn, etc). In addition, P and Cu can be used both as n- and p-type dopants, respectively. Other mechanisms used so far are nano-inclusion, where nanofiller materials are used to further reduce the lattice thermal conductivity [79].

The lattice thermal conductivity issue has also been approached by using different methods to grow Bi_2Te_3 nanostructure materials, namely by straight-forward arc melting, solvo- or hydro-thermal synthesis, the Bridgman technique, or other methods [83]. Besides Bi-Te-based alloys, Si nanowires (SiNWs) are other good candidates in the low temperature thermoelectric materials range [84, 85]. As mentioned above, BiTe-based compounds have dominated the low temperature range for a while with a figure of merit ranging from 1 to 1.5 since the 1950s. MgAsSb is a new material system reported as a competitive candidate to bismuth tellurides and interestingly with similar zT [86, 87]. The development of other material systems is important in this temperature range since more than two thirds of the main energy used is wasted in the temperature range below 300 °C. We should also not forget areas such as wearable electronics that use TEG technology [15, 88, 89], internet of things [19] and other electronic devices such as sensors.

2.5.2 Medium temperature (200 °C - 600 °C)

The mid-temperature regime has been dominated by PbTe alloys and group 14 (by IUPAC numbering [90]) based tellurides, mainly Ge [91] and Sn [92] based compounds. Different alloys and dopants have been investigated, as by [93] who studied Na, Mg, Mn and Se for p-type doping purposes, while I, La, Mn, Bi, and S were on the n-type side. Similarly, $(GeTe)_{0.85}(AgSbTe_2)_{0.15}$ also known as TAGS, short for Te/Ag/Ge/Sb [94, 95], was reported to be a good p-type TEM in the mid-temperature regime with a zT of up to 1.3. Unfortunately, because of toxicity and scarcity of the elemental constituents of PbTe-based and TAGS compounds, sustainability in these material groups is a challenge. Pb (lead) is listed as number two on the ATSDR (Agency for Toxic Substances and Disease Registry) 2019 substance priority list [96]; similarly, Te is both toxic and rare (with less than 0.004ppm in the Earth's crust) [29], while Ge is relatively expensive with an average price of 1305USD/kg as of Sept./2021 [97].

Single-crystalline SnSe based materials were recently proposed as a good and sustainable solution for thermoelectric application in the mid-temperature regime. The materials set record high thermoelectric properties, with an impressive zT of 2.6 at 923K for p-type [98] and zT values between 2.2 and 2.8 at 733K for Bi- and Br-doped n-type SnSe [99, 100]. However, the single-crystalline compounds suffer from oxidation due to the formation of Sn-based oxide, which leads to increased thermal conductance and therefore poor thermoelectric properties. The latter remains a challenge for poly-crystalline compounds [101], though C.Zhou et. al. [102] have shown that with careful reagent purification and removal of the oxide, an impressive low thermal conductivity was achieved at 0.07W/m.K (lower than single-crystalline) and zT=3.1 at 783K.

Skutterudites are other TEMs that gained worldwide attention in the late 20th and early 21st centuries in the temperature range between 200 and 600 °C. The compounds are in binary and/or ternary structures, with chemical formula MX_3 (where M is group 9 of the periodic table of elements and X represent the pnictogen elements P, As, and Sb). C. Uher [103] thoroughly describes the material's crystal structure, with the most interesting fact being that large structural voids are created from distorted and tilted MX_6 octahedrons. The voids, also called cages, can be filled with other species, resulting in

so-called filled skutterudites. Considerable work was done to try and find the best fillers, as well as the best synthesis methodology. The state-of-the-art reported zT is around 1 for electronegatively filled [104–106] and 2 for electropositively filled skutterudites [105, 107–111].

Clathrates are another known group of materials researched for thermoelectric applications in the mid-temperature range. The composition of the compounds is of two types: type I is $A_xB_yC_{46-y}$ [112–114] and type II is $A_xB_yC_{136-y}$ [115]with A, B and C, representing alkali or alkali earth metals, group 13 and group 14 elements, respectively. While clathrates have not yet shown ideal thermoelectric properties, the zT reported so far ranges from 0.5 to 1, which is ok, but further improvement would be appreciated.

2.5.3 High temperature (>600 °C)

Thermoelectricity at high temperature is challenging for most of TEMs due to service stability concerns. As of 2020, a limited number of materials have been reported as best candidates for high-temperature application, namely Oxide-, SiGe-, and Zintl-based TEMs [116]. Oxide-based TEMs were long regarded as not convenient for thermoelectric application due to very low carrier mobility and high lattice thermal conductivity; it was not until single crystal $NaCo_2O_4$ was discovered by I. Terasaki [117, 118] to have thermal power (100μW/m.K at 300K) comparable to Bi_2Te that it was believed to be a promising material system for high temperature application.

Today, several material systems have been investigated, and studies to optimize their transport properties have been carried out using heavy doping to increase the carriers' concentration and through nanostructuring [119] to reduce the lattice thermal conductivity. The relatively good compounds among those studied are n-type CaMnO [120, 121], SrTiO [122–125], CaCoO [126, 127] based TEMs which showed improved thermal power, though with high total thermal conductivity ranging between 150–200 μV/K (absolute values) and 1.6–4 W/m.Km, respectively.

Similarly, single and multi-crystalline p-type CaCoO [128–132], NaCoO [133], and many more (BiSrCoO, LaCoO, CuAlO, etc. based [118]) TEMs were researched and their

thermal conductivity was impressively reduced to below 0.5W/m.K, which is high relative to their n-type counterparts, but unfortunately with a poor zT just below 0.6. However, a better and more promising BiCuSeO-based oxide TEM [134–137] is currently a topic of interest due to reported high zT ranging between 1 and 1.5, though further improvement of thermal and electrical transport parameters is needed. Finally, other oxides reported by [116] are wide band gap ZnO, Ti/SnO_2, In_2O_3 and V_2O_5 based TEM; they produced a promising high Seebeck coefficient but also had high thermal conductivity around 5.8 W/m.K.

Table 2.1: Composition, thermoelectric properties, and synthesis methods of state-of-art thermoelectric materials. AM: arc melting, HP: hot pressing, SPS: spark plasma sintering, LM: levitation melting, BM: ball milling, HFIHS: high frequency induction heated sintering.

Material Family	Elemental composition	Temperature range [°C]	Conduction type	TE properties				Synthesis Method	Stability	Application	References
				$\sigma[10^4 S/m]$	κ [W/m.K]	S [μV/K]	ZT max				
Half heusler	XYZ X: Hf, Zr, V, Ta, Nb Y: Ti, Ni, Fe, Bi Z: Sn, Sb, Ge	400 - 900	n	6.6 - 12	2 - 3.5	180 - 300	1 - 1.5	AM + HP/SPS			[138–145]
			p	∼10	3 - 4	∼200	1 - 1.6	LM + BM +HP			
Bi telluride	BiTe, BiTeSe	<200	n	5 - 6	0.3 - 1.1	100 - 150	0.8 - 1.5	BM + HFIHS/SPS	Stable below 200 °C	Near room temperature application Sensors (in medical, automobile, etc).	[146–150]
	BiSbTe		p		<1	∼200					
MgAgSb	MgAgSb, MgAgSb+Zn/Ni	<200	p	∼5	∼0.7	∼210	∼0.75 @ RT ∼1.5 above 150 °C	BM + HP			[151, 152]
Group-XIV Telluride	PbTe, GeTe and SnTe	300 - <600	n & p	1 - 5	>1	abs(240 - 330)	1.2 - 2.5	Melting-Quenching-Annealing + SPS			[153–157]
Cu and Sn Selenides	Cu_2Se and SnSe	500 - 600	p	–	–	–	1 - 2 (for bulk) 2 - 3 (for thin film)	Annealing + SPS Metal deposition for thin films			[158–164]
Skutterudites (MX, M: Co, Ni and X : mostly Sb)	Fillers: Ba, Yb, Fe, Te, La, Mm, DD, Sr, Se etc	500 - 600	n	6.2 - 14	2 - 3.4	abs(150 - 230)	1 - 2	Melting - Quenching/Annealing + HP / SPS			[104, 109–111, 165–170]
	Fillers: DD, Fe, Sn, Ca, etc		p	1.5 - 8.9	1.8 - 2.8	∼180	∼1.5				
Clathrates ($A_xB_yC_{46-y}$ and $A_xB_yC_{136-y}$)	A: alkali or alkaline earth metals B: Group-XIII and XIV elements	200 - 500	n	2 - 8	0.5 - 1.2	∼200	<1	Melting - grinding - sintering - Annealing			[115, 171–173]
Oxides	Ca-Mn-O and Zn-O	600 - 900	n					Calcination - Cold press - SPS			[128, 129, 131, 174–182]
	Ca/Na/La/Bi-Co-O and $CuAlO_2$		p	1 - 5.8	0.5 - 2	∼200	<0.5	Calcination - Cold press - SPS SSS for CuAlO			
	BiCuSeO - system			∼1.7	0.65	200	1 - 1.5	Mechanical alloying and Resistance pressing sintering			[134, 183–185]

2.5.4 Silicide-based thermoelectric materials

Silicide-based TEM are among materials for thermoelectric energy conversion, specifically for power generators in the mid- and high-temperature applications [186–188]. Silicon germanium ($Si_{1-x}Ge_x$) and ruthenium silicide (Ru_2Si_3) were reported as good candidates for high temperature application. However, Ru_2Si_3 has not been studied much relative to SiGe because the compound is expensive and the alloy lacks dopant candidates. Uranium was tried as a dopant with different concentrations [189] and a zT of 0.04 to 0.09 (at 800°C) with the Seebeck coefficient way below -50$\mu V/$K. However, the compound also showed much improved thermoelectric zT, with doping with 4 at%Rh [190] and substituting Ru with Re and/or Si with Al [191], resulting in the zT equivalent of 0.8 and around 0.5, respectively. SiGe, on the other hand, is well regarded in the high temperature range due to its robustness to oxidation. Both n-type [192–194] and p-type [192, 195–197] SiGe-based TEM showed a higher figure of merit (close to 2) compared to the oxides. The zT was achieved using different optimisation techniques such as boosting the carrier concentration through doping, nanostructuring and/or forming nano-composites by including nano-materials (for example TiB_2 [197] or YSi_2 [195] nano-inclusion).

Other silicide semiconductors studied for thermoelectric applications are mostly silicide compounds based on alkaline earth and transition metals [187]. Alkaline earth silicides are mostly not reliable due to high chemical reactivity at low temperatures. The compounds based on transition metals ($FeSi_2$, $CrSi_2$, $MnSi_x$(x=1.71-1.76), $ReSi_{1.75}$) and Mg_2X (X are Si, Sn and/or Ge), are quite interesting and have most recently been studied for medium temperature applications (300-600 °C)owing to their good thermoelectric properties and cost effectiveness (cost below 200$/kg [198]). Moreover, despite $ReSi_{1.75}$ having a high figure of merit (around 0.7 at 800°C [199]), which could make it a SiGe counterpart at high temperature, it presents an anisotropic Seebeck coefficient along the a and c axes. Analogously, studies of Cr-based silicides faced challenges related to high thermal conductivity. CrSi2 is a degenerate semiconductor with a band gap of around 0.35 eV and therefore high electrical and thermal conductivity with zT ranging between 0.2 and 0.3.

2.5.4.1 Higher manganese silicides

Higher manganese silicides (HMS) are intermetallic compounds from the family of Nowotny chimney ladder compounds. The Nowotny phase's crystal structure was derived from the general formula T_nB_{2n-m} [200] and was similar to that of $TiSi_2$ group [201,202]. HMS exist in many phases such as, Mn_4Si_7, $Mn_{11}Si_{19}$, $Mn_{15}Si_{26}$ and $Mn_{27}Si_{47}$ (see figure 2.3), which, despite manifesting different lattice parameters (a=b=5.52-5.53Å and c=17.46-117.94Å), have similar electronic band gaps of 1.2 eV at room temperature and 0.8± 0.1eV above 700 °C [203]. The p-type HMS poses a thermoelectric zT of around 0.5 above 750 K and high mechanical strength (above 1000±40 HV).

The synthesis of HMS is usually done by mixing, melting and casting, followed by ball milling, and consolidated by both HP or SPS. Commonly, undoped HMS contains dispersed 50/50 MnSi and Si phases, which have a detrimental effect on the thermoelectric properties as well as the thermal stability of HMS. L.D. Ivanov [203] showed that annealing the HMS crystals for 400 hours increased the secondary phase's solubility; nonetheless, by substituting "Al" or "Ge" on the "Si" site, this project showed that doping with at most 0.5 at%Ge dissipates the MnSi striations, or at least would require less annealing time. To improve thermoelectric performance, different dopants were tested (by different researchers), and details on the state-of-the-art alloys' composition transport properties and figures of merit are summarized in table 2.2.

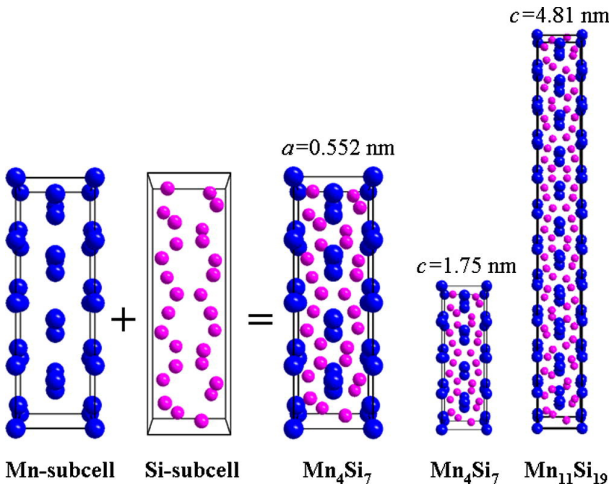

Figure 2.3: Graphical illustration of two of the HMS family's unit cell structure [204].

2.5.4.2 Magnesium silicides

Analogously, magnesium silicide (Mg_2Si or MGS) based TEM is the best n-type candidate for HMS (p-type) in silicide TE modules. The compound exhibits a narrow band gap of around 0.7 eV and a cubic crystal structure 2.4. Typically, MGS undoped has a zT of 0.1–0.2 [205, 206], though alloying/doping with different elements (Sn, Sb, Bi, Ge, Al, Cr,etc) and convergence of the conduction band boost the zT to around 2 (check table 2.2). Despite their good thermoelectric performance, MGS alloys suffer from mechanical instability. The typical MGS synthesis process follows a solid state diffusion process and hot pressing or plasma-activated sintering. Nonetheless, consolidation is still a challenge, especially for magnesium silicide stannides, due mainly to the low melting point of tin. Moreover, the challenging sintering process increases the production time of the alloys, therefore impeding the possibility of mass production. Further improvement of the MGS sintering method, most importantly making it easy to replicate, would be an important advancement in the medium temperature regime.

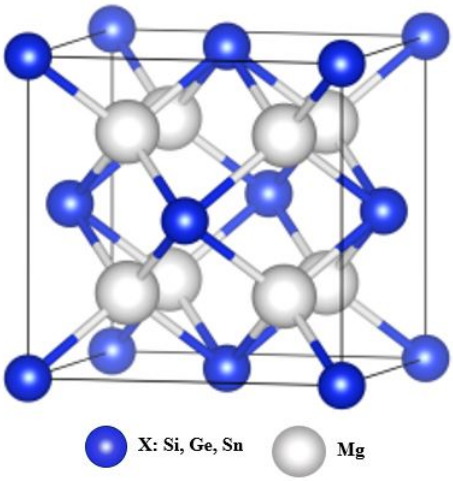

Figure 2.4: Conventional unit cell crystal structure of Mg_2X, X: Si, Ge, or Sn [207].

Table 2.2: State-of-the-art High zT Silicide thermoelectric materials, respective of temperature range, composition and synthesis methods. SSS: Solid-state synthesis, PPS: Pulse plasma sintering

Material type	Composition, dopants	Conduction type	Temperature range [C]	TE properties				Mechanical Properties	Synthesis method	Stability	Reference
				$\sigma[10^4$S/m]	κ [W/m.K]	S [μV/K]	ZT max				
HMS alloys	HMS	p	200 - 600	<2.7	>2	160 - 230	<0.5	CTE: 7- 12 [208] V. Hardness: 10.5 - 12.5 GPa Fracture t.: 1.6 - 2 MPam$^{1/2}$ [209]	Melting - SPS	-Mechanically strong -Thermally stable below 500 °C	[210–216]
	V, Cr, Re, Ge, Al, Ag, Ru.			3.25 - 7	1.5 - 3.4		0.5 - 1.1				
MgX, X: Si, Ge or Sn	Bi, Ge, Li, Sb,Al	n	<600	7.8 - 11	2 - 4	abs(100 - 350)	0.8 - 1.4	Vickers Hardness: 484.2±15.4 - 556±39 [209, 217]	SSS/co-melting - HP/SPS	Require oxidation protection above 400 °C Reduced mechanical hardness [208]	[206, 218–221]
	Bi, Cr, Al, Ge, Ag	p		∼10	∼2.5	∼200	∼1.5				[206, 222–224]
CrSi2	- SiGe nano inclusion -WSi - Mo or Nb doping	p	300 - 500	∼4	∼4.5	150 - 180	<0.3		Melting + SPS	Oxidation stable	[225–228]
RuSi	U	n	>600			<-50	<0.1		Arc melting - Crystallisation		[189]
	Rh					175	0.77				[189]
	Re	p	700		1.5	200	0.47				[229]
ReSi, FeSi	Mo and Cr, P, SiGe nano inclusion	n and p	>700				∼0.7		SPS or PPS	Thermally metastable especially FeSi-based alloys	[199, 230, 231]
SiGe	SiGe Nano structures	n	750 - 900	2.7 - 4.7	2 - 3	abs (250 - 350)	1 - 1.5		Melt spinning + SPS	Relatively very stable at high temperature.	[232–236]
	TiB2 and YSi2 nanostructure inclusions	p	>800	2.8 - 4 .4	3 - 5	250 - 350	1 - 2		Planetary milling + HP		

2.6 Material synthesis

2.6.1 Growth from the melt

The selection of TEM, as mentioned in previous section, depends on the materials' mechanical strength in addition to their electrical and thermal transport properties. TEM in a module are subjected to a high temperature gradient and mechanical compressive stress between the hot and cold side. Traditionally, the elemental constituents would be mixed and melt cast (by induction melting [237], arc melting [238] or any other capable furnaces) at high temperature to produce a homogeneous crystalline structure. However, the crystals grown using traditional melting and crystallization methods are not suitable for thermoelectric applications due to their high porosity and poor mechanical strength. Therefore, further processing techniques (pressing/sintering as in figure 2.5) are required to increase mechanical strength by optimally reducing the porosity of the cast ingots, as will be discussed in the next section.

Figure 2.5: Overview of the conventional melting and pouring synthesis method and further material processing from the as cast ingots

2.6.2 Solid state diffusion technique

Despite the practicality of the melting and casting method, some materials systems are very hard to synthesize using this method. In the case of $Mg_2Si_{1-x}Sn_x$, the presence of magnesium as one of the basic elements and its high affinity to oxygen containing atmosphere renders it almost impossible to treat the material at high temperature. Solid state reaction technique is one of the other forms of synthesis techniques. The starting elemen-

tal constituents are mixed in a controlled atmosphere (a glovebox, for instance, is used in an inert atmosphere) and similarly milled and cold pressed into pellets (figure 2.6). The pellets are then put in crucibles and annealed at high temperatures that are nevertheless lower than the melting temperatures of individual constituents. The optimal sintering or subsequent annealing parameters (temperature and time) are important to sufficiently react the mixed constituents and form pure and homogeneous crystalline phases.

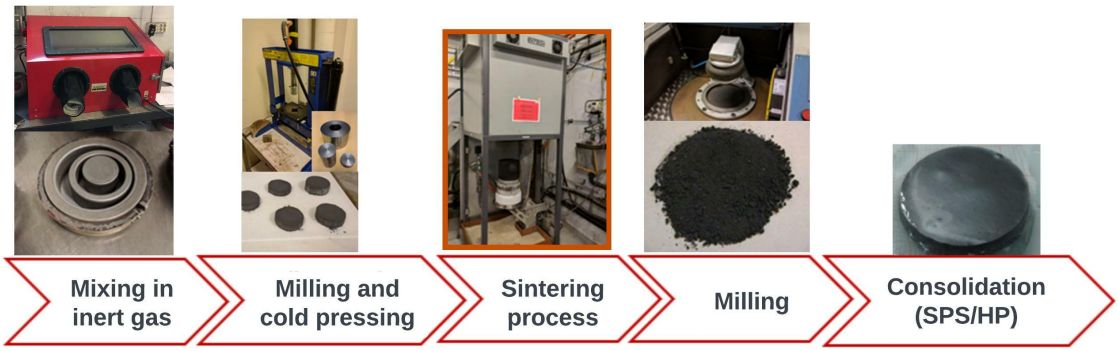

Figure 2.6: Overview of the solid-state synthesis method

2.6.3 Powder densification

Powder particles are compacted at a controlled temperature (below the melting temperature of individual/initial phases) and pressure to obtain dense and homogeneous bulk materials. During sintering the main driving forces are the powder particle roughness, the atoms' nature, the particles' defects at the grain boundaries and, most importantly, the average particle size of the powder. Therefore, grinding method and powder properties are among the main requirements to achieve a dense and homogeneous bulk compound.

The best-known laboratory densification methods for TEM are HP and SPS. During HP, pressure and temperature are simultaneously exercised on powder ground to nano/micro sized particles in an inert/vacuum filled furnace. The technique promotes the formation of a homogeneous phase pertaining to interdissolution between the starting elements and results in non-stochiometric or stochiometric alloys. However, the technique has several drawbacks:

- it requires a long holding time (compared to SPS and is therefore not efficient and presents a challenge for mass production;
- the produced pellets are porous and brittle, meaning that the resultant bulk materials present poor thermomechanical strength for thermoelectric applications;
- Z.Dashevsky and S.Skipidarov [239] have shown that during pressing, the thermoelectric properties (σ, κ and z) of the sintered pellet are higher towards the core of the vertically pressed pellet, stemming from the grains' preferential ordering during pressing;
- and finally, the thermal oxidation potential of the hot-pressed materials is higher than for cast materials.

SPS is a uniaxial force sintering technique that utilizes high heating and cooling rates (1000 °C/min) to enhance densification properties during power consolidation [240, 241]. The technique has recently been a leading technique for power compaction purposes due to resultant materials' high mechanical strength and homogeneous microstructure across the produced polycrystalline ceramics. Moreover, SPS, as counterpart of HP, has been a success at the laboratory scale; however, high throughput SPS systems are being developed and some on the market might be applicable on a mass production scale. The technique has found applications in several material systems, namely nanocomposites, hard metals, ceramics and diamond-based materials but most importantly in thermoelectric materials [242]. The benefits for thermoelectric materials are that SPS increases the grain boundaries in bulk materials, reduces the lattice thermal conductivity via increased interfacial phonon scattering and therefore plays a role in improving a TEM's figure of merit. Nonetheless, SPS presents some adverse effects such as expelled tellurium in BiTe-based alloy systems [242], Sn oxidation at the p-type polycrystalline SnSe alloy [243], melting of elements with low melting temperature such as Sn in $Mg_2Si_{1-x}Sn_x$ alloys, etc.

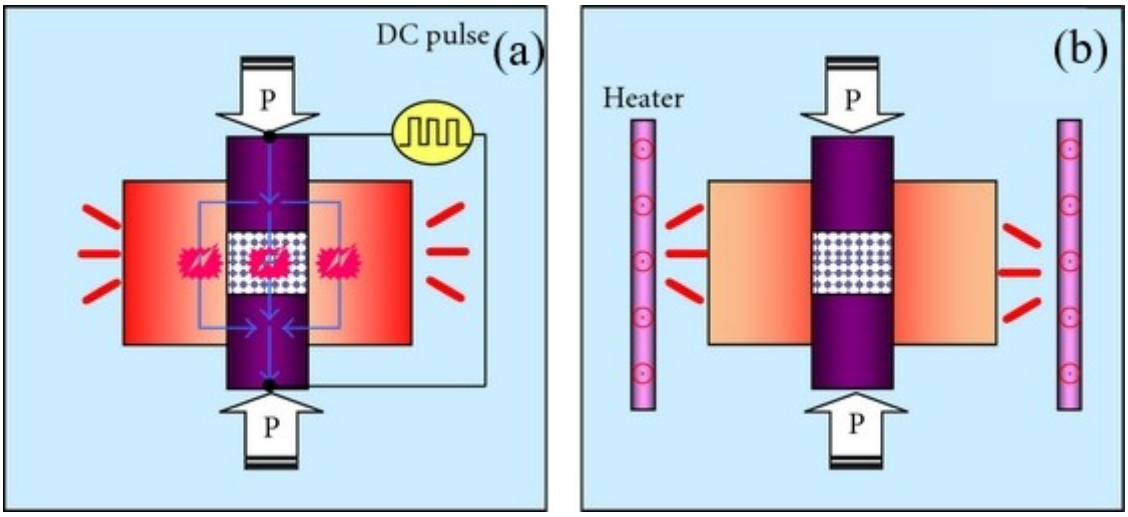

Figure 2.7: Comparison between (a) SPS and (b) HP concerning heat generation mechanisms' differences and physical structural similarities. Courtesy of P. Cavaliere et al. [240]

2.7 Material characterisation techniques

The properties of TEM are determined by conducting measurements of the parameters of the figure of merit, which are the thermoelectric power (or Seebeck coefficient), the electrical conductivity or resistivity ("σ" or "ρ"[mΩcm]) and the thermal conductivity "κ". These parameters are variables that the thermoelectric society uses as criteria to compare different compositions and decide which are of interest, in addition to tuning or optimising the alloys' nominal composition (decide dopants type and concentration). It has, therefore, been important to use quick and accurate methods to set reliable mass production guidelines.

2.7.1 Electrical conductivity measurement

In the early 1800s, electrical resistance (R) and conductance (G) were the physical quantities that could be determined by acquiring the current and voltage characteristics of a conductor or material under study. However, the reliability of these quantities was challenged by their dependence on specimen geometry, which means that samples of the same material could have different resistance. Resistivity, on the other hand, does not depend

on the shape of a material but its composition; it also depends on the synthesis methodology (i.e compounds with similar initial composition, synthesized in different batches may have different resistivities). The Van der Pauw method is a method adopted in many state-of-the-art test instruments to determine the resistivity and Hall voltage of the test sample. As detailed in section 2.3, the electrical conductivity very much depend on the charge carrier mobility "μ" (which is also a function of the effective mass) and concentration "n", both of which are fundamental parameters for semiconductor materials.

Van der Pauw test method.

Figure 2.8 (a) is a representation of two diagrams where in case of blue connection, red should be omitted and the other way around. Passing current I_{CA} and measuring the voltage drop in V_{BD} we can calculate R_1=V_{BD}/I_{CA} and similarly, for the red circuit, R_2=V_{BA}/I_{CD}. L.J. Van der Pauw [244] defines a relationship between R_1 and R_2 as in equation 2.19, which can be numerically solved for R_s the sheet resistance and the bulk resistivity calculated as by equation 2.20, where "d" is the sheet thickness

$$exp\left[-\pi * \frac{R_1}{R_s}\right] + exp\left[-\pi * \frac{R_2}{R_s}\right] = 1 \tag{2.19}$$

$$\rho = R_s * d \tag{2.20}$$

Moreover, the Van der Pauw method is used to test the Hall coefficient. If we apply an electric current in a sheet of semiconductor material and a magnetic field perpendicularly to the current as in figure 2.8 (b), electrons will accumulate on one side of the semiconductor as a result of the Lorentz force, thereby creating a potential difference known as the Hall voltage (V_H equation 2.21) due to uneven distribution of charge carriers.

$$V_H = \frac{IB}{qnd} \tag{2.21}$$

where I is the applied current, B is the magnetic field [Tesla], q is the carrier's charge [coulomb], n is the majority carrier concentration and d is the sheet thickness. Finally, the sheet carrier density can be determined as the product of the majority carrier concentration and the sheet's thickness ($n_s = n * d$) or by equation 2.22, and the majority charge carrier mobility (μ) by equation 2.23. It is, however, very important to note that Van der Pauw testing requires very good ohmic contacts, dense and uniform samples, and avoidance of Peltier and photovoltaic effects.

$$n_s = \frac{IB}{q \mid V_H \mid} \tag{2.22}$$

$$\mu = \frac{1}{qn_sR_s} \tag{2.23}$$

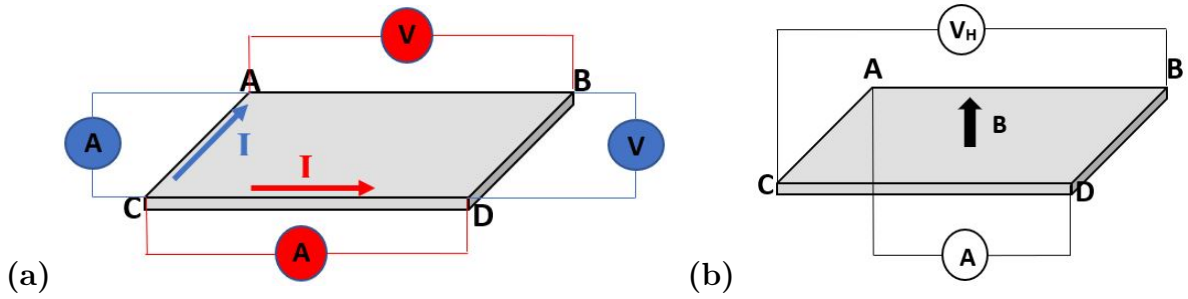

Figure 2.8: In diagram (a) red contacts show the current leads and flow, similarly to blue contacts and current flow. Diagram (b) shows diagonal contacts for current contacts and voltmeter leads for Hall voltage measurements. The direction of the magnetic field is out of plane.

2.7.2 Seebeck coefficient measurement

The Seebeck coefficient measurement is a straightforward technique relative to the other two zT parameters. The Seebeck coefficient is defined as the coefficient of proportionality between the voltage generated (ΔV) when a temperature difference is applied across a TEM. There are three commonly used methods depending on where the thermocouples (temperature sensors) and voltage test leads are connected as in figure 2.9. Details on the three methods, mode of operation, uncertainty measurements, etc can be found in references [245–247].

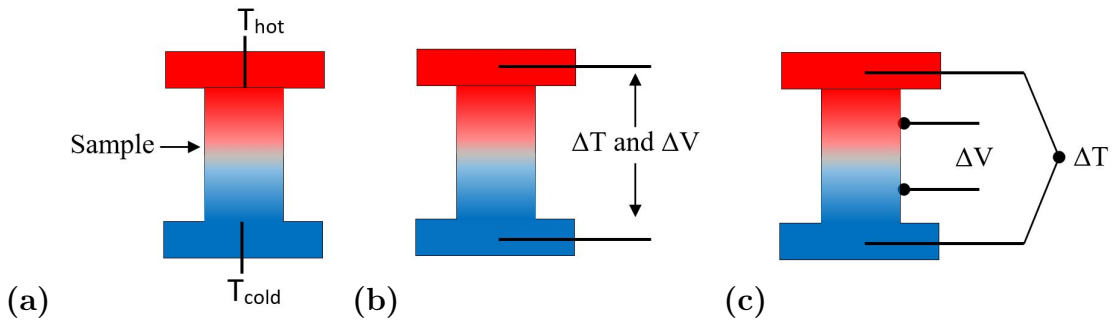

Figure 2.9: Three common Seebeck coefficient test methods: (a) the uniaxial 4-point method [245], (b) the 2-point method [246] and (c) the off-axis 4-point method [247]. The color code represents the temperature gradient between the hot side (red) and the heat sink (blue).

2.7.3 Thermal conductivity measurement

Thermal conductivity, on the other hand, is measured using different methods, mainly steady-state or transient-domain methods. When a steady-state method is used, the test system must reach chosen steady temperature so a signal can be recorded and Fourier's law used to compute the thermal conductivity (equation 2.24). The drawback of this method is that it is not time efficient. With the time-domain method, however, several signals or measurements are recorded during the heating process. Among the most used methods in the state-of-the-art instruments are the transient hot probe method for measuring thermal conductivity for gases, liquids, solids, etc. Moreover, the laser flash method for measuring thermal diffusivity is employed in many instruments. The laser flash technique is mainly used on thick discs where the laser heats one side of the sample and the temperature rise on the opposite side (though the sample thickness) is monitored and the thermal conductivity calculated as in equation 2.25.

$$\dot{Q} = -kA\frac{\Delta T}{d} \tag{2.24}$$

$$k(T) = a(T) * c_p(T) * \rho(T) \tag{2.25}$$

where k$[Wm^{-1}K^{-1}]$ is the thermal conductivity, $\dot{Q}$ is the heat flux [W/m^2], A is the surface area, a$[m^2s^{-1}]$ is the thermal diffusivity [m^2 sec^{-1}], c_p is the specific heat capacity [Joule/K], and ρ is the volume density.

Chapter 3

Thermoelectric modules

As described in section 2.1, thermoelectric (TE) modules can be coolers or power generators by the Peltier and Seebeck effects, respectively. Although, TE refrigeration devices have been the most extensively studied in the last half century, TE generators have found success in spaceships in areas where solar, chemical and fuel cell power sources are out of reach. TE devices has been stable and reliable; for instance, as part of the National Aeronautics and Space Administration (NASA) [248] active missions, Voyager 1&2 probes have been operational for over 44years today, demonstrating high stability in space applications. However, TE technology has not been as easy to introduce for earth applications, especially power generation, mainly because of the harsh environments the modules are required to operate in and requirements for, long-term stability, flexibility, etc.

Generally, TE devices are made of n- and p-type semiconductor materials, connected in parallel to accumulate current and in series to build-up voltage (see figure 3.1). For power generators, the device is sandwiched between a heat source and a heat sink, and the temperature gradient is the driving force which drives the charge carriers towards the cold side current collectors. The level of productivity is determined, first and foremost, by the TEM properties; however, factors such as TE elements' (legs) geometry, connecting schemes and other diverse requirements (service conditions, non stable thermal source, thermal mechanical stresses, etc) all must be taken into consideration. Furthermore, for earth applications, TE technology is expected to provide high power density, durable and production friendly modules. This chapter will focus on general principles of TE module

operation, design, performance testing and thermal stability evaluation to provide readers with basic knowledge about device design and characterization methods.

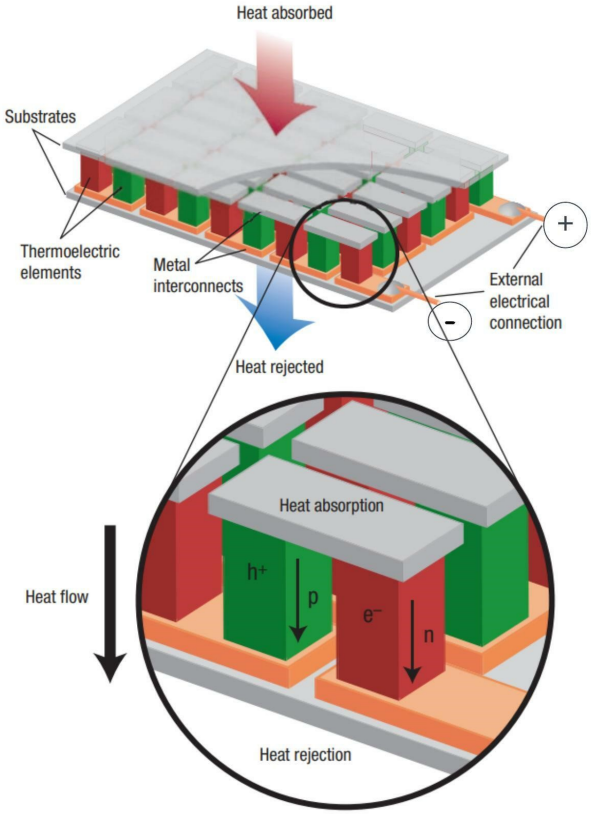

Figure 3.1: Schematic illustration of a TEG module's components, the electrical connectors and the heat flow & charge carrier directions [72]

3.1 Mode of operation

Typically, thermoelectric generators (TEG) comprise several thermocouples or unicouples (or cells), each composed of one n-type and one p-type TEM, connected electrically in series and thermally in parallel (see figure 3.2). The TE device is subjected to a heat flux from the heat source to a heat sink (Δ T) and each cell generates an output voltage integrated to form the module open-circuit voltage (V_{oc}), given by equation 3.1.

$$V_{oc} = \sum_{n=1}^{i} (V_{cell})_i = \sum_{n=1}^{i} (S_n(T) - (S_p(T))_i \, \Delta T \tag{3.1}$$

where S_n and S_p are the absolute value of Seebeck coefficients of n- and p-type TEM and both are functions of temperature. ΔT is the temperature gradient between the hot side and cold sides of the TE module.

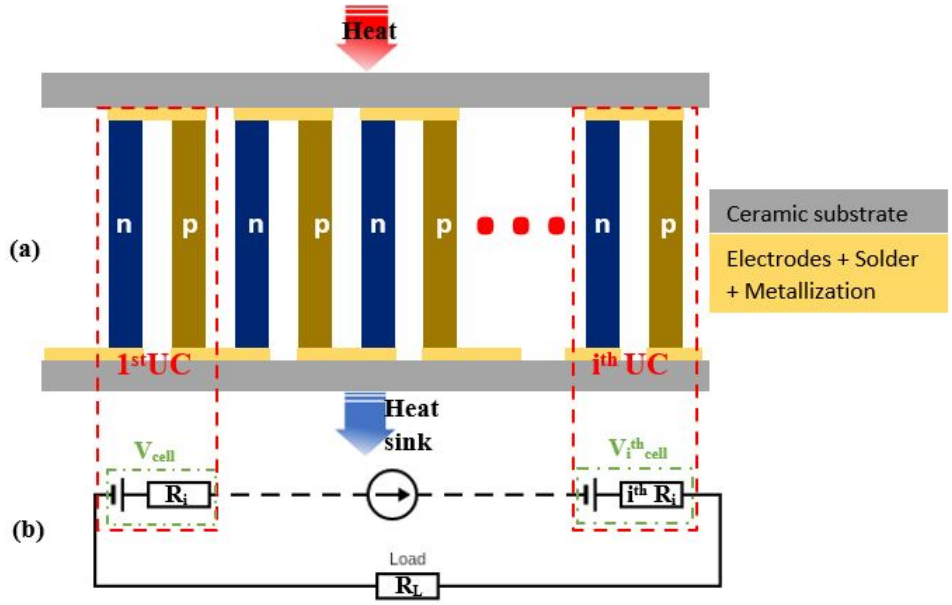

Figure 3.2: Schematic representation of a (a) TEG made of a series of n- and p-type thermoelectric unicouples (UC), and (b) the TEG equivalent simplified electric circuit.

Each thermoelement or cell has an internal resistance that comes from both the TEM themselves and the bonding layer (in yellow in figure 3.2). Therefore, the device's overall internal resistance will be the sum of the TE element's electrical resistance R_{TE} and the contact layer's (on both hot and cold side) resistance ($R_{contact}$) equation.

$$R_i = \sum_{n=1}^{i} \left(\frac{l}{\sigma_n(T) A_n} + \frac{l}{\sigma_p(T) A_p} \right)_i + R_{contact} \tag{3.2}$$

where σ_n and σ_p - are the n- and p-type TEM thermal dependent electrical conductivity, respectively. Similarly, $A_{n\&p}$ and l - are the cross-section areas and length of the TE legs, respectively. The $R_{contact}$ is an aggregate of individual electrical contact resistance of each unicouple at both the cold and hot side in the whole module.

The amount of power generated by a TEG depends on how much heat flux flows through the hot side and cold side of the module. The heat diffusion at the hot and cold side contact interfaces is complex; however, figure 3.3 shows a unicouple with representative contact layers and their respective thermal resistance. The heat flux at both cold and hot

junctions is comprised of the thermal conductivity of the unicouple/module, the Peltier effect and the joule heating as expressed by the first, second and third terms of equations 3.3 and 3.4, respectively.

$$\dot{Q}_h = S * I * T_{hot} + K\Delta T - \frac{1}{2}I^2 R_i \tag{3.3}$$

$$\dot{Q}_c = S * I * T_{cold} + K\Delta T + \frac{1}{2}I^2 R_i \tag{3.4}$$

where $\dot{Q}_{h,c}$ are the heat fluxes at the hot and cold junctions, respectively; $\Delta T = T_{hot} - T_{cold}$ the temperature difference between the hot and cold junctions of the thermocouple; R_i the internal contact resistance, R_L the load resistance (featured in figure 3.3); S and K are the Seebeck coefficient and thermal conductance of the unicouple, and finally, I is the current flowing in the thermocouple under load.

To achieve an optimal performance in a TEG, the thermal and electrical conductivity of the contact layers (between the TEM and both heat source and sink) must be very high, while remaining low in the TE legs.

The final point of interest is the thermoelectric power generated. Equating both equations 3.3 and 3.4, the thermoelectric power output would be as in equation 3.5.

$$P_{out} = I^2 R_i \tag{3.5}$$

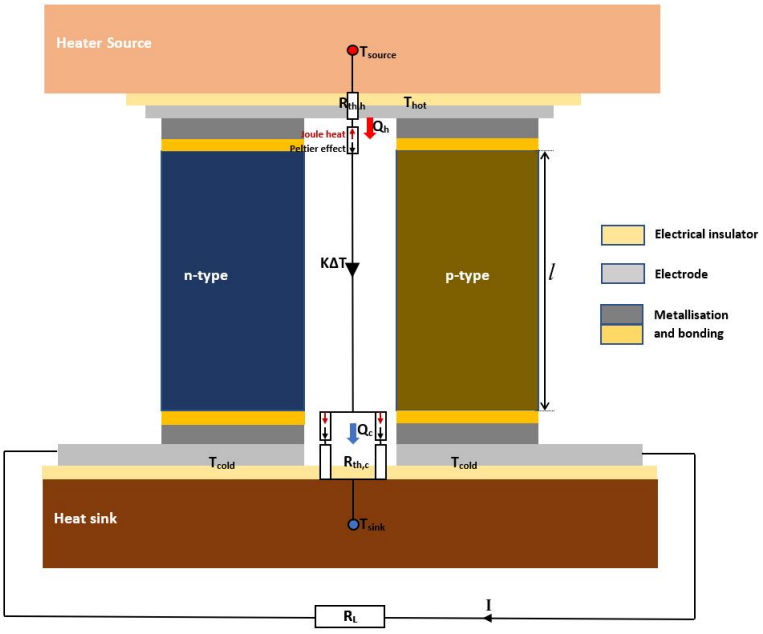

Figure 3.3: Schematic diagram of a n-p type unicouple illustrating the heat conductivity from the hot to the cold side of the module, thermal resistance components, and the Peltier and Joule heating effects at both sides of the thermocouple.

3.2 Module structural design

3.2.1 Introduction

TE module design is a broad area that includes the choice of TEMs (good TE properties and matching n- and p-type TEMs), calculation of the geometry and positioning of the TE legs, module operation conditions, heat exchanger modelling, and much more [249–251]. Despite the choices involved in module design, some components are typical of all modules such as ceramic plates, electrodes, solder, metallization, coating, encapsulation, etc. As illustrated in figure 3.3, the ceramic plate is used as an electric insulator, while the electrodes, solder and metallization layers ensure good electrical and thermal conductivity through both the hot and cold sides. Coating and encapsulation, on the other hand, are techniques used to protect the TEMs or the TE module in general from the surrounding conditions that might prevent the optimal operation of the module. Therefore, in addition to the TEMs' thermal, chemical and mechanical properties, the contact in-

terface composition is an important part of the module to consider when evaluating its stability/lifetime.

3.2.2 Metallization

Metallization refers to coating metal on the surface of other objects. It is an old technique that was originally used in applications such as mirror production and aluminium coating and is now used in applications such as flexible packaging, labels, gift wrapping, wall coverings, automotive trim, electronics packaging, etc. Metallization is used for different purposes depending on the area of application such as to improve security, barrier properties, optical reflectivity, electrical and thermal conductivity, etc.

In thermoelectric modules, metallization is similarly used to improve/ensure good thermal and electrical conductivity of the contact interface between the electrodes and the TE legs. The choice of metal and deposition technique depend on the type of target, in this case the TEMs on which the metal would be deposited; however, it is of the utmost importance that the metal layer adhere to the surface.

A good contact interface is a resultant of the formation of a thin intermetallic layer through controlled interdiffusion between the electrode and the TEM [267], with the diffusion process being accelerated/facilitated by the solder and blocked by the metallization layer. Moreover, the resultant contact interface should have good mechanical properties for long-term applications or withstanding thermal stresses. The typical mechanical property is the coefficient of thermal expansion (CTE), which should preferably be similar or almost equal for the metallization materials, solder, electrode and TEM. While there are several metallization techniques, those typically used on TEMs will be considered one by one.

- **Chemical vapour deposition (CVD)**: is a process wherein a 3D object is immersed in a fluid or volatile precursor, which chemically changes and leaves a solid and thin layer on the exposed surface of the object. Chemical deposition is classified based on the type or phase of the precursor, such as MOCVD, HPCVD, RTCVD, etc., corresponding to microwave plasma-assisted, hybrid-organic, and rapid thermal CVD [268], respectively.

- **Physical vapour deposition (PVD)** is a process in which a material is transferred from a solid target to the surface of a substrate on an atomic level. The deposition process occurs in a clean environment (under vacuum conditions) to reduce potential contaminants and minimize the partial pressure of all background gases. PVD is usually conducted using techniques such as magnetron sputtering, pulse laser deposition, electron beam evaporation, and ion beam processing, which are featured in instruments manufactured by Quorum Technologies and Angstrom Engineering. The most popular PVD technology (in thermoelectric modules) is sputtering deposition, which is a physical process wherein a thin film is deposited on a substrate under the influence of the momentum exchange between ions and atoms after colliding in the substrate's material. There are several types of sputtering technologies, including radio frequency sputtering, magnetron sputtering, and DC and AC current sputtering, to name a few.

  The sputtering techniques are named after the potentials/force applied to the target to induce plasma, which in turn supplies sputtering ions. Sputtering or PVD in general are used for numerous purposes such as improving the hardness, oxidation resistance, and electric and thermal conductivity of the targeted substrate. For thermoelectric modules, as mentioned in the introductory section, these techniques help to control the interdiffusion at the TEM-electrode interface and increase the electrical and thermal conductivity of the new intermetallic layer. Moreover, metallization is an important process for microscopy studies, like scanning electron microscopy (SEM), energy dispersive X-ray spectroscopy (EDS), and transmissive energy microscopy (TEM), when the materials under investigation are poor conductors and reinforced electrical conductivity is a requirement for high resolution outputs.

- **Other metallization techniques** There exist other metal deposition techniques, most of which fall in the PVD or CVD families. Some examples are plasma treatment, thermal evaporation technique, and organic or aluminum evaporation, among many others.

3.2.3 Coating and encapsulation

Coating or encapsulation is important for thermoelectric modules as a protective measure for the TEMs. TEGs are expected to operate in harsh environments, such as in automobiles, remote areas as part of the oil and gas or telecommunications industries, where corrosion presents a challenge. Because the modules are required to operate under air or other corrosive environments, it is necessary to coat the TE legs with an anti-corrosive material or even to encapsulate the whole module. Coating is done using some of the same methods as metallization, as well as by brush painting or simply using deep coating (where the bulk materials are submerged in the paint). Thermal spraying is another commonly used technique whereby metals and/or ceramics can be sprayed on other materials to provide corrosion protection or change the surface properties including wear resistance or thermal conductivity. TEGs, on the other hand, are encapsulated using laser sealing or vacuum encapsulation for long service life and zero oxidation.

3.2.4 Bonding technology

3.2.4.1 Standard bonding

Standard technologies such as welding or brazing, wire (Cu or Al) soldering and adhesion bonding, are more utilized to solder two solid materials. Brazing is popular for hard soldering in high temperature (>450 ∘C) applications. However, wire soldering and adhesion or laser bonding are common in the electronics industry, whether for packaging or for mounting purposes. Adhesives are used in several areas, especially in semiconductor manufacturing processes, where they are useful for surface preparation (grinding, and polishing), functionalization and mounting for wafer slicing purpose. Similarly, in processes related to thermoelectric modules, adhesive bonding specifically is important in cutting ingots/pellets into legs and in surface preparation (further detailed in chapter 4) for different characterization techniques. It is also used in modules as a soldering method, and in this case conductive resin is employed with silver, copper, and tin being the most used solders [252, 253], though different factors need be checked, such as matching the thermal expansion coefficients of electrodes and TEMs. Some examples of solder used in

TE module fabrication are PbSnAg-based for silicide-based modules [254], and some lead-free solders such as SnAgCu-, SnBi- and SnCu-based solders [255–257] for Cu electrodes specifically and BiTe-based TE modules.

The drawback of adhesion bonding is that it takes time to cure and it is necessary to apply pressure between the two parts to be soldered. Moreover, the bond is not mechanically reliable over time as it can become brittle, therefore weakening the module [258, 259]. Laser bonding is another soldering technique that is popular in electronics but not in TE modules, but which could be adopted since it is fast and provides a solid interface.

3.2.4.2 Solid state diffusion bonding

Unlike in the previous bonding methods, when bonding electrodes to the TE legs in solid state diffusion (SSD) bonding, a strip of metal is physically laid on top of the TEM [260], temperature and pressure are applied and the two materials interdiffuse to form an intermetallic compound (IMC). The composition of the IMC needs to be controlled for optimal performance of the contact interface; usually, phase diagrams are used to check the composition range of the metals. SSD technology outperforms direct and diffusion bonding, especially in high power electronic equipment, because it does not require thorough surface treatment and can be conducted in an oxygen-containing atmosphere. Moreover, it is more used in power module packaging [261–264], though it does present challenges as it requires pressure to be applied during bonding, making it hard to successfully perform on miniature or brittle compounds.

3.2.4.3 Solid liquid interdiffusion bonding

Solid liquid interdiffusion (SLID) bonding is another bonding technology most often used in electronics packaging. The technique is known to be efficient in high temperature electronics, which have applications in exhaust gas sensors, combustion engines in the automobile industry, oil and gas exploration, spaceships, etc. The bonding method is similar to SSD; however, in SLID a metal with a low melting temperature is sandwiched at the interface. The bonding temperature is set to reach the melting point of the low

temperature material and the liquid phase diffuses in the surrounding solid phases creating an ICM. The thermal and mechanical properties of the ICM are key to determining the reliability of the bond. In addition, a diffusion barrier is required to be able to control the bond thickness and elastically absorb mechanical stresses during operation. As with the other methods, the choice of the low temperature material (or bonding materials) is based on matching the CTE between the surrounding metals, though after bonding the CTE of the ICM should also be close to that of the surrounding materials. Ideally, a bond should be able to withstand plastic deformation or brittleness during operation, which would be present in case of mismatching CTEs. T.A. Tollefsen et.al. [265] have extensively studied Au-Sn SLID bonds and found that the resultant is promising and reliable for applications at temperatures higher than 500^0C and was able to withstand thermal cycles between 35 and 500^0C.

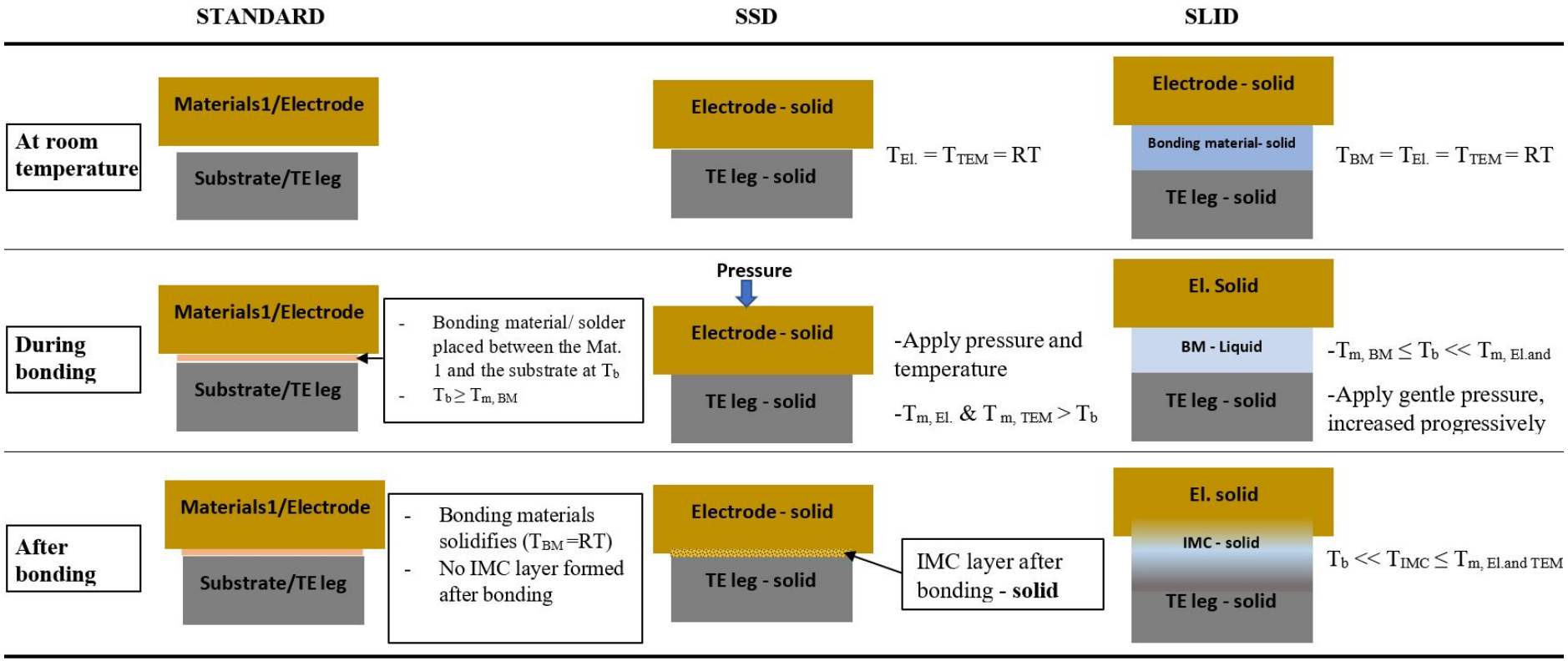

Figure 3.4: Schematic illustration of standard, SSD and SLID bonding technologies. T_b stands for bonding temperature, $T_{m,X}$ is the melting temperature of material "X" (electrode, TEM or the intermetallic compound (IMC)) and RT is the room temperature. Standard bonding refers to any other bonding type, soldering, laser bonding, etc.

3.3 Performance and stability of TE modules

3.3.1 Performance testing

Testing of the performance and stability of thermoelectric modules is conducted in conditions that mimic the real-life service environment. TEGs operating in space are subjected to less thermal stress than those operating on earth, where TEGs experience intermittent mechanical and thermal load over its lifetime. Thus, the mechanisms of reactions that reduce or affect the generator's efficiency over time are slower in space. Some of the test conducted to evaluate the performance of TEG are aging, and thermal cycles in varied environments

- **Isothermal aging**

  In terms of terrestrial applications, equipment such as exhaust systems for processing industries and hot process furnaces operate over a long period of time at constant temperatures. Therefore, TE modules operating in such environments must be able to withstand long-term use. As discussed in the previous section, evaluating systems requires designing materials that would withstand the service environment but also choosing adequate contacts (electrode) and bonding technology. Therefore, especially in the thermoelectric industry, contact layer durability is the key to lasting systems; because they are made from different materials and thus susceptible to embrittlement (due to different CTEs). Aging testing might be impossible to conduct in service conditions, and thus accelerated methods might be used, such as performing the test at higher temperatures than the service temperature.

- **Thermal cycles**

  Most areas where TEGs are operative, including the automobile industry, wearable technology, and so many more thermal harvesters to name a few, are subjected to frequent intermittent temperature changes. The assessment or performance testing of modules operating in these areas is done using thermal cycles, which are performed in the real-life temperature range. During the tests (as will be discussed at greater length in the next subsection), the open circuit voltage, the internal resistance and contact resistance, as well as the output power of the module, are monitored over

time. Unlike with isothermal aging tests, the temperature gap, and the duration of one cycle or half cycle are decisive parameters to accelerate thermal cycle testing.

3.3.2 Characterization of experimental modules

The thermal diffusion through the TE module from the hot plate to the heat sink drives the majority carriers in the same direction, therefore generating the Seebeck voltage, as in equation 3.1. To determine the maximum electrical power the TE module can generate, the module is subjected to a number (n) of isothermal segments at the same time the electronic load sinks the current and absorbs the power generated by the TEG (see figure 3.5). The open circuit voltage is recorded at zero load resistance, while the circuit current and voltage drop are recorded at different loads. By fitting the I-V curves equation 3.6, we can deduce the internal resistance as the slope of the I-V curve and the open circuit voltage as the intersection between the I-V curve the voltage curve.

$$V = R_L I = V_{OC} - R_i I \tag{3.6}$$

where V_{OC} the open circuit voltage and, R_i the unicouple or module internal resistance and R_L the load resistance.

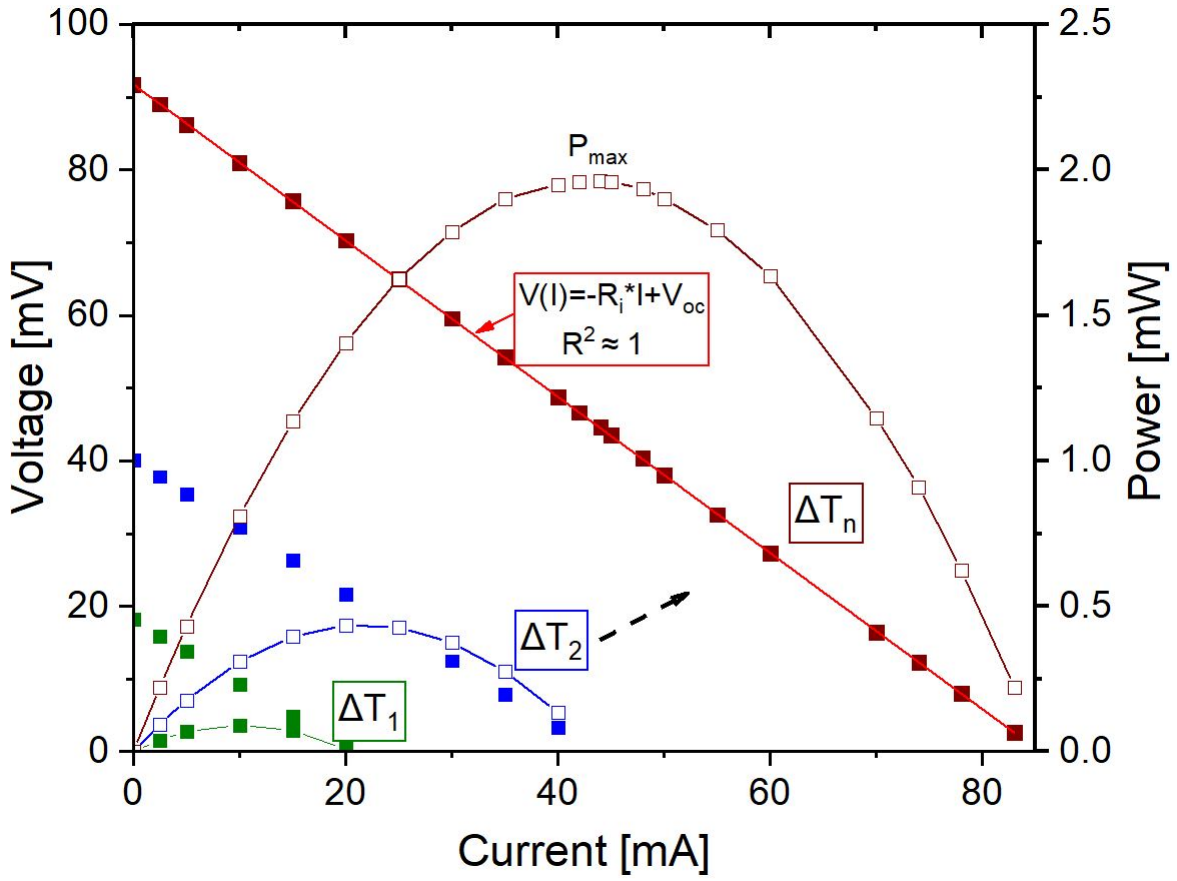

Figure 3.5: I-V curve at constant temperature $\Delta T_{(1-n)}$, the graph shows the maximum power point at V_{OC}=90mV, and R_i=1Ω.

By equation 3.6, we deduce the expression of current "I", and when we insert it in equation 3.5, we get:

$$P = I_2 R_L = V_{OC}^2 \frac{R_L}{(R_L + R_i)^2} \tag{3.7}$$

As shown above, the programmable electronic load's impedance is a function of the internal resistance of the TEG; therefore, the matched load should be equal to or matched to the TEG's impedance, and the power absorbed at load matched conditions (R_L=R_i) is the "maximum power of the module". Therefore equation 3.7 becomes

$$P_{max} = \frac{V_{OC}^2}{4R_i} \tag{3.8}$$

Similarly, the TEG or unicouple under experimentation reaches the maximum conversion efficiency at impedance matching conditions. Therefore, the conversion efficient is expressed as

$$\eta_{max} = \frac{P_{max}}{\dot{Q}_h} = \frac{P_{max}}{\dot{Q}_c + P_{max}} \tag{3.9}$$

The input power can be measured from the hot side or the cold side depending on where the heat flow meter is placed. Therefore, each of the above equations can be used respectively. Whereas η_{max} is the conversion efficiency of the module, $\dot{Q_{h,c}}$ are the heat flow through the hot side and heat exiting through the cold side of the module, respectively.

3.3.3 Thermally activated processes

3.3.3.1 Crystal defects

Because the main objective of this project is to study the performance and stability of silicide TEMs, and the studied TEMs are in crystalline form, thus the interest in first discussing crystals and defects. Compounds wherein atoms are in perfect geometrical configuration (also called perfect crystalline compounds) do not exist; imperfections are called defects and differ by the chemical nature of their geometrical configuration. Although they are called defects, they tend to make bulk materials interesting by creating room for improvement in areas such as the optical, mechanical and electrical properties of solid materials. Defects can be categorized in four classes:

- **Point defects** are zero-dimensional defects that consist of lattice site vacancies, substitutional defects, interstitial defects or vacancy-interstitial pair (Frenkel) defects. Lattice vacancies correspond to missing atoms in a given lattice site arrangement, while interstitial defects are when atoms are in between lattice sites. These can be similar to the matrix constituents or impurities and are therefore called intrinsic or extrinsic interstitials, respectively. Similarly, substitutional defects correspond to impurities added internationally (dopants) or present due to incomplete purification into the host lattice site. Finally, Frenkel defects occur due to the movement of atoms in the lattice site from an interstitial position to a pre-existing vacancy. The latter is usually due to external excitation; therefore, to determine the vacancy density, it is first necessary to reach the diffusion (excitation) temperature.

- **Linear defects** , on the other hand, are one-dimensional defects and correspond to the displacement of atoms in a linear pattern, leading to deformation of the lattice site symmetry along the line. These types of defects are also known as "dislocations"

which are classified in two forms, edge dislocations and screw dislocations; for further details, refer to [266].

- **Planar defects** are two-dimensional defects, that occur due to contact between two surfaces, two interfaces, or along grain boundaries. Surfaces and interfaces in semiconductors, specifically, have an immediate effect on the electronic properties of the junction or the contact layer, respectively. In fact, the defect at the contact can be considered as if it was a sheet of vacancies. This band of defects created would induce recombination of both minority and majority carries therefore depleting the semiconductors on both sides of the junction and at the same time reducing the output power. Analogously a high density of dangling bonds at the grain boundaries prevents any possibility of doping. Nonetheless, the effects of both the surface and grain boundaries defects can be attenuated by applying appropriate surfactants to annihilate the boundary states and has been reported to improve the TE properties of TEM [267].

- **Volume defects** are similar to planar defects discussed above; however, they are associated with the integrity of the interface between two semiconductor or metal-semiconductor. The issue arises from the fact that the contact layer generates a potential difference, and therefore an electric field across the interface. By the interdiffusion scenario, the interface grows with usually mismatching CTE to the neighbouring matrices, therefore could lead to plastic deformation. Other examples of volume defects are pores and voids, which are mostly a result of poor synthesis methods and could lead to cracks or other poor mechanical properties.

To summarize, the above mentioned crystal and interface defects relate to thermoelectricity in both a positive and negative way. Both interstitial point defects and the addition of dopants play a major role in optimizing the electrical and thermal transport properties of TEMs. Moreover, contact interfaces at the surface or between grains need to be well modelled to make sure the interdiffusion layer created does not suffer from significant lattice mismatch, for instance, or the effects of dangling bonds at the grain boundaries.

3.3.3.2 Diffusion

As briefly described in section 3.3.3.1, crystalline solids are characterized by imperfect lattices or non-regular presence of atoms in the interstitial sites. Although atoms are originally held firmly in their respective lattices, defects tend to initiate atomic diffusion from lattice-to-lattice sites or among interstitial sites. During the diffusion process, regularly placed atoms also need to yield to the migrating atom, which requires vibrational energy. The source of this energy could be an incident photon (in photo-voltaic systems) on the material or the passage of phonons across the lattice (by lattice vibration) induced by temperature. The Phonon dependence leads to the Boltzmann relation, which expresses the atomic diffusion rate as exponentially dependent on the applied temperature, as in equation 3.10.

$$D = D_0 e^{-E_p/k_B T} \tag{3.10}$$

where D is the diffusivity, $D_0{=}\nu\sigma^2$ is the prefactor, ν and σ lattice vibration frequency and diffusion length, respectively, and E_p is the diffusion activation energy. Considering a solid volume, a TE leg for instance, with a temperature gradient across two faces, one would expect a chaotic motion of atoms in all directions; the direction of atomic or ionic diffusion would preferably be from an area of higher to lower concentration of the charge carriers as well as from high to low temperature. The flux of atoms therefore fulfills Fick's first law, as in equation 3.11

$$F = -D\frac{dC}{dX} \tag{3.11}$$

Where F is the flux of atoms or ions, D the diffusivity or diffusion rate, and C the charge carrier concentration.

3.3.3.3 Interlayer diffusion

In TE modules, two or more layers are superposed at the hot side and the cold side to create a contact interface between electrodes (metallic) and the TEM (semi-metallic). The interface is designed to withstand thermal and mechanical stresses but at the same time act as a perfect thermal and electrical conductor. For this to be possible, controlled interdiffusion between the constituents at the junctions should create an intermetallic compound (IMC). However, the challenge is that the contact interface constituents usually

have different properties, such as coefficient of thermal expansion (CTE), which means that applying high temperatures would hinder the formation of a solid IMC. Moreover, IMCs should include a diffusion barrier layer to prevent undesired continuous diffusion.

3.3.3.4 Oxidation

Oxidation is another effect of thermal exposure of the TEM. In this project, we have focused on HMS TEMs and understanding not only the oxidation reaction kinetics (reaction rate, rate-boosting/limiting steps) and mechanisms of the materials but also exploring the effects of oxidation on the TE properties of the TEM and the modules' elements, especially contacts. Therefore, except for a presentation of basic oxidation theories subsequent discussions will refer to the oxidation of HMSs and constituents (dopants, impurities, etc). With regards to the oxidation kinetics, more information on the oxidation models are demonstrated in the next chapter section 4.3.3. Moreover, the oxidation mechanisms of the studied alloys were discussed in Paper II and III as summarized in chapter 5.

3.3.4 Thermomechanical activated processes

3.3.4.1 Elastic and plastic deformation

Solid materials – here we consider metals, semi-metals and alloys – are constituted of atoms that are in inter-atomic equilibrium. In the event of mechanical exposure, the atoms are displaced from their equilibrium state due to the applied force (tensile or compressive) and generate an opposite (attractive or repulsive, respectively) force to react to the applied load. Depending on the balance between the action and reaction forces, the solid material is subject to possible deformation as the atoms may regain their original position or move to a new position, which means forming new bonds. The deformation is called elastic if the particles return to their original state and positions; however, not all recoverable deformations are considered elastic, only those that are time independent. Otherwise, the deformation is plastic or irreversible.

3.3.4.2 Creep deformation

Creep fatigue is a plastic deformation that occurs when the amount of load and stress is kept constant for an extended period. As discussed in the previous section, deformation may be a result of thermal stress, and creep is a temperature dependent deformation, which can occur at any temperature (above absolute zero) depending on the material. However, since it is temperature sensitive, the higher the temperature the faster and more pronounced the creep phenomenon is over time. In general, at relatively low temperatures, engineering materials are designed to resist creep deformation by making sure that the stress applied during operation (depending on the area of application) does not exceed the yield strength. At high temperatures (close to and above $0.5\mathrm{T}_m$ - melting temperature), however, materials experience time-dependent creep deformation with lower stress than the yield strength.

Following the dislocation climb theory of steady-state creep developed by Garofalo(1963), the empirical steady-state creep rate was proposed as in equation 3.12.

$$\dot{\epsilon}_{ss} = A(sinh\alpha\nu)^n e^{-Q/RT} \tag{3.12}$$

where $\dot{\epsilon}_{ss}$ is the steady-state creep rate; A, α and n are constants that depend on the nature of the applied stress, the materials' structural nature, including the grain size and dislocations properties; and ν is the applied stress. At constant stress the stead-state creep rate follows the Arrhenius diffusion model.

Furthermore, B. Amit [268] found that for temperature higher than $0.5\mathrm{T}_m$ the predominant creep mechanisms in metal are dislocation creep, diffusion creep and gain-boundary sliding. Therefore, taking all the effects into consideration, the steady- state creep can be estimated as in equation 3.13 [268].

$$\dot{\epsilon}_{ss} = B\frac{DGb}{k_B T}\left(\frac{b}{d}\right)^p\left(\frac{\nu}{G}\right)^n \tag{3.13}$$

where, G is the elastic shear modulus, B is a dimensionless material constant which depends on the stacking faults energy, b is the Burgers vector (which is the magnitude and direction of the lattice deformation resulting from the lattice dislocation), k_B is the Boltzman's constant, T is the absolute temperature, D is the diffusivity constant (equation

3.11), ν is the applied stress, d is the grain size, n is the stress exponent and p is the inverse grain size

Thermoelectric systems are particularly susceptible to creep deformation because the compressive pressure, the heat to which TEMs are exposed to, in addition to the long-term application requirements , are a recipe for creep to occur.Several studies were conducted on different TEM systems, most importantly on materials featured in state-of-the- art TEGs (PbTe [269], BiTe [270], TAGS alloys [271], skutterudites [272], half-Heusler alloys [273] and, most relevant to this report, MGS-based TEM [274]). M.M. Al Malki et.al. [22] studied compressive creep loading at a homologous temperature (or ratio between the absolute temperature and the melting temperature of the TEM) range of 0.67-0.75 and 30MPa. The materials system responded with a 12.5% electrical conductivity loss and consequently 22% zT reduction after a 28 day test. Similarly, R.A.Michi et.al. [274] showed that a set of silicide TEM systems had a similar response and were resistant to the compressive creep compared to BiTe- or PbTe-based TEM systems.

3.3.4.3 Fatigue crack

TEGs experience thermal fatigue, which can lead to damage and possible failure, though the amount of damage vary from one material system to another and is largely dependent on the application environment. The performance of a TEG is studied using "aging" tests and "thermal cycling" tests under constant compressive pressure. Modules usually take longer to fail during aging tests, however during thermal cycles, numerous and successive heating and cooling speeds up thermal fatigue and premature fracture is prevalent. Aging tests are relevant to MMRTGs used in spaceships, but very limited for TEGs with terrestrial applications, such as recovering waste heat in industrial exhaust systems. Most terrestrial applications require high thermal cycle robustness. In fact, thermal stress induces thermal strain which, over time, initiates strain fatigue. Then failure starts from micro-crack(s), which, once initiated, propagate and lead to fractures (end of life). L. Guobin et. al. [275] express the thermal stress as in equation 3.14.

$$\sigma = y\alpha E\frac{\Delta T}{1-2\eta} \tag{3.14}$$

where σ is the thermal stress, y is the constraint coefficient, α is the linear expansion coefficient, E is the modulus of elasticity, η is the Poisson's ratio and Δ T is the temperature difference.

3.3.5 Stability of thermoelectric systems

The thermal stability of TE systems depends not only on the materials (TEM) used in the system, but also the bonding technology (contact materials, solders) and the operational environment. In this project, the oxidation robustness of the TEM and of the metal contacts in silicide thermocouples (modules) were investigated using thermogravimetric analysis (TGA) and thermal cyclic tests, respectively. Following these studies, we drew conclusions based on empirical observations, which are used as a basis to modelling TEMs to resist oxidation, to designing protective oxides and stable contact phases for silicide-based TEMs and modules.

With the onset of oxidation of an alloy at high temperatures, a concentration gradient of the alloy's constituents is also established between the core and the alloy-oxide interface. As a result, metal diffusion and oxygen permeability are regarded as the major oxidation rate's controlling reactions [276]. Carl Wagner [277] studied the diffusion processes during oxidation of alloys and showed their effect on the oxidation rate of the alloys. However, the Wagner theory is limited to binary compounds and is challenged by more complex alloys due to probable simultaneous diffusion of the alloys' constituents. Thus, metal diffusion for multi-component alloys and the stability of coexistent oxides would be key parameters that need to be better understood when designing an oxidation-resistant compound.

In this project, we focused on oxidation of the HMS compound and alloys, whereas Skomedal G. et.al. [278] looked at high temperature oxidation of MGS alloys. Their study showed that the design of $Mg_2Si_{(1-x)}Sn_x$ to develop a MgO protective layer, relies on optimizing the alloy composition to keep the Pilling-Bedworth ratio (PBR) below 1, by keeping the Sn content below 0.4 at.%. However, for application in thermoelectric generators, the research recommends applying high temperature coating(s) or encapsulating the MGS-based modules.

On the other hand, binary HMS compounds oxidize selectively, growing an SiO_2 protective oxide layer with a silicon depleted layer beneath the alloy-oxide interface. For thermoelectric applications, it is important to optimize the electrical carrier concentration by alloying or doping the parent HMS compound. The added impurities can improve the alloy's resistance to oxidation by reducing the lattice defect in the alloy, but they can also be oxidized and create a mixture of oxides, thus having a negative effect on oxidation resistance.The elements featured in the alloys studied in this project are Ge, Mo, and Al. All these elements have a certain affinity to oxygen, so to assure a good alloy model (resistant to oxidation), the alloy should form a mixture of oxides that are single phase individually, and the oxide layers must be superposed one on top of the other, with the less stable at the oxide-oxidant interface and SiO_2 at the alloy-oxide interface.

There are several problems that arise with multi-component alloys, with the homogeneity and multi-crystalline structure of allows being the main issue that raises concern about the oxidation of the silicides. Non-homogeneous HMS alloys grow simultaneous oxide phases at the ignition temperature and can be a source of mechanical instability when the scale is still thin. Similarly, for multi-crystalline compounds, impurities tend to segregate at the grain boundaries, which could lead to the formation of oxide layers at the grain boundaries. To counteract these problems, the concentration of the alloy's elements must be optimal, with oxidation consumption taken into consideration; moreover, the growth rate of SiO_2 should be faster than its other counterpart to ensure the silica layer covers the whole area as fast as possible.

Chapter 4

Materials and methods

This chapter presents the materials used specifically in this project, and summarized the methods employed to conduct the study reported in this Ph.D. thesis. Figure 4.1 shows a picture of the methodology followed, and the sub-chapters below dive deep into the specific topics.

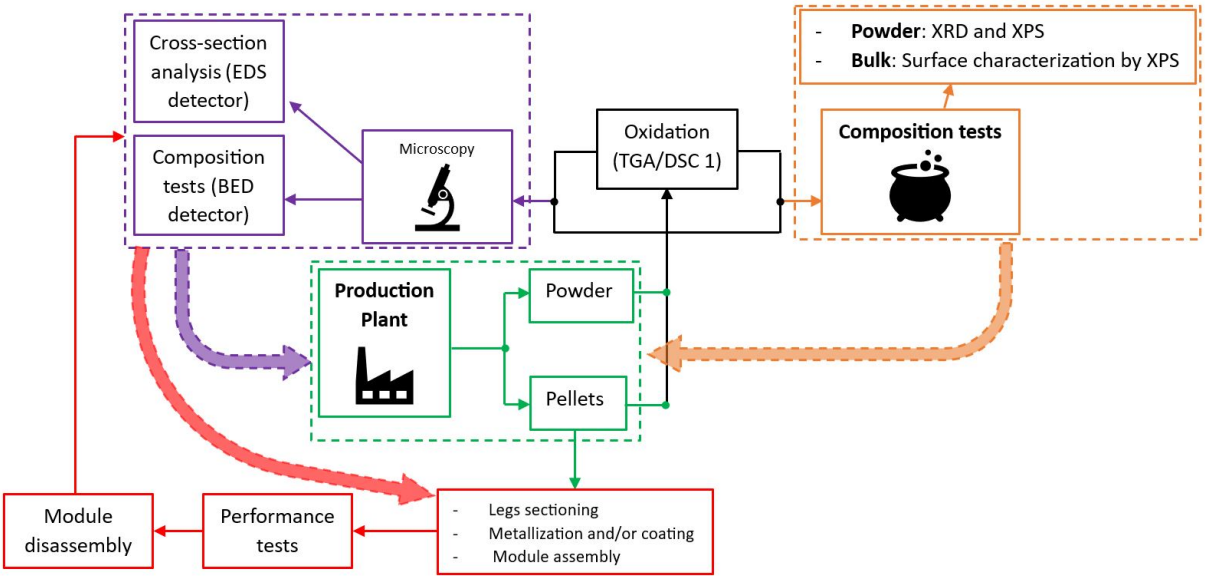

Figure 4.1: Schematic representation of the methodology used. The sections in the diagram are described using respective color codes as below

- **Green**: represents powder synthesis and pellets consolidation;
- **Orange**: represents the materials composition analysis, both pre- and post- oxidation

tests with XRD on powder samples and XPS on both powder and bulk materials.
- **Violet**: represents the microscopy imaging, composition and cross-section analysis using SEM/EDS.
- **Red**: represents the module characterization process including the module assembly, performance testing and post-characterization.
- The dotted arrows show the information feedback flow followed to optimize the performance of the TEM and modules.

4.1 Materials

The materials used for experimentation in this Ph.D. project were produced as part of the TESil (thermoelectric silicides) project [279] in collaboration with ELKEM ASA, TEGma, SINTEF, and the University of Oslo (UiO). HMS and MGS alloys of different compositions were synthesized as detailed in Paper I – III; the source of the raw alloys' constituents is given in Table 1 of Paper I. In short, the HMS alloys were synthesized by mixing all basic elements, melting and casting in an inert (Ar) atmosphere. After the cast ingot was milled to a micron-sized powder, the powder was sintered using conventional HP and/or SPS. The produced 30-36 mm diameter and 5 mm high discs were cut into different sizes according to their intended use or purpose: for example, TE module legs were a different size than the oxidation specimen.

4.2 Sample preparation

Specimen preparation at both the TEM and module levels is an important step to achieve reliable results. This includes samples sectioning, mounting, cleaning, and so on. To illustrate the importance of these sample preparation steps, let's look at a couple of examples. Sample dimension is an important parameter because the sample must conform to the dimensions of the specimen holder, which differ for different testing equipment. Sample size can also be an important factor for experimental studies. For example, the study of the thermal reactivity of a material requires thermal equilibrium in its environment,

and the smaller the cross section, the faster equilibrium is reached. Surface preparation is another important factor to be taken into consideration, mainly during TEG assembly but also for most experimental tests of bulk samples. For example, surface preparation is important before oxidation tests on bulk samples, similarly, it is required before any surface characterization, before coating, etc. This section details the methods used to prepare specimen surfaces for each sample category, step by step.

4.2.1 Preparation of oxidation specimens

Oxidation specimens require meticulous preparation in terms of size and surface cleanliness. The surface-to-volume (S/V) ratio is an important quantity in the study of oxidation of materials. As Planinsic and Vollmer [280] showed in their study of the effect of the S/V ratio on the thermal properties of cheese cubes using a conventional preheated oven, the higher the S/V ratio, the faster the whole specimen reached thermal equilibrium with the oven/furnace's inner volume.

The oxidation samples were cut into different sizes of width and length, but most importantly, each had a thickness of one millimeter or less ($\leq$ 1 mm). The sample sectioning was done using a high-precision ($\pm$ 0.01 mm) tabletop Minitom machine (from Struers), equipped with diamond cut-off wheel. Moreover, the sample edges were ground and fine polished to a mirror-like surface using SiC (from 320 to 2400 grit) paper and diamond suspension (from 9 to 1 μm) fluids. In between the surface preparation, the samples were cleaned with tap water, while after the last step they were ultrasonically cleaned in acetone for 3 minutes to remove any oil before weighing and starting the oxidation experiments.

4.2.2 Preparation of cross-section specimes

After oxidation tests, the composition of the samples was re-examined to study the effect of the test conditions they were subjected to and deduce the mechanisms of their respective reactions. The same steps were also followed to post characterize the module elements (legs), after performance tests. Tests were conducted to determine the surface and cross-

section characteristics using different techniques including high-resolution microscopy, X-ray diffractometry and spectroscopy, etc., all of which require sample mounting, surface preparation and surface cleaning.

4.2.2.1 Mounting

Sample mounting is important for different reasons. It is used when there are materials with loose particles, surfaces with thin and fragile layers, for cross section preparation, and in many more cases. In this project, mounting was used for surface preparation and cross section preparation for microscopy imaging. The mounting process was done using different resins depending on the test equipment requirements. Scanning electron microscopy, for example, requires electron conductivity of the sample from the top to the bottom; therefore, if the sample is resin mounted, the resin should be conductive to complete the circuit or coated with a conductive paste from top to base. Polyfast (Struers), a hot mounting conductive resin was used for SEM samples, while Clarofast resin (Struers) was used during cold mounting. For SEM, Polyfast is commendable not only for its low shrinkage and conductivity (as a result of carbon fillers) but also its fast mounting time of 5 minutes (heating + cooling time), relative to the 8 hours cure time needed for Clarofast.

4.2.2.2 Grinding and polishing

In this report, grinding refers to the rough polishing process. The grinding process was conducted on the TEM (example of oxidation samples and TE legs) and mounted specimen (for cross sections studies, for example) using Metaserv (Buehler) and Tegramin-30 (Struers) grinder polishers, respectively. The rough polishing process was started using silicon paper from 320-500 grits, gently applying pressure of 40 N depending on the roughness of the initial sample surface/hardness of the actual TEM, and water as a lubricant. The grinding method proceeded with less rough SiC paper up to fine grinding steps with 2400 SiC grit paper. At the same time, the pressure was reduced to 20 N and to 15 N during the fine grinding and polishing steps. The polishing steps were conducted using diamond suspension fluids of 9 μm to 1 μm. Contrary to HMS, MGS alloy surfaces were

prepared using DP-Lubricant Blue (Struers) as a lubricant to mitigate surface oxidation, and less pressure was applied compared to HMS due to low mechanical strength.

4.2.2.3 Surface cleaning

As mentioned in section 4.2.2.2 above, cleaning is important during surface preparation, but also before experimentation, even though the sample may have been meticulously cleaned during preparation. Prior to oxidation experiments, electroplating, coating, etc., the materials were rinsed and ultrasonically cleaned to make sure no grease (which can originate from any other process or any other motor running in the laboratory environment) or fat from hands or water droplets from breathing was on the samples. As noted in the section above, the type of solvent used was chosen based on the materials in question: acetone or ethanol were used for HMS while DP-Lubricant blue was used for MGS.

4.3 Thermal oxidation and oxidation kinetics

4.3.1 Thermal gravimetric analysis

The thermal oxidation experiments were conducted using a Thermal Analysis System TGA1 (Mettler Toledo) equipped with a differential scanning calorimeter (DSC) sensor. During thermal gravimetry, the mass of a specimen is measured continuously (with 50million points resolution over time, under applied heat). The sample's weight change is recorded in definite intervals of time using an inbuilt balance (sensitivity of 0.1 μg). For the powder samples, the initial sample weight was within 5-10 mg to ensure fast thermal homogeneity throughout the whole volume from the walls of the crucibles. Moreover, the powder samples were used to conduct constant heating rate (isoconversion) experiments and determine the oxidation reaction onset temperature. Unlike the powder samples, the bulk specimens were subjected to isothermal heat treatment, and which allowed us to deduce the oxidation kinetics, discussed in section 4.3.3 below. It is important to note that all faces of the bulk specimens should experience the same amount of heat. For example, if the specimen is laid down in a crucible, that means one edge is in contact

with the crucible therefore would experience more heat than the rest, possibly leading to dissimilar reactivity.

4.3.2 Differential scanning calorimetry

During thermal treatment, some reactions are not reflected by weight change, including melting, glass transition, etc. DSC is a technique that measures the amount of heat required to raise the temperature of the sample. In the TGA/DSC 1 instrument, DSC compares the results of the sample crucible and a reference crucible. The reference crucible is of similar shape, size (100 μl), and composition (Al_2O_3) as the sample crucible.

4.3.3 Oxidation kinetics

4.3.3.1 Determination and computation of oxidation rate(s)

In general, the oxidation rate is computed by measuring the sample (under investigation) and/or oxidant (gas) consumption over time, by measuring the sample thickness before and after oxidation, or by setting a series of reactions and measuring the oxide build up (thickness or volume) over time, which yields a kinetic plot of the reactions. However, observing oxidant consumption at a constant volume would be cumbersome and could lead to erroneous results because of the different densities of solids and gases involved. It would require extremely short reaction times to insure a constant volume. Similarly, obtaining a series of sample thicknesses is practically impossible since it requires extreme care to avoid rupture of the oxide film at the sample surface. In addition, thermal cycles over the oxide scale apply extra stress and could induce change in the kinetics of oxidation from the 1st to the nth experiment. The most used method, therefore, is observing the weight gain (ΔW) over time, also referred to as thermal gravimetric analysis. which will be further discussed in the next chapter.

Concerning pure metal oxidation, the oxidation reaction can be generalized by the equation 4.1.

$$\frac{x}{y}M(s) + \frac{1}{2}O_2(g) -> \frac{1}{y}M_xO_y(s) \tag{4.1}$$

The growth of oxide on the metal surface is a result of oxygen intake and/or metal loss, which results in equation 4.2

$$dn_{M_xO_y} = -2\frac{dn_{O_2}}{y} = -\frac{dn_M}{x} \tag{4.2}$$

where n is the number of moles of the metal oxide, oxygen and the metal,respectively; x and y are the oxide product subscript in equation 4.1. Assuming all the metal surfaces are uniformly exposed to oxidation and no volatile matter is lost during the oxidation, the oxide weight gain per unit area can also be expressed (using equation 4.2) as in equation 4.3, where $M(O_2)$ is the molar mass of oxygen.

$$\frac{\Delta W}{A} = -\frac{yM(O_2)dn_M}{xA} = -\frac{2M(O_2)dn_{O_2}}{A} = \frac{yM(O_2)dn_{M_xO_y}}{A} \tag{4.3}$$

Since the metal surface is flat and the single-phase oxide is built up uniformly, it would also be correct to express the oxide weight as

$$\Delta W_{M_xO_y} = M(M_xO_y)dn_{M_xO_y} \tag{4.4}$$

and, therefore, equation 4.4 allows us to determine the oxide volume as

$$\Delta V_{M_xO_y} = M(M_xO_y)\rho_{M_xO_y}dn_{M_xO_y} \tag{4.5}$$

where $\rho_{M_xO_y}$ is the solid oxide density and $M(M_xO_y)$ the molar mass of the metal oxide. Hence, the oxide thickness can be approximated as the oxide volume gain per the metal surface area ($X_{M_xO_y}$=Δ $V_{M_xO_y}$/A), which by introducing equation 4.3 and 4.5 becomes

$$X_{M_xO_y} = \frac{M(M_xO_y)}{M(O_2)\rho_{M_xO_y}y}\frac{\Delta W}{A} \tag{4.6}$$

We can therefore deduce the expression of the oxide thickness growth over time using equation 4.7 as the general oxidation rate.

$$\frac{dX_{M_xO_y}}{dt} = f(t) \tag{4.7}$$

4.3.3.2 Mechanism and rate of oxidation reactions

In nature there exist a few relatively pure metals (Au and Pt), due to that there are highly reactive, brittle, etc. As a result of this high reactivity, the oxidation reaction can occur following any route depending on the nature of the reactants. However, for the

sake of simplicity, N. Birks et.al. [281] summarize all the different mechanisms into two categories based on whether the product of the oxidation reaction is a stoichiometric or a non-stoichiometric compound. While the oxidation reaction may seem straightforward, it is complex if more than two reactants are involved. This complexity arises from the formation of multiple oxide phases when a more reactive element is incorporated, hence a probable source of mechanical stress between the coexisting oxides. However, complexity is not always detrimental as alloying or doping would reduce the native defects in metals and therefore reduce reactivity and in most cases increase the electrical and mechanical properties of the materials.

- **Parabolic rate equation**

  As illustrated in figure 4.2, the metal oxidation reaction consists of the diffusion of metal cations from the metal to the metal-oxidant scale and/or the diffusion of oxygen anions from the oxide-oxidant to the metal surface through the oxide scale. Since interdiffusion through the oxide scale is phenomenon governing the reaction rate, Fick's first law (see equation 3.11) would apply.

  According to Fick's law, the diffusion flux of the metal ions through the oxide is proportional to the rate of the oxide growth (thickness "X") over time

$$F_{M^{2+}} = \frac{1}{V_{MO}} \frac{dX}{dt} = D \frac{a''_M - a'_M}{X} \tag{4.8}$$

  Therefore,

$$\frac{dX}{dt} = V_{MO} D \frac{a''_M - a'_M}{X} \tag{4.9}$$

  where V_MO the molar volume of the metal oxide "MO", D the diffusivity rate constant, dX/dt is the oxide thickness growth rate per unity "time (t)", and a'$_M$,a"$_M$ are the metal vacancy concentration at the metal and oxide surfaces respectively

  Following Wagner's theory, if we assume thermodynamic equilibrium across the oxide scale based the continuous and adherent oxide scale, it follows that the local metal concentration gradient (Δa_M) at the metal-scale and scale-gas interfaces is constant. By integration of equation 4.9, we get

$$X^2 = 2kt + c = k_p t + c \tag{4.10}$$

where k= $V_{MO}D\Delta a_M$, k_p is the parabolic rate constant and c is the constant of integration. It is assumed that there was no oxide on the surface of the metal prior to oxidation.

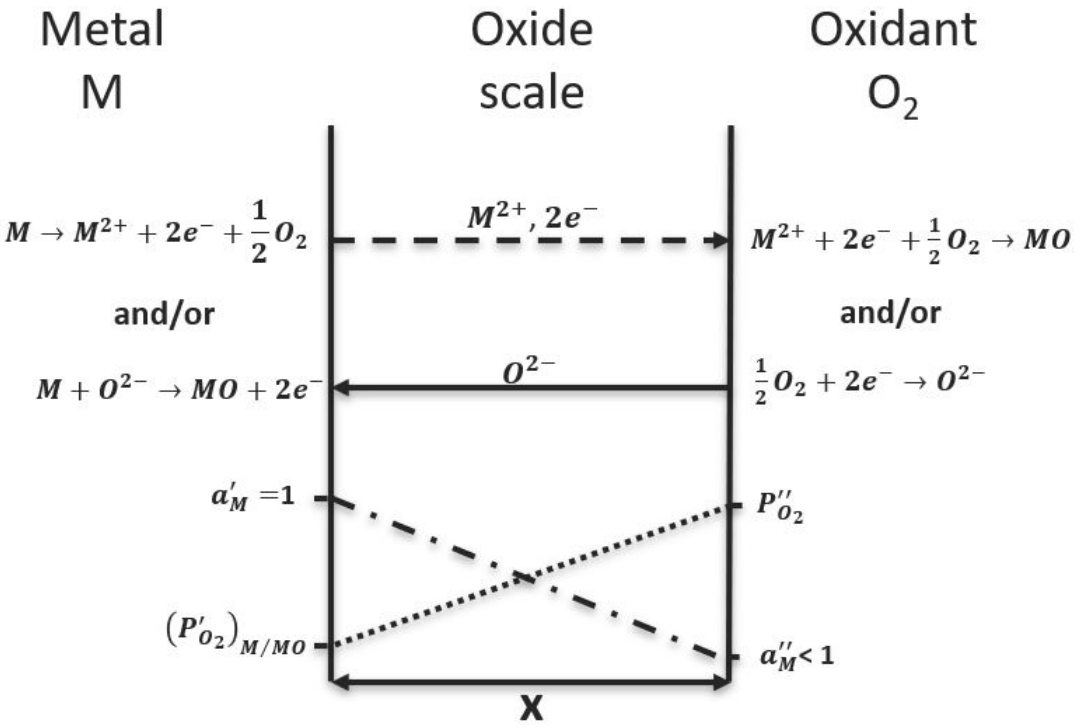

Figure 4.2: Metal oxide formation with ionic (metal and oxide) and electronic diffusion being the rate limiting factor (based on Wagner's model).

- **Linear rate model**

  From the general oxidation rate define in equation 4.7, the rate of the oxide thickness growth is constant. Therefore by integration we could deduce the linear rate equation 4.11

  $$X = k_l t \tag{4.11}$$

  Where k_l is the linear oxidation rate constant.

  Using the same analogy as the parabolic model, where metal and oxide interdiffusion is the rate controlling factor, it would be hard for the diffusion reaction to keep-up linearly as the oxide thickens. This means that the initial reaction occurring at the material's surface (oxygen adsorption and chemisorption) would be linear until a certain oxide thickness is achieved. Therefore, by simple analogy, the linear rate would represent thin oxide where the reactions are fast enough to keep the reaction rate constant.

- **Logarithmic rate model**

  The logarithmic rate law exist in two forms, the direct logarithmic law equation 4.12 or the inverse the inverse logarithmic model equation 4.13.

$$X = k_{log} log(at + t_0) \tag{4.12}$$

$$\frac{1}{X} = c - k_{ilog} log(t) \tag{4.13}$$

  Where a, b, c, $k_{log,ilog}$ are constants.

  Usually, the logarithmic oxidation model is derived empirically, though a few theoretical models were derived on thin oxide forming metal or semiconductors [282]. The interpretation of the logarithmic model is based on the fact the that after the initial gas adsorption and chemisorption at the metal surface, the ionic diffusion through the scale induces an electric field therefore the diffusion of electrons on the opposite side. As the oxide film covers the outer surface of the oxidizing materials, the reaction rate reduces as a result of the increased blocking of the electron flow in the oxide. A thorough review and different interpretations are provided in reference [281]; nevertheless, a common general conclusion is that the logarithmic model is only applicable at low or medium temperature. Moreover, in this project we empirically showed that the logarithmic model can be an intermediate regime between the linear and parabolic regimes at high temperature.

- **Combination of rate equations**

  The logarithmic law, as discussed, well suits oxidation of metals at low temperature and thin film oxides. Similarly, at high temperature metal oxidation is well represented by the parabolic law [283]. However, for protective oxides such as Cr- or Si-based oxides the logarithmic and parabolic law occur simultaneously and yield a polynomial oxidation model as in equation 4.14.

$$X^m = k_m t + C \tag{4.14}$$

  Where m is the polynomial order usually 3 or 4, so cubic or quartic oxidation laws. k_m and C are constants. Between the two , the cubic law is most frequently found in oxidation experimental studies. Empirically, the cubic law during high temperature oxidation is assumed to occur as a transitional stage from a logarithmic regime to a parabolic regime as the oxide scale thickens.

4.4 Module assembly

Several unicouple modules were assembled for test purposes in this project, as shown schematically in figure 5.1. The modules varied in terms of contact layer composition, bonding technique and use of TE coated/non coated legs. Moreover, depending on the choice of the bond composition, the legs would exposed to metallization or coating as briefly detailed below. At the end of the mentioned preparations, the module or unicouple assembly will be mounted in a home made stability test rig as shown in figure 4.3. The rig can be operated in ambient condition, however it is equipped with a vacuum chamber that the test can be encapsulated in 4.4.

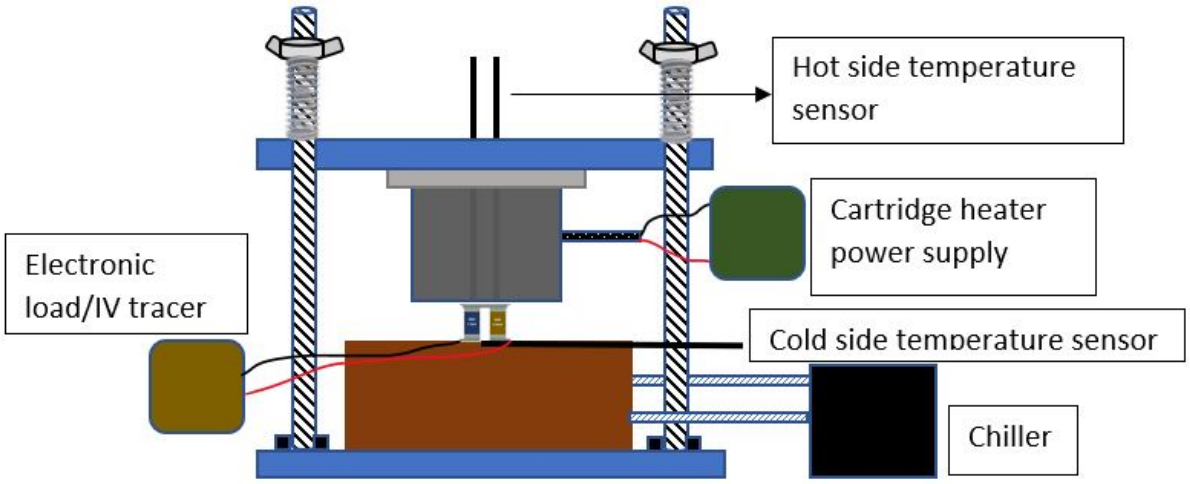

Figure 4.3: Schematic diagram of the home made durability test rig.

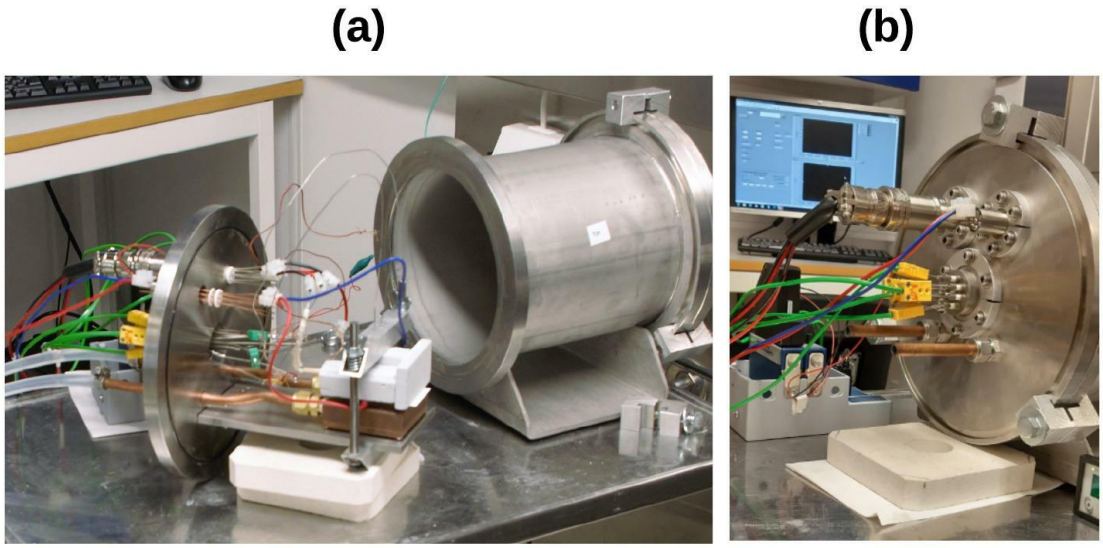

Figure 4.4: TEG performance and long term stability test rig. Tests can be conducted in (a) ambient condition and (b) vacuum or back filled gas conditions.

4.4.1 Coating

With thermal exposure in an oxygen-containing atmosphere, TE elements are exposed to oxidation. To alleviate the oxidation issue, the TE legs were coated prior to being mounted in the modules. A high temperature coating was applied using deep coating or brushing (gently using a brush) with a commercial aluminum-based heat resistant paint (POR-20). The paint should not be too thick but thick enough to block the oxidant from reaching the TEM surface. Therefore, two or three layers of paint were applied. Each layer was allowed to dry in an oven at 150 °C for three hours and allowed to cool down in ambient condition before the next layer was applied.

4.4.2 Metallization

As mentioned in section 3.2.2, good contact interfaces between electrodes and TEMs are characterized by high electrical and thermal conductivity. Metallization is a technique that incorporates one or many metallic compound(s) in the contact layer to increase both

electrical and thermal transport parameters.

There are different metallization techniques, as summarized in section 3.2.2. However, in this project, sputtering and electroplating were the only methods used. A turbomolecular pumped coater (Q150T, Quorum) was used to coat a 50 nm Au layer on each of the n- and p-type TEMs on both the hot and cold sides. For electroplating, the contact surfaces were electroplated with silver using a pure silver electrode in a homemade solution. The solution was composed of distilled water, 0.1 mole of silver nitrate ($AgNO_3$) and citric acid (roughly 0.01 mole) to adjust the solution's pH to around 3.1.

4.5 Electrical characterisation

On the TE modules level, electrical characterization is used to determine the contact resistance at the contact interfaces, module's inner resistivity, and the power density of the modules. As a result the state of the contact interfaces can be evaluated over time. The variables of interest in the section are module short circuit and voltage, which are mentioned in the detailed description of the experiments in section 3.3.2. IviumStat (from Ivium Technologies) is a general-purpose instrument that can be operated as an impedance analyser for corrosion analysis, potentiometry, amperometry, etc. For our specific purpose, the instrument was used in the "transient chronopotentiometry" mode. Here it is used as the electronic load as on figure 4.3. During chronopotentiometry, a series of current signals (maximum 255) can be applied to the module under test and the resulting voltage drop recorded over time (of 10 νs step size). IviumSoft was used to collect I-V data by setting different current levels as set points and recording the potential drop in the module, as shown in figure 4.5 below.

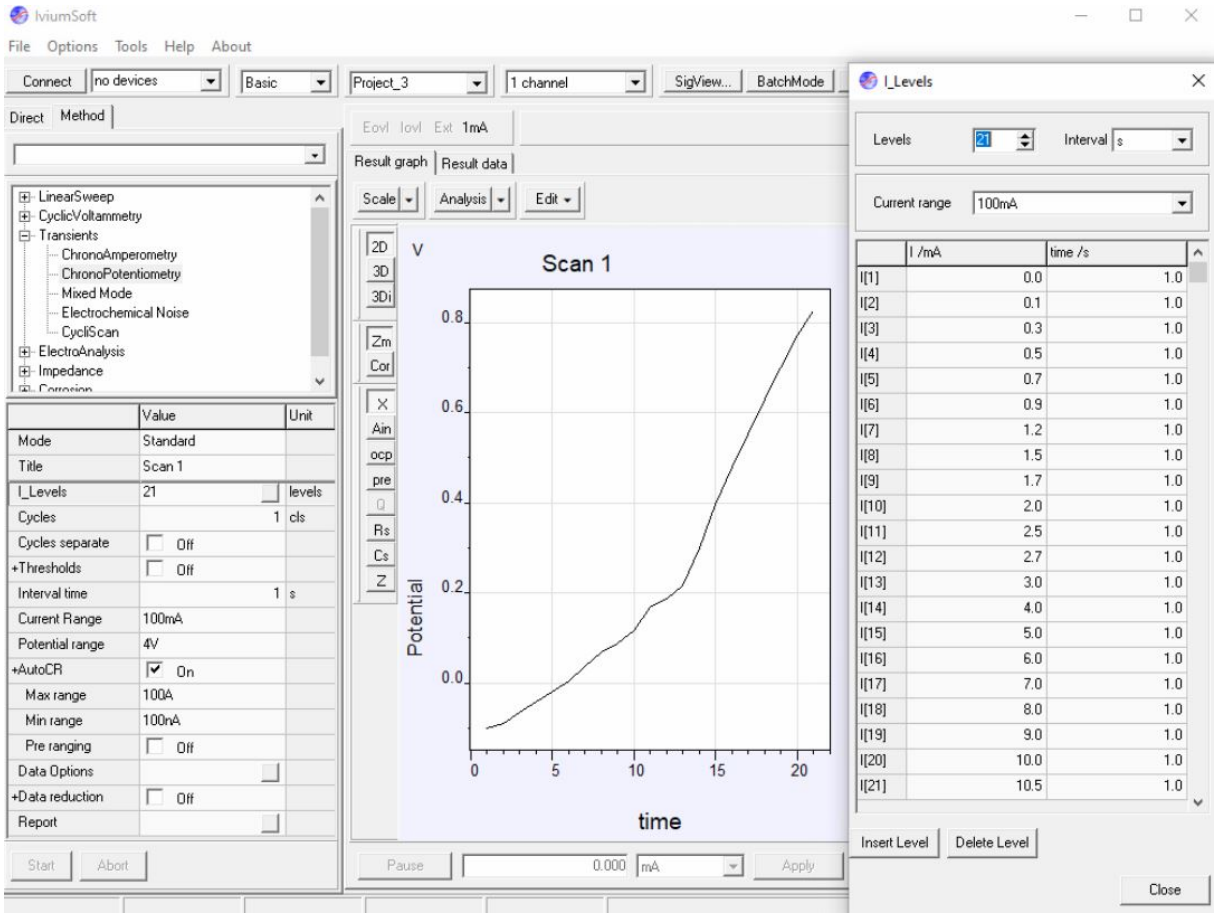

Figure 4.5: I-V data collection method using IviumStat software, operated in chronopotentiometry mode. On the left had side of the picture is the current level series (21 in this figure).

4.6 Microstructure imaging and analysis

Before and after different oxidation and performance tests on TEM and modules, respectively, the samples were imaged on the microscopic level to study the effects of the tests. Similarly, the composition of the samples was also recorded pre- and post-characterization to deduce not only the effect of the tests but also the mechanisms the reactions followed as described below.

4.6.1 Scanning electron microscopy

Two scanning electron microscopes (SEM) from "Zeiss Merlin" and "JEOL 772" both with an energy dispersive X-ray spectrometer (EDS) and back-scattered electron detectors were used, though at different times during the project. They were operated with an accelerating voltage of 10-15 kV and 5-10 mm working distance, depending on the desired resolution. By use of the back scattered-composition images, the specimen composition was analysed by spot, phase mapping and/or line scanning using ESPRIT software from Bruker.

4.6.2 Powder x-ray diffractometry

Powder X-ray diffractometry (XRD) was conducted on the oxidation powder samples to analyze composition before and after oxidation tests. The XRD was performed using D8 Advance XRD instrument (Bruker). As mentioned in Paper III, the XRD method was set at 40 kV and 40 mA with a Cu X-ray tube. The diffraction pattern was recorded in step sizes of 0.02° in the 2θ range of 10-80°. Finally, for qualitative and quantitative analysis, phase identification was conducted using EVA software (Bruker) using the ICDD PDF-2 database.

4.6.3 X-ray photoelectron spectroscopy

X-ray photoelectron spectroscopy (XPS) is another technique that was used for surface characterization before and after the oxidation tests for composition analysis. The tests were conducted using a Kratos Asis Ultra^{DLD} spectrometer with an X-ray monochromatic source at 10 A, 15 kV and 1486.6 eV (hν). For more details on the survey and spectra resolution, please refer to Paper II and III (in the appendices). The depicted spectrum was analysed using CasaXPS software, and the binding energy axis was calibrated using carbon photo-emission peak (at 284.8K).

Chapter 5

Results and discussions

This chapter summarizes the main experimental results obtained during the Ph.D. project and highlights the project's contributions to research on medium temperature TEGs. As mentioned in section 4.1, the TE materials (p-type HMS and n-type MGS) and modules were synthesized and characterized in cooperation with different partners. This Ph.D. thesis reports the study conducted on the thermal and mechanical stability of the TE materials and modules. The results are presented in the form of scientific articles published in peer-reviewed journals. Moreover, the order in which articles are presented follows the logical sequence of the research so that the results are more comprehensible to the reader. The copies of the papers (as published) are attached in the Appendices section for reference.

5.1 Evaluation of the performance of HMS-MGS based thermoelectric modules (Paper I)

This first milestone was to assemble functional TE generators in the form of simple uni-couple TE modules and evaluate their performance over time. The study was published as Paper A. Silicide-based TEM have shown potential for heat recovery in the temperature range of 200-400 °C because the main component, silicon, and the rest of the components are environmentally friendly and abundant (therefore cheap). At the time this study

was conducted, there were few publications/reports on HMS-MGS based modules. While more work has been done on the materials level, specifically on improving the figure of merit by improving the thermal and electrical transport properties, as well as the mechanical properties of the TEMs, less is known on the module level about the HMS-MGS combination.

Because there is such limited knowledge on the module level, the preliminary study presented in Paper I was conducted to help optimize the materials synthesis route and consolidation methods. But most importantly it was conducted to help choose different module components such as the current collectors and bonding materials. The choice of these components are very important due to difference between the CTEs of HMS and MGS, which are around7.89µm/mK and 21.05µm/mK, respectively. Moreover, the study was conducted on two modules (referred to as module 1 and module 2 in this summary) made from n-type MGS ($Mg_{2.01}Si_{0.49}Sn_{0.5}Sb_{0.01}$) and p-type HMS ($Mn_{0.98}Mo_{0.02}Si_{1.73}Mg_{2.01}Ge_{0.02}$). As shown in figure 5.1, silver current collectors were used, together with silver paste and a thin gold coating as a diffusion barrier. It is important to note that module 1 has no gold metal layer, while module 2 is gold metalized at the contact interface.

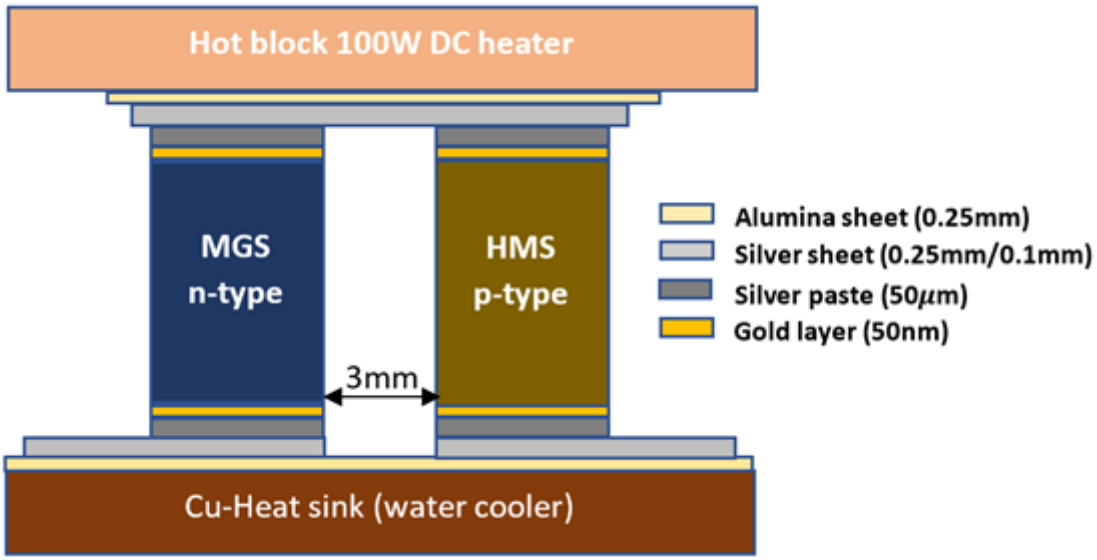

Figure 5.1: Schematic representation of an HMS-MGS based unicouple module test assembly.

The assembly was mounted on a home made rig, equipped with a DC powered 100W heater Inconel block on the hot side and a water-cooled (using a minichiller 280 Huber

Kalten-maschinenbau AG) copper block on the cold side. The TE modules were subjected to isothermal and thermal cyclic tests in the temperature range mentioned above. Finally, the modules were disassembled and post-characterized using a microhardness tester (FutureTech FM-700 with a load of 200 g) along with a scanning electron microscope equipped with an electron dispersive spectrometer (SEM-EDS), for microhardness testing and cross- section composition study, respectively.

The performance of the assembled modules raised red flags on the TE legs and the module in general. First and foremost, MgO and SiO_2 oxides were manifested on MGS and HMS compounds, respectively, as the main oxides. Although the kinetics of the oxide formation had not yet been determined, the lack of wetting on the contact areas was attributed to the early formation of one or both oxides, which impeded the wetting mechanisms of the bonding material. Secondly, based on module 1, a 2 μm intermetallic layer was successfully formed on the hot side of the MGS alloy, and the CTE of the formed IMC was close to that of MGS (22.5 x $10^{-6}K^{-1}$ and 21.05 x $10^{-6}K^{-1}$, respectively). However, there was an insufficient level of diffusion control between the bonding material and the TEM.

The results of experiments on module 1 lead to the design of module 2, where a gold layer was added to act as a diffusion barrier. Module 2 was tested for 300 thermal cycles over 2200 hours, and the results were promising. The Au improved the wetting ability of the bonding materials on the HMS interface, resulting in a more robust bond. In addition, the metallization considerably slowed down the interdiffusion rate, especially on the MGS interface. Overall, the study found that the bonding materials fit the p-type TEM, but not as well as the n-type MGS compound. This finding leads to a third recommendation, namely that the bonding method on the MGS must be improved to assure optimal and definite thickness of the contact layer. Similarly, other bonding technologies such as solid-liquid interdiffusion (SLID), plasma or laser bonding should be tried to improve the contact layer at the electrode-HMS interface.

5.2 High temperature oxidation of the silicide-based thermoelectric alloys

As pointed out in the preliminary study, it is fundamental to consider the high temperature oxidation of n- and p-type TEMs. This is because oxidation is inevitable due to the hostility of the environment and temperature, in which the modules operate. Therefore, it is important to study the kinetics and mechanics of the oxidation reactions of the compounds in question and feed the knowledge back to the materials design stage to engineer resilient and oxidation-robust MGS and HMS alloys. Since Skomedal et al. [278] thoroughly studied the high temperature oxidation of similar MGS and alloys (a summary of the study is provided in section 3.3.5 above, this project exclusively investigated the oxidation of HMS alloys. The results, which were presented and published in Paper II and III, are summarized in the subsections below.

5.2.1 High temperature oxidation of higher manganese silicide and alloys (Paper II)

The high temperature oxidation of HMS alloys was conducted with three main objectives in mind: to determine the effects of the alloys' composition, the densification methods, and the environment on the kinetics and mechanisms of oxidation of the alloys. The composition of alloys studied are $MnSi_{(1.75-x)}Y_x$, where "Y" represents Ge and Al as dopants on the silicon site, and "x" ranges from 0 to 0.01. For more information on the synthesis route and parameters, see paper B in the appendix. It is important to note that the consolidation effects mentioned above were investigated using specimens prepared from the as-cast ingots, HP sintered and SPS pellets. While the environmental effect was empirically examined by comparing the oxidation tests conducted in dry and humid air environments. TGA/DSC 1 (Mettler Toledo) was employed to conduct thermal oxidation experiments in both environments, with a constant heating rate of 5 °C/min and 50 mL/min gas purging rate for iso-conversion tests. For bulk samples, the tests were run isothermally at different temperatures up to 600 °C with dwell times up to 200 hours. Finally, the oxidized powder and bulk residue were post characterized for composition

using XPS, and the microstructure of the non-oxidized and oxidized bulk samples were analysed using SEM/EDS.

A. **Composition effect – oxidation of powder samples**

The iso-conversion experiments revealed that the oxidation onset temperature was in the range of 200–400 °C; moreover, the fewer the impurities in the HMS matrix, the higher the onset temperature was. Nevertheless, with Ge and Al dopants below 1 at% the weight gain was not significant below 600 °C which is far beyond the application temperature range; however, even at high temperatures the weight gain was between 4 to 5% with 0.5 and 1 at%, respectively, for Al-doped alloys. Composition analysis using XPS showed that the powder residue of all the investigated HMS alloys contained SiO_2 as the main oxide phase, little MnO oxide phase and Al- and Ge-based oxide phases for the doped compounds.

The pure (no dopants) and Al-doped HMS showed 3.7% and 8% of the total binding energy spectrum, respectively, associated with Si_2O_3, which was not seen in the Ge-doped compound. The presence of low Si oxidation state oxide accentuates the low oxidation rate in the pure HMS and also sheds light on the high oxide weight in the Al-doped HMS which may be associated with the formation of a conglomerate of oxides. In addition, deconvolution of O 1s spectra indicated that the Mn oxide phase increased with Al doping and decreased with Ge doping.

B. **Effect of densification methods – bulk samples**

The comparative analysis was based on the compounds densified by metallurgical casting, HP and SPS. Isothermal oxidation experiments conducted in ambient air with a 24 hour dwell time showed that at temperatures below 400 °C the oxide layer was very thin. However, at higher temperatures, for example 600 °C, the weight gain was tangible and distinct for the three consolidation methods. The as- cast specimen had 7.5 $\mu g/mm^2$, the HP sintered had 29 $\mu g/mm^2$, and 1.8 $\mu g/mm^2$ for the SPS one after 24 hours, revealing not only the relationship between the bulk density and oxidation robustness, but also the importance of the chosen consolidation method.

C. **Effect of humidity – bulk samples**

The humidity effect was investigated over a period longer than the usual 24 -hour retention time: up to 200 hours. When the experiment was conducted in ambient air, the TGA curve showed cyclic weight gain and loss in periodic steps of 11 hours gain and 13 hours loss. Moreover, the parallel DSC analysis of the events indicated that the weight gain and loss corresponded with exothermic and endothermic reactions, respectively. Clearly, the trend reflected the difference in vapor pressure over a day, with the mass gain occurring during the night and the losses occurring during the day. At higher temperatures (above 500 °C), the reaction followed the same trend, but this time with longer exothermic segments (16 hours) than endothermic ones (8 hours). The presence of H_2O was certainly noticed and did not seem to affect the SiO_2 scale growth; however, the effect of humidity on the stability of SiO_2 was not thoroughly investigated.

To summarize, a study of high temperature oxidation of $MnSi_{(1.75-x)}Y_x$ alloys was conducted and showed that the alloys grow a protective SiO_2 scale at temperatures below 500 °C. The oxidation kinetics were studied and presented and the oxidation mechanisms were broadly discussed as illustrated in figure 5.2. Moreover, the level of protectiveness was discussed, with synthesis, consolidation methods and operational environment being the main points of discussion. It was also determined that an alloy's composition is closely related to its oxidation potential and therefore has a positive influence on the robustness of the oxide layer with Ge as dopant but not to the same extent as with Al. The effect of composition was limited not only to alloy design but also to the purity of the raw feedstock during the synthesis stage. Finally, the samples densified by HP were 3 times less robust than their as-cast counterparts, while the SPS samples showed higher mechanical integrity and therefore higher thermal oxidation resistance. As a result, the mechanical compactness of the produced bulk materials is important to achieve an oxidation-resistant compound.

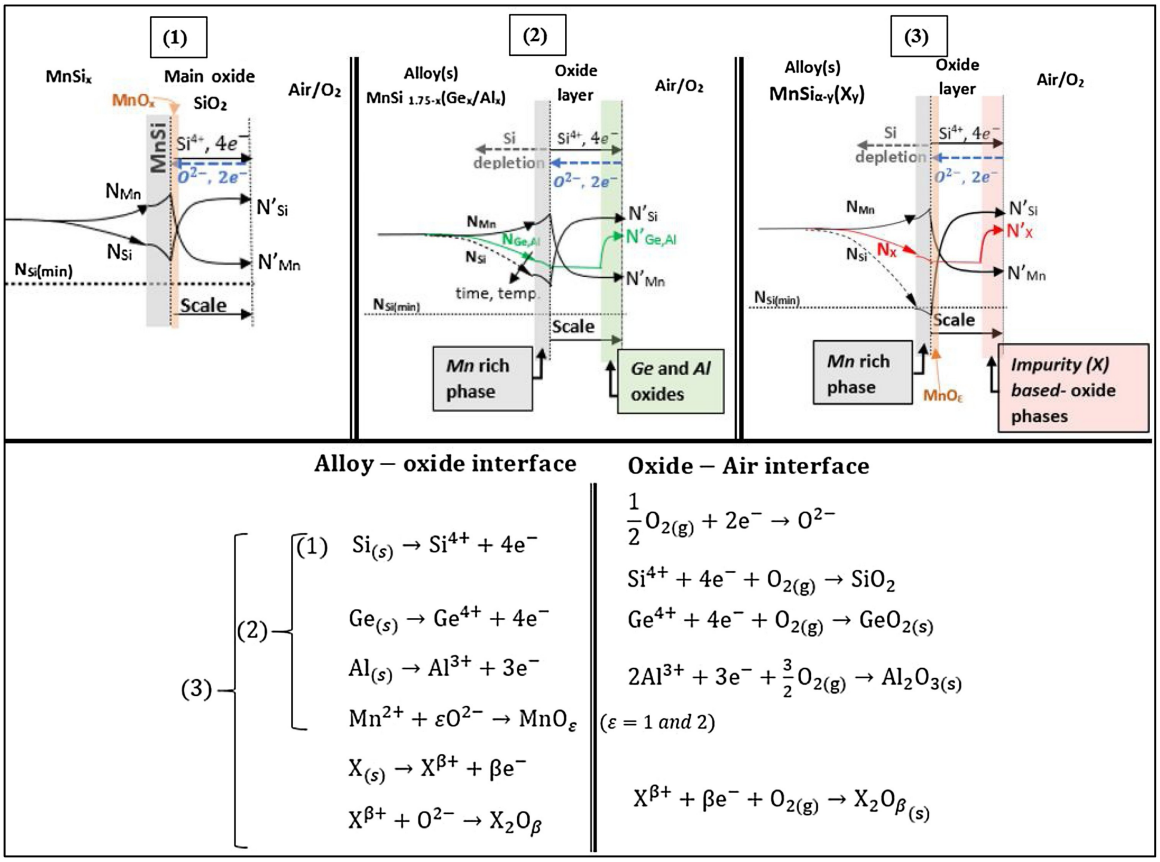

Figure 5.2: Schematic illustration of the HMS alloys' oxidation profile, showing the mechanisms of oxidation of the alloys. The alloys' purity and composition are considered as well as the effects of dopants.

5.2.2 The effect of dopant and doping site on the high-temperature oxidation of higher manganese silicides (Paper III).

Following Paper II above, there is a strong link between the composition of an alloy and its robustness to oxidation. Previously, $MnSi_{(1.75-x)}Ge_x$ sintered using SPS was found to be the oxidation-resistant compound among the alloys studied. However, in the race to improve thermoelectric transport properties, further fine-tuning and tweaking are needed to reach the full potential of the alloys. This implies a parallel oxidation study of the new alloys to ensure similar if not better resistance to oxidation. $Mn_{(y-\alpha)}Mo_\alpha Si_{(1.75-\beta)}Ge_\beta$ with y=0.99 – 1.011, α= 0.005 – 0.02 and β= 0.005 – 0.01 alloys were examined. The oxidation experiments were conducted using TGA/DSC1 (Mettler Toledo) in dry air, and the experimental residue's composition was analysed using X-ray powder diffraction

(XRD) spectroscopy and XPS. Similarly, post-oxidation testing with XPS was conducted, to study the surface composition of the bulk specimen, and SEM/EDS (JEOL 772) used to map the cross-section elemental or phase composition of the same solid samples.

A. **Isoconversion results**

The constant heating rate experiments were conducted at a temperature of between 25 and 1100 °C with a 5 °C/min. The onset temperature for all alloys was in the temperature range of interest (module operation temperature range) 200 – 400 °C. Even though, the oxidation reaction started below 400 °C, the oxide content was too far below the detection limit for XRD (with at most only 10 μg/mm^2 weight gain) to be able to identify the exact oxide phases present. However, after conducting the test up to high temperatures, not only could XRD identify the oxide phases, but DSC could identify silica using its crystallization temperature form alpha quartz to beta tridymite between 420 °C to 960 °C, respectively. Similarly, Ge and Mo oxides were also detected.

B. **Isothermal oxidation results**

The oxidation reaction kinetics of the studied alloys occurred in three regimes corresponding to the temperature ranges of $<$ 250 °C, 300–400 °C and above $>$ 400 °C. At temperature lower than 250 °C, the alloys' oxidation rate was too low to grow a significant layer, even over an extended period. Slightly above this temperature, the oxide weight gain per unit area of the specimen fitted the linear rate law. This oxidation model was found to be a result of a fast accumulation of gas adsorbate on the alloy surface. The same model was observed at temperatures higher than 400 °C but the reaction occurred in a very short period, less than one hour. After this time, the oxide scale thickens (but still too thin at hundreds of Angstroms) and eventually follows a logarithmic oxidation model. The chemisorbed gas at the alloy surface reacts forming a defect gradient and resulting in a electric field at the alloy-oxide interface, making ionic transport possible on the respective faces of the interface.

At temperature close to 500 °C and above, the logarithmic law is still representative of the compounds' oxidation model, but for a short period. Over time the scale would follow the parabolic model whether the dwell time was 24 hours or 200 hours.

The surface and cross-section composition tests showed that when the oxidation reaction started, a conglomerate of oxides was formed (SiO_2, GeO_2, MoO_3 and Mn was manifested in ternary oxides). As the oxidation phenomenon progressed the oxides coexisted, though SiO_2 was dominant, fully covering the alloy surface by the end leaving the Ge and Mo oxides at the SiO_2 – air interface.

The empirical data and knowledge regarding kinetics and mechanisms acquired during this study allowed us to draw a time temperature transformation (TTT) diagram as in figure 5.3. The oxidation map shown was built using actual data of the isothermal onset temperature and end set temperatures during the TGA oxidation experiments. The green and red curve represent the start and the end of a given oxidation test on one alloy in the 200–600 °C temperature range, with each test run for 24 hours. Moreover, the color codes represent the oxidation regime an alloy would be represented by depending on its elemental composition. Using this method, we were able to draw an oxidation map from the TTT diagram (usually used in metallurgical processes).

The study showed that doping on the Mn site did not have an enormous effect on the oxidation of the studied alloys; however, the fact that the materials were multiphase alloys did have a major effect. With non-phase homogeneous compounds, each phase reacted independently, involving all the alloy constituents. The longer the alloys were exposed to oxidation, SiO_2 oxide grew dominantly to cover the alloy and stood between the alloy and other oxides, therefore assuring some level of resistance to oxidation. Nevertheless, even though a TE properties test was not conducted post-oxidation, it is evident that with some material loss due to oxidation the TEM would lose some TE potential. This should therefore be taken into consideration when designing materials.

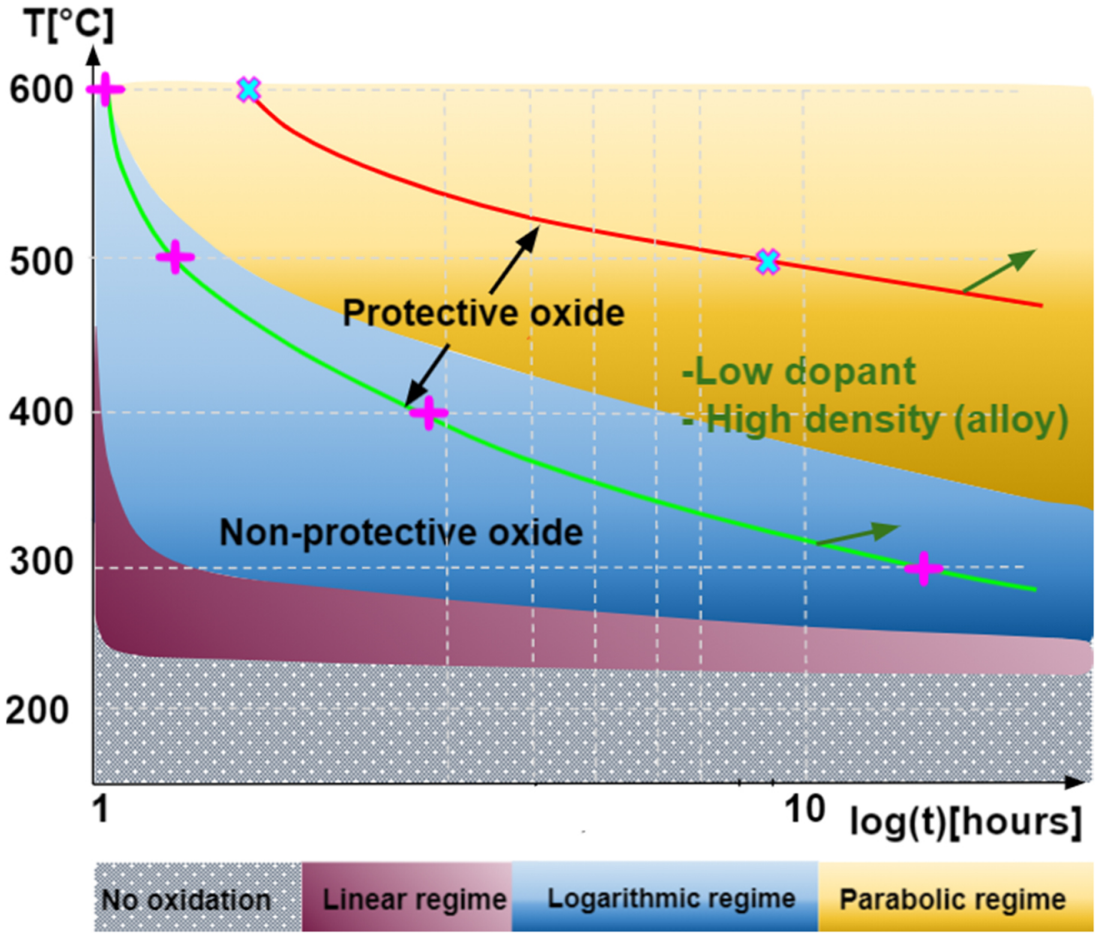

Figure 5.3: TTT diagram of HMS alloys oxidation. The green and red curves represent the start and end of a given oxidation experiment conducted isothermally at a temperature between of 200–600 °C

.

5.3 Measurement of the contact resistance in silicide-based thermoelectric modules

(***The content of this section will be the basis of a scientific journal article***)

5.3.1 Introduction

Section 5.2 presents the research results obtained in this study specifically pertaining to the oxidation and stability of silicide-based TEMs, and the results were published as Paper II and III. In addition, the stability of silicide-based TE modules was also briefly reported and discussed in Paper I; however, questions relating to the modules' electrical characterization were left unanswered. Therefore, this research intends to design and model functional p-type HMS and n-type MGS-based TE modules and evaluate their performance and durability over time.

Apart from TEMs, TE modules are composed of numerous components, namely the electrically conductive electrodes, the contact interface between the TEM electrodes, and the electrical insulating substrate. All these layers play an important role in ensuring the productivity, reliability, and effectiveness of the module over time. The module's productivity is directly related to the thermoelectric properties of the TEM (as described in Chapter 2), but it is also highly dependent on the electrical and thermal conductivity of contact layers between TEM and electrodes. Chapter 3 gives details on designing the TEM – electrode interface, where actions such as metallization are applied to reduce the electrical resistivity of the interface and increase the thermal conductivity. Moreover, the choice of a good bonding technology is very important since it ensures the mechanical reliability of the bond initially. Paper I of this dissertation discusses the formation of a good bond consisting of an intermetallic (IMC) layer between the TEM and electrode, usually by solid diffusion; nonetheless, it also discusses the importance of limiting the diffusion process by including a diffusion barrier. Finally, section 3.3 of the same chapter gives a good description of the performance and stability testing of TE modules, which was followed during this research.

As mentioned above, the TEM–electrode interfaces' performance and durability were the main focuses of this study. The main task was to design a good bonding layer, which consisted of deciding on the components of the contact layer and on the bonding technology. Different bonding technologies are shown in section 3.2.4 and a good summary of the listed technology is provided in Figure 3.4. One of the biggest challenge of the HMS–MGS based TE modules is finding good electrodes and bonding materials that fit both TEMs, mainly because of the tremendous difference between their coefficients of thermal expansion, which are 7.89 and 21.05 μm/m.K [208], respectively.

Among the proposed alternatives for MGS alloys, Ni [284–286] and Ag [286] electrodes were found to be good fits for the alloys. The bonding experimentation was conducted by co-sintering the electrodes with the TEMs using one- or two-step SPS technique. This resulted in very good IMC and homogeneous interfaces with very low specific contact resistance in the range of 10–50 $\mu\Omega\text{cm}^2$. Though the technique seems to provide incredible contact interfaces, it is not straightforward and requires advanced instruments that may not be at everyone's disposal. Therefore, some other techniques were studied such as brazing. Ihou Mouko H. et.al. [287] manufactured TE modules based on n-type $Mg_2Si_{0.6}Sn_{0.4}$ and p-type $MnSi_{1.77}$ and achieved a power density of 0.95 W/cm^2 at hot side of 450 °C and ΔT of 400 °C. Also by brazing, Graff J. S. et.al. [254] achieved a power density of 53 μW cm^{-2} using a Cu electrode on both n-type $Mg_2Si_{0.3}Sn_{0.675}Bi_{0.025}$ and p-type $Mn_{x-\epsilon}Mo_{\epsilon}Si_{1.75-\delta}Ge_{\delta}$ at the hot side of 250 °C and ΔT of 100 °C. However, they did not provide information on the quality of their modules' electrode contacts.

In this study the aim was to design reliable contact interfaces between n-type $Mg_2Si_{0.3}Sn_{0.675}Bi_{0.025}$ and p-type $Mn_{1.005}Mo_{0.005}Si_{1.75}$ based modules with Ag electrodes on both the cold and hot sides. The bonding process should be able to form a mechanically robust IMC contact layer capable of limiting the cross diffusion between the TEMs and the contact interface constituents. A. Ayachi et.al. [288] studied the effect of Ag electrodes on n-type MGS alloys. They showed that due to diffusion of Ag in the n-type Mg_2Si and Mg_2Sn binaries, the Ag_{Mg} defect counteracted Bi-related defects and resulted in reduction of the thermoelectric properties (especially the charge carrier concentration). As a solution, the solid liquid interdiffusion bonding (SLID) method was chosen since it is conducted at low temperature [289], and form a solid IMC that can withstand high

temperatures. In addition, a gold metallic layer was introduced in the contact interface as a diffusion barrier to reduce prolonged Ag diffusion in the MGS matrix. Finally, an automated contact resistance test rig was designed and built to evaluate the electrical resistivity of the formed IMC interfaces using the four-wire or Kelvin resistance measurement method. With the above processes, the best performing module was subjected to durability tests, in which several thermal cycle tests were carried out between 222 °C and 455 °C on the hot side of the TE module equivalent to a ΔT of 200 °C and 400 °C, respectively.

5.3.2 Methodology

5.3.2.1 Material and module production

The methodology is presented in figure 5.4. The study is divided into three parts: tthe first is to model the contact interfaces between the TEMs and the electrodes on both the hot and cold sides of the TE modules. The thermoelectric materials used in this study are n-type $Mg_2Si_{0.3}$ $Sn_{0.675}Bi_{0.025}$ and p-type $Mn_{1.005}Mo_{0.005}Si_{1.75}$. The synthesis process of the TEMs will not be detailed in this section. However, for the reader's information, the synthesis route of the n-type MGS alloys was published in [288, 290], and the p-type HMS alloys were synthesized as described in [254] and Paper II and III in the appendix of this dissertation.

During the bonding tests several trials were conducted by varying the content of layers among a silver sheet (electrodes), electrically conductive silver paste, an indium sheet, an electron-plated silver layer and a sputtered gold layer, as shown in figure 5.4 (a). Moreover, as shown in the Au and Ag-In binary phase diagrams figure 5.5, many IMC phases can be formed by SLID bonding, especially the ζ (pertaining to Au- and Ag-rich phase) for both the Ag-In and Au-In. $AuIn_2$+In(S) can also be the other phases on the Au-In side due to the formation temperature.

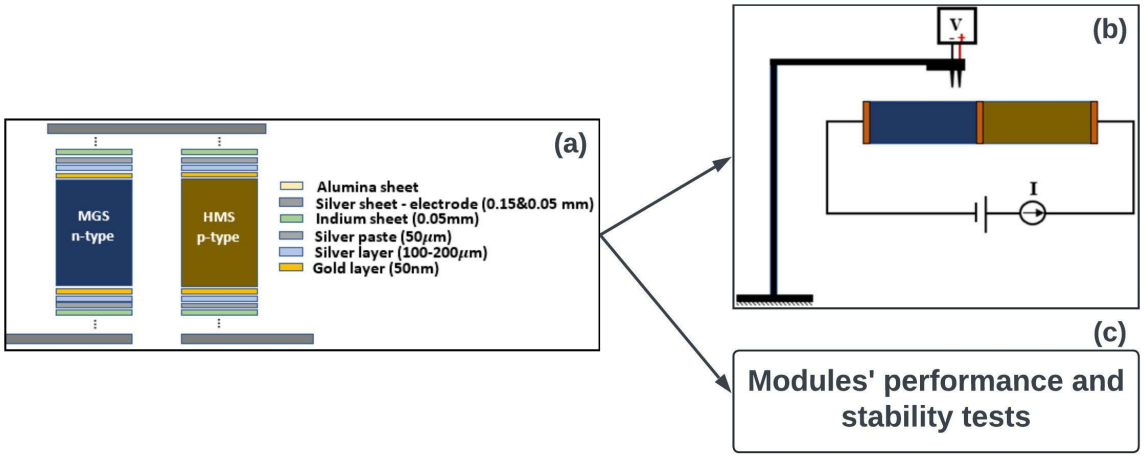

Figure 5.4: (a) The unicouple bonding model with a description of bonding layer components, (b) The schematic illustration of the contact resistance measurement process using PCM test rig.

Furthermore, the bonding process was conducted by mechanically clipping the module (with contact layer components) between two plates using two spring loaded poles (see figure 4.3), and applying a compressive pressure of around 1.5 MPa. A three-step SLID bonding method was carried out in vacuum of around 4.2 Pa to 6 Pa, with a fast heating rate of 20 °C and held for 10 min. After 10 minutes, the system was kept under vacuum but left to cool naturally (equivalent to 3 °C/min) until it reached room temperature where it was held for 30 minutes. The process was repeated two more times, but for the last step the system was kept at the bonding temperature for 1 hour. The bond was quite solid after the SLID bonding.

After the module assembly, steps two and three consisted of conducting the electrical contact resistance at the electrode – TEM contact interfaces and the durability tests as illustrated in figure 5.4 (b) and (c), respectively. Further details are provided below in their respective sub-sections.

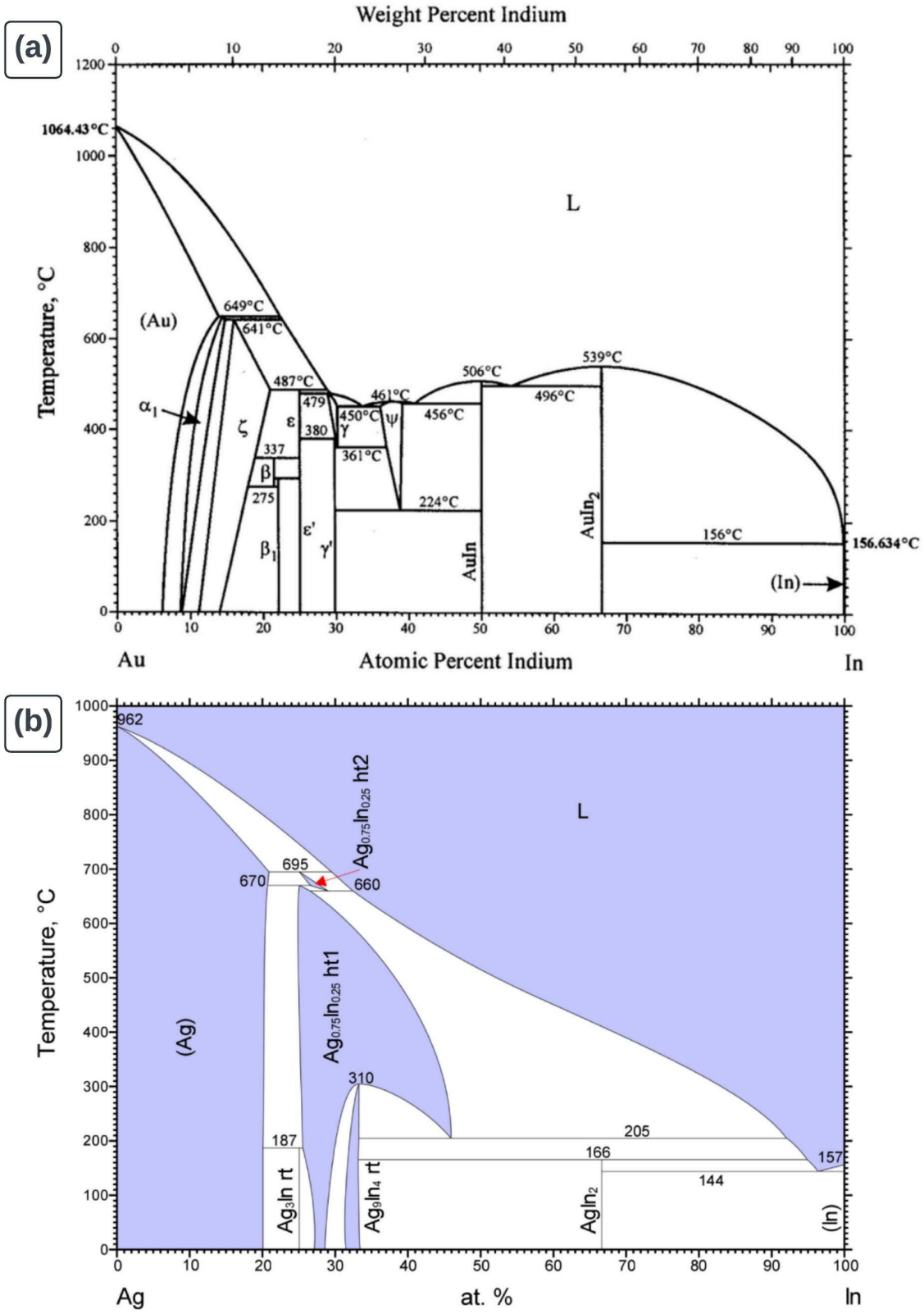

Figure 5.5: (a) The Au-In binary phase diagram and (b) the Ag-In phase diagram

5.3.2.2 Contact resistance measurement

The contact resistance was measured using a home-built three axes point contact measurements (PCM) test rig. The PCM hardware model design and construction process is detailed in "Appendix D" attached to this dissertation. The same appendix file contains the details on the test rig's control program. However, the full PCM 3D model is shown in figure 5.6, while the complete and functional test rig (with computer and electronics) assembly is shown in figure 5.7. The functional test rig, as shown in table 5.1, is characterized by a high positioning accuracy of 1 μm, signal resolution (7 1/2-digit digital multimeter (DMM)), highly reproducible results of around 0.5%, and finally very fast scan in time.

Table 5.1: The PCM technical specifications

Description	**Specification**	**Comment**
Positioning accuracy	1µm step size	—
Max. scanning area	100 x 100 [mm]	higher on request
Signal resolution	7 1/2-digit DMM	—
Reproducibility	0.5% - 1%	on solid surface
Measurement time	1.4 sec/scan point	it can be lower
Total Size	350*350*400 [mm]	—
Total Weight	5kg	no electronics appliances

In four-point contact mode the apparatus acquires the potential difference along equipotential lines perpendicular to the electric field set by the current supply. Therefore, for this specific case study, the four-point technique was used to measure the contact resistance across bonding layers at the TEM–electrode interfaces of the TE unicouple.

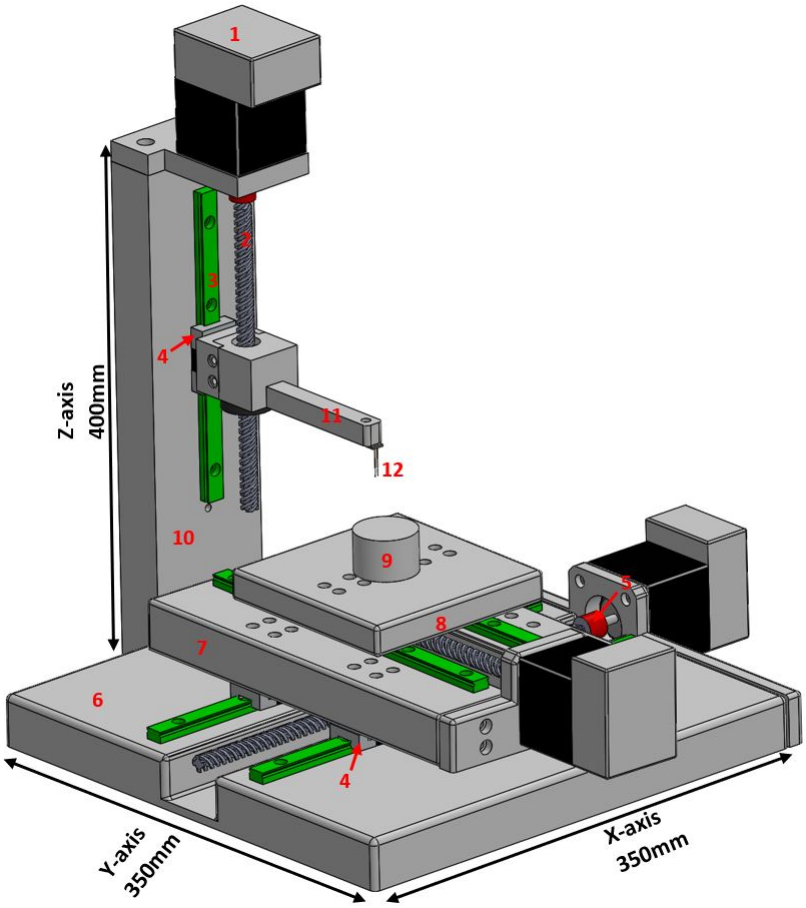

Figure 5.6: The complete 3D model of the PCM test rig, with all components numbered respectively.

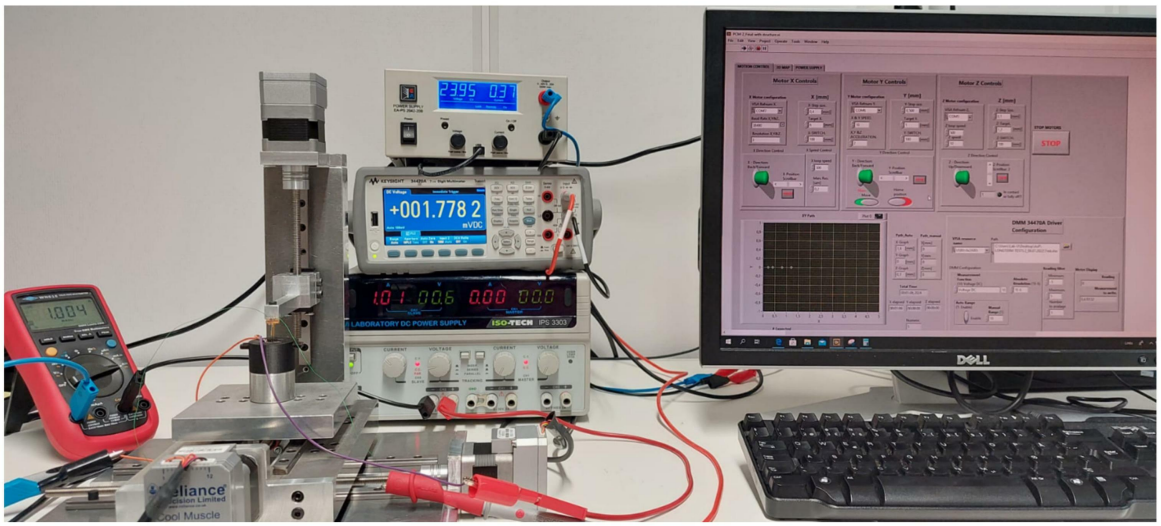

Figure 5.7: The complete test rig setup comprising the PCM test rig, the electronic hardware components, the computer with a control program and the test sample.

Sample preparation for PCM

HMS–MGS based unicouples were assembled as described in sections 4.4 and 5.3.2. Figure 5.8 is a flow chart that shows the process from collecting TE legs (after cutting and surface preparation), assembling the unicouple(s) up to resin-mounting the PCM test sample. The assembly process consists of modelling the contact layer composition, assembling the module and accessing the quality of the modules/unicouples until it is satisfactory. For PCM tests the HMS - MGS unicouple was mounted in non-conductive resin and after the specimen's cross-section was prepared as described in section 4.2.2. It is recommended that the test sample be polished to a mirror-like surface to reduce the uncertainty of the results and increase repeatability.

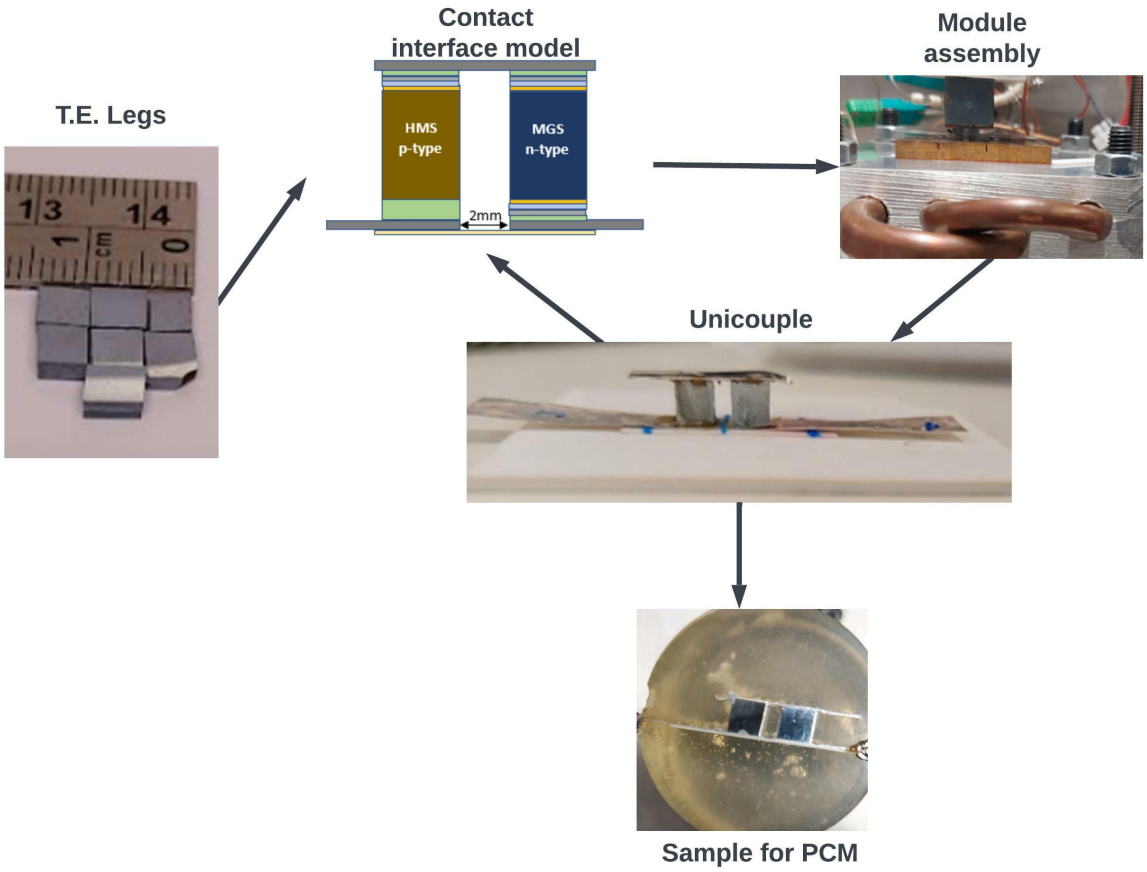

Figure 5.8: The sample production flow chart from the cutting of the unicouple legs, contact layer modelling, module assembly and unicouple resin mounting.

Since the task is to measure the contact resistance across all four interfaces, the scan area

was set to start from the electrically insulated resin and continue until another resin area across the sample. Moreover, a constant DC current was set to 0.3 A. The full test rig with all components and electronics is shown in figure5.7 above. The PCM test measures the potential difference across the defined area and the contact resistance will be deduced by Ohm's law, which states that the actual resistance is proportional to the ratio between the potential difference across two test points and the current passing through the same points.

5.3.3 Results and discussion

5.3.3.1 Contact resistance

The PCM rig was successfully built as described in the methods section. The key specifications (in table 5.1) are the linear positioning accuracy, which can be up to 1μm, 0.5% data reproducible capacity on solid or hard surfaces, and finally, a measurement time of 1.4 sec/data point. This time can be improved by making sure the sample surface is flat, because if it is not, the probe is given room to travel through on the z-axis to avoid scratching the sample surface, thus increasing the overall scan time.

Figure 5.9 (a) is a heat map representing the voltage drop across the unicouple by passing a current of 0.3 A through the unicouple (at the unpaired electrode terminals). Figure 5.9 (b), on the other hand, is a schematic illustration of the TEMs (MGS bottom and HMS on top), the bonding layer composition, as in figure 5.8 (contact interface model) above, and the red dotted lines are the line scan path taken by the PCM rig during the PCM process. As shown by the scale on the right-hand side of the image in (a), the grey surface is the electrically non-conductive area, which in this case corresponds to the area covered by resin epoxy or the alumina (Al_2O_3) sheet at the non-coupled electrodes as shown on the far-right image of figure 5.9 (b). Moreover, the remaining surface consists of the TE legs and, most importantly, the TEM–electrode contact interfaces. Starting from the left-hand side of figure 5.9 (a), on the x-axis at 1 [mm] position are the cold side interfaces, while at 3.8 [mm] are the hot side interfaces on both TEMs.

Mapping the normalized voltage, which is the ratio between the voltage drop across a

resistor and the corresponding current (equation 5.1), gives a broad view of the electrical resistivity of the defined area. In case the electrode contacts are part of the test area as on 5.9 (a), the map provides a visual quality check of the contacts as a function of the normalized voltage drop across them. It is important to note that to distinguish different parts of the heat map, the left-hand and right-hand side contacts are called cold side and hot side contacts, respectively, referring to how the module was assembled during bonding. Considering the MGS–electrode contacts, the hot side is relatively homogeneous with around 0.4 Ω contact resistance. However, the cold size looks less homogeneous and less conductive with the lowest point at 0.4 mΩ and the highest at 1.96 Ω. This can be associated to the temperature difference between the two edges, where the bonding temperature (of 200 °C) is reached on the hot side but not exactly reached on the opposite side, though the temperature goes above the melting temperature of indium (156 °C).

$$\Delta V_{normalized} = \frac{\Delta V}{Current} \tag{5.1}$$

Using the same analogy on the HMS side, the results are the opposite: on the cold side the contact is homogeneous and the electrical properties are better than on the hot side. At the cold side, the normalized voltage is around 0.27 Ω and looks homogeneous along the whole interface, except some non-conductive spots, while the hot side contact covers a wide range from 1.76 to 3.4 Ω. With reference to Paper I of this dissertation, the initial contacts on the HMS alloys were not as reliable as the MGS, so this did not come as a surprise. However, it is clear that there was some improvement on the cold side, though the durability of that bond remains unknown.

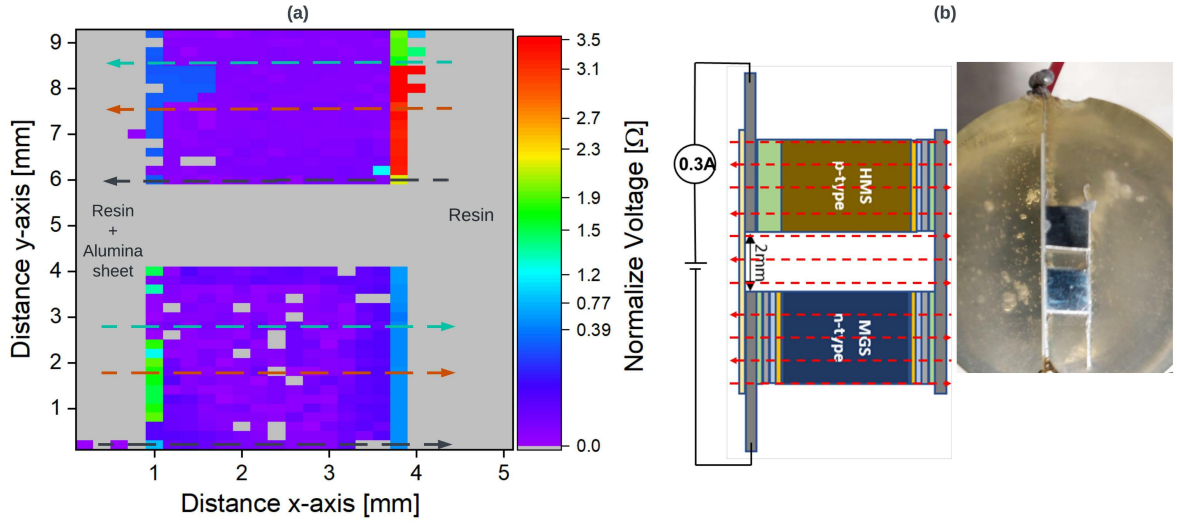

Figure 5.9: (a) The four-point contact measured potential difference across the unicouple under a 0.3 A current. (b) This illustrates the specimen disposition during the PCM test; the red lines are the path taken by the surface scanner.

Furthermore, apart from the mapping possibility, as shown above, the test rig can be operated in line scan mode where the contact resistance across the interfaces is clearer. Figure 5.10 shows three line scans conducted as illustrated in figure 5.4 (b) on the same test sample as in figure 5.9(b). Many line scans (seventeen to be exact) were taken across the scan area; the compilation of all scans spectra can be found in "Appendix E". The three line scans were chosen based on the different spots characterizing the different areas of bonding interface as presented in the map above. Data from line scans 1, 4 and 5 (abbreviated as L.s.1, L.s.4 and L.s.5) are shown on the map in black,: orange and cyan respectively. Moreover, the cold side interface on MGS will herein be referred to as interface (a), and the hot side interface as interface (b) (b_1 on MGS and b_2 on HMS), while (c) is the cold side on the HMS TEM, as shown on in figure 5.10.

Spots 1 to 5 are the specific contact resistance at the interfaces, with the contact resistance at interface (a) being around 0.79 $m\Omega cm^2$, as it corresponds to the longer edge (in Green on the heat map). Considering all recorded data at this interface, table 5.2 shows that the minimum contact resistance is 5.42 $n\Omega cm^2$, the average is 0.39 $m\Omega cm^2$ and the standard deviation is 87.4%. This shows how dispersed the data is at the interface; however, it also shows that the method has potential and invites further investigation to try to optimize

both the contact layer composition and the bonding method, with the goal of creating a homogeneous bond. The interface (b) comprises the hot side on the MGS side and the Ag electrode interface that has 0.16 mΩcm^2 and 1.36 mΩcm^2 on the HMS–electrode interface. Finally, contact layer (c) has the lowest contact resistance at 0.11 mΩcm^{2}but showed some nonconductive spots. The nonconductive spots observed in the MGS alloys could be poles; however; further microscopic analysis would be required to confirm this.

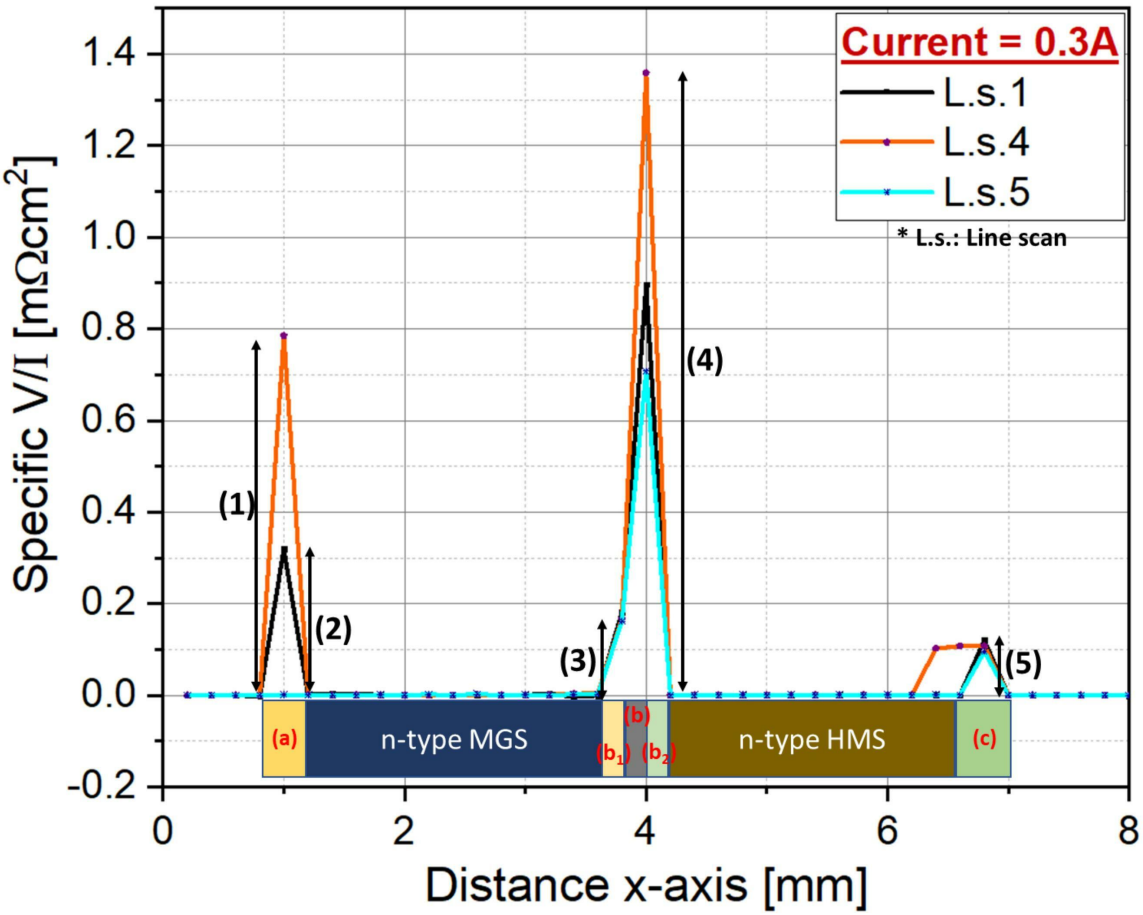

Figure 5.10: The line scan results on an HMS-MGS assembled as an n-p semiconductor junction with a silver electrode, to measure the contact resistance across the junction. (a) - (c) represent the contact interfaces, while labels (1) - (5) represent the specific contact resistance at each contact interface.

To summarize, the SLID bonding technology adopted showed that the contact interfaces were initially solid. However, the contact resistance measurement revealed that most of the interfaces are non-homogeneous which means that further improvement is required.

Moreover, in comparison to the best contact resistance values in the literature for HMS–MGS modules (10-50 $\mu\Omega cm^2$ [284–286]), the interface (c) contact resistance is one order of magnitude higher than the reported values, while the worst contact is 28 times higher than the reported values. The simple and straightforward nature of the SLID technology used in this research is provides motivation to fine tune the parameters and try to improve the quality of the contacts in the future.

Table 5.2: Statistics of the contact resistance values at the electrode-TEM interfaces. Layers (a)–(c) refer to the contact interfaces as in figure 5.10.

Statistical measure	**Specific $\Delta V/I$ [$m\Omega cm^2$]**			
	Layer (a)	Layer (b)		Layer (c)
		(at b_1)	(at b_2)	
Minimum	5.42E-06	0.15	0.36	0.00
Maximum	0.79	0.18	1.39	0.12
Average	0.39	0.17	1.12	0.07
Standard deviation	87.4%	2.1%	81.3%	13.0%

5.3.3.2 Durability of HMS-MGS based TE Module

As shown in figure 5.4 (c), the third part of the study was to subject the assembled TE unicouple to durability tests. The tests consist of exposing the module to thermal cycle stress between 200 °C and 400 °C and empirically evaluating its degradation across three parameters: the open circuit voltage (V_{oc}), the internal resistance (R_i) and module output power over time. A more detailed description of the test process can be found in section 3.3.

- **Power density** Figure 5.11 shows the current versus the potential difference data acquired by load matching as described in section 3.6. This allows us to get the I-V plot and the power generated by the TEG at different ΔT from 100 to 400 °C. Looking at the desired application temperature (between 200 ° C and 400 ° C),

the maximum power point at a ΔT of 200 °C is 0.44 mW, which is equivalent to 1.1 mW/cm^2 power density. Meanwhile, at a ΔT of 400 °C, the maximum output power is 1.96 mW (i.e 4.9 mW/cm^2). The internal resistances at both temperature are 0.9 ohm and 1.7 ohm, respectively.

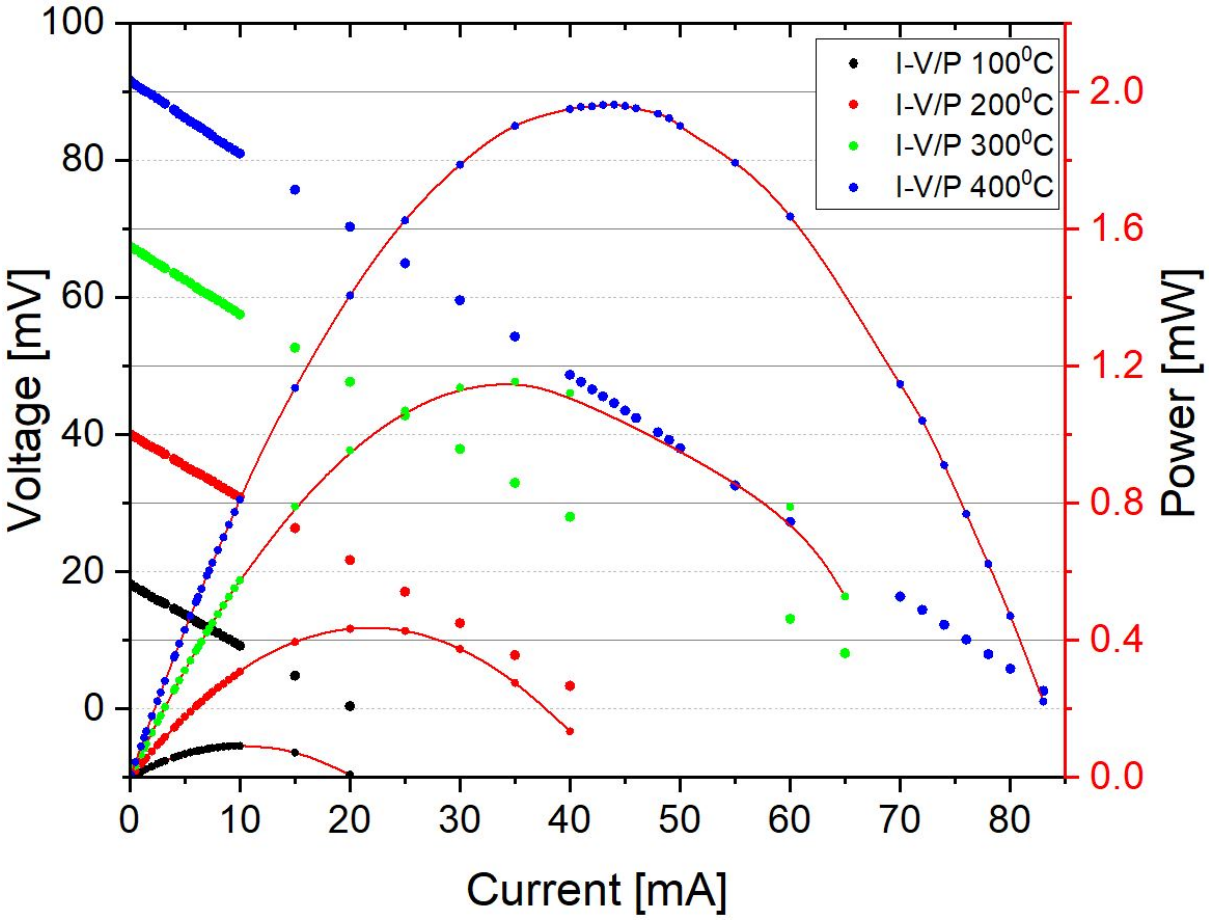

Figure 5.11: A current versus voltage drop plot of the HMS-MGS unicouple from 100 °C to 400 °C.

In the above results, the internal resistance was measured right after assembling the modules. However, the internal resistance is almost equal to the contact resistance. This means that the contact resistance makes the most of modules' inner resistance, again showing the importance of improving the electrode contacts.

- **Durability test results**

  After the IV scan, the stability of the TE unicouple was tested by subjecting the TEG to thermal cycles and recording the $V_{oc}$and the module internal resistance and tracking the maximum power point. Figure 5.12 shows the three parameters

over time at 200 °C and 400 °C, respectively. The stability tests were conducted for over 350 thermal cycles of 1.5 hours full cycle and were carried out for more than 600 hours. At the start of the experiment, during the ten first thermal cycles the V_{oc} and P_{max} increase while R_i falls rapidly. This is because the module is still in the bonding process. However, after that, both the V_{oc} and P_{max} dives and R_i spikes as a result of technical problems with the hot side power supply. The issue lasted around 100 hours; in the area highlighted in orange in both figures 5.12 (a) and (b), the process is marked by a gradual increase in the internal resistance and decrease in the output power. However, after the instrument was replaced, the module recovered to reach the maximum power output of 1.6 mW and 7.48 mW at 200 and 400 °C ΔT, respectively.

The module withstood the thermal stresses up to 294 thermal cycles. Figure 5.12 (a) shows that at ΔT of 200 °C, the power output started to decrease by 0.56 μW/cycle, which is also reflected in the internal resistance increase of 85 $\mu\Omega$/cycle. However, the degradation was not as significant as at the higher temperature: at 400 °C the power decrease rate was 13 μW/cycle while the internal resistance increase was close to a rate of 0.8 mΩ/cycle. By extrapolation, this rate of degradation, especially at 400 °C, translates to the module's being able to withstand the thermal stress for up to 115 thermal cycles after noticeable degradation until the maximum power reaches 80% of the initial rated capacity.

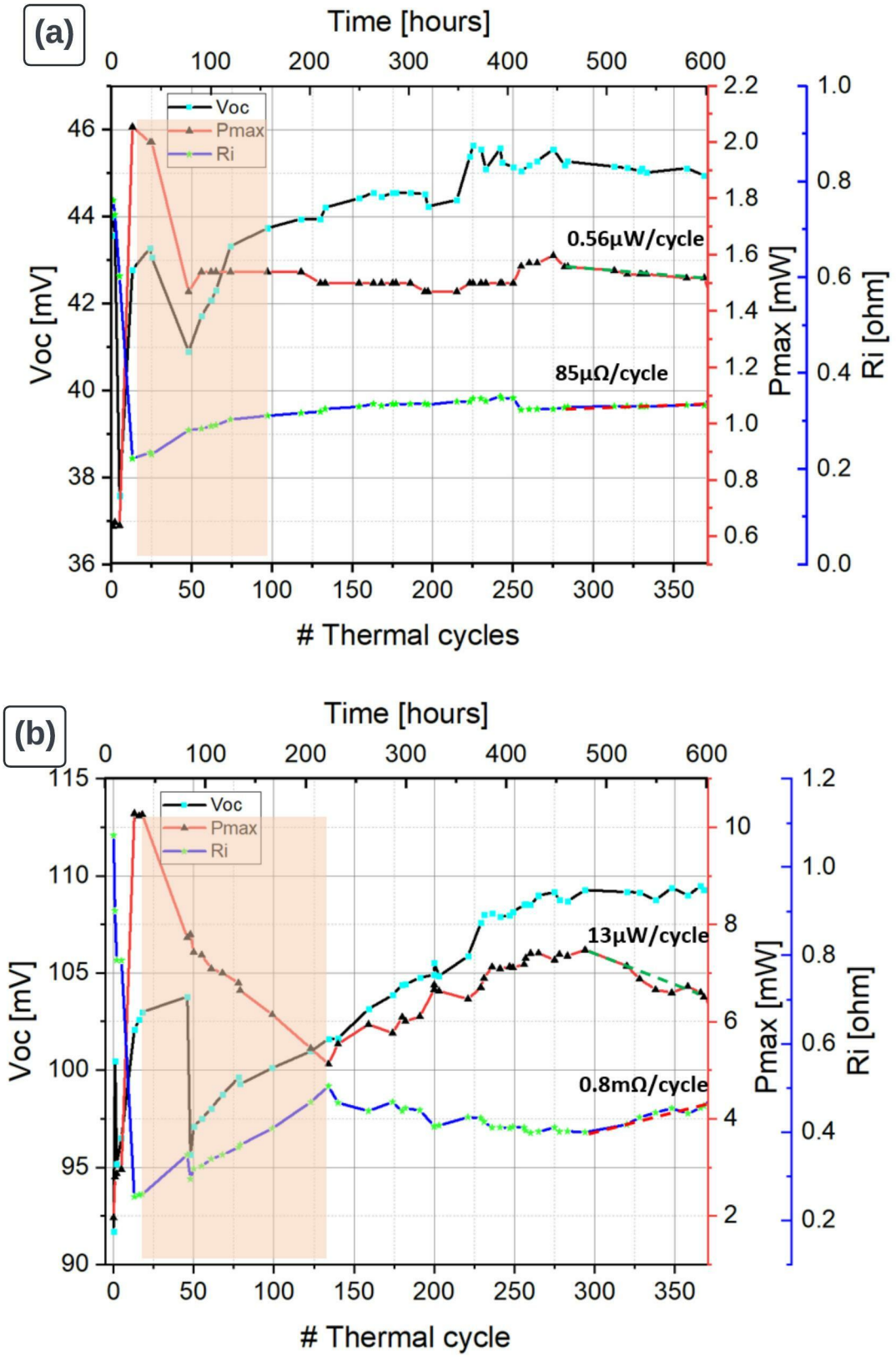

Figure 5.12: The durability test results are presented in terms of the open circuit voltage (V_{oc}), maximum power output (P_{max}) and the module internal electrical resistance (R_i) over the number of thermal cycles, (a) at 200 °C (b) at 400 °C.

5.3.4 Conclusion

In this research, a PCM rig was developed and used to measure contact resistance across electrode contact in the HMS-MGS based TE module. The developed PCM system is capable of achieving a linear positioning of 1μm, signal resolution of 7.5 digits and 0.5% reproducible results with less than 1.4 sec/data-point. The test rig makes it possible to map the recorded signal, revealing the electrical characteristics of the scan surface. In the case study in question, it was shown that the contact resistance of a TE unicouple can be measured with high precision using line scanning. The electrode contacts studied showed that the best contact had 0.11 mΩcm^2, while the least reliable contact at the hot side of the HMS contact was evaluated at 1.36mΩcm^2. This technology can be used by the TE community to electrically characterize the electrode contacts and TEM in TE modules by measuring the electrical resistivity of the contacts using the four-point method.

Furthermore, the durability of the modeled and built TE electric module was studied. The unicouple module generated up to 1.6 mW and 7.48 mW at 200 °C and 400 °C, respectively. During long-term stability test, the module was robust during the first 300 thermal cycles, after the module's degradation rate was recorded at 13 μW/cycle power reduction equivalent to 0.8 mΩ/cycle at 400 °C. Finally, by the degradation rate it was found that the unicouple would last 115 more thermal cycles before the output power is reduced by 20 %.

Chapter 6

Conclusion and Recommendations

6.1 Conclusion

The research reported in this Ph.D thesis was conducted to investigate the long-term stability of silicide based thermoelectric modules in laboratory varied thermal conditions. The modules were assembled from TEMs modeled, synthesized and consolidated in a parent project (TESil project) as presented in section 4.1, and broadly detailed in published papers I to III. The main factors found to hinder the stability of the modules were the oxidation of the TEMs and the degradation of the contact interfaces between the TEMs and electrodes.

The oxidation studies conducted on HMS alloys showed that, the kinetics and mechanisms of reactions had direct relationship with the materials synthesis routes, composition and the operational environment. The effect of the HMS alloys' composition on their oxidation potential was examined by studying the oxidation of the alloys, with varied composition from undoped HMS to different levels of doping and dopants. Among the dopants, Al and Ge were experimented as substitutes on the Si site, while Mo was at the Mn site as reported in publication B and C.

The undoped HMS oxidized at temperature below 500° for more than 24hours, were found to have mainly SiO_2 oxide which grew continuously along the edges of the specimens and over time settled (which means protecting the alloy). However, with Ge and Al doping

($MnSi_{1.75-\alpha}X_{\alpha}$, X – Ge or Al), the oxide scale was not only composed of silica but also Ge and Al based oxides (GeO_2 and Al_2O_3, respectively). With the mixture of oxides in the scale, the protectiveness of the alloys was compromised and noticeable level of Mn oxide was detected. Nevertheless, the latter was count balanced by controlling the dopant concentration, where doping with 0.5 at%Ge resulted into a more oxidation resistant alloys than with Al.

Furthermore, the oxidation studies continued with alloys with Mo doping on the Mn site ($Mn_{x-\alpha}Mo_{\alpha}Si_{y-\beta}Ge_{\beta}$). The study showed that at temperature lower than 300 °C, the oxidation reaction was governed by chemical reactions on the alloys' surfaces, while above 450 °C, ionic diffusion across the alloy-oxide interface was the rate determining factor. However, the protectiveness of the alloys being the crucial goal to achieve, doping on Mn site with Mo did not have major effects on the alloys' protectiveness. As reported in paper III, in spite of all elements being present in the oxide layer, the alloys showed resilience, where overtime protective SiO_2 dominated the rest of oxide phases and reduced or stopped further materials consumption (an illustration of the mechanisms is shown in Figure 14 of paper III).

Similarly, the effect of powder consolidation methods (used to produce the bulk pellets) was investigated using three categories of samples, produced by, melt casting (or as cast ingots), hot pressing and spark plasma sintering. Ingots compacted using spark plasma sintering were found to have higher robustness to oxidation, and therefore concluded that, along with producing composition-optimal alloys, it is also important to consider the mechanical integrity of the alloys to guarantee an oxidation resistant compound.

Furthermore, unicouple modules were assembled base on n-type MGS and p-type HMS. The main concern on the module level was the TEM–electrode's contact interface, in that regard, silver electrode were used and were bond to the TEM by SLID technique. The assembled modules were evaluated by measuring the contact resistance across the contact interfaces. On the MGS–Ag interfaces the contact resistance was as low as 0.11 $m\Omega cm^2$, however, on the HMS–Ag interfaces especially the hot side, the contact resistance was as high as 1.36 $m\Omega cm^2$. The issue with the HMS was associated to the low CTE of the alloy, which means that further work are required to address this problem.

Finally, long-term stability tests were conducted on the assembled module. The modules generated up to 1.1mW/cm^2 and 4.9 mW/cm^2 power density at 200 °C and 400 °C, respectively. During durability test in vacuum, the modules withstood thermal cyclic stresses to more than 300 thermal cycles until the module degradation caused the power output to reduce by 20%. The thermal degradation of the tested TEGs, was found to be a result of poor contact layers' mechanical and electrical properties.

6.2 Futher work

In this project, the oxidation of HMS alloys was conducted in conjunction with the TEMs development and the effects of the production processes reported and addressed along the way. Similar approach can be adopted for the study of thermal oxidation of other TEM systems under development, as it allows to keep track of not only the composition effect on oxidation of the final alloys, but also the effects (if any) of each production step on oxidation of the final compound. Nevertheless, this study showed that silicide based TEMs develop a protective oxide layer composed of the majority of the alloy's elements. Therefore, it would be recommended to couple the oxidation studies with testing the TE properties before and after oxidation tests, and thereafter be able to quantitatively determine the oxidation effect on the charge carrier concentration (for instance).

The module performance tests were conducted on unicouples modules. With SLID bonding it was cumbersome to arrange the bonding experiment, therefore, could be difficult to duplicate in case of multiple unicouples assembly. Therefore, future work can be dedicated to designing an assembly platform that render the assembly easy and at best automated. As a result, the technology can be utilized for mass production of modules on industrial level.

Lastly, a thorough study of the composition of the contact interfaces would be welcome to understand the mechanisms that lead to degradation. This would also be an input to optimize the contact layer composition towards prolonging the life of the modules.

Bibliography

[1] I. Asimov, *Life and Energy*. New York - USA: Avon Publishers of Bard, Camelot, Discus and Equinox Books, 1962.

[2] IEA, "Global energy demand and CO_2 emissions trends in the stated policies scenario, 2019-2030." https://www.iea.org/data-and-statistics/charts/global-energy-demand-and-co2-emissions-trends-in-the-stated-policies-scenario-2019-2030. Accessed on: 13/07/2021.

[3] IEA, "Global Energy Review 2021," https://www.iea.org/reports/global-energy-review-2021. Accessed: 09/07/2021.

[4] Intergovernmental Panel on Climate Change, *"Climate Change 2014"*. New York, NY, USA: Cambridge University Press, 2014.

[5] IEA, "Renewables 2021, Global Status Report." https://www.ren21.net/wp-content/uploads/2019/05/GSR2021_Full_Report.pdf. Accessed: 13/07/2021.

[6] DNV - GL, "Energy tansition outlook 2020," https://download.dnvgl.com/eto-2020-download. Accessed: 14/07/2021.

[7] USA,Department of Energy, "Quadrenial technology review 2015," https://www.energy.gov/sites/prod/files/2017/03/f34/quadrennial-technology-review-2015_1.pdf. Accessed: 14/07/2021.

[8] T. C. Hung, T. Y. Shai, and S. K. Wang, "A review of organic rankine cycles (ORCs) for the recovery of low-grade waste heat," *Energy*, vol. 22, no. 7, pp. 661–667, 1997.

[9] G. E. V. Ochoa, A. E. B. Gamero, and J. M. C. Vanegas, "A world overview of organic rankine cycle as waste heat recovery alternative," *Respuestas*, vol. 24, no. 3, pp. 6–13, 2019.

[10] R. Saidur, M. Rezaei, W. K. Muzammil, M. H. Hassan, S. Paria, and M. Hasanuzzaman, "Technologies to recover exhaust heat from internal combustion engines," *Renewable and Sustainable Energy Reviews*, vol. 16, no. 8, pp. 5649–5659, 2012.

[11] NASA, "Multi-mission radioisotope thermoelectric generator." https://rps.nasa.gov/power-and-thermal-systems/power-systems/future/. Accessed: 14/07/2021.

[12] D. Champier, "Thermoelectric generators: A review of applications," *Energy Conversion and Management*, vol. 140, pp. 167–181, 2017.

[13] B. Orr, A. Akbarzadeh, M. Mochizuki, and R. Singh, "A review of car waste heat recovery systems utilising thermoelectric generators and heat pipes," *Applied Thermal Engineering*, vol. 101, pp. 490–495, 2016.

[14] MATRIX, "World's first smartwatch you don't have to charge." https://www.powerwatch.com/ Accessed: 23/06/2022.

[15] Z. Lu, H. Zhang, C. Mao, and C. M. Li, "Silk fabric-based wearable thermoelectric generator for energy harvesting from the human body," *Applied Energy*, vol. 164, pp. 57–63, 2016.

[16] M. K. Mishu, M. Rokonuzzaman, J. Pasupuleti, M. Shakeri, K. S. Rahman, S. Binzaid, S. K. Tiong, and N. Amin, "An adaptive TE-PV hybrid energy harvesting system for self-powered IoT sensor applications," *Sensors*, vol. 21, no. 8, p. 2604, 2021.

[17] A. Velez-Estevez, L. Gutiérrez-Madroñal, and I. Medina-Bulo, "IoT-TEG 4.0: A new approach 4.0 for test event generation," *IEEE Transactions on Reliability*, pp. 1–13, 2021. doi: 10.1109/TR.2021.3087781.

[18] W. Wang, X. Chen, Y. Liu, X. Wang, and Z. Liu, "Thermo-electric energy harvesting powered IoT system design and energy model analysis," in *2019 IEEE 13th In-*

ternational Conference on Anti-counterfeiting, Security, and Identification (ASID), pp. 303–308, 2019. doi:10.1109/ICASID.2019.8925180.

[19] D. Narducci, "Thermoelectric harvesters and the internet of things: technological and economic drivers," *Journal of Physics: Energy*, vol. 1, no. 2, p. 024001, 2019.

[20] L. Gutiérrez-Madroñal, I. Medina-Bulo, and J. J. Domínguez-Jiménez, "IoT–TEG: Test event generator system," *Journal of Systems and Software*, vol. 137, pp. 784–803, 2018.

[21] G. Skomedal, L. Holmgren, H. Middleton, I. S. Eremin, G. N. Isachenko, M. Jaegle, K. Tarantik, N. Vlachos, M. Manoli, T. Kyratsi, D. Berthebaud, N. Y. D. Truong, and F. Gascoin, "Design, assembly and characterization of silicide-based thermoelectric modules," vol. 110, pp. 13–21, 2016.

[22] G. Rogl and P. Rogl, "Skutterudites: Progress and challenges," in *Novel Thermoelectric Materials and Device Design Concepts* (S. Skipidarov and M. Nikitin, eds.), ch. 9, pp. 177–201, Cham, Switzerland: Springer, 2019.

[23] C. B. Vining, "An inconvenient truth about thermoelectrics," *Nature Mater*, vol. 8, no. 2, pp. 83–85, 2009.

[24] TecTeg, "Thermoelectric power module selection purchase." https://tecteg.com/store-thermoelectric-power-module-selection-purchase/. Accessed: 15/07/2021.

[25] Gentherm, "Automotive | Gentherm." https://gentherm.com/en/solutions/automotive. Accessed: 15/05/2021.

[26] Alphabet Energy, "Thermoelectric generator equipment | energy XPRT." https://energy-xprt.com/products/keyword-thermoelectric-generator-161590. Accessed: 15/07/2021.

[27] Ferrotec, "Thermoelectric modules." https://www.ferrotec.com/products-technologies/thermoelectric-modules/. Accessed: 15/07/2021.

[28] IEA, "Global Energy Review 2019," https://iea.blob.core.windows.net/assets/dc48c054-9c96-4783-9ef7-462368d24397/Global$_E$$nergy_R$$eview_2$019.$pdf$ $Accessed$: 13/07/2021.

[29] O. M. Løvvik, E. Flage-Larsen, and G. Skomedal, "Screening of thermoelectric silicides with atomistic transport calculations," *Journal of Applied Physics*, vol. 128, no. 12, p. 125105, 2020.

[30] ATSDR, "Substance priority list | ATSDR." https://www.atsdr.cdc.gov/spl/index.html. Accessed: 20/07/2021.

[31] T. C. Holgate, R. Bennett, T. Hammel, T. Caillat, S. Keyser, and B. Sievers, "Increasing the efficiency of the multi-mission radioisotope thermoelectric generator," *Journal of Elec Materi*, vol. 44, no. 6, pp. 1814–1821, 2015.

[32] Y. Zhang, M. Cleary, X. Wang, N. Kempf, L. Schoensee, J. Yang, G. Joshi, and L. Meda, "High-temperature and high-power-density nanostructured thermoelectric generator for automotive waste heat recovery," *Energy Conversion and Management*, vol. 105, pp. 946–950, 2015.

[33] J. Svarc, "Most efficient solar panels 2022." https://www.cleanenergyreviews.info/blog/most-efficient-solar-panels Accessed: 20/07/2021.

[34] W. Liu, X. Tan, K. Yin, H. Liu, X. Tang, J. Shi, Q. Zhang, and C. Uher, "Convergence of conduction bands as a means of enhancing thermoelectric performance of n-type $\mathrm{mg_2si_{1-x}sn_x}$ solid solutions," *Phys. Rev. Lett.*, vol. 108, p. 166601, 2012.

[35] N. Jaziri, A. Boughamoura, J. Müller, B. Mezghani, F. Tounsi, and M. Ismail, "A comprehensive review of thermoelectric generators: Technologies and common applications," *Energy Reports*, vol. 6, pp. 264–287, 2020.

[36] D. Y. N. Truong, *Thermoelectric Properties of Higher Manganese Silicides*. PhD thesis, University of Waterloo, Ontario, Canada, 2015.

[37] A. Nozari, P. Norouzzadef, F. Suarez, and D. Vashaee, "Thermoelectric silicides: a review," vol. 56, pp. 1–27, 2017.

[38] A. Teknetzi, E. Tarani, E. Symeou, D. Karfaridis, D. Stathokostopoulos, E. Pavlidou, T. Kyratsi, E. Hatzikraniotis, K. Chrissafis, and G. Vourlias, "Structure and thermoelectric properties of higher manganese silicides synthesized by pack cementation," *Ceramics International*, vol. 47, no. 1, pp. 243–251, 2021.

[39] N. Parse, S.-a. Tanusilp, W. Silpawilawan, K. Kurosaki, and S. Pinitsoontorn, "Enhancing thermoelectric properties of higher manganese silicide (HMS) by partial ta substitution," *Journal of Elec Materi*, vol. 49, no. 5, pp. 2726–2733, 2020.

[40] I. Aoyama, M. I. Fedorov, V. K. Zaitsev, F. Y. Solomkin, I. S. Eremin, A. Y. Samunin, M. Mukoujima, S. Sano, and T. Tsuji, "Effects of ge doping on micromorphology of MnSi in $MnSi_{1.7}$ and on their thermoelectric transport properties," *Japanese Journal of Applied Physics*, vol. 44, no. 12, pp. 8562–8570, 2005.

[41] W. Luo, H. Li, Y. Yan, Z. Lin, X. Tang, Q. Zhang, and C. Uher, "Rapid synthesis of high thermoelectric performance higher manganese silicide with in-situ formed nano-phase of MnSi," *Intermetallics*, vol. 19, no. 3, pp. 404–408, 2011.

[42] S. N. Girard, X. Chen, F. Meng, A. Pokhrel, J. Zhou, L. Shi, and S. Jin, "Thermoelectric properties of undoped high purity higher manganese silicides grown by chemical vapor transport," *Chem. Mater.*, vol. 26, no. 17, pp. 5097–5104, 2014.

[43] V. Ponnambalam, D. T. Morelli, S. Bhattacharya, and T. M. Tritt, "The role of simultaneous substitution of cr and ru on the thermoelectric properties of defect manganese silicides $MnSi_x$ $(1.73 < x < 1.75)$," vol. 580, pp. 598–603, 2013.

[44] T. Homma, T. Kamata, N. Saito, S. Ghodke, and T. Takeuchi, "Effects of re substitution for mn on microstructures and properties in re-substituted higher manganese silicide thermoelectric material," *Journal of Alloys and Compounds*, vol. 776, pp. 8–15, 2019.

[45] A. Yamamoto, S. Ghodke, H. Miyazaki, M. Inukai, Y. Nishino, M. Matsunami, and T. Takeuchi, "Thermoelectric properties of supersaturated re solid solution of higher manganese silicides," *Japanese Journal of Applied Physics*, vol. 55, no. 2, p. 020301, 2016.

[46] W. Liu, X. Tang, H. Li, K. Yin, J. Sharp, X. Zhou, and C. Uher, "Enhanced thermoelectric properties of n-type $Mg_{2.16}(Si_{0.4}Sn_{0.6})_{1-y}Bi_y$ due to nano-sized sn-rich precipitates and an optimized electron concentration," *J. Mater. Chem.*, vol. 22, no. 27, p. 13653, 2012.

[47] W. Liu, Q. Zhang, K. Yin, H. Chi, X. Zhou, X. Tang, and C. Uher, "High figure of merit and thermoelectric properties of bi-doped $Mg_2Si_{0.4}Sn_{0.6}$ solid solutions," *Journal of Solid State Chemistry*, vol. 203, pp. 333–339, 2013.

[48] Y. Gelbstein, J. Tunbridge, R. Dixon, M. J. Reece, H. Ning, R. Gilchrist, R. Summers, I. Agote, M. A. Lagos, K. Simpson, C. Rouaud, P. Feulner, S. Rivera, R. Torrecillas, M. Husband, J. Crossley, and I. Robinson, "Physical, mechanical, and structural properties of highly efficient nanostructured n- and p-silicides for practical thermoelectric applications," *Journal of Elec Materi*, vol. 43, no. 6, pp. 1703–1711, 2014.

[49] N. Vlachos, G. S. Polymeris, M. Manoli, E. Hatzikraniotis, A. U. Khan, C. B. Lioutas, E. C. Stefanaki, E. Pavlidou, K. M. Paraskevopoulos, J. Giapintzakis, and T. Kyratsi, "Effect of antimony-doping and germanium on the highly efficient thermoelectric si-rich-Mg_2(Si,Sn,Ge) materials," *Journal of Alloys and Compounds*, vol. 714, pp. 502–513, 2017.

[50] G. S. Polymeris, N. Vlachos, E. Symeou, and T. Kyratsi, "Thermoelectric properties of bi-doped $Mg_2Si_{0.6}Sn_{0.4}$ solid solutions synthesized by two-step low temperature reaction combined with hot pressing," *physica status solidi (a)*, vol. 215, no. 17, p. 1800136, 2018.

[51] X. Chen, J. Zhou, J. B. Goodenough, and L. Shi, "Enhanced thermoelectric power factor of re-substituted higher manganese silicides with small islands of MnSi secondary phase," *J. Mater. Chem. C*, vol. 3, no. 40, pp. 10500–10508, 2015.

[52] S. Ghodke, A. Yamamoto, H.-C. Hu, S. Nishino, T. Matsunaga, D. Byeon, H. Ikuta, and T. Takeuchi, "Improved thermoelectric properties of re-substituted higher manganese silicides by inducing phonon scattering and an energy-filtering effect at grain boundary interfaces," *ACS Appl. Mater. Interfaces*, vol. 11, no. 34, pp. 31169–31175, 2019.

[53] D. M. Rowe, *Thermoelectrics handbook: macro to nano*, vol. 1. CRC/Taylor & Francis, 2006.

[54] P. J. Taylor, A. A. Wilson, T. Hendricks, F. Drymiotis, O. Villalpando, and J.-P. Fleurial, "Novel measurements and analysis for thermoelectric devices," in *Novel Thermoelectric Materials and Device Design Concepts* (S. Skipidarov and M. Nikitin, eds.), pp. 277–293, Springer International Publishing, 2019.

[55] A. Polozine, S. Sirotinskaya, and L. Schaeffer, "History of development of thermoelectric materials for electric power generation and criteria of their quality," *Mat. Res.*, vol. 17, no. 5, pp. 1260–1267, 2014.

[56] R. P. Huebener, "Less can be more: Semiconductors," in *Conductors, Semiconductors, Superconductors: An Introduction to Solid State Physics*, pp. 65–85, Springer International Publishing, 2015.

[57] P. Pichanusakorn and P. Bandaru, "Nanostructured thermoelectrics," *Materials Science and Engineering: R: Reports*, vol. 67, no. 2, pp. 19–63, 2010.

[58] C. Kittel, H. Charles Kittel, K. Charles, H. Kroemer, and K. Herbert, *Thermal Physics*. W. H. Freeman, 1980.

[59] H. Ibach and H. Lüth, *Solid-State Physics*. Springer Berlin Heidelberg, 2009.

[60] C. Kittel, *Introduction to Solid State Physics*. Berkeley, California: John Wiley & Sons Inc, 2004.

[61] H. J. Goldsmid, *Introduction to Thermoelectricity*. Springer, 2016. Google-Books-ID: X2GmCwAAQBAJ.

[62] N. M. Ravindra, B. Jariwala, A. Bañobre, and A. Maske, *Thermoelectrics: Fundamentals, Materials Selection, Properties, and Performance*. Springer, 2018. Google-Books-ID: hBxrDwAAQBAJ.

[63] S. Stackhouse and L. Stixrude, "Theoretical methods for calculating the lattice thermal conductivity of minerals," *Reviews in Mineralogy and Geochemistry*, vol. 71, no. 1, pp. 253–269, 2010.

[64] D. M. Rowe, *CRC Handbook of Thermoelectrics*. CRC Press, 2018-12-07. Google-Books-ID: n4O1DwAAQBAJ.

[65] H. J. Goldsmid, "Optimisation and selection of semiconductor thermoelements," in *Introduction to Thermoelectricity* (H. J. Goldsmid, ed.), Springer Series in Materials Science, pp. 43–62, Springer, 2010.

[66] S. Stackhouse and L. Stixrude, "Theoretical methods for calculating the lattice thermal conductivity of minerals," vol. 71, pp. 253–269, 2010.

[67] L. Chaput, P. Pécheur, J. Tobola, and H. Scherrer, "Transport in doped skutterudites: Ab initio electronic structure calculations," *Phys. Rev. B*, vol. 72, no. 8, p. 085126, 2005.

[68] M. A. Green, "Intrinsic concentration, effective densities of states, and effective mass in silicon," *Journal of Applied Physics*, vol. 67, no. 6, pp. 2944–2954, 1990.

[69] Z. Dashevsky and S. Skipidarov, "Investigating the performance of bismuth-antimony telluride," in *Novel Thermoelectric Materials and Device Design Concepts* (S. Skipidarov and M. Nikitin, eds.), pp. 3–21, Springer International Publishing, 2019.

[70] J. Park, M. Dylla, Y. Xia, M. Wood, G. J. Snyder, and A. Jain, "When band convergence is not beneficial for thermoelectrics," *Nat Commun*, vol. 12, no. 1, p. 3425, 2021.

[71] Y. Tang, Z. M. Gibbs, L. A. Agapito, G. Li, H.-S. Kim, M. Nardelli, S. Curtarolo, and G. J. Snyder, "Convergence of multi-valley bands as the electronic origin of high thermoelectric performance in $CoSb_3$ skutterudites," *Nature Mater*, vol. 14, no. 12, pp. 1223–1228, 2015.

[72] G. J. Snyder and E. S. Toberer, "Complex thermoelectric materials," *Nature Materials*, vol. 7, no. 2, pp. 105–114, 2008.

[73] E. Velmre, "Thomas johann seebeck (1770-1831): Thomas johann seebeck (1770-1831).," vol. 13, no. 4, pp. 276–282, 2007.

[74] L. Chen, R. Liu, and X. Shi, "Chapter 4 - review of inorganic thermoelectric materials," in *Thermoelectric Materials and Devices* (L. Chen, R. Liu, and X. Shi, eds.), pp. 81–145, Elsevier, 2021.

[75] B. Russ, A. Glaudell, J. J. Urban, M. L. Chabinyc, and R. A. Segalman, "Organic thermoelectric materials for energy harvesting and temperature control," *Nat Rev Mater*, vol. 1, no. 10, pp. 1–14, 2016.

[76] X. Chen, Z. Zhou, Y.-H. Lin, and C. Nan, "Thermoelectric thin films: Promising strategies and related mechanism on boosting energy conversion performance," *Journal of Materiomics*, vol. 6, no. 3, pp. 494–512, 2020.

[77] I. T. Witting, T. C. Chasapis, F. Ricci, M. Peters, N. A. Heinz, G. Hautier, and G. J. Snyder, "The thermoelectric properties of bismuth telluride," *Advanced Electronic Materials*, vol. 5, no. 6, p. 1800904, 2019.

[78] N. S. Abishek and K. Gopalakrishna Naik, "Influence of gallium doping on structural and thermoelectric properties of bismuth telluride," *Journal of Crystal Growth*, vol. 565, p. 126141, 2021.

[79] F. M. El-Makaty, H. K. Ahmed, and K. M. Youssef, "Review: The effect of different nanofiller materials on the thermoelectric behavior of bismuth telluride," *Materials & Design*, vol. 209, p. 109974, 2021.

[80] I. T. Witting, T. C. Chasapis, F. Ricci, M. Peters, N. A. Heinz, G. Hautier, and G. J. Snyder, "The thermoelectric properties of bismuth telluride," *Advanced Electronic Materials*, vol. 5, no. 6, p. 1800904, 2019.

[81] W. M. Yim and F. D. Rosi, "Compound tellurides and their alloys for peltier cooling: A review," *Solid-State Electronics*, vol. 15, no. 10, pp. 1121–1140, 1972.

[82] Y. Pan and J.-F. Li, "2.1 - bismuth telluride," in *Thermoelectric Energy Conversion* (R. Funahashi, ed.), Woodhead Publishing Series in Electronic and Optical Materials, pp. 45–67, Woodhead Publishing, 2021.

[83] H. Mamur, M. R. A. Bhuiyan, F. Korkmaz, and M. Nil, "A review on bismuth telluride (bi2te3) nanostructure for thermoelectric applications," *Renewable and Sustainable Energy Reviews*, vol. 82, pp. 4159–4169, 2018.

[84] S. Lee, K. Kim, D.-H. Kang, M. Meyyappan, and C.-K. Baek, "Vertical silicon nanowire thermoelectric modules with enhanced thermoelectric properties," *Nano Lett.*, vol. 19, no. 2, pp. 747–755, 2019.

[85] S. Elyamny, E. Dimaggio, S. Magagna, D. Narducci, and G. Pennelli, "High power thermoelectric generator based on vertical silicon nanowires," *Nano Lett.*, vol. 20, no. 7, pp. 4748–4753, 2020.

[86] Y. Zheng, C. Liu, L. Miao, C. Li, R. Huang, J. Gao, X. Wang, J. Chen, Y. Zhou, and E. Nishibori, "Extraordinary thermoelectric performance in MgAgSb alloy with ultralow thermal conductivity," *Nano Energy*, vol. 59, pp. 311–320, 2019.

[87] H. Zhao, J. Sui, Z. Tang, Y. Lan, Q. Jie, D. Kraemer, K. McEnaney, A. Guloy, G. Chen, and Z. Ren, "High thermoelectric performance of MgAgSb-based materials," *Nano Energy*, vol. 7, pp. 97–103, 2014.

[88] W.-Y. Chen, X.-L. Shi, J. Zou, and Z.-G. Chen, "Wearable fiber-based thermoelectrics from materials to applications," *Nano Energy*, vol. 81, p. 105684, 2021.

[89] Z. Soleimani, S. Zoras, B. Ceranic, Y. Cui, and S. Shahzad, "A comprehensive review on the output voltage/power of wearable thermoelectric generators concerning their geometry and thermoelectric materials," *Nano Energy*, vol. 89, p. 106325, 2021.

[90] IUPAC, "Periodic table of elements." https://iupac.org/what-we-do/periodic-table-of-elements/. Accessed: 17/09/2021.

[91] J. Dong, F.-H. Sun, H. Tang, J. Pei, H.-L. Zhuang, H.-H. Hu, B.-P. Zhang, Y. Pan, and J.-F. Li, "Medium-temperature thermoelectric GeTe: vacancy suppression and band structure engineering leading to high performance," *Energy Environ. Sci.*, vol. 12, no. 4, pp. 1396–1403, 2019.

[92] Y. Zhang, J. Sun, J. Shuai, X. Tang, and G. Tan, "Lead-free snte-based compounds as advanced thermoelectrics," *Materials Today Physics*, vol. 19, p. 100405, 2021.

[93] P. K. Sharma, T. D. Senguttuvan, V. K. Sharma, and S. Chaudhary, "Revisiting the thermoelectric properties of lead telluride," *Materials Today Energy*, vol. 21, p. 100713, 2021.

[94] A. Kumar, P. A. Vermeulen, B. J. Kooi, J. Rao, S. Schwarzmüller, O. Oeckler, and G. R. Blake, "A cubic room temperature polymorph of thermoelectric TAGS-85," *RSC Adv.*, vol. 8, no. 74, pp. 42322–42328, 2018.

[95] T. Schröder, T. Rosenthal, N. Giesbrecht, M. Nentwig, S. Maier, H. Wang, G. J. Snyder, and O. Oeckler, "Nanostructures in Te/Sb/Ge/Ag (TAGS) thermoelectric materials induced by phase transitions associated with vacancy ordering," *Inorg. Chem.*, vol. 53, no. 14, pp. 7722–7729, 2014.

[96] ATSDR, "Substance priority list | ATSDR," 2020. https://www.atsdr.cdc.gov/spl/index.html. Accessed: 20/09/2021.

[97] SMM, "Indium / germanium / gallium." https://www.metal.com/Indium-Germanium-Gallium. Accessed: 20/09/2021.

[98] L.-D. Zhao, S.-H. Lo, Y. Zhang, H. Sun, G. Tan, C. Uher, C. Wolverton, V. P. Dravid, and M. G. Kanatzidis, "Ultralow thermal conductivity and high thermoelectric figure of merit in SnSe crystals," *Nature*, vol. 508, no. 7496, pp. 373–377, 2014.

[99] A. T. Duong, V. Q. Nguyen, G. Duvjir, V. T. Duong, S. Kwon, J. Y. Song, J. K. Lee, J. E. Lee, S. Park, T. Min, J. Lee, J. Kim, and S. Cho, "Achieving ZT=2.2 with bi-doped n-type SnSe single crystals," *Nat Commun*, vol. 7, no. 1, p. 13713, 2016.

[100] C. Chang, M. Wu, D. He, Y. Pei, C.-F. Wu, X. Wu, H. Yu, F. Zhu, K. Wang, Y. Chen, L. Huang, J.-F. Li, J. He, and L.-D. Zhao, "3D charge and 2D phonon transports leading to high out-of-plane ZT in n-type SnSe crystals," *Science*, vol. 360, no. 6390, pp. 778–783, 2018.

[101] X. Lou, S. Li, X. Chen, Q. Zhang, H. Deng, J. Zhang, D. Li, X. Zhang, Y. Zhang, H. Zeng, and G. Tang, "Lattice strain leads to high thermoelectric performance in polycrystalline SnSe," *ACS Nano*, vol. 15, no. 5, pp. 8204–8215, 2021.

[102] C. Zhou, Y. K. Lee, Y. Yu, S. Byun, Z.-Z. Luo, H. Lee, B. Ge, Y.-L. Lee, X. Chen, J. Y. Lee, O. Cojocaru-Mirédin, H. Chang, J. Im, S.-P. Cho, M. Wuttig, V. P. Dravid, M. G. Kanatzidis, and I. Chung, "Polycrystalline SnSe with a thermoelectric figure of merit greater than the single crystal," *Nat. Mater.*, 2021.

[103] C. Uher, "2.2 - thermoelectric properties of skutterudites," in *Thermoelectric Energy Conversion* (R. Funahashi, ed.), Woodhead Publishing Series in Electronic and Optical Materials, pp. 69–123, Woodhead Publishing, 2021.

[104] P. Zhao, H. Sun, F. Yu, B. Wang, H. Zhao, D. Wang, D. Yu, Y. Tian, and B. Xu, "Thermoelectric performance of p-type $Ca_xFe_{1.3}Co_{2.7}Sb_{12}$ skutterudites from high pressure synthesis," *Journal of Alloys and Compounds*, vol. 851, p. 156928, 2021.

[105] O. Caballero-Calero, M. Rull-Bravo, D. Platzek, M. D. Cárdenas, R. Fernández, A. Moure, J. F. Fernández, and M. Martín-González, "Tubular ring thermoelectric module for exhaust pipes: From skutterudite nanopowders to the final device," *Energy*, vol. 234, p. 121223, 2021.

[106] G. Rogl, A. Grytsiv, P. Heinrich, E. Bauer, P. Kumar, N. Peranio, O. Eibl, J. Horky, M. Zehetbauer, and P. Rogl, "New bulk p-type skutterudites $DD_{0.7}Fe_{2.7}Co_{1.3}Sb_{12-z}X_x$ (X= Ge, Sn) reaching zT >1.3," *Acta Materialia*, vol. 91, pp. 227–238, 2015.

[107] D. Jin, Z. Ruan, B. Duan, J. Li, P. Zhai, H. Yang, H. Wang, G. Li, and L. Zhou, "Rapid preparation of high-performance $S_{0.4}Co_4Sb_{11.2}Te_{0.8}$ skutterudites with a highly porous structure," *Journal of the European Ceramic Society*, vol. 41, no. 8, pp. 4484–4489, 2021.

[108] G. Rogl, A. Grytsiv, P. Rogl, N. Peranio, E. Bauer, M. Zehetbauer, and O. Eibl, "n-type skutterudites $(R,Ba,Yb)_yCo_4Sb_{12}$ (R=Sr, La, Mm, DD, SrMm, SrDD) approaching ZT≅2.0," *Acta Materialia*, vol. 63, pp. 30–43, 2014.

[109] B. Wang, D. Fang, W. Yi, S. Zhao, J. Li, J. Li, Y. Zhao, and H. Jin, "Synthesis and thermoelectric performance of $Ni_{0.3}Co_{3.7}Sb_{12}$ skutterudite filled with electronegative guest se," *Ceramics International*, vol. 47, no. 12, pp. 17753–17759, 2021.

[110] D. Qin, W. Shi, W. Xue, H. Qin, J. Cao, W. Cai, Y. Wang, and J. Sui, "Solubility study of y in n-type $Y_xCe_{0.15}Co_4Sb_{12}$ skutterudites and its effect on thermoelectric properties," *Materials Today Physics*, vol. 13, p. 100206, 2020.

[111] F. Zelenka, J. Strádal, P. Brož, J. Vřešťál, J. Buršík, A. Zemanová, G. Rogl, and P. Rogl, "Study of thermal stability of n-type skutterudites $Sr_{0.07}Ba_{0.07}Yb_{0.07}Co_4Sb_{12}$ by differential thermal analysis and knudsen effusion method," *Calphad*, vol. 73, p. 102258, 2021.

[112] K. Kishimoto, M. Hayashi, and K. Akai, "Thermoelectric properties and band structures of vacancy-containing sn-based clathrates $K_8Sn_{44-x}Ge_x$," *Journal of Solid State Chemistry*, vol. 303, p. 122471, 2021.

[113] B. Liu, H. Ma, D. Huo, H. Liu, B. Liu, J. Chen, and X. Jia, "Thermoelectric properties of in-substituted ge-based clathrates prepared by HPHT," *Journal of Materiomics*, vol. 4, no. 1, pp. 68–74, 2018.

[114] S. Utsunomiya, K. Kishimoto, S. Koda, K. Akai, R. Fujita, H. Asada, and T. Koyanagi, "Preparation and thermoelectric properties of sintered type-II clathrates $(K,Ba)_{24}(Al,Sn)_{136}$," *Journal of Alloys and Compounds*, vol. 693, pp. 1039–1044, 2017.

[115] R. Takeshita, K. Kishimoto, H. Asada, and K. Akai, "Thermoelectric properties of type-i clathrate $Na_8Ga_8Ge_{38}$," *Journal of Solid State Chemistry*, vol. 294, p. 121911, 2021.

[116] M. N. Hasan, H. Wahid, N. Nayan, and M. S. M. Ali, "Inorganic thermoelectric materials: A review," *International Journal of Energy Research*, vol. 44, no. 8, pp. 6170–6222, 2020.

[117] I. Terasaki, Y. Sasago, and K. Uchinokura, "Large thermoelectric power in $NaCo_2O_4$ single crystals," *Phys. Rev. B*, vol. 56, no. 20, pp. R12685–R12687, 1997.

[118] J. Wei, L. Yang, Z. Ma, P. Song, M. Zhang, J. Ma, F. Yang, and X. Wang, "Review of current high-zt thermoelectric materials," *J Mater Sci*, vol. 55, no. 27, pp. 12642–12704, 2020.

[119] K. Park, J. S. Son, S. I. Woo, K. Shin, M.-W. Oh, S.-D. Park, and T. Hyeon, "Colloidal synthesis and thermoelectric properties of la-doped SrTiO3 nanoparticles," *J. Mater. Chem. A*, vol. 2, no. 12, pp. 4217–4224, 2014.

[120] D. Srivastava, F. Azough, R. Freer, E. Combe, R. Funahashi, D. M. Kepaptsoglou, Q. M. Ramasse, M. Molinari, S. R. Yeandel, J. D. Baran, and S. C. Parker, "Crystal structure and thermoelectric properties of sr–mo substituted $camno_3$: a combined experimental and computational study," *J. Mater. Chem. C*, vol. 3, no. 47, pp. 12245–12259, 2015.

[121] Y. Wang, Y. Sui, X. Wang, and W. Su, "Effects of substituting La^{3+}, Y^{3+} and Ce^{3+} for Ca^{3+} on the high temperature transport and thermoelectric properties of $CaMnO_3$," *J. Phys. D: Appl. Phys.*, vol. 42, no. 5, p. 055010, 2009.

[122] D. Ekren, F. Azough, and R. Freer, "2.11 - oxide thermoelectric materials," in *Thermoelectric Energy Conversion* (R. Funahashi, ed.), pp. 303–331, Woodhead Publishing, 2021.

[123] S. Bernik, "2.10 - oxide thermoelectric materials: Compositional, structural, microstructural, and processing challenges to realize their potential," in *Thermoelectric Energy Conversion* (R. Funahashi, ed.), pp. 269–302, Woodhead Publishing, 2021.

[124] M. Acharya, S. S. Jana, M. Ranjan, and T. Maiti, "High performance (ZT>1) n-type oxide thermoelectric composites from earth abundant materials," *Nano Energy*, vol. 84, p. 105905, 2021.

[125] T. T. Khan and S.-C. Ur, "Thermoelectric properties of the perovskite-type oxide $SrTi_{1-x}Nb_xO_3$ synthesized by solid-state reaction method," *Electron. Mater. Lett.*, vol. 14, no. 3, pp. 336–341, 2018.

[126] F. Delorme, C. F. Martin, P. Marudhachalam, D. Ovono Ovono, and G. Guzman, "Effect of ca substitution by sr on the thermoelectric properties of $Ca_3Co_4O_9$ ceramics," *Journal of Alloys and Compounds*, vol. 509, no. 5, pp. 2311–2315, 2011.

[127] Y. Liu, L. Zhang, S. E. Shirsath, J. Zheng, Y. Liu, C. Ulrich, and S. Li, "Manipulation of charge carrier concentration and phonon scattering via spin-entropy and size effects: Investigation of thermoelectric transport properties in la-doped $Ca_3Co_4O_9$," *Journal of Alloys and Compounds*, vol. 801, pp. 60–69, 2019.

[128] R. Hinterding, Z. Zhao, M. Wolf, M. Jakob, O. Oeckler, and A. Feldhoff, "Ceramic composites based on $Ca_3Co_{4-x}O_{9+\sigma}$ and $La_2NiO_{4+\sigma}$ with enhanced thermoelectric properties," *Open Ceramics*, vol. 6, p. 100103, 2021.

[129] X.-L. Tang, Z.-H. Ge, Z. Li, and K. Zhao, "Enhanced thermoelectric properties of $Ca_3Co_{4-x}O_{9+\sigma}$ ceramics by sr substitution," *Solid State Sciences*, vol. 104, p. 106190, 2020.

[130] M. Bittner, L. Helmich, F. Nietschke, B. Geppert, O. Oeckler, and A. Feldhoff, "Porous $Ca_3Co_4O_9$ with enhanced thermoelectric properties derived from sol–gel synthesis," *Journal of the European Ceramic Society*, vol. 37, no. 13, pp. 3909–3915, 2017.

[131] G. Xu, R. Funahashi, M. Shikano, I. Matsubara, and Y. Zhou, "Thermoelectric properties of the bi- and na-substituted $Ca_3Co_4O_9$ system," *Appl. Phys. Lett.*, vol. 80, no. 20, pp. 3760–3762, 2002.

[132] N. Kanas, S. P. Singh, M. Rotan, M. Saleemi, M. Bittner, A. Feldhoff, T. Norby, K. Wiik, T. Grande, and M.-A. Einarsrud, "Influence of processing on stability, microstructure and thermoelectric properties of $Ca_3Co_{4-x}O_{9+\sigma}$," *Journal of the European Ceramic Society*, vol. 38, no. 4, pp. 1592–1599, 2018.

[133] W. Zhang, K. Zhu, J. Liu, J. Wang, K. Yan, P. Liu, and Y. Wang, "Influence of the phase transformation in Na_xCoO_2 ceramics on thermoelectric properties," *Ceramics International*, vol. 44, no. 14, pp. 17251–17257, 2018.

[134] G.-K. Ren, S. Wang, Z. Zhou, X. Li, J. Yang, W. Zhang, Y.-H. Lin, J. Yang, and C.-W. Nan, "Complex electronic structure and compositing effect in high performance thermoelectric BiCuSeO," *Nat. Commun.*, vol. 10, no. 1, p. 2814, 2019.

[135] B. Feng, G. Li, Z. Pan, Y. Hou, C. Zhang, C. Jiang, J. Hu, Q. Xiang, Y. Li, Z. He, and X. Fan, "Effect of ba and pb dual doping on the thermoelectric properties of BiCuSeO ceramics," *Materials Letters*, vol. 217, pp. 189–193, 2018.

[136] Y. Liu, L.-D. Zhao, Y. Zhu, Y. Liu, F. Li, M. Yu, D.-B. Liu, W. Xu, Y.-H. Lin, and C.-W. Nan, "Synergistically optimizing electrical and thermal transport properties of BiCuSeO via a dual-doping approach," *Advanced Energy Materials*, vol. 6, no. 9, 2016.

[137] J.-L. Lan, Y.-C. Liu, B. Zhan, Y.-H. Lin, B. Zhang, X. Yuan, W. Zhang, W. Xu, and C.-W. Nan, "Enhanced thermoelectric properties of pb-doped BiCuSeO ceramics," *Advanced Materials*, vol. 25, no. 36, pp. 5086–5090, 2013.

[138] J. Yu, C. Fu, Y. Liu, K. Xia, U. Aydemir, T. C. Chasapis, G. J. Snyder, X. Zhao, and T. Zhu, "Unique Role of Refractory Ta Alloying in Enhancing the Figure of Merit of NbFeSb Thermoelectric Materials," *Advanced Energy Materials*, vol. 8, no. 1, 2018.

[139] H. Zhu, J. Mao, Y. Li, J. Sun, Y. Wang, Q. Zhu, G. Li, Q. Song, J. Zhou, Y. Fu, R. He, T. Tong, Z. Liu, W. Ren, L. You, Z. Wang, J. Luo, A. Sotnikov, J. Bao, K. Nielsch, G. Chen, D. J. Singh, and Z. Ren, "Discovery of TaFeSb-based half-Heuslers with high thermoelectric performance," *Nature Communications*, vol. 10, no. 1, 2019.

[140] N. Shutoh and S. Sakurada, "Thermoelectric properties of the $Ti_x(Zr_{0.5}Hf_{0.5})_{(1-x)}NiSn$ half-heusler compounds," *Journal of Alloys and Compounds*, vol. 389, no. 1, pp. 204–208, 2005.

[141] S. Populoh, M. H. Aguirre, O. C. Brunko, K. Galazka, Y. Lu, and A. Weidenkaff, "High figure of merit in (Ti,Zr,Hf)NiSn half-Heusler alloys," *Scripta Materialia*, vol. 66, no. 12, pp. 1073–1076, 2012.

[142] L. Chen, Y. Liu, J. He, T. M. Tritt, and S. J. Poon, "High thermoelectric figure of merit by resonant dopant in half-Heusler alloys," *AIP Advances*, vol. 7, no. 6, p. 065208, 2017.

[143] R. He, H. Zhu, J. Sun, J. Mao, H. Reith, S. Chen, G. Schierning, K. Nielsch, and Z. Ren, "Improved thermoelectric performance of n-type half-Heusler $MCo_{1-x}Ni_xSb$ (M=Hf, Zr)," *Materials Today Physics*, vol. 1, pp. 24–30, 2017.

[144] X. Yan, W. Liu, H. Wang, S. Chen, J. Shiomi, K. Esfarjani, H. Wang, D. Wang, G. Chen, and Z. Ren, "Stronger phonon scattering by larger differences in atomic mass and size

in p-type half-Heuslers $Hf_{1-x}Ti_xCoSb_{0.8}Sn_{0.2}$," *Energy & Environmental Science*, vol. 5, no. 6, pp. 7543–7548, 2012.

[145] C. Fu, H. Wu, Y. Liu, J. He, X. Zhao, and T. Zhu, "Enhancing the Figure of Merit of Heavy-Band Thermoelectric Materials Through Hierarchical Phonon Scattering," *Advanced Science*, vol. 3, no. 8, 2016.

[146] K. Ahmad, C. Wan, M. A. Al-Eshaikh, and A. N. Kadachi, "Enhanced thermoelectric performance of Bi2Te3 based graphene nanocomposites," *Applied Surface Science*, vol. 474, pp. 2–8, 2019.

[147] N. S. Abishek and K. Gopalakrishna Naik, "Influence of gallium doping on structural and thermoelectric properties of bismuth telluride," *Journal of Crystal Growth*, vol. 565, p. 126141, 2021.

[148] F. M. El-Makaty, K. Andre Mkhoyan, and K. M. Youssef, "The effects of structural integrity of graphene on the thermoelectric properties of the n-type bismuth-telluride alloy," *Journal of Alloys and Compounds*, vol. 876, p. 160198, 2021.

[149] K. Ahmad, C. Wan, and P.-a. Zong, "Thermoelectric properties of BiSbTe/graphene nanocomposites," *Journal of Materials Science: Materials in Electronics*, vol. 30, no. 13, pp. 11923–11930, 2019.

[150] S. Sharma and U. Schwingenschlögl, "Thermoelectric Response in Single Quintuple Layer Bi2Te3," *ACS Energy Letters*, vol. 1, no. 4, pp. 875–879, 2016.

[151] Y. Zheng, C. Liu, L. Miao, C. Li, R. Huang, J. Gao, X. Wang, J. Chen, Y. Zhou, and E. Nishibori, "Extraordinary thermoelectric performance in MgAgSb alloy with ultralow thermal conductivity," *Nano Energy*, vol. 59, pp. 311–320, 2019.

[152] H. Zhao, J. Sui, Z. Tang, Y. Lan, Q. Jie, D. Kraemer, K. McEnaney, A. Guloy, G. Chen, and Z. Ren, "High thermoelectric performance of MgAgSb-based materials," *Nano Energy*, vol. 7, pp. 97–103, 2014.

[153] M. Dutta, R. K. Biswas, S. K. Pati, and K. Biswas, "Discordant Gd and Electronic Band Flattening Synergistically Induce High Thermoelectric Performance in n-type PbTe," *ACS Energy Letters*, vol. 6, no. 4, pp. 1625–1632, 2021.

[154] Y. Zhang, J. Sun, J. Shuai, X. Tang, and G. Tan, "Lead-free SnTe-based compounds as advanced thermoelectrics," *Materials Today Physics*, vol. 19, p. 100405, 2021.

[155] J. Dong, F.-H. Sun, H. Tang, J. Pei, H.-L. Zhuang, H.-H. Hu, B.-P. Zhang, Y. Pan, and J.-F. Li, "Medium-temperature thermoelectric GeTe: vacancy suppression and band structure engineering leading to high performance," *Energy & Environmental Science*, vol. 12, no. 4, pp. 1396–1403, 2019.

[156] G. Tan, F. Shi, S. Hao, L.-D. Zhao, H. Chi, X. Zhang, C. Uher, C. Wolverton, V. P. Dravid, and M. G. Kanatzidis, "Non-equilibrium processing leads to record high thermoelectric figure of merit in PbTe–SrTe," *Nature Communications*, vol. 7, no. 1, 2016.

[157] P. K. Sharma, T. D. Senguttuvan, V. K. Sharma, and S. Chaudhary, "Revisiting the thermoelectric properties of lead telluride," *Materials Today Energy*, vol. 21, p. 100713, 2021.

[158] W. Wei, C. Chang, T. Yang, J. Liu, H. Tang, J. Zhang, Y. Li, F. Xu, Z. Zhang, J.-F. Li, and G. Tang, "Achieving High Thermoelectric Figure of Merit in Polycrystalline SnSe via Introducing Sn Vacancies," *Journal of the American Chemical Society*, vol. 140, no. 1, pp. 499–505, 2018.

[159] B. Zhong, Y. Zhang, W. Li, Z. Chen, J. Cui, W. Li, Y. Xie, Q. Hao, and Q. He, "High superionic conduction arising from aligned large lamellae and large figure of merit in bulk $Cu_{1.94}Al_{0.02}Se$," *Applied Physics Letters*, vol. 105, no. 12, p. 123902, 2014.

[160] X. L. Huang, D. W. Ao, T. B. Chen, Y. X. Chen, F. Li, S. Chen, G. X. Liang, X. H. Zhang, Z. H. Zheng, and P. Fan, "High-performance copper selenide thermoelectric thin films for flexible thermoelectric application," *Materials Today Energy*, vol. 21, p. 100743, 2021.

[161] X. Lou, S. Li, X. Chen, Q. Zhang, H. Deng, J. Zhang, D. Li, X. Zhang, Y. Zhang, H. Zeng, and G. Tang, "Lattice Strain Leads to High Thermoelectric Performance in Polycrystalline SnSe," *ACS Nano*, vol. 15, no. 5, pp. 8204–8215, 2021.

[162] C. Zhou, Y. K. Lee, Y. Yu, S. Byun, Z.-Z. Luo, H. Lee, B. Ge, Y.-L. Lee, X. Chen, J. Y. Lee, O. Cojocaru-Mirédin, H. Chang, J. Im, S.-P. Cho, M. Wuttig, V. P. Dravid, M. G. Kanatzidis, and I. Chung, "Polycrystalline SnSe with a thermoelectric figure of

merit greater than the single crystal," *Nature Materials*, vol. 20, no. 10, pp. 1378–1384, 2021.

[163] G. Tang, W. Wei, J. Zhang, Y. Li, X. Wang, G. Xu, C. Chang, Z. Wang, Y. Du, and L.-D. Zhao, "Realizing High Figure of Merit in Phase-Separated Polycrystalline $Sn_{1-x}Pb_xSe$," *Journal of the American Chemical Society*, vol. 138, no. 41, pp. 13647–13654, 2016.

[164] M. Li, D. L. Cortie, J. Liu, D. Yu, S. M. K. N. Islam, L. Zhao, D. R. G. Mitchell, R. A. Mole, M. B. Cortie, S. Dou, and X. Wang, "Ultra-high thermoelectric performance in graphene incorporated Cu_2Se: Role of mismatching phonon modes," *Nano Energy*, vol. 53, pp. 993–1002, 2018.

[165] G. Rogl, A. Grytsiv, P. Rogl, N. Peranio, E. Bauer, M. Zehetbauer, and O. Eibl, "n-Type skutterudites $(R,Ba,Yb)_yCo_4Sb_{12}$ (R=Sr, La, Mm, DD, SrMm, SrDD) approaching ZT≅2.0," *Acta Materialia*, vol. 63, pp. 30–43, 2014.

[166] G. Rogl, A. Grytsiv, P. Rogl, E. Bauer, M. Hochenhofer, R. Anbalagan, R. C. Mallik, and E. Schafler, "Nanostructuring of p- and n-type skutterudites reaching figures of merit of approximately 1.3 and 1.6, respectively," *Acta Materialia*, vol. 76, pp. 434–448, 2014.

[167] G. Rogl, A. Grytsiv, P. Heinrich, E. Bauer, P. Kumar, N. Peranio, O. Eibl, J. Horky, M. Zehetbauer, and P. Rogl, "New bulk p-type skutterudites $DD_{0.7}Fe_{2.7}Co_{1.3}Sb_{12-x}X_x$ (X=Ge, Sn) reaching ZT>1.3," *Acta Materialia*, vol. 91, pp. 227–238, 2015.

[168] D. Jin, Z. Ruan, B. Duan, J. Li, P. Zhai, H. Yang, H. Wang, G. Li, and L. Zhou, "Rapid preparation of high-performance $S_{0.4}Co_4Sb_{11.2}Te_{0.8}$ skutterudites with a highly porous structure," *Journal of the European Ceramic Society*, vol. 41, no. 8, pp. 4484–4489, 2021.

[169] M. J. Kruszewski, Ciupiński, and R. Zybała, "Review of rapid fabrication methods of skutterudite materials," *Materials Today: Proceedings*, vol. 44, pp. 3475–3482, 2021.

[170] O. Caballero-Calero, M. Rull-Bravo, D. Platzek, M. D. Cárdenas, R. Fernández, A. Moure, J. F. Fernández, and M. Martín-González, "Tubular ring thermoelectric module for exhaust pipes: From Skutterudite nanopowders to the final device," *Energy*, vol. 234, p. 121223, 2021.

[171] S. Utsunomiya, K. Kishimoto, S. Koda, K. Akai, R. Fujita, H. Asada, and T. Koyanagi, "Preparation and thermoelectric properties of sintered type-II clathrates $(K,Ba)_{24}(Al,Sn)_{136}$," *Journal of Alloys and Compounds*, vol. 693, pp. 1039–1044, 2017.

[172] K. Kishimoto, M. Hayashi, and K. Akai, "Thermoelectric properties and band structures of vacancy-containing Sn-based clathrates $K_8Sn_{44-x}Ge_x$," *Journal of Solid State Chemistry*, vol. 303, p. 122471, 2021.

[173] B. Liu, H. Ma, D. Huo, H. Liu, B. Liu, J. Chen, and X. Jia, "Thermoelectric properties of In-substituted Ge-based clathrates prepared by HPHT," *Journal of Materiomics*, vol. 4, no. 1, pp. 68–74, 2018.

[174] D. Srivastava, F. Azough, R. Freer, E. Combe, R. Funahashi, D. M. Kepaptsoglou, Q. M. Ramasse, M. Molinari, S. R. Yeandel, J. D. Baran, and S. C. Parker, "Crystal structure and thermoelectric properties of Sr–Mo substituted $CaMnO_3$: a combined experimental and computational study," *Journal of Materials Chemistry C*, vol. 3, no. 47, pp. 12245–12259, 2015.

[175] F. Delorme, C. F. Martin, P. Marudhachalam, D. Ovono Ovono, and G. Guzman, "Effect of Ca substitution by Sr on the thermoelectric properties of $Ca_3Co_4O_9$ ceramics," *Journal of Alloys and Compounds*, vol. 509, no. 5, pp. 2311–2315, 2011.

[176] Y. Wang, Y. Sui, X. Wang, and W. Su, "Effects of substituting La^{3+}, Y^{3+} and Ce^{3+} for Ca^{3+} on the high temperature transport and thermoelectric properties of $CaMnO_3$," vol. 42, no. 5, p. 055010, 2009.

[177] M. Ohtaki, K. Araki, and K. Yamamoto, "High Thermoelectric Performance of Dually Doped ZnO Ceramics," *Journal of Electronic Materials*, vol. 38, no. 7, pp. 1234–1238, 2009.

[178] M. Shikano and R. Funahashi, "Electrical and thermal properties of single-crystalline $(Ca_2CoO_3)_{0.7}CoO_2$ with a $Ca_3Co_4O_9$ structure," *Applied Physics Letters*, vol. 82, no. 12, pp. 1851–1853, 2003. Publisher: American Institute of Physics.

[179] N. Kanas, S. P. Singh, M. Rotan, M. Saleemi, M. Bittner, A. Feldhoff, T. Norby, K. Wiik, T. Grande, and M.-A. Einarsrud, "Influence of processing on stability, microstructure and

thermoelectric properties of $Ca_3Co_{4-x}O_{9+\sigma}$," *Journal of the European Ceramic Society*, vol. 38, no. 4, pp. 1592–1599, 2018.

[180] Y. Liu, L. Zhang, S. E. Shirsath, J. Zheng, Y. Liu, C. Ulrich, and S. Li, "Manipulation of charge carrier concentration and phonon scattering via spin-entropy and size effects: Investigation of thermoelectric transport properties in La-doped $Ca_3Co_4O_9$," *Journal of Alloys and Compounds*, vol. 801, pp. 60–69, 2019.

[181] W. Zhang, K. Zhu, J. Liu, J. Wang, K. Yan, P. Liu, and Y. Wang, "Influence of the phase transformation in Na_xCoO_2 ceramics on thermoelectric properties," *Ceramics International*, vol. 44, no. 14, pp. 17251–17257, 2018.

[182] M. Bittner, L. Helmich, F. Nietschke, B. Geppert, O. Oeckler, and A. Feldhoff, "Porous $Ca_3Co_4O_9$ with enhanced thermoelectric properties derived from Sol–Gel synthesis," *Journal of the European Ceramic Society*, vol. 37, no. 13, pp. 3909–3915, 2017.

[183] B. Feng, G. Li, Z. Pan, Y. Hou, C. Zhang, C. Jiang, J. Hu, Q. Xiang, Y. Li, Z. He, and X. Fan, "Effect of Ba and Pb dual doping on the thermoelectric properties of BiCuSeO ceramics," *Materials Letters*, vol. 217, pp. 189–193, 2018.

[184] J.-L. Lan, Y.-C. Liu, B. Zhan, Y.-H. Lin, B. Zhang, X. Yuan, W. Zhang, W. Xu, and C.-W. Nan, "Enhanced Thermoelectric Properties of Pb-doped BiCuSeO Ceramics," *Advanced Materials*, vol. 25, no. 36, 2013.

[185] Y. Liu, L.-D. Zhao, Y. Zhu, Y. Liu, F. Li, M. Yu, D.-B. Liu, W. Xu, Y.-H. Lin, and C.-W. Nan, "Synergistically Optimizing Electrical and Thermal Transport Properties of BiCuSeO via a Dual-Doping Approach," *Advanced Energy Materials*, vol. 6, no. 9, 2016.

[186] G. Kim, H. Shin, J. Lee, and W. Lee, "A Review on Silicide-Based Materials: Thermoelectric and Mechanical Properties," *Metals and Materials International*, vol. 27, no. 7, pp. 2205–2219, 2021.

[187] A. Nozariasbmarz, A. Agarwal, Z. A. Coutant, M. J. Hall, J. Liu, R. Liu, A. Malhotra, P. Norouzzadeh, M. C. Öztürk, V. P. Ramesh, Y. Sargolzaeiaval, F. Suarez, and D. Vashaee, "Thermoelectric silicides: A review," *Japanese Journal of Applied Physics*, vol. 56, no. 5S1, p. 05DA04, 2017.

[188] M. I. Fedorov and G. N. Isachenko, "Silicides: Materials for thermoelectric energy conversion," *Japanese Journal of Applied Physics*, vol. 54, no. 7S2, p. 07JA05, 2015.

[189] Y. Arita, K. Terao, S. Mitsuda, Y. Nishi, T. Matsui, and T. Nagasaki, "Thermoelectric properties of URu_2Si_2 and $U_2Ru_3Si_5$," *Journal of Nuclear Materials*, vol. 294, no. 1, pp. 206–208, 2001.

[190] Y. Arita, S. Mitsuda, Y. Nishi, T. Matsui, and T. Nagasaki, "Thermoelectric properties of Rh-doped Ru_2Si_3 prepared by floating zone melting method," *Journal of Nuclear Materials*, vol. 294, no. 1, pp. 202–205, 2001.

[191] K. Kishida, A. Ishida, T. Koyama, S. Harada, N. L. Okamoto, K. Tanaka, and H. Inui, "Thermoelectric properties of ternary and Al-containing quaternary $Ru_{1-x}Re_xSi_y$ chimney–ladder compounds," *Acta Materialia*, vol. 57, no. 6, pp. 2010–2019, 2009.

[192] Y. Li, J. Li, J. Du, J. Han, Q. Xiang, and C. Zhang, "Influence of fast neutron and gamma irradiation on the thermoelectric properties of n-type and p-type SiGe alloy," *Journal of Nuclear Materials*, vol. 528, p. 151856, 2020.

[193] M. R, V. P, K. S, S. K. R, and J. T. T, "Synergetic enhancement of thermoelectric and mechanical properties of n-type SiGe-p alloy through solid state synthesis and spark plasma sintering," *Materials Research Bulletin*, vol. 118, p. 110483, 2019.

[194] A. Vishwakarma, S. Bathula, N. S. Chauhan, R. Bhardwaj, B. Gahtori, A. K. Srivastava, and A. Dhar, "Facile synthesis of nanostructured n-type SiGe alloys with enhanced thermoelectric performance using rapid solidification employing melt spinning followed by spark plasma sintering," *Current Applied Physics*, vol. 18, no. 12, pp. 1540–1545, 2018.

[195] S. Ahmad, R. Basu, P. Sarkar, A. Singh, A. Bohra, S. Bhattacharya, R. Bhatt, K. N. Meshram, S. Samanta, P. Bhatt, M. Navaneethan, Y. Hayakawa, A. K. Debnath, S. K. Gupta, D. K. Aswal, K. P. Muthe, and S. C. Gadkari, "Enhanced thermoelectric figure-of-merit of p-type SiGe through TiO_2 nanoinclusions and modulation doping of boron," *Materialia*, vol. 4, pp. 147–156, 2018.

[196] S. Wongprakarn, S. Pinitsoontorn, S.-a. Tanusilp, and K. Kurosaki, "Enhancing thermoelectric properties of p-type SiGe alloy through optimization of carrier concentration and

processing parameters," *Materials Science in Semiconductor Processing*, vol. 88, pp. 239–249, 2018.

[197] S. Ahmad, A. Singh, A. Bohra, R. Basu, S. Bhattacharya, R. Bhatt, K. N. Meshram, M. Roy, S. K. Sarkar, Y. Hayakawa, A. K. Debnath, D. K. Aswal, and S. K. Gupta, "Boosting thermoelectric performance of p-type SiGe alloys through in-situ metallic YSi_2 nanoinclusions," *Nano Energy*, vol. 27, pp. 282–297, 2016.

[198] S. LeBlanc, "Thermoelectric generators: Linking material properties and systems engineering for waste heat recovery applications," *Sustainable Materials and Technologies*, vol. 1-2, pp. 26–35, 2014.

[199] Y. Sakamaki, K. Kuwabara, G. Jiajun, H. Inui, M. Yamaguchi, A. Yamamoto, and H. Obara, "Crystal Structure and Thermoelectric Properties of $ReSi_{1.75}$ Based Silicides," *Materials Science Forum*, vol. 426-432, pp. 1777–1782, 2003.

[200] H. Völlenkle, A. Wittmann, and H. Nowotny, "The crystal structure of $Rh_{10}Ga_{17}$ and Ir_3Ga_5," *Monatshefte für Chemie und verwandte Teile anderer Wissenschaften*, vol. 98, no. 1, pp. 176–183, 1967.

[201] G. Flieher, H. Völlenkle, and H. Nowotny, "New descendants of the $TiSi_2$ structure," *Monatshefte für Chemie / Chemical Monthly*, vol. 99, pp. 2408–2415, Nov. 1968.

[202] G. Kim, H. Shin, J. Lee, and W. Lee, "A Review on Silicide-Based Materials: Thermoelectric and Mechanical Properties," *Metals and Materials International*, vol. 27, no. 7, pp. 2205–2219, 2021.

[203] L. D. Ivanova, "Higher Manganese Silicide Based Materials," *Journal of Thermoelectricity*, no. 3, 2009.

[204] Z.-Q. Zou, W.-C. Li, J.-M. Liang, and D. Wang, "Self-organized growth of higher manganese silicide nanowires on Si(111), (110) and (001) surfaces," *Acta Materialia*, vol. 59, no. 20, pp. 7473–7479, 2011.

[205] P. Vivekanandhan, R. Murugasami, S. Appu Kumar, and S. Kumaran, "Structural features and thermoelectric properties of spark plasma assisted combustion synthesised Magnesium silicide doped with Aluminium," *Materials Chemistry and Physics*, vol. 241, p. 122407, 2020.

[206] J. Li, X. Li, B. Cai, C. Chen, Q. Zhang, Z. Zhao, L. Zhang, F. Yu, D. Yu, Y. Tian, and B. Xu, "Enhanced thermoelectric performance of high pressure synthesized Sb-doped Mg_2Si," *Journal of Alloys and Compounds*, vol. 741, pp. 1148–1152, 2018.

[207] C.-E. Kim, A. Soon, and C. Stampfl, "Unraveling the origins of conduction band valley degeneracies in $Mg_2Si_{1-x}Sn_x$ thermoelectrics," *Physical Chemistry Chemical Physics*, vol. 18, no. 2, pp. 939–946, 2015.

[208] A. de P. Shyikira, G. Skomedal, and P. Hugh Middleton, "Performance evaluation and stability of silicide-based thermoelectric modules," *Materials Today: Proceedings*, vol. 44, pp. 3467–3474, 2021.

[209] P. Dharmaiah, C.-h. Lee, G. Song, and S.-J. Hong, "Mechanical and thermoelectric properties of environment friendly higher manganese silicide fabricated using water atomization and spark plasma sintering," *Intermetallics*, vol. 119, p. 106705, 2020.

[210] Y. Miyazaki, H. Hamada, K. Hayashi, and K. Yubuta, "Crystal Structure and Thermoelectric Properties of Lightly Vanadium-Substituted Higher Manganese Silicides $Mn_{1-x}V_xSi_\gamma$," *Journal of Electronic Materials*, vol. 46, no. 5, pp. 2705–2709, 2017.

[211] X. Chen, A. Weathers, D. Salta, L. Zhang, J. Zhou, J. B. Goodenough, and L. Shi, "Effects of (Al,Ge) double doping on the thermoelectric properties of higher manganese silicides," *Journal of Applied Physics*, vol. 114, no. 17, p. 173705, 2013. Publisher: American Institute of Physics.

[212] Z. Gao, Z. Xiong, J. Li, C. Lu, G. Zhang, T. Zeng, Y. Ma, G. Ma, R. Zhang, K. Chen, T. Zhang, Y. Liu, J. Yang, L. Cao, and K. Jin, "Enhanced thermoelectric performance of higher manganese silicides by shock-induced high-density dislocations," *Journal of Materials Chemistry A*, vol. 7, no. 7, pp. 3384–3390, 2019.

[213] S. Ghodke, A. Yamamoto, H.-C. Hu, S. Nishino, T. Matsunaga, D. Byeon, H. Ikuta, and T. Takeuchi, "Improved Thermoelectric Properties of Re-Substituted Higher Manganese Silicides by Inducing Phonon Scattering and an Energy-Filtering Effect at Grain Boundary Interfaces," *ACS Applied Materials & Interfaces*, vol. 11, no. 34, pp. 31169–31175, 2019.

[214] Q. Wang, S. Song, X. Yang, Z. Liu, Y. Ma, X. San, J. Wang, D. Zhang, S.-F. Wang, and Z. Li, "Incorporating element doping and quantum dot embedding effects to enhance the

thermoelectric properties of higher manganese silicides," *Journal of Materiomics*, vol. 7, no. 2, pp. 377–387, 2021.

[215] A. Teknetzi, E. Tarani, E. Symeou, D. Karfaridis, D. Stathokostopoulos, E. Pavlidou, T. Kyratsi, E. Hatzikraniotis, K. Chrissafis, and G. Vourlias, "Structure and thermoelectric properties of higher manganese silicides synthesized by pack cementation," *Ceramics International*, vol. 47, no. 1, pp. 243–251, 2021.

[216] M. Saminathan, J. Palraj, P. Wesley, M. Moorthy, Ravikirana, and S. Perumal, "Thermoelectric properties of p-type Si-rich higher manganese silicide for mid-temperature applications," *Materials Letters*, vol. 302, p. 130444, 2021.

[217] P. Vivekanandhan, R. Murugasami, and S. Kumaran, "Microstructure and mechanical properties of magnesium silicide prepared via spark plasma assisted combustion synthesis," *Materials Letters*, vol. 231, pp. 109–113, 2018.

[218] D. Shiojiri, T. Iida, H. Kakio, M. Yamaguchi, N. Hirayama, and Y. Imai, "Enhancement of thermoelectric performance of Mg_2Si via co-doping Sb and C by simultaneous tuning of electronic and thermal transport properties," *Journal of Alloys and Compounds*, vol. 891, p. 161968, 2022.

[219] G. Mesaritis, E. Symeou, A. Delimitis, M. Constantinou, G. Constantinides, M. Jeagle, K. Tarantik, and T. Kyratsi, "Synthesis, characterization and thermoelectric performance of Mg_2(Si,Sn,Ge) materials using Si-kerf waste from photovoltaic technology," *Journal of Alloys and Compounds*, vol. 826, p. 153933, 2020.

[220] G. Yuan, S. Han, X. Lei, J. Hu, W. Liu, Q. Wang, C. Chen, Q. Zhang, Q. Zhang, and M. Gu, "The enhancement of thermoelectric performance of p-type Li doped $Mg_2Ge_{0.4}Sn_{0.6}$ by Si addition," *Scripta Materialia*, vol. 166, pp. 122–127, 2019.

[221] A. U. Khan, N. V. Vlachos, E. Hatzikraniotis, G. S. Polymeris, C. B. Lioutas, E. C. Stefanaki, K. M. Paraskevopoulos, I. Giapintzakis, and T. Kyratsi, "Thermoelectric properties of highly efficient Bi-doped $Mg_2Si_{1-x-y}Sn_xGe_y$ materials," *Acta Materialia*, vol. 77, pp. 43–53, 2014.

[222] G. K. Goyal, S. Mukherjee, R. C. Mallik, S. Vitta, I. Samajdar, and T. Dasgupta, "High Thermoelectric Performance in $Mg_2Si_{0.3}Sn_{0.7}$ by Enhanced Phonon Scattering," *ACS Applied Energy Materials*, vol. 2, no. 3, pp. 2129–2137, 2019.

[223] J. de Boor, T. Dasgupta, U. Saparamadu, E. Müller, and Z. F. Ren, "Recent progress in p-type thermoelectric magnesium silicide based solid solutions," *Materials Today Energy*, vol. 4, pp. 105–121, 2017.

[224] X. Tang, Y. Zhang, Y. Zheng, K. Peng, T. Huang, X. Lu, G. Wang, S. Wang, and X. Zhou, "Improving thermoelectric performance of p-type Ag-doped $Mg_2Si_{0.4}Sn_{0.6}$ prepared by unique melt spinning method," *Applied Thermal Engineering*, vol. 111, pp. 1396–1400, 2017.

[225] S. Perumal, S. Gorsse, U. Ail, B. Chevalier, R. Decourt, and A. M. Umarji, "Effect of co-substitution of Mn and Al on thermoelectric properties of chromium disilicide," *Journal of Materials Science*, vol. 48, no. 1, pp. 227–231, 2013.

[226] N. K. Upadhyay, L. A. Kumaraswamidhas, B. Gahtori, S. Bathula, S. Muthiah, R. Shyam, N. S. Chauhan, R. Bhardwaj, and A. Dhar, "Enhancement in thermoelectric performance of bulk $CrSi_2$ dispersed with nanostructured SiGe nanoinclusions," *Journal of Alloys and Compounds*, vol. 765, pp. 412–417, 2018.

[227] M. Mikami and Y. Kinemuchi, "Microstructure and thermoelectric properties of WSi_2-added $CrSi_2$ composite," *Journal of Alloys and Compounds*, vol. 690, pp. 652–657, 2017.

[228] Y. Ohishi, A. Mohamad, Y. Miyazaki, H. Muta, K. Kurosaki, and S. Yamanaka, "Thermoelectric properties of $Cr_{1-x}Mo_xSi_2$," *Journal of Physics and Chemistry of Solids*, vol. 87, pp. 153–157, 2015.

[229] K. Kishida, A. Ishida, T. Koyama, S. Harada, N. L. Okamoto, K. Tanaka, and H. Inui, "Thermoelectric properties of ternary and Al-containing quaternary $Ru_{1-x}Re_xSi_y$ chimney–ladder compounds," *Acta Materialia*, vol. 57, no. 6, pp. 2010–2019, 2009.

[230] N. Liu, S. E. Rezaei, W. A. Jensen, S. Song, Z. Ren, K. Esfarjani, M. Zebarjadi, and J. A. Floro, "Improved Thermoelectric Performance of Eco-Friendly $\beta-FeSi_2-SiGe$ Nanocomposite via Synergistic Hierarchical Structuring, Phase Percolation, and Selective Doping," *Advanced Functional Materials*, vol. 29, no. 38, 2019.

[231] F. Dąbrowski, Ciupiński, J. Zdunek, J. Kruszewski, R. Zybała, A. Michalski, and K. Jan Kurzydłowski, "Microstructure and thermoelectric properties of p and n type doped β-FeSi2 fabricated by mechanical alloying and pulse plasma sintering," *Materials Today: Proceedings*, vol. 8, pp. 531–539, 2019.

[232] S. Ahmad, A. Singh, A. Bohra, R. Basu, S. Bhattacharya, R. Bhatt, K. N. Meshram, M. Roy, S. K. Sarkar, Y. Hayakawa, A. K. Debnath, D. K. Aswal, and S. K. Gupta, "Boosting thermoelectric performance of p-type SiGe alloys through in-situ metallic YSi_2 nanoinclusions," *Nano Energy*, vol. 27, pp. 282–297, 2016.

[233] S. Ahmad, R. Basu, P. Sarkar, A. Singh, A. Bohra, S. Bhattacharya, R. Bhatt, K. N. Meshram, S. Samanta, P. Bhatt, M. Navaneethan, Y. Hayakawa, A. K. Debnath, S. K. Gupta, D. K. Aswal, K. P. Muthe, and S. C. Gadkari, "Enhanced thermoelectric figure-of-merit of p-type SiGe through TiO_2 nanoinclusions and modulation doping of boron," *Materialia*, vol. 4, pp. 147–156, 2018.

[234] S. Wongprakarn, S. Pinitsoontorn, S.-a. Tanusilp, and K. Kurosaki, "Enhancing thermoelectric properties of p-type SiGe alloy through optimization of carrier concentration and processing parameters," *Materials Science in Semiconductor Processing*, vol. 88, pp. 239–249, 2018.

[235] Y. Li, J. Li, J. Du, J. Han, Q. Xiang, and C. Zhang, "Influence of fast neutron and gamma irradiation on the thermoelectric properties of n-type and p-type SiGe alloy," *Journal of Nuclear Materials*, vol. 528, p. 151856, 2020.

[236] M. R, V. P, K. S, S. K. R, and J. T. T, "Synergetic enhancement of thermoelectric and mechanical properties of n-type SiGe-P alloy through solid state synthesis and spark plasma sintering," *Materials Research Bulletin*, vol. 118, p. 110483, 2019.

[237] L. J.-Z. Z. X.-B. ZHOU Ai-Jun, CUI Heng-Guan, "Structure and morphology of induction-melted higher manganese silicide," *Acta Phys.-Chim. Sin.*, vol. 27, no. 12, pp. 2915–2919, 2011.

[238] Y. Sadia, M. Elegrably, O. Ben-Nun, Y. Marciano, and Y. Gelbstein, "Submicron Features in Higher Manganese Silicide," *Journal of Nanomaterials*, vol. 2013, p. e701268, 2013.

[239] Z. Dashevsky and S. Skipidarov, "Investigating the Performance of Bismuth-Antimony Telluride," in *Novel Thermoelectric Materials and Device Design Concepts* (S. Skipidarov and M. Nikitin, eds.), pp. 3–21, Cham: Springer International Publishing, 2019.

[240] P. Cavaliere, B. Sadeghi, and A. Shabani, "Spark Plasma Sintering: Process Fundamentals," in *Spark Plasma Sintering of Materials: Advances in Processing and Applications* (P. Cavaliere, ed.), pp. 3–20, Cham: Springer International Publishing, 2019.

[241] F. Zhang, Y. Quan, M. Reich, O. Kessler, and E. Burkel, *Sintering and Heat Treatment of Titanium Alloys by Pulsed Electric Current Sintering*. IntechOpen, 2013. Publication Title: Sintering Applications.

[242] S. Mitra and T. Maiti, "Thermoelectric Materials Synthesized by Spark Plasma Sintering (SPS) for Clean Energy Generation," in *Spark Plasma Sintering of Materials: Advances in Processing and Applications* (P. Cavaliere, ed.), pp. 493–514, Cham: Springer International Publishing, 2019.

[243] Y.-X. Chen, Z.-H. Ge, M. Yin, D. Feng, X.-Q. Huang, W. Zhao, and J. He, "Understanding of the Extremely Low Thermal Conductivity in High-Performance Polycrystalline SnSe through Potassium Doping," *Advanced Functional Materials*, vol. 26, no. 37, pp. 6836–6845, 2016.

[244] L. J. van der Pauw, "A method of measuring specific resistivity and hall effect of discs of arbitrary shape," *Philips Research Reports*, vol. 13, no. 37, pp. 1–9, 1958.

[245] S. Iwanaga, E. S. Toberer, A. LaLonde, and G. J. Snyder, "A high temperature apparatus for measurement of the Seebeck coefficient," *Review of Scientific Instruments*, vol. 82, no. 6, p. 063905, 2011.

[246] J. de Boor, C. Stiewe, P. Ziolkowski, T. Dasgupta, G. Karpinski, E. Lenz, F. Edler, and E. Mueller, "High-Temperature Measurement of Seebeck Coefficient and Electrical Conductivity," *Journal of Electronic Materials*, vol. 42, no. 7, pp. 1711–1718, 2013.

[247] Y. Liu, C. Fu, H. Xie, X. Zhao, and T. Zhu, "Reliable measurements of the Seebeck coefficient on a commercial system," *Journal of Materials Research*, vol. 30, no. 17, pp. 2670–2677, 2015.

[248] NASA, "Missions."

[249] L. Francioso, C. De Pascali, V. Sglavo, A. Grazioli, M. Masieri, and P. Siciliano, "Modelling, fabrication and experimental testing of an heat sink free wearable thermoelectric generator," *Energy Conversion and Management*, vol. 145, pp. 204–213, 2017.

[250] S. Zhou, B. G. Sammakia, B. White, P. Borgesen, and C. Chen, "Multiscale modeling of Thermoelectric Generators for conversion performance enhancement," *International Journal of Heat and Mass Transfer*, vol. 81, pp. 639–645, 2015.

[251] S. Zhou, B. G. Sammakia, B. White, and P. Borgesen, "Multiscale modeling of thermoelectric generators for the optimized conversion performance," *International Journal of Heat and Mass Transfer*, vol. 62, pp. 435–444, 2013.

[252] H.-X. Mi, M.-X. Wu, S. Cao, Z.-Y. Huang, L. Han, and J. Xu, "Effect of solder and barrier layer elements on the thermoelectric properties of $Bi_{0.5}Sb_{1.5}Te_3$," vol. 6, no. 10, p. 106310, 2019.

[253] Y. N. Nguyen and I. Son, "Thermomechanical stability of Bi_2Te_3-based thermoelectric modules employing variant diffusion barriers," *Intermetallics*, vol. 140, p. 107404, 2022.

[254] J. S. Graff, R. Schuler, X. Song, G. Castillo-Hernandez, G. Skomedal, E. Enebakk, D. N. Wright, M. Stange, J. de Boor, O. M. Løvvik, and M. Schrade, "Fabrication of a Silicide Thermoelectric Module Employing Fractional Factorial Design Principles," *Journal of Electronic Materials*, vol. 50, no. 7, pp. 4041–4049, 2021.

[255] C.-H. Lee, W.-T. Chen, and C.-N. Liao, "Effect of antimony on vigorous interfacial reaction of Sn–Sb/Te couples," *Journal of Alloys and Compounds*, vol. 509, no. 16, pp. 5142–5146, 2011.

[256] C.-n. Chiu, C.-h. Wang, and S.-w. Chen, "Interfacial Reactions in the Sn-Bi/Te Couples," *Journal of Electronic Materials*, vol. 37, no. 1, pp. 40–44, 2008.

[257] S.-w. Chen, C.-y. Wu, H.-j. Wu, and W.-t. Chiu, "Interfacial reactions in Sn/Bi_2Te_3, Sn/Bi_2Se_3 and $Sn/Bi_2(Te_{1-x}Se_x)_3$ couples," *Journal of Alloys and Compounds*, vol. 611, pp. 313–318, 2014.

[258] C.-h. Wang, M.-h. Li, C.-w. Chiu, and T.-y. Chang, "Kinetic study of solid-state interfacial reactions of p-type $(Bi, Sb)_2Te_3$ thermoelectric materials with Sn and Sn–Ag–Cu solders," *Journal of Alloys and Compounds*, vol. 767, pp. 1133–1140, 2018.

[259] C.-H. Chuang, Y.-C. Lin, and C.-W. Lin, "Intermetallic Reactions during the Solid-Liquid Interdiffusion Bonding of $Bi_2Te_{2.55}Se_{0.45}$ Thermoelectric Material with Cu Electrodes Using a Sn Interlayer," *Metals*, vol. 6, no. 4, 2016.

[260] X. R. Ferreres, A. Gazder, A. Manettas, and S. Aminorroaya Yamini, "Solid-State Bonding of Bulk PbTe to Nickel Electrode for Thermoelectric Modules," *ACS Applied Energy Materials*, vol. 1, no. 2, pp. 348–354, 2018.

[261] S.-W. Fu and C. C. Lee, "Direct silver to aluminum solid-state bonding processes," *Materials Science and Engineering: A*, vol. 722, pp. 160–166, 2018.

[262] C. Zhang, M. Q. Li, and H. Li, "Diffusion behavior at void tip and its contributions to void shrinkage during solid-state bonding," *Journal of Materials Science & Technology*, vol. 34, no. 8, pp. 1449–1454, 2018.

[263] Z. Chen, M. Cai, Z. Liu, Y. Chen, X. Yi, F. Wang, and W. Zhu, "Amorphization and intermetallic nucleation in early-stage interfacial diffusion during Sn-solder/Ni solid-state bonding," *Journal of Alloys and Compounds*, vol. 859, p. 158399, 2021.

[264] S. Zhang, W. Wang, S. Ma, H. Yan, L. Jiao, and Q. Li, "A solid state bonding technology for metal plate by shear-extrusion and the analysis of microstructure and bonding strength," *Journal of Manufacturing Processes*, vol. 59, pp. 477–486, 2020.

[265] T. A. Tollefsen, A. Larsson, O. M. Løvvik, and K. Aasmundtveit, "Au-Sn SLID Bonding—Properties and Possibilities," *Metallurgical and Materials Transactions B*, vol. 43, no. 2, pp. 397–405, 2012.

[266] "Defects in Semiconductors," in *The Materials Science of Semiconductors* (A. Rockett, ed.), pp. 289–356, Boston, MA: Springer US, 2008.

[267] S. Shin, J. W. Roh, H.-S. Kim, and R. Chen, "Role of surfactant on thermoelectric behaviors of organic-inorganic composites," *Journal of Applied Physics*, vol. 123, no. 20, p. 205106, 2018.

[268] A. Bhaduri, "Creep and Stress Rupture," in *Mechanical Properties and Working of Metals and Alloys* (A. Bhaduri, ed.), Springer Series in Materials Science, pp. 257–316, Singapore: Springer, 2018.

[269] C. Li, G. Snyder, and D. Dunand, "Compressive creep behaviour of hot-pressed PbTe," *Scripta Materialia*, vol. 134, pp. 71–74, 2017.

[270] Z.-P. Guan and D. C. Dunand, "Compressive creep behavior of cast Bi_2Te_3," *Materials Science and Engineering: A*, vol. 565, pp. 321–325, 2013.

[271] M. C. Chang, M. T. Agne, R. A. Michi, D. C. Dunand, and G. J. Snyder, "Compressive creep behavior of hot-pressed GeTe based TAGS-85 and effect of creep on thermoelectric properties," *Acta Materialia*, vol. 158, pp. 239–246, 2018.

[272] M. M. Al Malki, X. Shi, P. Qiu, G. J. Snyder, and D. C. Dunand, "Creep behavior and post-creep thermoelectric performance of the n-type Skutterudite alloy $Yb_{0.3}Co_4Sb_{12}$," *Journal of Materiomics*, vol. 7, no. 1, pp. 89–97, 2021.

[273] M. M. Al Malki, Q. Qiu, T. Zhu, G. J. Snyder, and D. C. Dunand, "Creep behavior and postcreep thermoelectric performance of the n-type half-Heusler alloy $Hf_{0.3}Zr_{0.7}NiSn_{0.98}Sb_{0.02}$," *Materials Today Physics*, vol. 9, p. 100134, 2019.

[274] R. A. Michi, G. Kim, B.-W. Kim, W. Lee, and D. C. Dunand, "Compressive creep behavior of hot-pressed $Mg_{1.96}Al_{0.04}Si_{0.97}Bi_{0.03}$," *Scripta Materialia*, vol. 148, pp. 10–14, 2018.

[275] L. Guobin, W. Jianjun, J. Yanfei, and L. Guiyun, "The nucleation and propagation of a thermal fatigue crack in 4 Cr_2NiMoV steel," *Journal of Materials Processing Technology*, vol. 100, no. 1, pp. 63–66, 2000.

[276] D. J. Young, "Chapter 14 - Alloy Design," in *High Temperature Oxidation and Corrosion of Metals (Second Edition)* (D. J. Young, ed.), pp. 685–701, Elsevier, second edition ed., 2016.

[277] C. Wagner, "Theoretical Analysis of the Diffusion Processes Determining the Oxidation Rate of Alloys," *Journal of The Electrochemical Society*, vol. 99, no. 10, p. 369, 1952.

[278] G. Skomedal, A. Burkov, A. Samunin, R. Haugsrud, and H. Middleton, "High temperature oxidation of Mg_2(Si-Sn)," *Corrosion Science*, vol. 111, pp. 325–333, 2016.

[279] "TESil." https://www.elkem.com/innovation/research-projects/tesil/. Accessed: 18/03/2022.

[280] G. Planinšič and M. Vollmer, "The surface-to-volume ratio in thermal physics: from cheese cube physics to animal metabolism," *European Journal of Physics*, vol. 29, no. 2, pp. 369–384, 2008.

[281] N. Birks, G. H. Meier, and F. S. Pettit, *Introduction to the High Temperature Oxidation of Metals*. Cambridge: Cambridge University Press, 2 ed., 2006.

[282] B. Chattopadhyay, "Thin film oxidation and the logarithmic rate law," *Thin Solid Films*, vol. 16, no. 1, pp. 117–124, 1973.

[283] B. N. Popov, "Chapter 11 - High-Temperature Corrosion," in *Corrosion Engineering* (B. N. Popov, ed.), pp. 481–523, Amsterdam: Elsevier, 2015.

[284] J. de Boor, C. Gloanec, H. Kolb, R. Sottong, P. Ziolkowski, and E. Müller, "Fabrication and characterization of nickel contacts for magnesium silicide based thermoelectric generators," *Journal of Alloys and Compounds*, vol. 632, pp. 348–353, May 2015.

[285] T. Sakamoto, T. Iida, Y. Honda, M. Tada, T. Sekiguchi, K. Nishio, Y. Kogo, and Y. Takanashi, "The Use of Transition-Metal Silicides to Reduce the Contact Resistance Between the Electrode and Sintered n-Type Mg2Si," *Journal of Electronic Materials*, vol. 41, pp. 1805–1810, June 2012.

[286] N. H. Pham, N. Farahi, H. Kamila, A. Sankhla, S. Ayachi, E. Müller, and J. de Boor, "Ni and Ag electrodes for magnesium silicide based thermoelectric generators," *Materials Today Energy*, vol. 11, pp. 97–105, Mar. 2019.

[287] H. Ihou Mouko, K. Romanjek, M. Mejri, M. Oulfarsi, S. El Oualid, P. Malinconi, Y. Thimont, B. Malard, C. Estournès, N. David, and A. Dauscher, "Manufacturing and performances of silicide-based thermoelectric modules," *Energy Conversion and Management*, vol. 242, p. 114304, Aug. 2021.

[288] S. Ayachi, R. Deshpande, P. Ponnusamy, S. Park, J. Chung, S. Park, B. Ryu, E. Müller, and J. de Boor, "On the relevance of point defects for the selection of contacting electrodes: Ag as an example for Mg2(Si,Sn)-based thermoelectric generators," *Materials Today Physics*, vol. 16, p. 100309, Jan. 2021.

[289] H.-K. Sung, C. Wang, and N.-Y. Kim, "Reliability study of Au-in solid-liquid interdiffusion bonding for GaN-based vertical LED packaging," *Journal of Micromechanics and Microengineering*, vol. 25, p. 127002, Nov. 2015. Publisher: IOP Publishing.

[290] N. Farahi, C. Stiewe, D. Y. N. Truong, J. d. Boor, and E. Müller, "High efficiency Mg2(Si,Sn)-based thermoelectric materials: scale-up synthesis, functional homogeneity, and thermal stability," *RSC Advances*, vol. 9, pp. 23021–23028, July 2019. Publisher: The Royal Society of Chemistry.

[291] U. electronic, "Spring contact probe quad-00." https://www.uweelectronic.de/en/products/spring-contact-probe-quad-00.html. Accessed on 22/08/2022.

[292] R. precision limited, "Catalog: Precise motion control solutions." https://www.reliance.co.uk/wp-content/uploads/2022/04/Reliance-Precision-RG36-Issue-B2-Standard-Products-Range-WEB.pdf. Accessed on 22/08/2022.

[293] A. de Padoue Shyikira, "Pcm direct sample mounting process." https://www.youtube.com/watch?v=WtIZH62QRCY.

Appendices

Paper I

Performance evaluation and stability of silicide-based thermoelectric modules

Authors: **Antoine de Padoue Shyikira**, Gustein Skomedal, Peter Hugh Middleton

Materials Today: Proceedings 44 (2021) 3467–3474

Contents lists available at ScienceDirect

Materials Today: Proceedings

journal homepage: www.elsevier.com/locate/matpr

Performance evaluation and stability of silicide-based thermoelectric modules

Antoine de Padoue Shyikira [a,*], Gustein Skomedal [a,b], Peter Hugh Middleton [a]

[a] University of Agder, Norway
[b] Elkem ASA – Kristiansand, Norway

ARTICLE INFO

Article history:
Received 21 October 2019
Received in revised form 26 April 2020
Accepted 7 May 2020
Available online 12 June 2020

Keywords:
Thermoelectric module
Silicides
Degradation
Stability

ABSTRACT

Long-term studies on thermoelectric generators based on N-type magnesium silicide ($Mg_{2.01}Si_{0.49}Sn_{0.5}Sb_{0.01}$) and P-type higher manganese silicide ($Mn_{0.98}Mo_{0.02}Si_{1.73}Ge_{0.02}$) materials are presented, in the operating temperature range of 200 °C–400 °C. Emphasis is put on the performance and reliability of the current collector configuration, especially on the hot side of the module, and on the thermomechanical stresses that are created during operation and lifetime testing as a result of large temperature gradients experienced across the thermoelectric legs. With silver (Ag) paste as contact material, the long term-stability of the uni-couples was carried out on non-metalized legs and gold metalized legs under ambient conditions. Under isothermal and thermocycling tests, the non-metalized legs showed a gradual decrease in open circuit voltage (after a period of 200 h) and increase in internal resistance. Conversely, the module made of metalized legs was robust and stable for the same isothermal period. However, after 300cycles the n-type material showed mechanical failure (cracks) but the p-type resisted. Post-operation analysis by SEM/EDS and mechanical testing revealed that oxidation, adherence of the contact material and diffusion of the bonding material were the cause of performance degradation of the unicouples.

1. Introduction

Silicide-based thermoelectric materials (TEM) are promising materials for the future of thermoelectrics. These materials are among the best candidates for mass production [1], due to high abundancy of raw materials in the earth crust (especially silicon 2nd, magnesium 8th and manganese 12th [2]), low cost and non-toxicity. For a long time, ($Si_{1-x}Ge_x$) was proven to be good for thermoelectric application in radioisotopes thermoelectric generators [3], though new compounds were proposed and studied, including compounds based on higher manganese silicide (HMS) [4,5] and magnesium silicide (MGS). These compounds have shown good transport properties, with figures of merit around 0.6 and 1.5, respectively, and more research is still being carried out to optimize the transport properties. Moreover, coupling of HMS and MGS in a module was proposed by many researchers for terrestrial application [6,7,8], though the combination has not been implemented in any of the modules on the market.

Today, more research has focused at the materials level, improving the transport properties, figure of merit and the mechanical properties. However, not much research has been done at the module level, especially on the MGS-HMS combination, and even less work has been conducted on electrodes and electrode-TEM interfaces. Previous work from our group Skomedal et al. [6], worked on modelling, designing, assembling HMS (p-type) – MGS (n-type) modules and testing their performance and stability over time. The three unicouples used in the module showed good performance, which reached a peak power of 3.24 W at a hot side temperature of 735 °C, and 1.04 W maximum power at 405 °C. Moreover, Nakamura et al. [9], studied a π shaped module based on Mg_2Si and $MnSi_{1.73}$, as n- and p-type TEMs, respectively. With Ag electrode, Ag bonding material and Ni diffusion barrier, their module produced 4.4 kW/m^2 at 548 °C. However, both Skomedal and Nakamura's modules degraded during thermal cycles mainly due to oxidation of the MGS, and coefficient of thermal expansion (CTE) mismatches at the bonding interface. By contrast, De Boor et al. [10], has investigated the stability of Mg_2Si and nickel electrode contact. The contact was successfully formed by mutual sintering the TEM and the electrode (at 1123 K), which resulted in a 10–30 μm Mg-Si-Ni reaction layer. The study was done under

* Corresponding author.
E-mail addresses: antoine.d.shyikira@uia.no, tonnydepadoue15@gmail.com (A.P. Shyikira).

https://doi.org/10.1016/j.matpr.2020.05.193
2214-7853/

isothermal treatment for 168 h at 823 K and no cracks were observed by SEM, which the authors claim was a result of a relatively thick contact layer that also hindered diffusion of Mg to the Ni side. However, they recommend thermal cycle runs to investigate and confirm the reliability of Mg_2Si -Ni contact.

Kaibe et al. [11], studied cascaded modules made of p-Mn-Si and n-Mg-Si on the hot side and Bi-Te base alloys on the cold side with which they achieved 12% efficiency at 550 °C. Their results were promising, though the stability of the cascaded module remained an issue due to complex chemical phenomena occurring overtime, from electrodes (Ni-plated Cu electrodes) to bonding materials involving oxidation and intermetallic diffusion which should be investigated. Similarly, Hee Seok Kim et al. [7], studied a segmented TE module, with MGS(Mg_2Si) – HMS ($MnSi_{2-x}$, x = 0.25–0.273) mounted on top at the high temperature segment and n- and p- type Bi-Te module on the cold side. Contact electrodes were made from Cu on both the hot side and cold side, with 50 nm Ti and 1 μm Ag layers. Under isothermal heat treatment between 23 and 520 °C for 30 h, they achieved a contact resistance of 50μΩcm^2 and a contact resistance to total module resistance ratio of 2%, moreover, they achieved a specific power density of 42.9 W/kg with a 498 °C temperature difference. Among other possibilities, Ni and Ag electrodes [10,12–15], Cu electrodes [7,14], and molybdenum (Mo) [6] have been mostly studied. It seems, from the aforementioned electrodes that Ag was the most reliable followed by Ni, with around 10μΩcm^2 vs 25-5010μΩcm^2 specific resistance on MGS [10,12].

Some of the key factors that affect performance and stability over time for TE modules are diffusion at the electrode/bonding material – TEM interface, bonding strength and contact resistance. At module contacts, diffusion is a deteriorative factor, however, as reported by Liu et al. [16], it is also important to note that limited diffusion is important for crack free contacts. However, diffusion during operation should be avoided as, in some cases diffusion can alter the doping and turn an n-type into a p-type TEM; this would seriously shorten the in-service lifetime of the device. Altering the doping would reduce the charge carrier concentration and affect the performance of the module by lifetime shortage or reduction of the mechanical reliability. So apart from the strong bond through diffusion, a diffusion barrier is also important to stop further diffusion during operation. Moreover, a strong and reliable bond requires good matching of the coefficient of thermal expansion (CTE) of the electrode and the TEM. In the current study, the CTE for a mixture of phases has been approximated using a model by Karunaratne M.S.A. et al. [17] equation 1, where, $\bar{\alpha}, \omega_i, \rho_i, \bar{\alpha}_i$ stand for the CTE of the alloy/mixture, the weight fraction of phase i, the density of phase i, and the CTE of individual phase i.

$$\bar{\alpha} = \frac{\sum \bar{\alpha}_i \{\omega_i/\rho_i\}}{\sum \{\omega_i/\rho_i\}} \quad (1)$$

It is difficult to model thermal contact resistance as it requires coupling the phonons carrying heat from the heating element through the interface to the TE leg. Well-known models include the acoustic mismatch model and the diffusive mismatch model [18]. However, the modern molecular dynamic simulation [19] suggested that the phonons at the interface scatters as a mixture of acoustic scattering and diffusive scattering, so the bond strength is a deterministic factor of the interface contact resistance. Therefore, if the coefficients of thermal expansion (CTE) of the materials is closely matched, a good contact can be achieved by sintering them together to allow diffusion to take place and therefore a strong bond developed. However, the materials reactivity level towards higher temperatures and the stability of the bond over high thermal stress, operational diffusion passivation, high electrical, chemical and thermal conductivity are the next challenges to overcome.

2. Materials and methods

2.1. Materials and modules

The uni-couple modules were assembled using MGS ($Mg_{2.01}Si_{0.49}Sn_{0.5}Sb_{0.01}$) as n-type and HMS ($Mn_{0.98}Mo_{0.02}Si_{1.73}Ge_{0.02}$) as p-type. The powder materials used in this research are synthesized

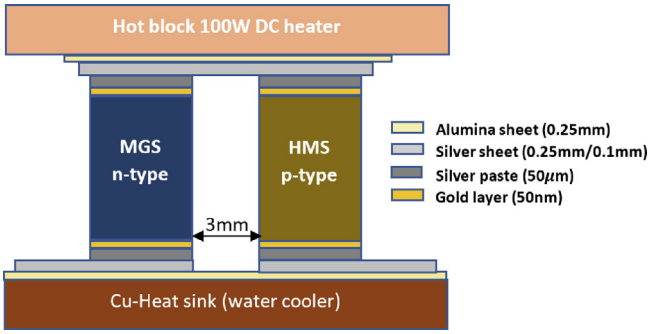

Fig. 1. A detailed schematic representation of a unicouple module test-assembly.

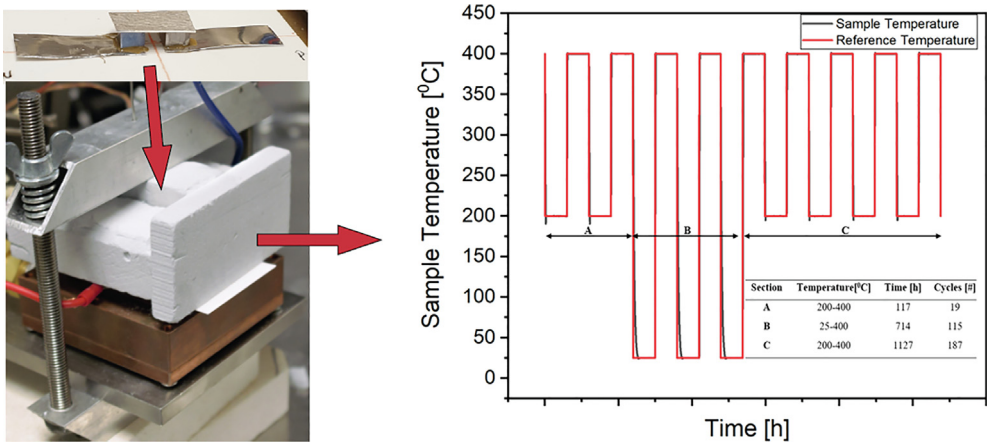

Fig. 2. An illustration of full thermocycle tests setup (the uni-couple, the homemade rig for stability tests and the temperature range the thermal cycles were conducted).

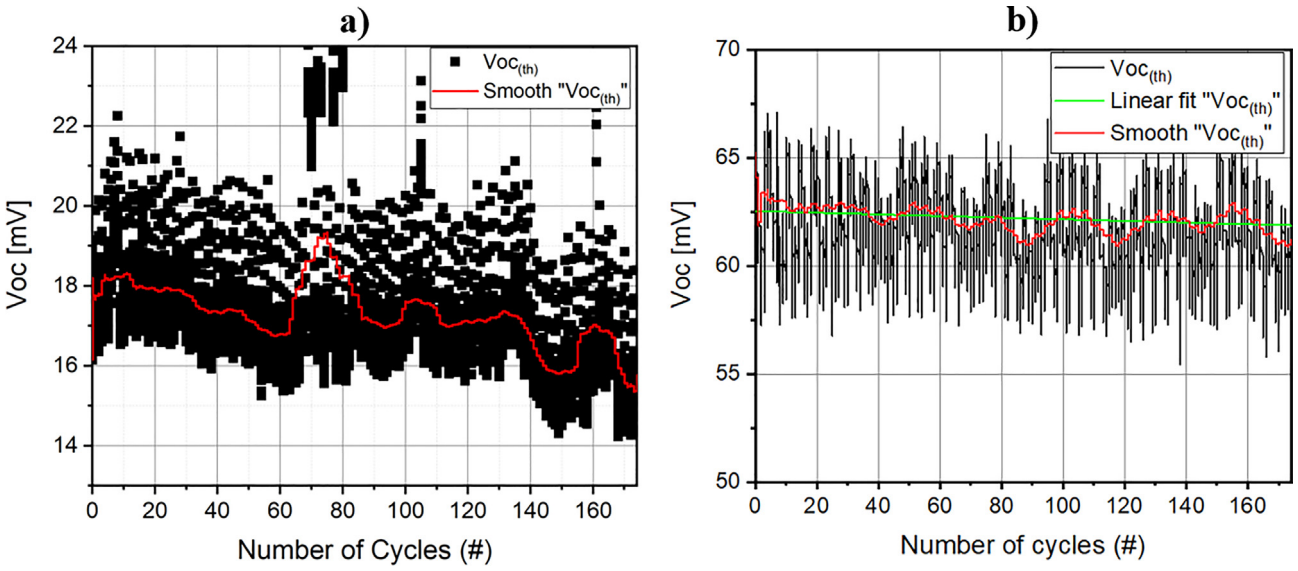

Fig. 3. The thermal open circuit voltage (Seebeck voltage) recorded over time (module 2), plotted against the number of cycles (in black), the red curve shows the "adjacent averaged Voc_{th}" trend, which shows the decrease of Voc_{th} over time, for the voltage recorded: a) at 200 °C and b) at 400 °C. (For interpretation of the references to colour in this figure legend, the reader is referred to the web version of this article.)

and sintered by different partners (Elkem, Sintef, and UiO) in Thermoelectric Silicides (TESil) project. HMS was synthesized by melting (in an induction furnace) and casting in a graphite mould. From the cast ingots, powder was produced by ball milling down to micro-size powder, using a Herzog HSM 100 vibratory mill and a Planetary Ball mill 100. Furthermore, the powder was consolidated into pellets by Spark Plasma Sintering (SPS) (Dr. Sinter, SPS-825). However, MGS was synthesized through solid state route and pelletized by conventional Hot Pressing (HP) (home made at the University of Oslo-Norway). Further thorough details from materials modelling, powder synthesis and pellet consolidation are not yet public as it is still an ongoing project. Pellets of 20–36[mm] diameter and 5 mm height, for the HMS and MGS were cut using a Minitom (Struers) equipped with a diamond saw (Diamond Cut-off Wheel MOD13, 127 mm (5″) dia. × 0.4 mm × 12.7 mm dia.) into legs of 4x4x3[mm] (±50μm dimensions after cutting, grinding and polishing steps). Finally, all cubes were ground by silicon carbide up to 2400grit grinding papers and polished in 3 steps using 6μm,3μm and 1μm diamond suspensions (Struers).

As illustrated by Fig. 1, the thermoelectric modules were assembles using silver (Ag) sheet (Sigma Aldrich) of 0.25 mm thick electrode on the hot side and Ag sheet (Sigma Aldrich) of 0.1 mm thick on the cold side. A layer of a conductive silver paste (Sigma Aldrich) was painted at the interface of the electrode-TE leg as bonding material both on the hot side and cold side. For module one, the n- and p-type unicouples were not metallized, while for module two the legs were metallized by 50 nm sputtered Au layer (on both the cold and hot side) using a turbomolecular pumped coater (Q150T, Quorum). Finally, on the hot and cold side alumina (Al_2O_3) sheet was utilized as an electric insulator (to avoid overload) between the heat source and heat sink.

2.2. Performance tests

The Performance and stability tests were conducted on a homemade rig, as shown in Fig. 2 equipped with a DC powered 100 W heater Inconel block (Dalton WattFlex, USA) on the hot side and a water-cooled copper block, with Minichiller 280 (Huber Kältenmaschinenbau AG, Germany) as an external cooler on the cold side. On the rig, one uni-couple is clamped, and pressure applied from top using two springs at both HMS and MGS sides, which respective temperatures are monitored by K-type thermocouples. The Seebeck (thermal) voltage and temperature are acquired using a National Instruments Data Acquisition Module (NI9210), and, the system is equipped with an electronic load form Array (3721A 80 V/40A 400 W), as a current load which also act as a Current-Voltage (IV) data acquisition system. All appliances are automatically controlled virtually via a LabVIEW control system. Skomedal thesis [20] has provided more details on the rig and experimental set-up.

The TE elements' performance is tested under isothermal (isothermal sections are shown in the full temperature program, supplementary S9) and thermal cycle conditions (following the temperature program shown on Fig. 2 above) under ambient conditions. The whole temperature program presented in the supplementary section S9, consists of one isothermal section recorded from 200 °C–400 °C with 50 °C step size and 3 thermocycle sections followed in the test as detailed on the table on the right-hand bottom corner with 3 h holding time per half cycle. The aging tests were recorded in the isothermal sections with 24 h retention time at each temperature on the hot side and the cold side fixed at 20 °C.

2.3. Post-characterization

After the long-term tests, further studies were conducted on the tested legs to investigate the effects of long-term operation on the legs under thermal stresses. The carried-out tests were the Seebeck coefficient and resistivity (where the homemade rigs was used), Vickers microhardness tests (using FutureTech FM-700 with a load of 200 g) and cross-section microstructure analysis (using a Field Emission Scanning Electron Microscope (FE-SEM) equipped with an Electron Dispersive Spectrometer (EDS) detector from JEOL (JSM-7200F)). Particularly, the electrode -TE leg contact regions (both n- and p-types) were the focus of the study. After disassembling the modules, the legs were clipped with metal clips (fixation clips from Struers) and hot mounted in a conductive resin (Polyfast from Struers). The resin cast legs were ground using a similar recipe as in section 2.1, and polished using polycrystalline diamond suspension up to 1μm (DP-Suspension, alcohol based

<0.5%water content – Struers). At the end of every grinding step and polishing step, the pellets (the hot mounted specimen) were cleaned in ethanol and dried using a low-pressure warm air by a hair drier.

3. Results

Performance and stability tests were conducted on two modules for over 25thermocycles in 200 h (on module 1) and over 300 thermocycles in 2200 h (on module 2). At the same time, the thermally generated open circuit voltage ($Voc_{(th)}$) was monitored along the stability tests. Fig. 3 a) and b) shows the $Voc_{(th)}$ plotted against the number of thermocycles in the temperature range of 200 °C–400 °C (module 2), where the $Voc_{(th)}$ is presented as separate reading at 200 °C and 400 °C. The uni-couple experienced 16.5% $Voc_{(th)}$ gradual decrease in the 200 °C–400 °C temperature range after more than 180cycles. Moreover, 115 thermocycles were run at 25 °C–400 °C temperature range, the thermal stress resulted in a reduction of 24.5% of the initial $Voc_{(th)}$ as also represented in supplementary results (S1). The reduction of the open circuit voltage, as reported by other research on HMS and MGS based modules [6] is mostly a result of the module inner resistance increase (with 20% contact resistance share) especially at the interface of the TEM and electrode. Unfortunately, the internal resistance was not measured in this study due to high contact resistance (12Ω initially), which lead to failure to record meaningful current–voltage (IV) data. To reduce the initial contact resistance, extra pressure was exercised on the unicouple, however the resistance could not be further decreased, due to the possibility of breakage of the brittle MGS leg (as it was sintered by hot press). At the end of the tests on module 2, the contact resistance had increased to more than double the initial value up to 26.76Ω, but this was mainly due to mechanical failure, especially on the n-type leg.

Fig. 4 a) and b) represents a cross section of the module one's MGS hot side and cold side interfaces, respectively, after 25 thermocycles from 200 to 400 °C. After the tests, the MGS leg-electrode had a more solid bond at the hot side than on the cold side. The SEM picture of the cross-section in Fig. 4 a) shows that the MGS had a better bond at the electrode-MGS interface, by the visible formation of an interdiffusion layer from diffusion of Sn from the TE alloy and In from the paste. However on the cold side the bond looks decent, though the Sn diffusion is not homogeneous along the interface as it can be noticed on Fig. 4 b). It is possible that the latter lack of homogeneity caused a solid bond in some regions but looser contacts in regions with more Ag. For further understanding, full composition/phase EDS maps can be consulted in the supplementary results on both the hot (supplementary S2) and cold side (supplementary S3) interfaces. It is, important to note (check the S2 and S3 supplementary) that the MGS leg had more physical damages (though anticipated) and oxidation along the grain boundaries which was the major cause of degradation.

In contrast to MGS, the HMS (module 1) contact regions on both hot and cold sides were mechanically weaker after 25cycles. Fig. 4 c) represents the hot side region of the HMS-Ag paste interface and the EDS compositional map (right hand side image) which the back scattered SEM image reveals a thin gap and a thin oxide layer at the interface, respectively. The observed gap is a result of weak adherence of the paste to HMS possibly due to lack of Ag wetting on the HMS surface, which would explain the weak mechanical properties of the bond. In addition, the Ag wetting on the cold side of the p-type leg was far worse than on the hot side (which makes sense). For post-analysis, the contact at the HMS-Ag cold side interface was non-existent which would be justified as an unbalance between the cohesive and adhesive force of the paste, or non-optimal cure conditions (between 140 °C and 150 °C for 30 to 60 min). More EDS analysis are posted in supplementary results (S4), where individual elements are mapped separately.

Fig. 5 shows the module 2, which differs from module 1 by an Au metallization layer of 50 nm to improve the electrical conductivity, increasing the bond wetting and acting as a diffusion barrier at the interface. Stability evaluation was conducted for over 300 thermocycles in 2200 h. On HMS, Fig. 5 a), it can be seen that the metallization layer improved the contact, more on the hot side (left hand side image) than on the cold side (right hand side image). The line scan through the cold side interface reveals a gap that sets the metallization material apart from the TE alloy, however no Au layer could be seen at or across the alloy. This is because at the cold side, the temperature was held at 20 °C and would rise to around 34 °C (as shown on the supplementary results S9) at higher temperatures; hence not enough to prompt diffusion on either side. Moreover, the EDS phase to element ratio and elemental maps (supplementary S5) reveals that at the TE alloy surface a silica oxide is formed at the interface. Though coated and covered by the Ag electrode, the gap at the interface had exposed the HMS surface to an oxidizing agent, where the oxide growth was an additional stress factor that inhibited any chance to bond over time. Similarly, Fig. 5 b) represents the MGS leg from Module 2, with the right and left hand side images representing the hot and cold side interfaces. Apparently, the contact at the hot side looks good, however the Au layer was not seen at the MGS-Ag interface, the main question is, where is the Au layer? The temperature at which the experiments were carried at was too low to melt Au, nevertheless Au has a higher affinity to Ag relative to any phases of the MGS alloy, therefore there is a high probability that Au may have diffused in the Ag paste, and was not detected by the EDS mapping or line scan due to the concentration being below the detection limit.

The cold side interfaces for both legs show poor contact on HMS and mechanical plastic degradation along the MGS-Ag paste interface, cracks were also observed all over the MGS leg. One of the major causes, especially on the electrode-leg interfaces, was the mismatch in coefficients of thermal expansion (CTE), between the components at the interface between the hot side and the legs. The estimated linear thermal expansion for Ag is 19.5 and for Au is 14.2 (μm/mK)) [21], while the estimates for CTEs of the TE legs were computed using a theoretical model for mixtures/alloys by Karunaratne et al. [17] as HMS is 7.89 (μm/mK)), a value which is in accordance to the value published on Mn_4Si_7 by [22] taking dopants under consideration, and MGS is 21.05 (μm/mK) by equation 1–1 using parameters shown in Table 1, the experimental result is nearly the same to the values reported on $Mg_{2.08}Si_{0.4-x}Sn_{0.6}Sb_x$ ($0 \leq x \leq 0.072$) by [23].

The Seebeck coefficient and the microhardness were measured on the legs with Au metallization. The Seebeck coefficient of HMS was found to be 517.5μv/K and that of MGS was +42.3μv/K. It was expected to have a negative Seebeck coefficient for MGS as an n-type semiconductor, but it also had positive regions of the leg. The inhomogeneity of n- and p-type layers in the MGS, at first thought had to be due to the diffusion of Ag and/or Gold in the alloy based on their electronic configurations ([Kr] $4d^{10}$ $5\,s^1$ and [Xe] 4f14 5d10 6 s1, respectively), but the EDS could not prove the presence of Ag or Au based phases in the MGS. However, diffusion of the Sn and Sb from the alloy mainly from the area close to the bonding interface, was the possible cause of the n- and p-type phases in the MGS leg. Furthermore, the Vickers microhardness tests were measured on both metallized legs before and after tests. The microhardness was found to be 556HV and 1000HV before the tests on the n-type leg and p-type legs, respectively. In comparison to the values obtained after the stability tests (322 ± 39HV and

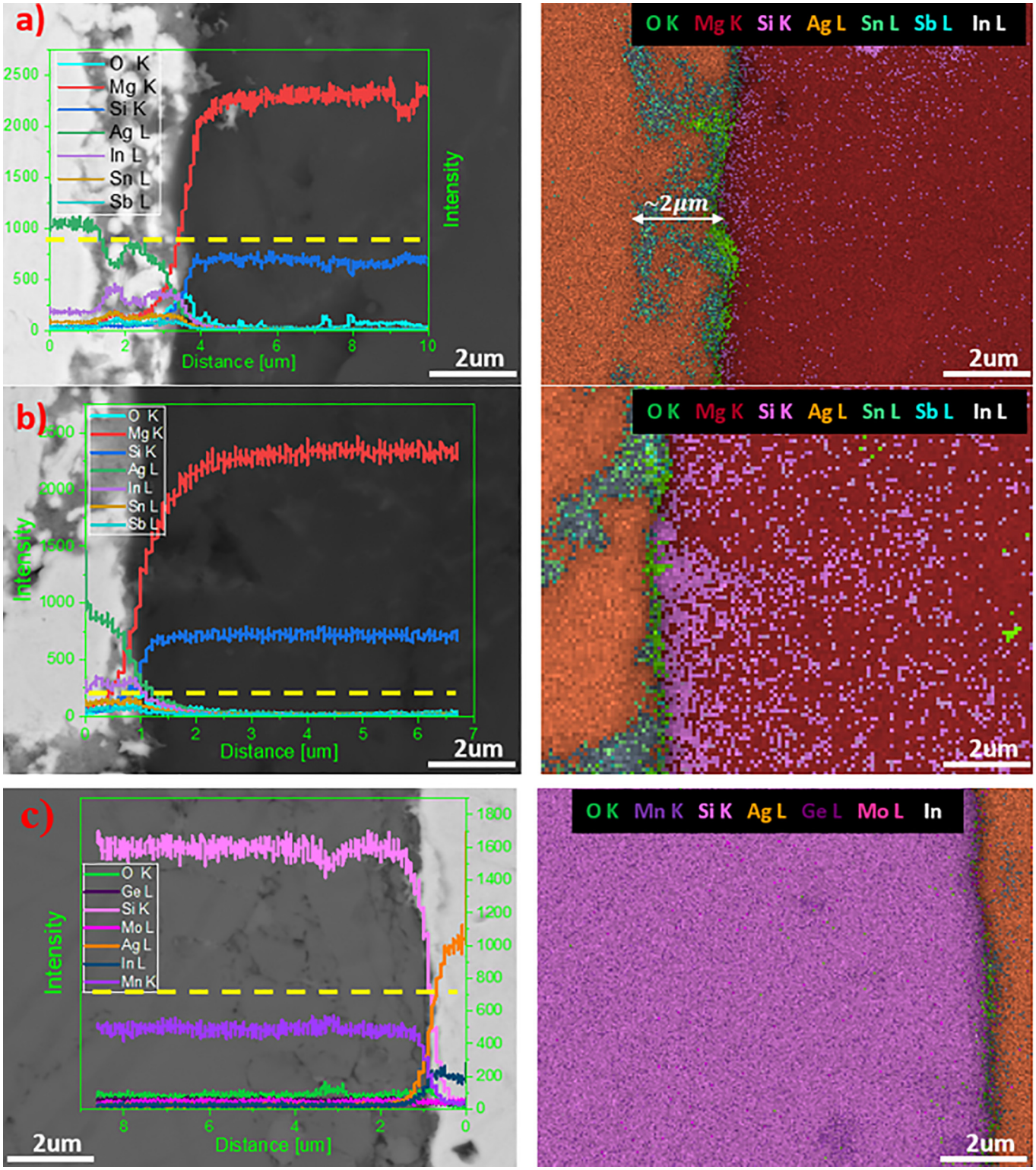

Fig. 4. SEM-EDS line scan and element overlay map of the Ag paste-TE legs (module 1) interfaces, visualized from cross-sections after 25cycles a) MGS-Ag cross-section, where clearly 2 μm visible interdiffusion layer was formed mainly composed of Ag, In, Sn, and Mg corresponding to 34 wt%, 22 wt%, 9 wt%, and 9 wt%, respectively; b) MGS-Ag interface (module 1) at the cold side, where no reaction layer was formed, c) the p-type TE leg (HMS) in module 1, which only a thin layer of silica can be noticed at the interface.

920 ± 37HV, respectively), the MGS experiences 42% reduction, while the HMS was not mechanically affected, and this was confirmed by the back scattered electrons images on SEM.

To summarize, module 1 and module 2 were comparatively discussed, mainly based on the post-stability tests. On both modules the MGS legs (non-metalized and metalized) degraded considerably. As discussed in the previous paragraph, the CTE mismatch may have played a role in the degradation, however the density/-porosity of the MGS legs also facilitated and promoted oxidation of the legs. Based on the second module the metallization reduced

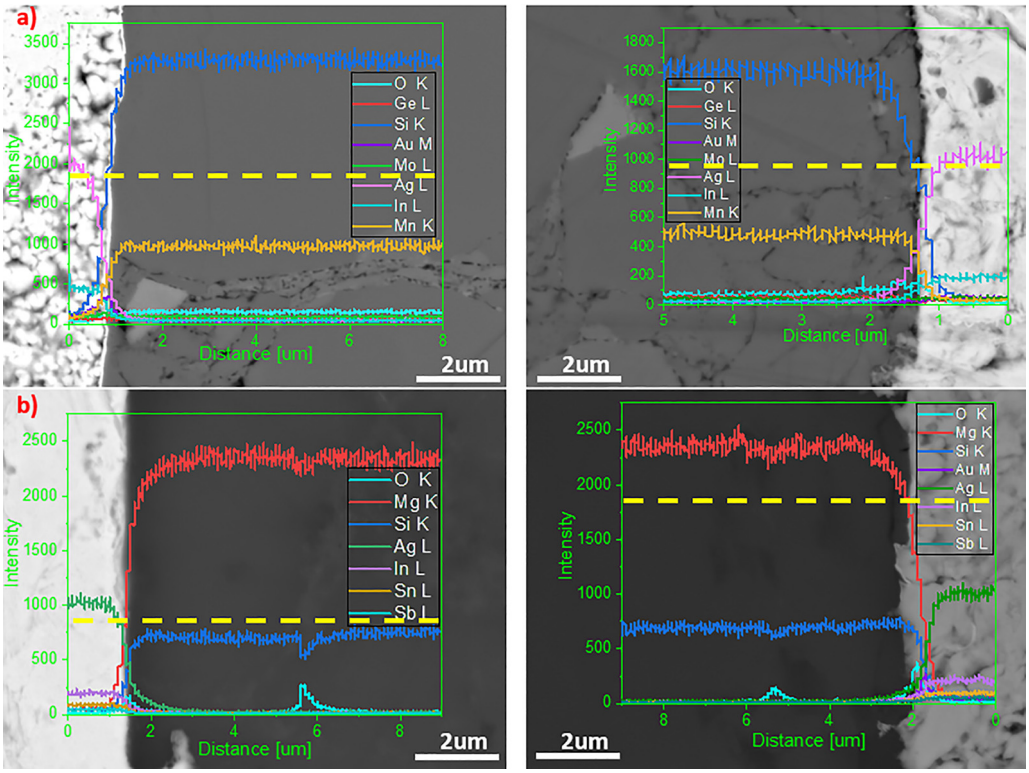

Fig. 5. SEM-EDS representation of the module 2, HMS and MGS legs after more than 300cycles: a) A line scan across the Ag paste -HMS interface at the hot side of the module. The SEM back scattered image shows a long bright strip of Au and a homogeneous Ag paste on the left surface and an unreacted HMS on the left-hand side is the cold side of HMS which shows poor contact and no metallization layer. b) EDS line scan analysis across the hot and cold side of the MGS leg revealing that no Au was still present at the hot side region, though present at the cold side.

Table 1
The parameters used to approximate the CTE of the MGS and HMS alloys.

Phases	$Mg_{2.05}Sn_{0.5}Si_{0.485}Sb_{0.015}$			$Mn_{0.98}Mo_{0.02}Si_{1.73}Ge_{0.02}$				CTE [um/mK]
	wt%	Density [g/cm^3]	CTE [um/mK]	wt%	Density [g/cm^3]	CTE [um/mK]	Ref.	
Mg	43	1.74	25	–	–	–		**21.05**
Si	14	2.32	3	–	–	–	[21]	
Sn	42	7.31	23.4	–	–	–		
Sb	1.4	6.68	10.4	–	–	–		
Mn	–	–	–	51.148	7.43	22		**7.89**
Mo	–	–	–	1.805	10.28	5	[21]	
Si	–	–	–	45.682	2.32	3		
Ge	–	–	–	1.366	5.323	6.1		

diffusion of Sn and Sb as no interdiffusion layer was noticed after more than 2000 h, however the leg still showed mechanical degradation and mixed phases of n- and p-type regions. Meanwhile the HMS legs were mechanically robust. The main drawback was the bonding technique, the legs were expected to form the bond at the beginning of the tests and the method worked for the hot side, though the cold side was badly affected by very low temperatures. The lack of good contact led to oxidation of the TE legs surfaces which weakened the interfaces hindered the bonding possibility. The current research did not examine the extent of oxidation of the MGS (it was discussed based on Skomedal et al. [24] study), but oxidation is believed to be one of the major contributors to degradation of the TE material.

4. Discussion

The Ag bonding material on the non-metalized module (module 1) did not withstand the thermal stresses it was subjected to. This was mainly caused by the wetting of the bonding material and/or the CTE mismatch at the bonding area. The source of less adherence was mainly due to bonding surface oxidation preventing any possible contact between the bonding surface and bonding material. MgO was the main oxide species formed on MGS and SiO_2 (quartz) on HMS; These oxides inhibited the wetting of the bonding material, creating stress related to CTE mismatch (with CTEs, MgO = $10.8 \times 10^{-6}\,K^{-1}$ [25,26]and $SiO_2 = 12.38 \times 10^{-6}\,K^{-1}$ [27]). As discussed in section 3 and represented by EDS map in the supplementary S2, a 2μm layer of Mg-Ag-In-Sn-Sb-O with a 70% In-Sn-Sb rich phase can be seen on the hot side, the CTE of the intermetallic layer formed at the interface ranges between 21 and $22.5 \times 10^{-6}\,K^{-1}$ approximated based on CTEs of alloys published by [28]. It matches well with the CTE of both the silver paste and the TE alloy. However, there has been lack of control of diffusion which could predominantly lead to reducing the CTE in the case of presence of silicon rich phases close to the interface. Similarly, based on the supplementary S3, the cold side followed a similar process trend, though slowly due to temperature difference relative to the hot side. Lastly, both supplementary S2 and S3 show oxide phases across the MGS leg, most of the oxidation is along

cracks and grain boundaries which led to plastic deformation presumably during thermal cycles.

Conversely, with the metallized unicouple subjected to over 300 thermal cycles, the thermal stress after 2200 h had improved electrode-TE leg interface strength both for HMS and MGS. The contact at the hot side of the Au-HMS interface was improved by the increased wettability by Au, though the bond was not mechanically solid, which was caused by lack of intermetallic layer formation between Au, Ag, and HMS. With MGS, the Au metallization slowed down diffusion relative to the module 1 at the hot side of MGS leg interface and had a stronger mechanical bond than HMS. However, the Au layer could not be visualized at the interface as revealed by the SEM images. The disappearance of the Au layer may have been caused by the fact that the MGS leg degraded catastrophically, as it presented deep cracks all over the surface. It is believed that poor mechanical stability was due to the initial consolidation effect on MGS legs. Initially the MGS legs were consolidated by hot press (HP) techniques and was more porous than the SPS compacted HMS, which led to oxidation more on the grain boundaries and ensuing high mechanical degradation. Consolidation by SPS would be much recommended to reduce porosity and increase hardness of the TEM, additionally, based on the HMS hot side bond, it could be seen that the Au wets best at temperature higher than room temperatures for silicides.

The main outcome has been that that the bonding material fits well with the n-type TE material, but not as good with the p-type due to the CTEs mismatch between the two materials. Moreover, it would be better to apply relatively high temperature bonding as is possible with Solid-Liquid interdiffusion (SLID) bonding methods [29] or plasma bonding of the electrodes prior to mounting the stability experiments. The latter would increase mechanical strengths of the bond prior to subjecting the unicouples to mechanical and thermal stresses. On the other hand, it is recommended that the MGS requires consolidation by SPS as hot pressing promotes oxidation of the legs, due to high porosity and brittleness of the legs exposed to thermal stresses.

5. Conclusion

The current study investigated the performance and stability of HMS and MGS based uni-couples with similar electrodes (Ag) and bonding material (Ag) on both hot and cold sides, though distinct from the metallization (Au) on one of the modules. After the stability tests, the HMS legs endured mechanical stress and had improved contact interface with Au metallization relative to the Ag paste alone. However, the MGS leg – module 1, had formed a solid bond with the Ag paste with a reaction layer of 2 μm on the hot side made of Ag-In-Sn ternary phase. The contrary was observed on MGS – module 2; there was no reaction layer observed, but this could have been the difference in exposure time between both modules. Moreover, all MGS legs (module 1 and 2) endured mechanical damages (cracks), which were related to the porosity of the hot-pressed MGS bulk material that promoted oxidation and led to plastic deformation. This work recommends further studies to investigate a combination with SPS consolidated MGS, and finally to find a better bonding material for the HMS with matching CTE.

CRediT authorship contribution statement

Antoine de Padoue Shyikira: Data curation, Conceptualization, Methodology, Investigation, Writing - original draft, Writing - review & editing. **Gustein Skomedal:** Methodology, Supervision, Writing - review & editing. **Peter Hugh Middleton:** Supervision, Writing - review & editing.

Declaration of Competing Interest

The authors declare that they have no known competing financial interests or personal relationships that could have appeared to influence the work reported in this paper.

Acknowledgements

The author would like to acknowledge all partners: Elkem ASA, Sintef, and the University of Oslo (UiO) in TESil project, for their help form material synthesis, pellet consolidation and transport properties tests. We acknowledge financial support from the Research Council of Norway (Project No 269326)

Appendix A. Supplementary data

Supplementary data to this article can be found online at https://doi.org/10.1016/j.matpr.2020.05.193.

References

[1] N. Farahi, C. Stiewe, D.Y.N. Truong, J. de Boor, E. Muller, High efficiency Mg2(Si, Sn)-based thermoelectric materials: scale-up synthesis, functional homogeneity, and thermal stability, RSC Adv. 9 (40) (2019) 22772–23424.
[2] "Lumen learning geology," Lumen, [Online]. Available: https://courses.lumenlearning.com/geology/chapter/reading-abundance-of-elements-in-earths-crust/. [Accessed 30 03 2020].
[3] A. Nozari, P. Norouzzadef, F. Suarez, D. Vashaee, Thermoelectric silicides: a review, Japanese J. Appl. Phys. 56 (May 2017) (2017) 1–27.
[4] A.A. Ivanova, L.D. Baikov, Higher manganese silicide based materials, J. Thermoelectricity 3 (2009) 60–66.
[5] D.M. Row, CRC Handbook of Thermoelectrics, CRC Press, New York, 1995.
[6] G. Skomedal, L. Holmgren, H. Middleton, I.S. Eremin, G.N. Isachenko, M. Jaegle, K. Tarantik, N. Vlachos, M. Manoli, T. Kyratsi, D. Berthebaud, N.Y.D. Truong, F. Gascoin, Design, assembly and characterization of silicide-based thermoelectric modules, Energy Conversion Manage. 110 (2016) 13–21.
[7] H.S. Kim, K. Kikuchib, T. Itoh, T. Iida, M. Tayaa, Design of segmented thermoelectric generator based on cost-effective and light-weight thermoelectric alloys, Mater. Sci. Eng. B 185 (2014) 45–52.
[8] T.P. Generator, Thermoelectric Generator Power Bulk Materials BiTe, PbTe, TEG, [Online]. Available: http://tecteg.com/wp-content/uploads/2015/03/Table-Consisting-of-Various-Thermoelectric-Materials-Researched-for-Power-Generation.pdf. [Accessed 07 12 2017].
[9] T. Nakamura, K. Hatakeyama, M. Minowa, Y. Mito, K. Arai, T. Iida, K. Nishio, Power-generation performance of a pi-structured thermoelectric module containing Mg2Si and MnSi1.73, J. Elec. Mater. 44 (10) (2015) 3592–3597.
[10] J. de Boor, D. Droste, C. Schneider, J. Janek, E. Mueller, Thermal stability of magnesium silicide/nickel contacts, J. Electron. Mater. 45 (10) (2016) 5313–5320.
[11] H. Kaibe, I. Aoyama, M. Mukoujima, T. Kanda, S. Fujimoto, T. Kurosawa, H. Ishimabushi, K. Ishida, L. Rauscher, Y. Hata, S. Sano, Development of thermoelectric generating stacked modules aiming for 15% of conversion efficiency, 24th International Conference on Thermoelectrics, New York, 2005.
[12] N.H. Pham, N. Farahi, H. Kamila, A. Sankhla, S. Ayachi, E. Müller, J. De-Boor, Ni and Ag electrodes for magnesium silicide based thermoelectric generators, Mater. Today Energy 11 (2019) 97–105.
[13] T. Nemoto, T. Iida, J. Sato, T. Sakamoto, T. Nakajima, Y. Takanashi, Power generation characteristics of Mg2Si uni-leg thermoelectric generator, J. Elec. Mater. 41 (6) (2012) 1312–1316.
[14] T. Nemoto, T. Iida, J. Sato, T. Sakamoto, N. Hirayama, T. Nakajima, Y. Takanashi, Development of an Mg2Si Unileg thermoelectric module using durable Sb-doped Mg2Si Legs, J. Electron. Mater. 42 (7) (2013) 2192–2198.
[15] K. Mitra, S. Mahapatra, T. Dasgupta, Fabrication of nickel contacts for Mg2Si based thermoelectric generators via an induction assisted rapid monoblock sintering technique, J. Elec. Mater. 48 (3) (2019) 1754–1757.
[16] W. Liu, S. Bai, Thermoelectric interface materials: A perspective to the challenge of thermoelectric power generation module, J. Materiomics, vol. Article in Press, 2019.
[17] M.S.A. Karunaratne, S. Kyaw, A. Jones, R. Morrell, R.C. Thomson, Modelling the coefficient of thermal expansion (CTE) in MCrAlY bond coatings and Ni based superalloys, J. Mater. Sci. 51 (2016) 4213–4226.
[18] Weishu Liu, Shengqiang Bai, Thermoelectric interface materials: a perspective to the challenge of thermoelectric power generation module, J. Materiomics (2019), https://doi.org/10.1016/j.jmat.2019.04.004.
[19] D.G. Cahill, P.V. Braun, G. Chen, D.R. Clarke, S. Fan, K.E. Goodson, P. Keblinski, W.P. King, G.D. Mahan, A. Majumdar, H.J. Maris, S.R. Phillpot, E. Pop, L. Shi, Nanoscale thermal transport. II, 2003-2012, Appl. Phys. Rev., 1, 011305 (2014); https://doi.org/10.1063/1.4832615, pp. 1-45, 2014.

[20] G. Skomedal, Thermal durability of novel thermoelectric materials for waste heat recovery, The University of Agder - http://hdl.handle.net/11250/2391043, Grimstad-Norway, 2016.
[21] S. MSE, List of Thermal Expansion Coefficients (CTE) for Natural and Engineered Materials, MSE Supplies, 05 09 2019. [Online]. Available: https://www.msesupplies.com/pages/list-of-thermal-expansion-coefficients-cte-for-natural-and-engineered-materials. [Accessed 03 10 2019].
[22] A. Allam, P. Boulet, M.C. Record, Linear thermal expansion coefficients of higher manganese silicide compounds, Phys. Procedia 55 (2014).
[23] P. Gao, I. Berkun, R.D. Schmidt, M.F. Luzenski, X. Lu, P.B. Sarac, E.D. Case, T.P. Hogan, J. Elec. Mater. (2013).
[24] G. Skomedal, A. Burkov, A. Samunin, R. Haugsrud, H. Middleton, High temperature oxidation of Mg2(Si-Sn), Corros. Sci. 111 (2016) 325–333.
[25] Crystran, "Magnesium Oxide (MgO),", Online Available: https://www.crystran.co.uk/optical-materials/magnesium-oxide-mgo 2012 Accessed 18 03 2020.
[26] M.A.S. Rao, K. Narender, Studies on Thermophysical Properties of CaO and MgO by gamma-ray attenuation, J. Thermodyn. 2014 (2014) 1–8.
[27] A. Materials, "Silica - Silicond dioxide," 13 03 2001. [Online]. Available: https://www.azom.com/properties.aspx?ArticleID=1114. [Accessed 18 03 2020].
[28] T. Gancarz, P. Fima, J. Pstrus, Thermal expansion, electrical resistivity, and spreading area of Sn-Zn-In alloys, J. Mater. Eng. Perform. 23 (5) (2014) 1524–1529.
[29] T.A. Tollefsen, A. Larsson, O.M. Løvvik, K. Aasmundtveit, Au-Sn SLID bonding - properties and possibilities, Metal. Mater. Trans. B 43B (2012) 397–405.

Available online at www.sciencedirect.com

ScienceDirect

materialstoday: PROCEEDINGS

Supplementary (S) results

The supplementary results **(figure S1)**, shows the $Voc_{(th)}$ on module 2 in three thermal cycle regions recorded at 200^0C. As mentioned in the main manuscript, the recoded Seebeck voltage does not change at high temperatures (400^0C). However, thermal cycles between 25-400^0C, showed very large loss due to the temperature gap which was 24.5% and with the 200-400^0C the loss was 16.5%.

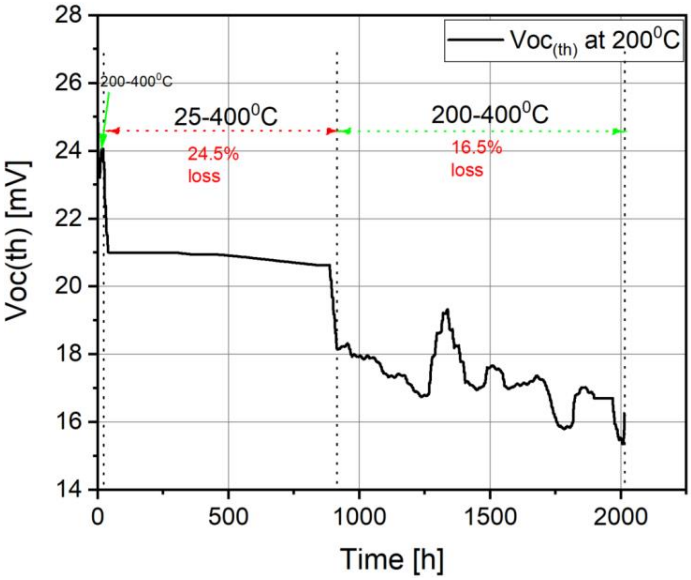

S1. Seebeck effect voltage recorded at 2000C for the whole test period

SEM – EDS Maps

The maps represented by **S2 – S8** supplementary results, provide more information on the state of the legs disassembled from module 1 and module 2. Moreover, they all show the interface after the tests and are comprised of back scattered image, elemental overlay map or element to phase ratio map, a line scan through the contact area interface, and specific individual element maps, respectively.

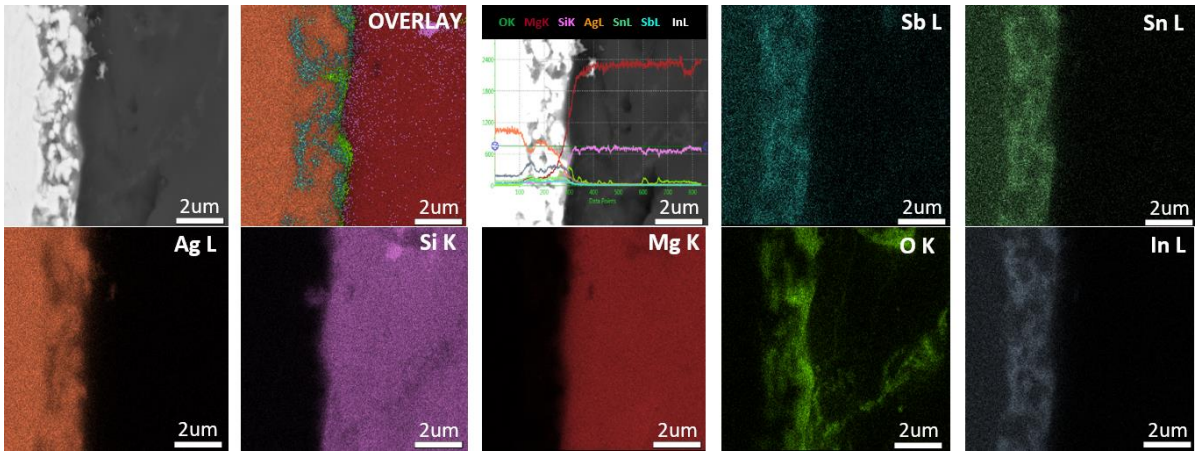

S2. EDS map of the non-metallized MGS cross section, showing the electrode-MGS interface at the hot side

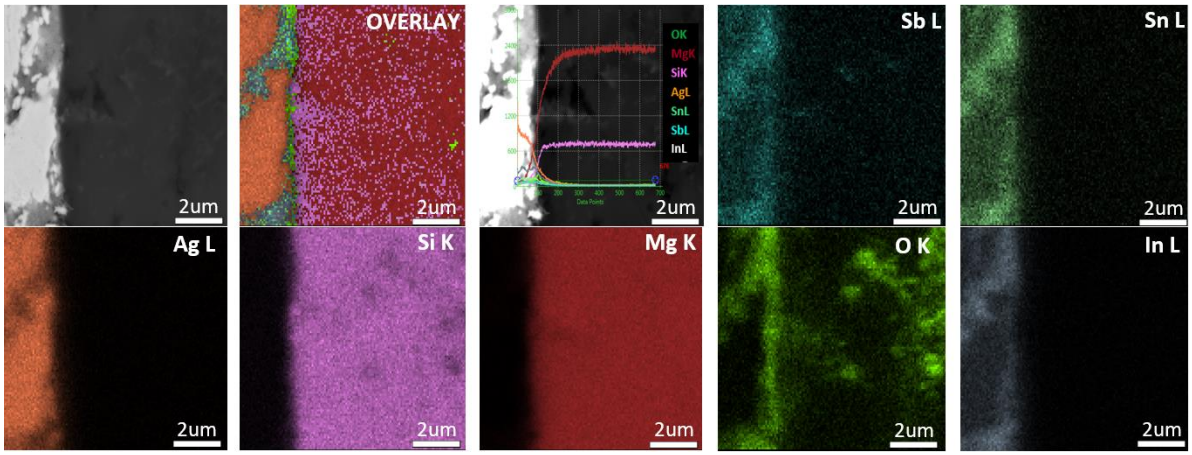

S3.EDS map of the non-metallized MGS cross section, showing the electrode-MGS interface at the cold side

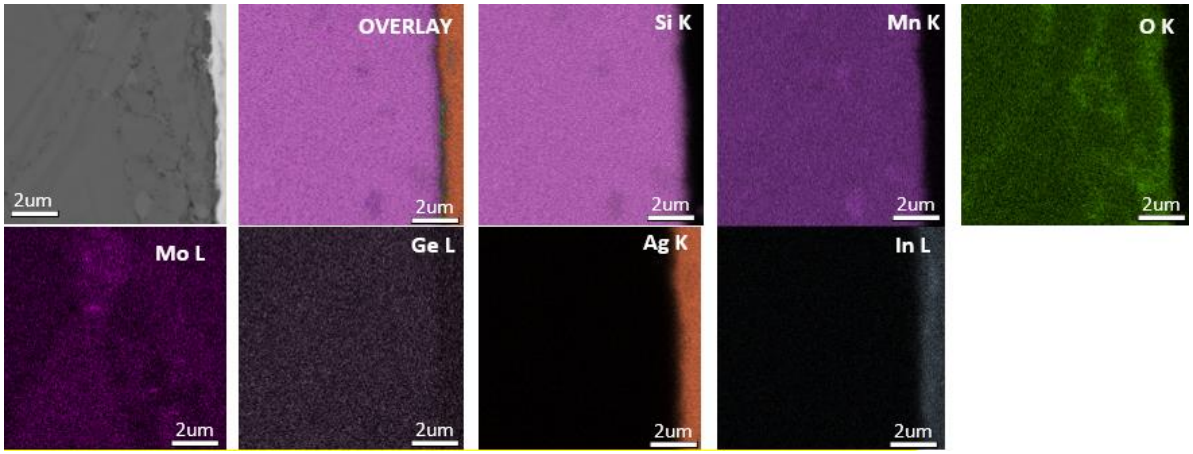

S4. EDS map of the non-metallized HMS cross section, showing the electrode-HMS interface at the hot side

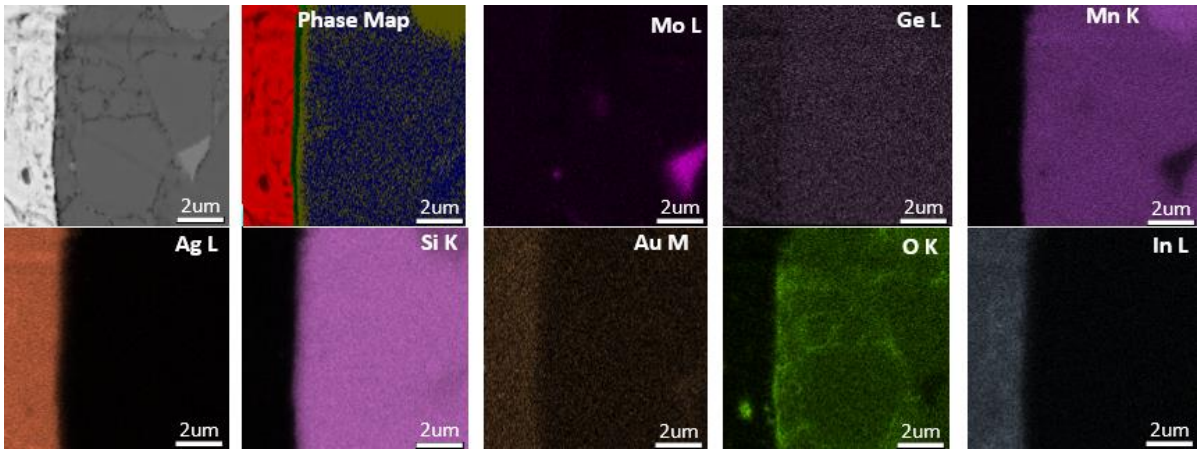

S5.EDS map of Au metallized HMS cross section, showing the electrode-HMS interface at the cold side

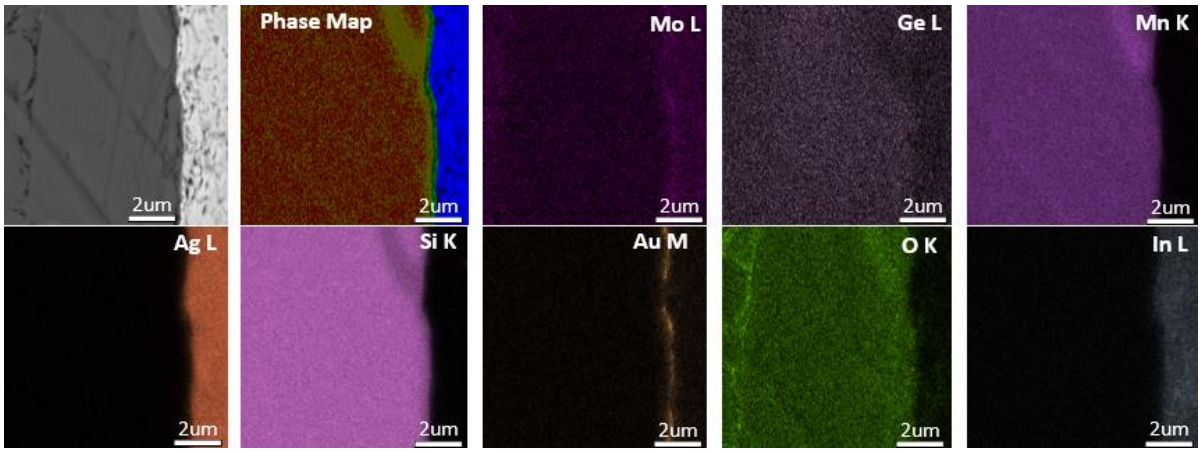

S6.EDS map of Au metallized HMS cross section, showing the electrode-HMS interface at the hot side

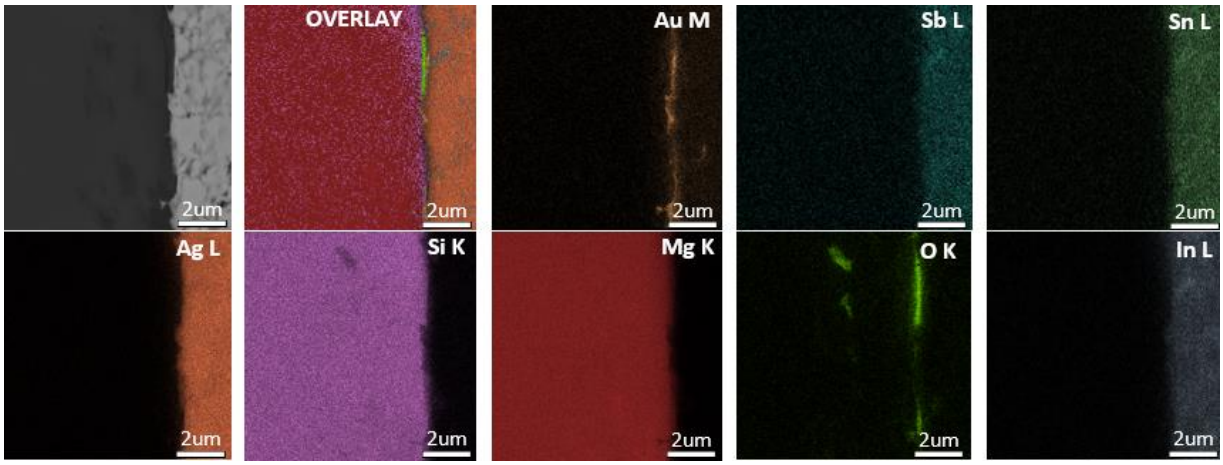

S7.EDS map of Au metallized MGS cross section, showing the electrode-MGS interface at the cold side

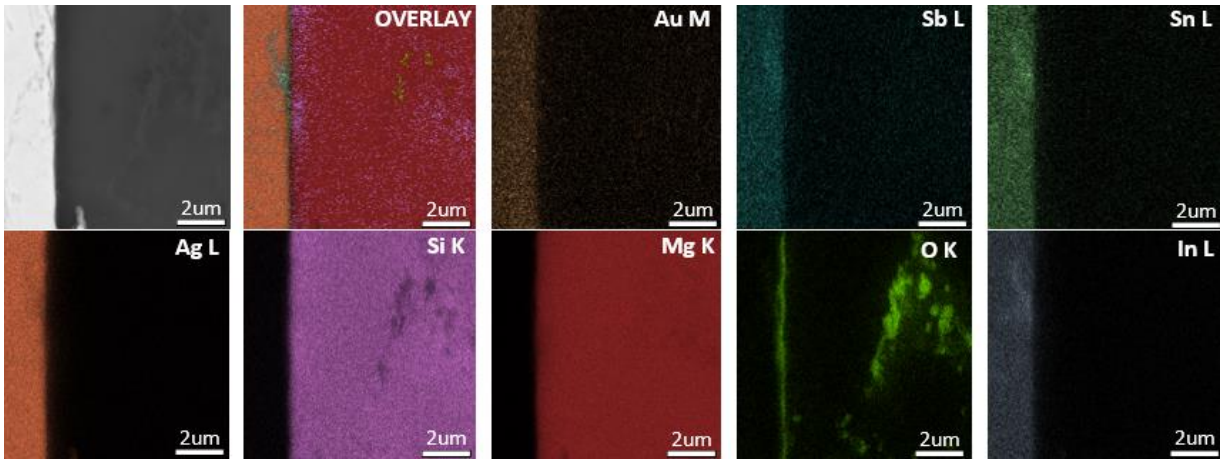

S8.EDS map of the metallized MGS cross section, showing the electrode-MGS interface at the hot side

Full temperature program

Finally, the supplementary S9, represents the full temperature program for the module two test, and also represent the module one though with reduced thermal cycles.

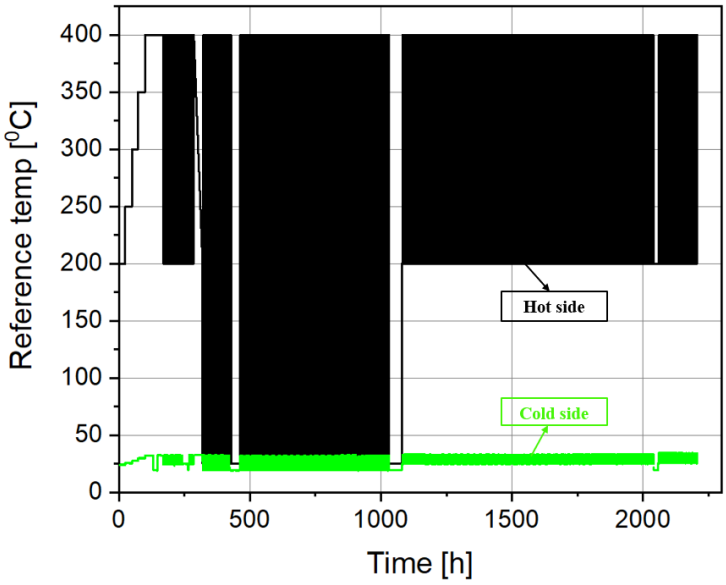

S9. Full temperature program on the hot side(black) and cold side (light green), run on module 2

Paper II

High temperature oxidation of higher manganese silicides

Authors: **Antoine de Padoue Shyikira**, Naureen Akhtar, Gunstein Skomedal, Tor Oskar Sætre, Peter Hugh Middleton

Corrosion Science 185 (2021) 109327

Contents lists available at ScienceDirect

Corrosion Science

journal homepage: www.elsevier.com/locate/corsci

High temperature oxidation of higher manganese silicides

Antoine de Padoue Shyikira [a,*], Naureen Akhtar [a], Gunstein Skomedal [a,b], Tor Oskar Sætre [a], Peter Hugh Middleton [a]

[a] University of Agder, Norway
[b] Elkem ASA –Kristiansand, Norway

ARTICLE INFO

Keywords:
Higher manganese silicides
High temperature corrosion
Selective oxidation
Silicide thermoelectric materials
Microstructures

ABSTRACT

The oxidation kinetics and mechanisms of higher manganese silicides (HMS) $MnSi_{1.75}$, $MnSi_{(1.75-x)}Ge_x$, $MnSi_{(1.75-x)}Al_x$ (with x = 0.005 and 0.01)were studied and the effects of densification methods and dopant concentration discussed. Oxidation experiments were conducted using thermogravimetry (TGA), while post characterization with X-ray Photoelectron Spectroscopy (XPS) and Scanning Electron Microscope (SEM) showed that spark plasma sintering (SPS) is a better densification method than hot pressing (HP). Except for undoped HMS, HMS doped with 0.5at% Ge had the lowest oxidation rate. Stable formation of a SiO_2 protective layer was the main reason for improved oxidation resistance in air in the temperature range 200 °C–500 °C.

1. Introduction

Stochiometric $MnSi_x$ (with $1.71 \leq x \leq 1.75$) alloys [1,2] are among the most promising p-type silicide thermal electric materials. The interest stems mainly from the relatively high abundance of the main constituent elements (with Si 2nd and Mn 12th), low cost, mechanical and chemical stability, low toxicity, and ease of production [3]. However, pure HMS has a relatively low thermoelectric figure of merit (zT), ranging from 0.3−0.5 at temperatures below 500 °C [3,4]. For decades, researchers have been working to improve the zT values by optimizing the electrical transport properties and decreasing the lattice thermal conductivity [5]. In particular Biernert and Gillen [6], a decent improvement has been reached through optimization of synthesis and consolidation parameters [7,8], Nanostructuring [2,9], phase engineering, and electronic engineering.

Among HMS dopants candidates, aluminium (Al) [10], and germanium (Ge) [11,12] have been reported as the most effective substitutes of Si on the silicon site. Dharmaiah et al. [13] reported a thermal conductivity decrease by 25 %, with Ge as a substitution on the Si site ($MnSi_{1.75-x}$ Ge_x), which attributed to increased phonon scattering by pores and voids, and the figure of merit (zT) increased up to 0.6 [12] and 0.62 at 560 °C [14]. Moreover, Luo et al. [10] studied the $MnSi_{1.80-x}Al_x$ alloys with $0 \leq x \leq 0.009$, where an optimal and increased charge carrier concentration was observed at x = 0,0015 with 0.65 (zT) at 527 °C. However, adding impurities can make the alloy more prone to oxidation [15] or oxidation resistant [16,17].

Along with improving the thermoelectric properties of HMS alloys, a parallel oxidation study is important while designing the thermoelectric material. $MnSi_x$ are relatively stable up to 600 °C in oxidative atmospheres [18], however doping or alloying with reactive elements, causes the oxidation state to vary with the dopant type and concentration [19]. Few HMS oxidation studies have been carried out at temperatures above 1000 °C, and even fewer below 600 °C. Ning et al. [20], studied the oxidation of uncoated and glass ceramic coated $MnSi_{1.74}$ at 600 °C for 500 h in air. The uncoated samples grew a SiO_2 layer of 5 μm with a Si depleted region (MnSi) of the same thickness and the same trend was observed by Funahashi et al. [21], although they had carried out their tests for a short period of 10 h. Likewise, they also observed that their uncoated sample showed a decrease in the Seebeck coefficient as well as a decrease in the electronic conductivity both of which implied a lower power factor compared to "as-sintered" samples. However, coated samples showed resistance to oxidation and retained the same power factor after heat treatment.

Similarly, M. Salvo et al. [22], studied the thermal oxidation of HMS and included thermal cycling in their testing procedures comprising of 10 cycles with 1 h dwell time from ambient to 600 °C in air. With XRD they observed Mn_2O_3 and some SiO_2(cristobalite)in the sub-surface. Si has a high affinity to oxygen relative to Mn, however the silicon concentration in the depleted region at the alloy-oxide may reach a minimum, thus Mn contributes to the oxide formation. This was discussed by

* Corresponding author.
E-mail addresses: tonnydepadoue15@gmail.com, antoine.d.shyikira@uia.no (A.P. Shyikira).

https://doi.org/10.1016/j.corsci.2021.109327
Received 21 September 2020; Received in revised form 12 February 2021; Accepted 13 February 2021
Available online 18 February 2021

X. j.Liu et al. [23] regarding the oxidation of Fe-Si alloys, where they revealed the effect of the silicon content and temperature on oxidation of Fe-Si and confirmed Wagner's theory of oxide structure between two oxidation-prone elements.

For further and better understanding of the oxidation robustness of HMS and its alloys, thermal oxidation of $MnSi_{1.75-\alpha}X_\alpha$ (X: Ge or Al) alloys was studied in the intermediate (300 °C −500 °C) and high (600 °C) temperature ranges. This study mainly discusses the effect of temperature, optimal dopant concentration, and consolidation methods on oxidation of the investigated compounds. Moreover, the dopants being reactive to oxygen, the so-called "third element effect" [24] is discussed based on SiO_2 – GeO_2/Al_2O_3 oxides coexistence.

2. Experimental

2.1. Material and bulk specimen preparation

HMS alloys synthesized from different compositions of Silicon and Manganese, doped with Al and Ge at the silicon site (see Table 2 for nominal composition) were synthesized by Elkem ASA [25]. The raw materials were mixed, melted in an induction furnace under argon atmosphere, and then cast in a graphite mould. The ingots were crushed, and ball milled down to micron-sized powder, using a Herzog HSM 100 vibratory mill. Sample pellets were then made from the powder and sintered by Spark Plasma Sintering (SPS) (Dr. Sinter, SPS-825 – NTNU-Trondheim) and conventional Hot Pressing (HP) (homemade vertical HP – University of Oslo) to produce 30−36 mm diameter x5 mm discs. These were cut to size (1 × 3 × 4 [mm]) with a diamond cut-off wheel (Struers), mechanically ground and polished using SiC paper (up to 2400grit paper), and diamond suspensions (from 9 μm to 1 μm), respectively. Finally, the samples were ultrasonically cleaned in acetone for 3 min and rinsed in acetone before carrying out the analytical work.

2.2. Thermal treatment

The thermal oxidation experiments were conducted using a thermogravimetric analyzer (TGA/DSC 1, Mettler Toledo) in both ambient air and dry air. The powder samples (before densification) were put in 150 μL alumina crucibles for iso-conversion tests from 25−1000 °C, with 5 °C/min constant heating rate, and 50 mL/min reaction gas purging rate. For isothermal experiments, the pressed discs of HMS were heat-treated at 300 °C, 350 °C, 400 °C, 450 °C/500 °C, and 600 °C for 15 h/24 h, 72 h, and 200 h.

2.3. Characterization and micro-structure

2.3.1. Oxidation kinetics

To determine the kinetic behaviour, the empirical model derived by Pilling and Bedworth was used, in which the experimental weight gain per unit area of the sample is plotted against time during a constant heating rate supplied to the apparatus (Eq. (1)) [26]. From this analysis, the parabolic oxidation rate can be determined.

$$\frac{\left(m_{oxide}/A\right)^n}{t} = k_p \tag{1}$$

Where: m_{oxide} - stand for the mass of oxide, A – the surface area of the specimen, t – time, and k_p is the oxidation rate. Similarly, following the Arrhenius oxidation model [27,28], the relationship between the oxidation rate and the temperature is expressed by Eq. 2 which enables the sample oxidation activation energy (E_p) to be calculated (see Fig. A3).

$$k_p = k_0 e^{\left(-E_p/RT\right)} \tag{2}$$

Where: k_0 – is the pre-exponential factor; R and T: the gas constant and temperature, respectively; and E_p – is the oxidation activation energy. Finally, the oxide thickness (x_{oxide}) is approximated by Eq. 3, where ρ_{oxide} represent the oxide density (with SiO_2 assumed to be the sole oxide).

$$x_{oxide} = \frac{m_{oxide}/A}{\rho_{oxide}} \tag{3}$$

2.3.2. Composition

The residues of the oxidized powder samples were experimentally characterized by X-ray photoelectron spectroscopy (XPS). The data were collected with a Kratos Axis Ultra^{DLD} spectrometer using a monochromatic Al KαX-ray source (1486.6 eV) operated at 10 A and 15 kV. Pass-energies of 160 eV and 40 eV were used for the survey spectra and the detailed core-level spectra, respectively. The energy step sizes of 1 eV and 0.1 eV were chosen for the survey and the detailed core-level spectra, respectively. Binding energies were referenced to the C 1s photoemission peak centred at 284.8 eV for adventitious carbon absorbed on the sample surface. A detailed analysis of the XPS data was

Table 1
Overview of all raw materials feedstock used in synthesis (wt%).

	ESS	Silgrain HQ	Mn	LC-SiMn
Source	REC Solar	Elkem	Alfa Aeser	Eramet
Shape	~1 mm powder	0.2−0.8 mm powder	1−10 mm flakes	
Si	>99.999	>99.8	1.3	29.47
Mn	–	–	>98.5	59.25
Fe	<0.0001	0.04	–	10.55
Al	<0.0001	0.09	–	–
Ti	<0.0001	0.001	–	0.293
Ca	<0.001		–	0.005
P	<0.0001	0.002	–	0.096
B	<0.0001	0.003	–	–
C	–	–	0.007	0.036
Cr + Co + Ni + Cu				~0.2

Table 2
List of samples ID, nominal composition, and synthesis routes.

Sample ID	Nominal composition	Synthesis
HMS_a	$MnSi_{1.75}$	α, σ, τ
HMS_b	$MnSi_{1.75}$	α
HMS_c	$MnSi_{1.75}$	γ
Ge0.5_c	$MnSi_{1.745}Ge_{0.005}$	γ, σ
Ge1_c	$MnSi_{1.74}Ge_{0.01}$	γ
Al0.5_c	$Mn_{0.99}Si_{1.745}Al_{0.005}$	γ
Al1_c	$Mn_{0.99}Si_{1.74}Al_{0.01}$	γ
Ge0.5_b	$MnSi_{1.745}Ge_{0.005}$	α, τ
Ge1_b	$MnSi_{1.74}Ge_{0.01}$	α, σ
Al0.5_b	$Mn_{0.99}Si_{1.745}Al_{0.005}$	α, τ
Al1_b	$Mn_{0.99}Si_{1.74}Al_{0.01}$	α

α: Melting (1450 °C) + casting; **γ:** Melting (1600 °C) + casting; **σ:** hot pressing (850 and/or 950 °C); **τ:** SPS (850 °C).

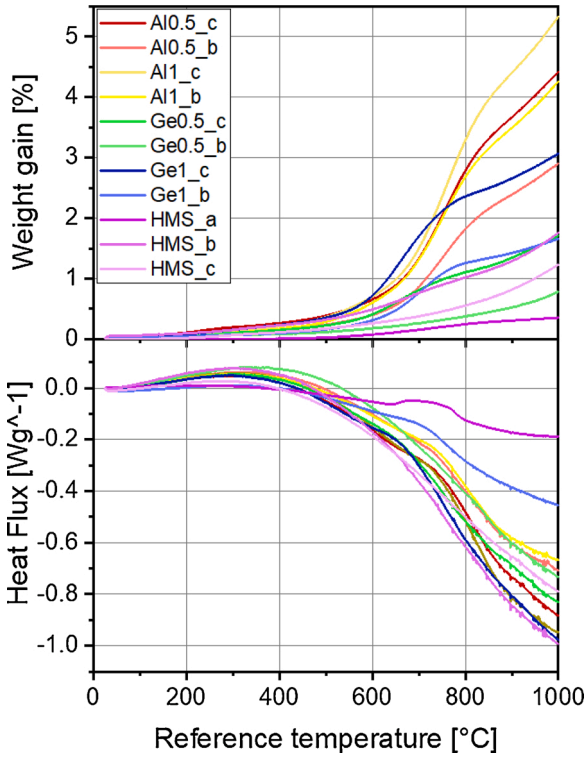

Fig. 1. Top: Thermogravimetric weight change of HMS alloys (powder samples) oxidized in air from 25 °C -1000 °C by TGA/DSC 1, Bottom: Differential scanning calorimetric (DSC) representation of the alloys presented on top, respectively.

performed using the least square fitting program Winspec developed at the LISE, University of Namur, Belgium. Peak fitting of the XPS spectra involved the subtraction of a Shirley type background and peak deconvolution using a linear combination of Gaussian and Lorentzian functions. The spectra were deconvoluted into the least number of components, which gives a good fit of the experimental data.

2.3.3. Microstructure analysis

The microstructures of the oxidized and non-oxidized specimen were imaged using a scanning electron microscope (SEM, Zeiss Merlin) equipped with an energy dispersive X-ray spectrometer (EDS). The microscope was operated at 15 kV (accelerating voltage), and the working distance ranging from 5 to 5.6 mm. From backscattered images, oxide phase composition was detected by EDS and analysed by elemental mapping and line scan using ESPRIT software from BRUKER.

3. Results

3.1. Constant heating rate

3.1.1. Thermogravimetric analysis

In the beginning, all powder samples (Table 2) were oxidised in the air from 25 °C -1000 °C at 5 °C/min using TGA. Fig. 1 shows that in general, the weight gain of all samples begins in the temperature range between 200−400 °C with a very slow oxidation rate. Undoped HMS (a, b, and c) show more robustness to oxidation relative to doped HMS, with total weight gain averaging between 0.35 % and 1.75 % corresponding to HMS_a and HMS_b, respectively.

Furthermore, the HMS alloys investigated were Ge and Al-doped with 0.5–1 at% dopant concentration, represented by subscript "b" and "c". The TGA weight change Fig. 1, shows that all alloys of batch "c" oxidized at a much higher rate than the ones in "b". From the synthesis route presented in Table 2, the two batches are distinct only from the melting temperature. The microstructure of the compounds (see Fig. 2) revealed that batch c had a high amount of SiC precipitates and a substantial amount of MnSi secondary phase, conversely batch b has a high amount of MnSi phase, and less SiC precipitates. The SiC formation during melting and casting originates from the reaction of the melt and the graphite crucible. Moreover, it is seen how the samples with higher Ge and Al amount results in a more heterogeneous microstructure. With increasing Al or Ge, the amount of MnSi phases (light grey) increases substantially. In addition, Ge doped samples have Ge precipitate phases with the amount increasing with higher dopant concentration. Also, slight amounts of SiC in samples batch a, and c – e are seen, while sample b shows Si phase around the grain boundaries.

Between 600 °C and 800 °C, the Ge and Al-doped powders oxidised much faster than undoped HMS, the increase in oxidation rate is associated with the reactivity of the dopant towards oxidation. The results revealed that the doped HMS compounds oxidation kinetics depends on the dopant type and concentration, where Al-doped alloys have the highest oxidation rate, hence higher weight gain of 5.33 % (1 at% Al) and 4.2 % (0.5 at% Al). A similar trend can be seen on Ge doped alloys, though the oxidation rate is around half that of Al-doped alloys.

3.1.2. Oxide composition

The composition of the oxidised powder at 1000 °C was carried out using XPS to investigate the different species that were formed as a result of the oxidation process in the undoped and the doped samples. Fig. 3 displays the high-resolution spectra of Mn 2p, Si 2p, O 1s, Al 2p, and Ge 2p core lines. The Mn 2p spectra showed two distinct peaks at ~ 642 eV and ~ 654 eV assigned to the 3/2 and 1/2 spin-orbit splitting components, respectively. The binding energy of the main peaks is indicative of the manganese in the higher-oxidation state (Mn^{4+}) [29]. Manganese forms oxide species in at least three oxidation states, Mn^{2+}, Mn^{3+}, and Mn^{4+} which exhibit significant multiplet splitting [30,31]. These multiplet splitting structures have overlapping binding energies that make it challenging for quantitative analysis. However, Mn 2p spectra also showed a shoulder at the higher binding energy side at ~ 646 eV, characteristic of Mn^{2+} [30,32]. This suggests that the Mn-oxide also contains MnO, besides MnO_2. However, the quantification of each type is not straightforward due to similar binding energies [31].

The Si 2p XPS spectra showed an intense peak centred at 103.7 eV and a small feature at the low binding energy side (~ 102 eV) as indicated by an arrow. The main peak is assigned to Si^{4+} while low binding energy is indicative of Si in the low-oxidation state (3+) [33]. The O 1s spectra also displayed two main features where a high binding energy component is consistent with Si-oxide [33], while low binding energy component is representative of Mn-oxide [34]. The observed binding energies of Al 2p and Ge 2p core-level spectra identify the presence of Al_2O_3 [35] and GeO_2 [36].

A more detailed analysis of Si 2p and O 1s core-level spectra is displayed in Figs. 4 and 5 respectively. These results show that oxidation results in the formation of SiO_2 as the main phase. In Fig. 4, the integrated area under the peak for the low binding energy component (Si^{3+}) is 3.7 % (for undoped compound) that of the total spectrum and increases with Al doping (up to 8.0 %). However, this component is not present in a Ge doped sample where Si exists in 4+ oxidation state only.

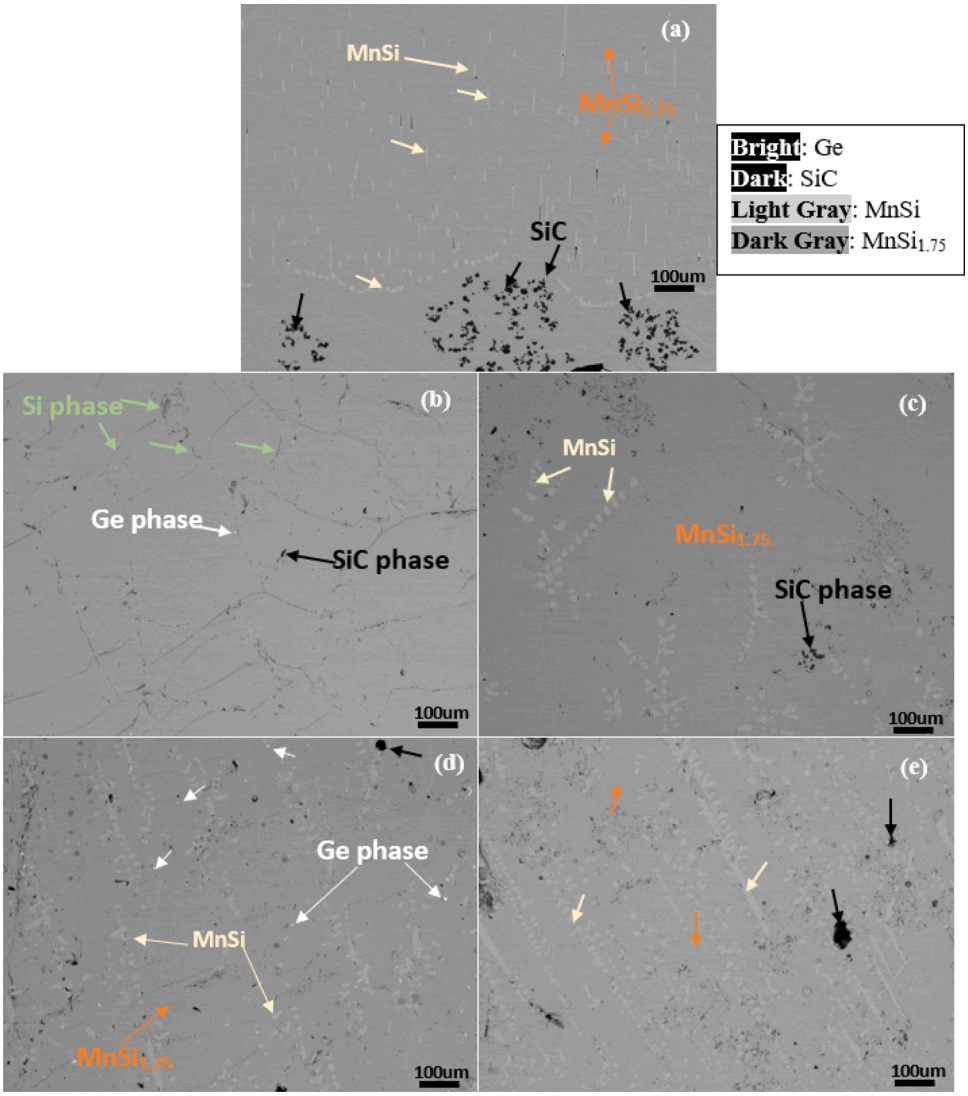

Fig. 2. SEM - backscattered electron images on cross-section of alloys (a) $MnSi_{1.75}$, (b) $MnSi_{1.745}Ge_{0.005}$, (c)$MnSi_{1.745}Al_{0.005}$, (d) $MnSi_{1.74}Ge_{0.01}$, and (e)$MnSi_{1.74}Al_{0.01}$, showing large variation in microstructure with different additions of Ge and Al. With increasing Al or Ge, the amount of MnSi phases (light grey) increases substantially. Ge doped samples present Ge precipitate phases which increase proportionally to the dopant concentration. Also, slight amounts of SiC in samples a, and c – e, while sample b shows Si phase (green arrows) around the grain boundaries.

For the O 1s core-level spectrum Fig. 5, four components were needed to obtain the best fitting. Two components on the low binding energy side were assigned to Mn-oxide while the most intense peak is arising from the SiO_2 phase. The component with the highest binding energy could be associated with physi-sorbed water [34]. In Al-doped samples, components corresponding to Al-O could not be resolved due to very proximate binding energy with Mn-oxide components [37]. Ge doped sample revealed the presence of another component at 532.1 eV due to GeO_2 [36]. Deconvoluted O 1s spectra were evidence of an increase in the Mn-oxide phase with Al doping while a decrease with Ge doping. Analysis of Al 2p and Ge $2p_{3/2}$ core level region evidenced the presence of Al_2O_3 and GeO_2 in Al-doped and Ge-doped samples, respectively Fig. 6.

3.2. Isothermal oxidation

3.2.1. Effect of consolidation techniques

To investigate the effect of different consolidation techniques on the oxidation resistance, as-cast, HP sintered, and SPS $MnSi_{1.74}Ge_{0.01}$ alloys were oxidized at 300 °C, 350 °C, 400 °C, 450 °C, and 600 °C; isothermally treated in ambient air for 24 h, see Fig. 7. All samples had insignificant scale growth at low temperatures (<400 °C). For temperatures above 400 °C, the weight gradually increased. The as-cast specimens Fig. 7(a) showed an irregular weight gain for all temperatures with a total weight gain of 7.5 μg/mm^2 after 24 h at 600 °C. The HP sampled showed the highest weight increase for all temperatures, with a total weight gain of 29 μg/mm^2 after 24 h at 600 °C, while the SPS sample had much lower oxidation rates, with only a weight increase of 1.8 μg/mm^2 for the same test conditions. A slow weight loss was noticed for some of the samples oxidised at lower temperatures (Fig. 8(a)) especially below 450 °C. The weight loss is possibly due to adsorption/desorption of humidity, volatile compound CO, or CO_2 [38,39], due to variation in the humidity of the laboratory air used for the tests.

The effect of densification methods on oxidation was further investigated on pure HMS synthesized using “siligrain HQ Table 1” (a low purity 99.8 wt% Si feedstock) and densified by SPS and HP. Fig. 8(a) shows the weight gain of the SPS samples, with very small weight gains for all temperatures, with a total weight gain of 4.8 μg/mm^2 after 24 h at

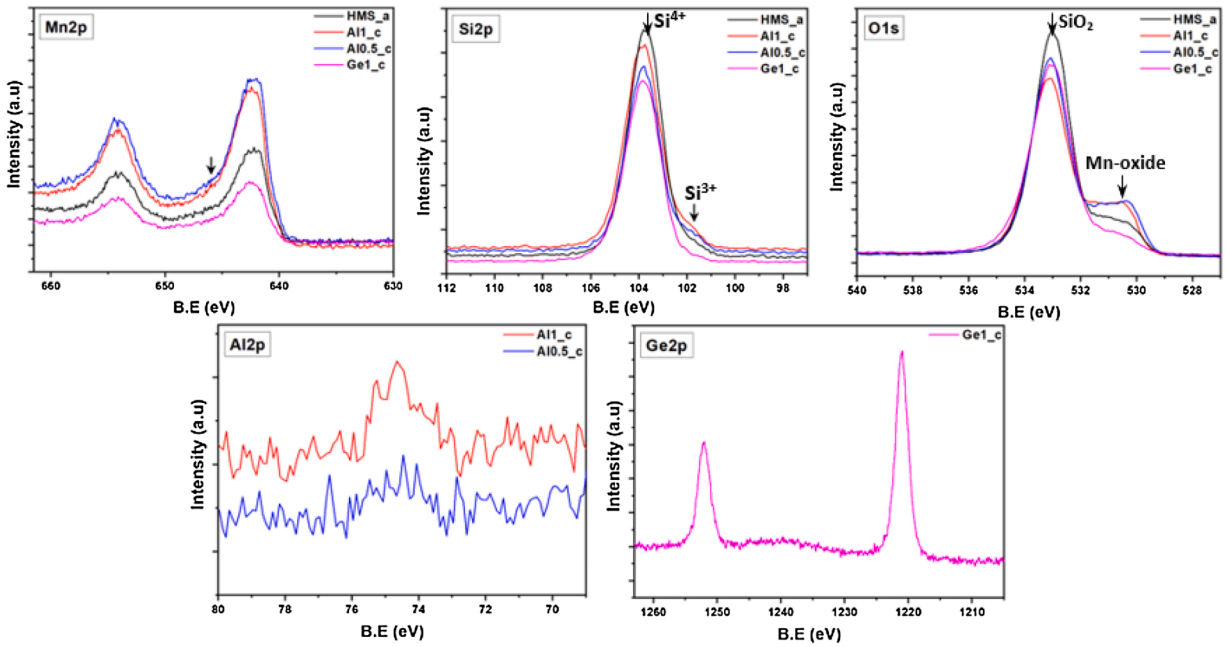

Fig. 3. X-ray photoemission spectra of the Mn 2p, Si 2p, O 1s, Al 2p, and Ge 2p core level regions.

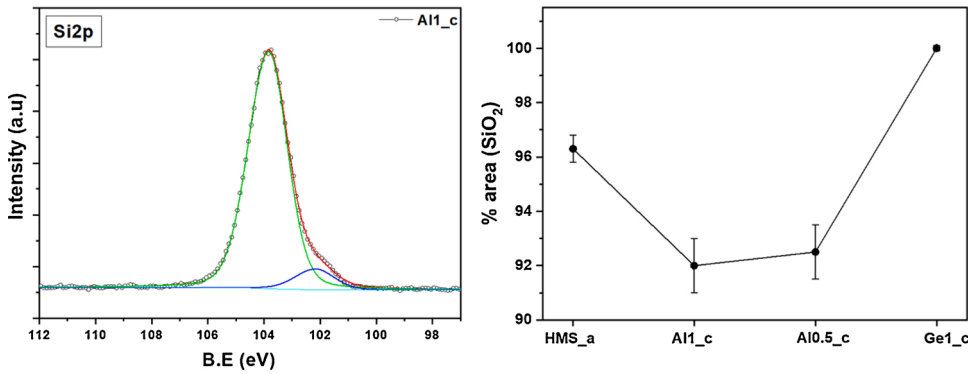

Fig. 4. Left panel: X-ray photoemission spectra of the Si 2p core level region with peak fitting results. Right panel: Integrated area for the SiO_2 component for undoped and doped samples.

600 °C, slightly higher than the SPS sample with a higher purity feedstock. However, for the HP sintered specimens (see Fig. 8(b)), the samples oxidized catastrophically at high temperatures up to two orders of magnitude higher than the SPS compounds. The catastrophic oxidation process occurred after initial cubic growth from 300 to 400 °C followed by linear growth at 450 °C and finally catastrophic oxidation above 600 °C. The latter was discussed by Branco N. P. [27], who defines cubic oxidation as a combination of linear and parabolic oxidation, which at higher temperatures becomes only linear and at further increased temperature the material oxidizes catastrophically.

Similarly, the cast and HP sintered specimen Fig. A1, presents the TGA data for the 0.5 at% Ge doped HMS ($MnSi_{1.745}Ge_{0.005}$) samples. The immediate observation is that this compound was more resilient towards oxidation than the 1 at% Ge doped HMS and pure HMS, and the scale growth (especially at low temperatures) was negligible below 500 °C.

3.2.2. *Composition effect*

The alloy composition has a major impact on oxidation kinetics, both due to the direct effect of dopants on the oxidation mechanisms, but also due to the effect of composition on the microstructure development and phase composition achieved during processing. Fig. A1(c) and Fig. 7(c) shows the 0.5 at% Ge and 1 at% Ge HMS doped HMS alloys, respectively, consolidated by SPS and heat-treated using a similar method. At temperatures below 400 °C, no significant effects of dopant type or concentration are seen. However, at 600 °C both the weight gain and the oxide thickness were much higher for the 1 at% Ge sample than the one containing 0.5 at% (see Fig. 9), corresponding to around 0.65 μg/mm^2 (or 248 nm thickness) and 1.7 μg/mm^2 (0.6 μm thickness). The same trend was noticed for HP samples and better confirmed by the low purity Si-based HMS Fig. 8. Unlike the Ge doped compounds, the siligrain-based alloys oxidized at low (300 °C) and high temperatures, the latter oxidized following parabolic model with rate constants of 0.616

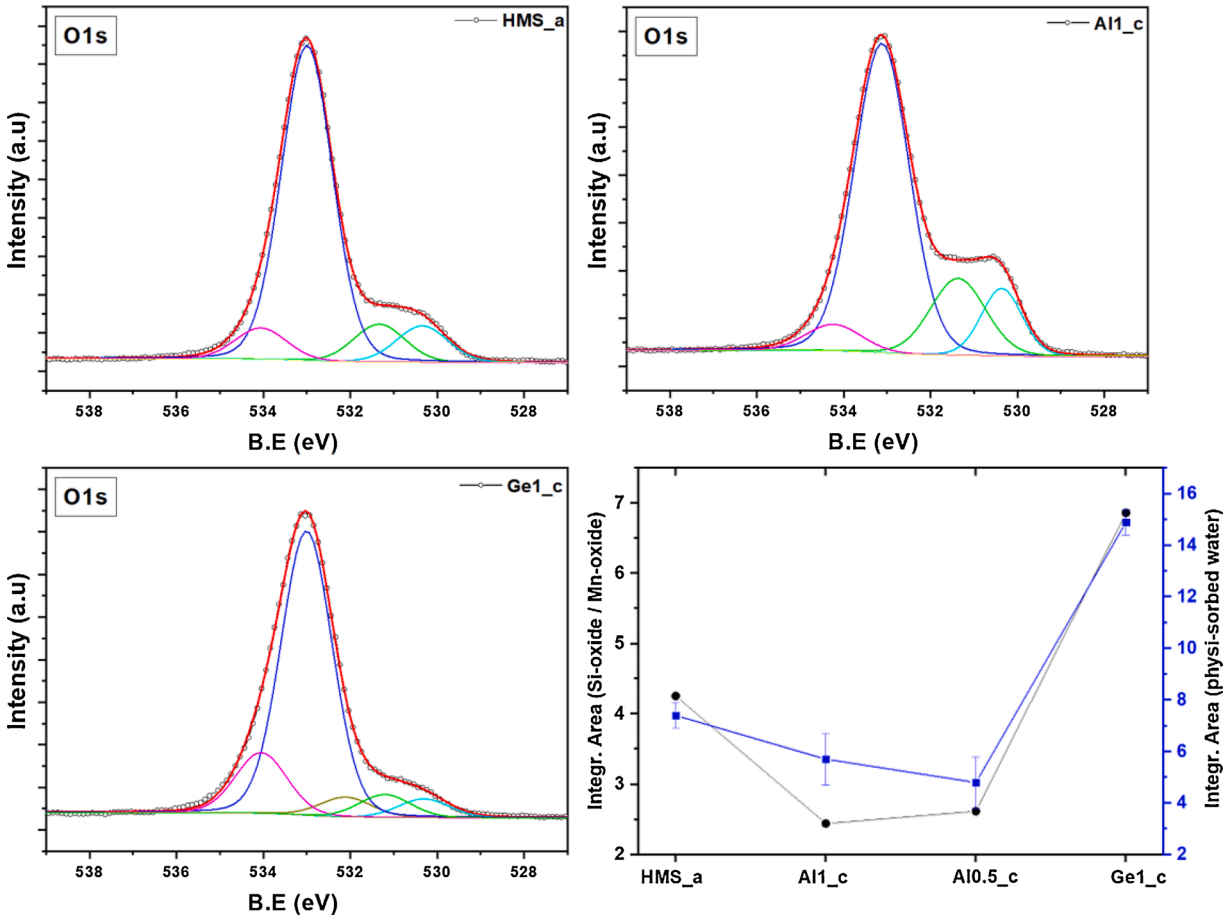

Fig. 5. X-ray photoemission spectra of the O 1s core level region with peak fitting results of HMS_a, Al1_c, and Ge1_c. Bottom right: Integrated area ratio of SiO2 component to Mn-oxide component for undoped and doped samples (in black). Integrated area for the component associated to physi-sorbed water is also shown (in blue).

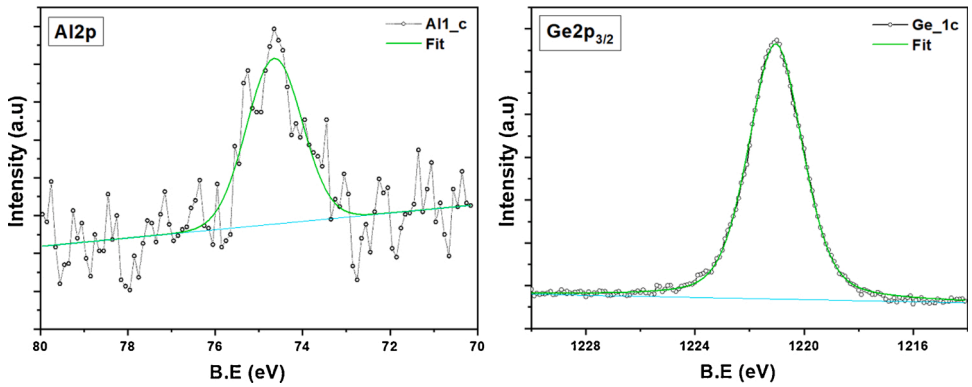

Fig. 6. X-ray photoemission spectra of the O 1s core level region with peak fitting results.

$\mu g^2/mm^4h$ and 2 $\mu g^2/mm^4h$, respectively. At high temperature, the compound based on less pure silicon oxidized with two orders of magnitude higher rate than the 0.5 at% Ge HMS (5.44 $\mu g^2/mm^4h$ oxidation rate). Thus, the higher the impurities/dopant the higher the oxidation potential and the behaviour agrees with the isoconversion results.

3.2.3. *Effect of humidity*

Long-term oxidation experiments were carried out on Ge doped specimens in ambient air for up to 200 h retention time, to investigate the oxidation mechanisms over time. Fig. 10(a), shows the weight change and relative heat flux of the Ge doped specimens in ambient air for up to 200 h retention time. The TGA curve reveals that the sample's oxidation occurs in periodic steps of 11 h weight gain and 13 h weight loss per cycle, while from the relative heat flux graph, the exothermic and endothermic behaviour alternates in line with the weight loss and gain, respectively. The weight gain and loss cyclic trend was identified over the entire period and reflected the difference in vapor pressure over the day (24 h). Where the observations showed that the mass gain occurred during the night and mass loss during the day with a very high

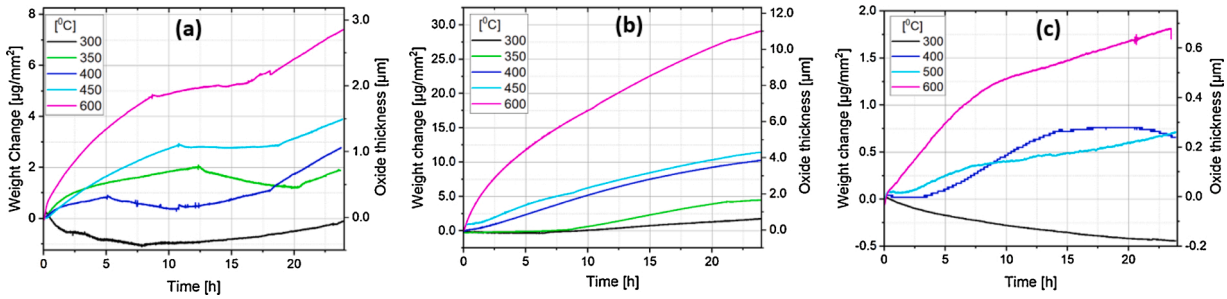

Fig. 7. Thermogravimetric weight change of 1at% Ge HMS alloys isothermally (temperature: 300 °C-600 °C) oxidized in laboratory air for 24 h, a) as-cast, b) milled and consolidated by HP, c) milled and consolidated by SPS.

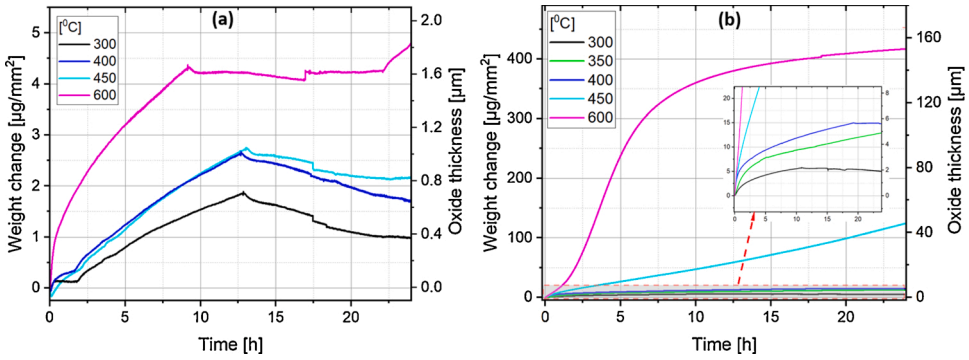

Fig. 8. Thermogravimetric analysis results of pure HMS synthesized from low purity Si feedstock, densified by a) SPS, b) HP; and heat-treated in air.

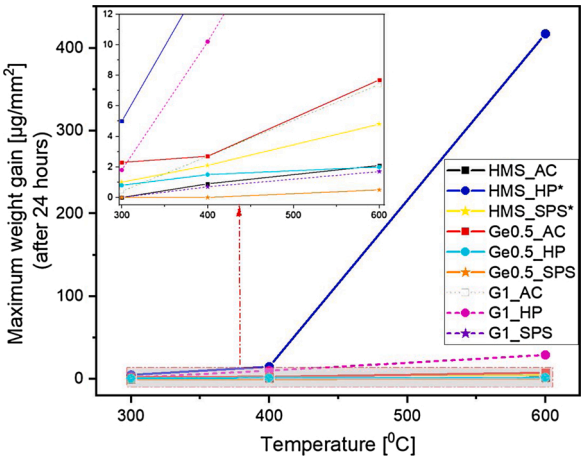

Fig. 9. Weight gain after 24 h isothermal oxidation at 300 °C, 400 °C and 600 °C. * are alloys synthesized from low purity silicon feedstock.

temperature drop during the night (~11 °C on average), and the level was even higher on one rainy evening where the relative humidity in the room was much higher than for a dry day. Finally, the weight gain segments occurred in two steps, the first consisting of the adsorption of oxygen at the alloy surface which initiates the diffusion of metal cations and formation of SiO_2 ($\alpha-$quartz) oxide with a parabolic diffusion constant of 0.732 $\mu g^2/mm^4 h$. While the second is characterized by a reduced diffusion rate of 0.21 $\mu g^2/mm^4 h$ diffusion constant. The same trend was observed for all the cycles, though, with time the oxidizing agent diffusion constant gradually decreases, this is consistent with the notion that the scale grows slowly, and the oxidation rate decreases with time.

At higher temperature (600 °C), the reaction follows the same trend, though with longer weight gain segments than weight loss, as shown by Fig. 10(b). The exothermic reaction lasted 16 h, while the endothermic reaction lasted 8 h, which is contrary to the specimen run in ambient air, this time the mass gain lasted longer. On the other hand, the alloy was also heat treated in dry air at 400 °C Fig. 10(c), to investigate the oxygen partial pressure or humidity contribution on the oxidation of the 0.5 % Ge doped alloy. The TGA and DSC curves show a completely different trend in dry air compared to that in ambient air, and the scale size attained at 47 h in dry air is thicker than that reached in ambient air.

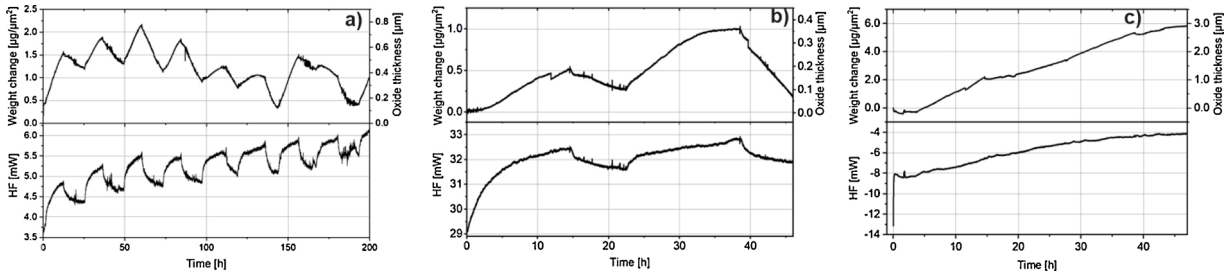

Fig. 10. Long-term TGA oxidation of 0.5at% Ge HMS consolidated by SPS, heat-treated: a) in air for 200 h at 400 °C, b) in air for 47 h at 600 °C, and c) in dry air for 47 h at 400 °C.

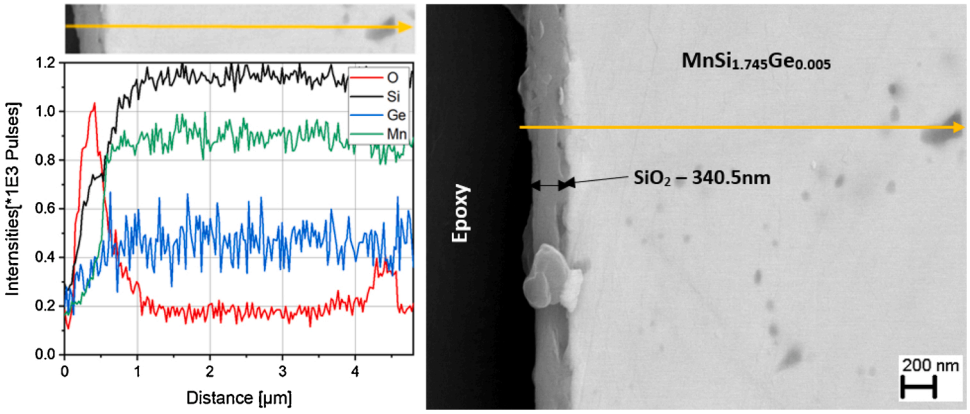

Fig. 11. SEM/EDS representation of $MnSi_{1.745}Ge_{0.005}$ (SPS consolidated) and oxidized at 400 °C for 200 h. (left) EDS line scan spectrum, (right) SEM image showing the cross-section of the interface between alloy and oxide scale layers.

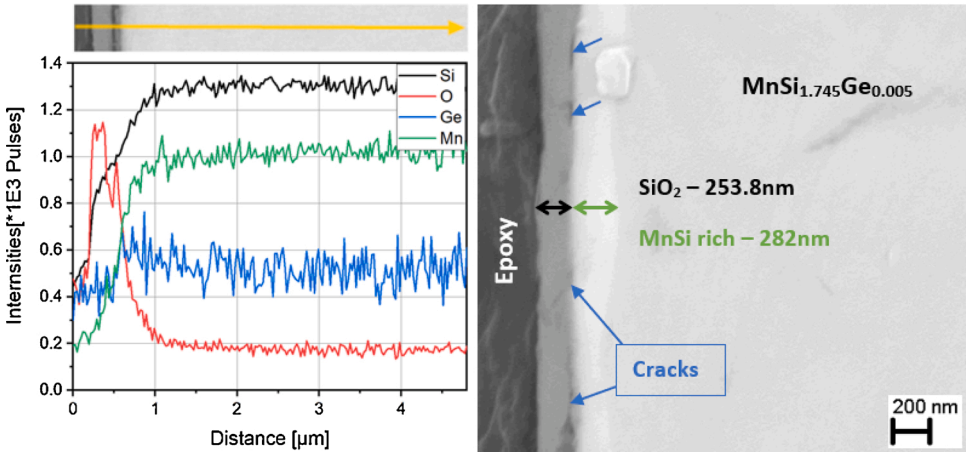

Fig. 12. SEM/EDS representation of $MnSi_{1.745}Ge_{0.005}$ (SPS consolidated) and oxidized at 600 °C for 50 h. (left) EDS lines can spectrum, (right) SEM image showing the cross-section of the interface between alloy and oxide scale layers.

Therefore, the heat treatment in dry air reveals that the weight losses are possibly due to physi-sorbed water (also seen by XPS) which forms in H_2O contained atmosphere with high vapor pressure.

3.3. Oxide scale crystal structure, morphology, and composition

SEM images of the cross section of the oxidised surface of the 0.5at% Ge doped sample is seen in Fig. 11 (400 °C, 200 h) and Fig. 12 (600 °C, 50 h). A thin layer of SiO_2 is visible for both samples, uniformly covering the entire surface. The thickness is around 340 nm for the sample oxidised at 400 °C for 200 h and 250 nm for the sample oxidised at 600 °C for 50 h. For the latter sample, also a 280 nm Mn-depleted layer is visible directly below the SiO_2 layer. Some cracks are also visible both between the layers and within the SiO_2 layer.

Moreover, Fig. 13 presents SEM micrographs of the cross-sections of $MnSi_{1.745}Ge_{0.005}$, heat-treated in the air for 24 h at 300 °C, 400 °C, and 600 °C. At 300 °C no trace of oxide scale was visualized even with high resolution. At 400 °C a SiO_2 scale was observed; however, the silicon depletion layer was smaller, and the scale was not uniform along the surface of the sample. Above 600 °C, both the Si depleted region and the scale could be distinguished, with more than half a micrometre oxide (0.5 µm) width. The oxide scale contained trace of Si-, Mn- and Ge-oxide based phases Fig. 13(c).

Fig. 14(a) shows the SEM/EDS elemental map (far right) of the HMS (based on low purity Si-feedstock) oxidized at 600 °C. The oxide is noticed on the grain boundaries, and some of the grains were fully oxidized. The oxide is mainly SiO_2 and partially Mn, and Fe-based. Fig. 14(b) presents a sample with similar composition densified by SPS. The EDS analysis shows that the oxidation robustness is improved with consolidation by SPS relative to the HP densification method, however, a long strip of MnO can also be noticed in the middle of the oxide. The diffusion of Mn^{2+} and Mn^{4+} cations through the scale-alloy interface, promoting the formation of MnO and MnO_2 oxides was a result of a nonprotective SiO_2 scale.

4. Discussion

4.1. Oxidation of pure HMS

HMS ($MnSi_{1.75}$) compounds synthesized from the more purified Si

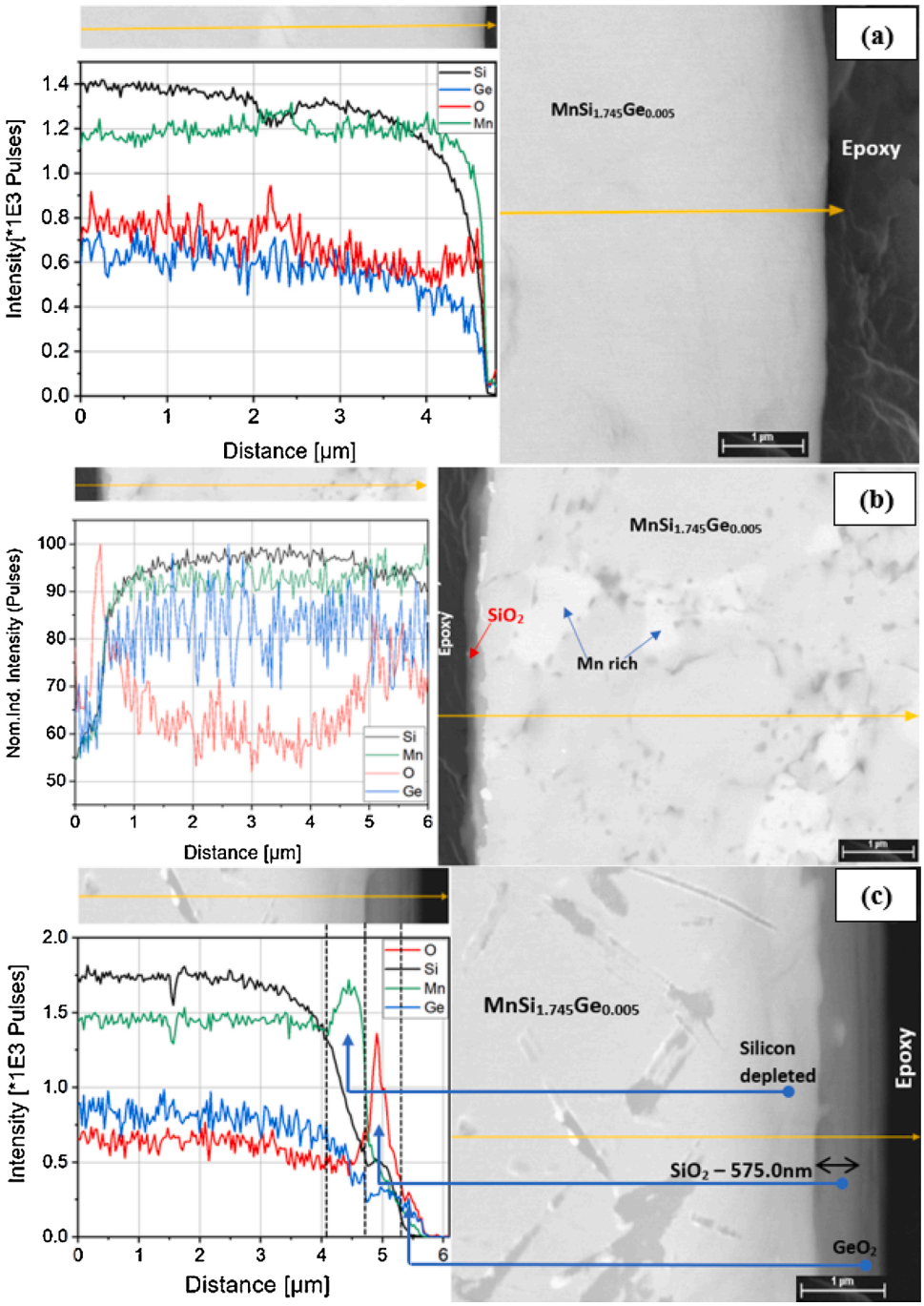

Fig. 13. Cross sectional comparison of the $MnSi_{1.745}Ge_{0.005}$ consolidated by Hot Press and oxidized at a)300 °C b)400 °C and c)600 °C in air for 24 h.

feedstock (see Table 1) were more robust to oxidation among all studied alloys. The alloy selectively grew SiO_2(α-quartz above 300 °C and β-quartz above 575 °C), where the silica oxide coexisted with a silicon depleted layer (see Fig. 16(1)). The alloy provides sufficient and gradual flux of Si to the specimen surface, developing an external silica oxide at the Alloy-Oxide interface. Carl Wagner [40], provided a necessary but not sufficient condition for the formation of an exclusive formation of one oxide in the case of metal "A" alloyed with "B", as shown by Eq. 4.

$$N_{B(\min)} = \frac{1}{16 Z_B c}\left(\frac{\pi k_{pB}}{D}\right)^{1/2} \quad (4)$$

Where: $N_{B(\min)}$ – Minimum concentration of the alloying element, Z_B – Atomic number, c – number of gram-atoms of the metal per unit volume, π – the dissociation pressure of the oxide "BO", k_{pB} – the oxidation rate constant of the parabolic rate law and D - the interdiffusion coefficient.

Ning H. et al. [20] conducted oxidation experiments on $MnSi_{1.74}$, the specimen edge cross-section was composed of mainly SiO_2 and MnSi phases at 600 °C after 500 h, however, in the current study, XPS revealed that the oxide layer was also composed of minor Mn-oxide that originate from Mn^{2+} and Mn^{3+} oxidation states, though only at high temperature. In the initial stages of oxidation, Si preferentially oxidises and form a relatively dense and stable SiO_2. If the molar fraction of Si at the alloy-SiO_2 is close to minimum, the diffusion of O^{2-} ions through the SiO_2 layer will cause some oxidation of Mn at the interface, but due to the low diffusivity of O^{2-} in Mn-oxides this layer will not grow further.

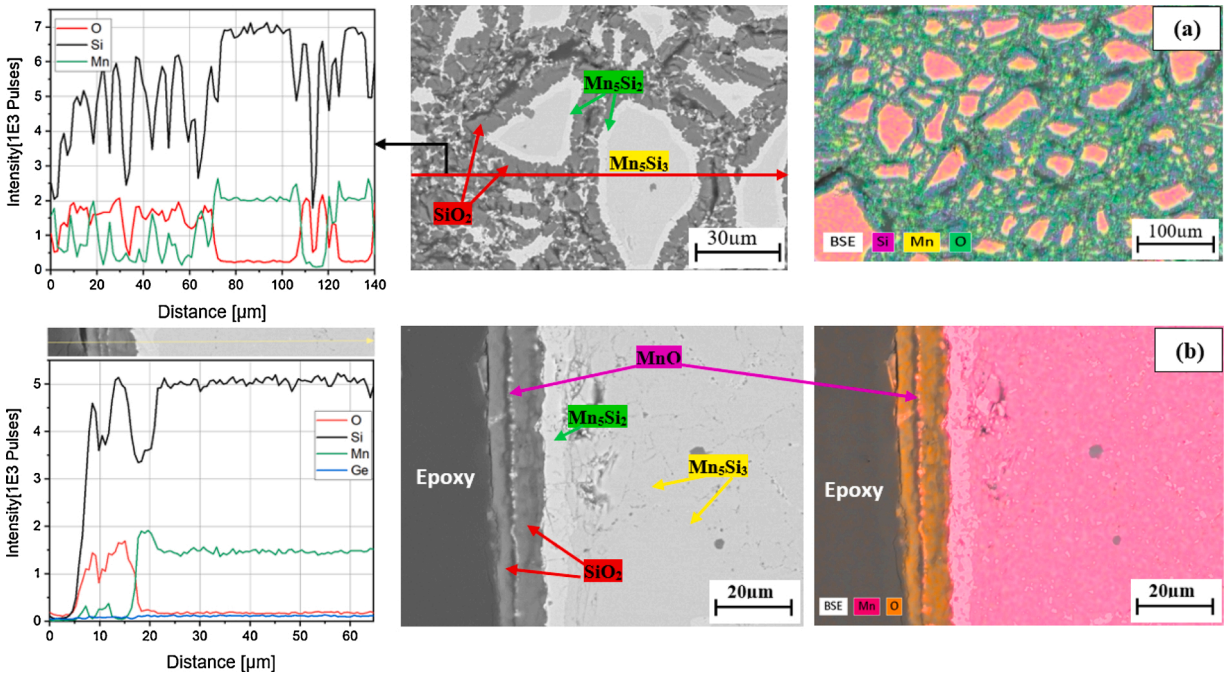

Fig. 14. Cross-sectional EDS composition analysis of pure HMS synthesized based on siligrain HQ (Si feedstock) and consolidated by a) Hot Press at 950 °C and b) SPS, both TGA oxidised at 600 °C for 24 h.

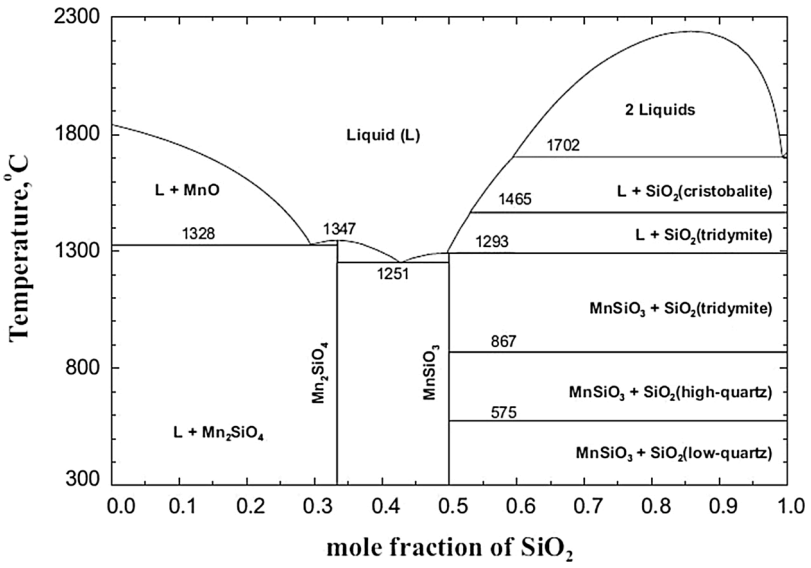

Fig. 15. Optimized Phase diagram of MnO-SiO_2 oxide phases [42].

Furthermore, the long-term coexistence of the formed oxides is a crucial stability deterministic factor. This was not thoroughly investigated by the current study, nevertheless, it was experimentally investigated by Robie R.A. et al. [41] and revealed that the $MnSiO_3$(rhodonite) crystalline phase was grown at 890 °C for 20 h thermal exposure. A similar observation was made using theoretic models (factsage.com [42] and FISHER model [43]) under MnO-SiO_2 phase equilibrium simulations as a minor phase, however, the manganese silicate ($MnSiO_3$) was not observed both at low and high (600 °C) temperatures in this study (Fig. 15).

4.2. Oxidation of doped HMS

Based on the kinetics of oxidation results (chapter 3), the doped alloys showed high potential to oxidation in comparison to the pure HMS. Comparatively, Ge-doped alloys were marginally distinct from the pure HMS than the Al-doped compounds as by the isoconversion (Fig. 1) and isothermal oxidation results. “Al” and “Si” were reported to be two among three elements that, by selective oxidation form a slow-growing and protective scale [44] together with chromium. From the high molar concentration of silicon (Si) in the alloys, Si preferentially has higher

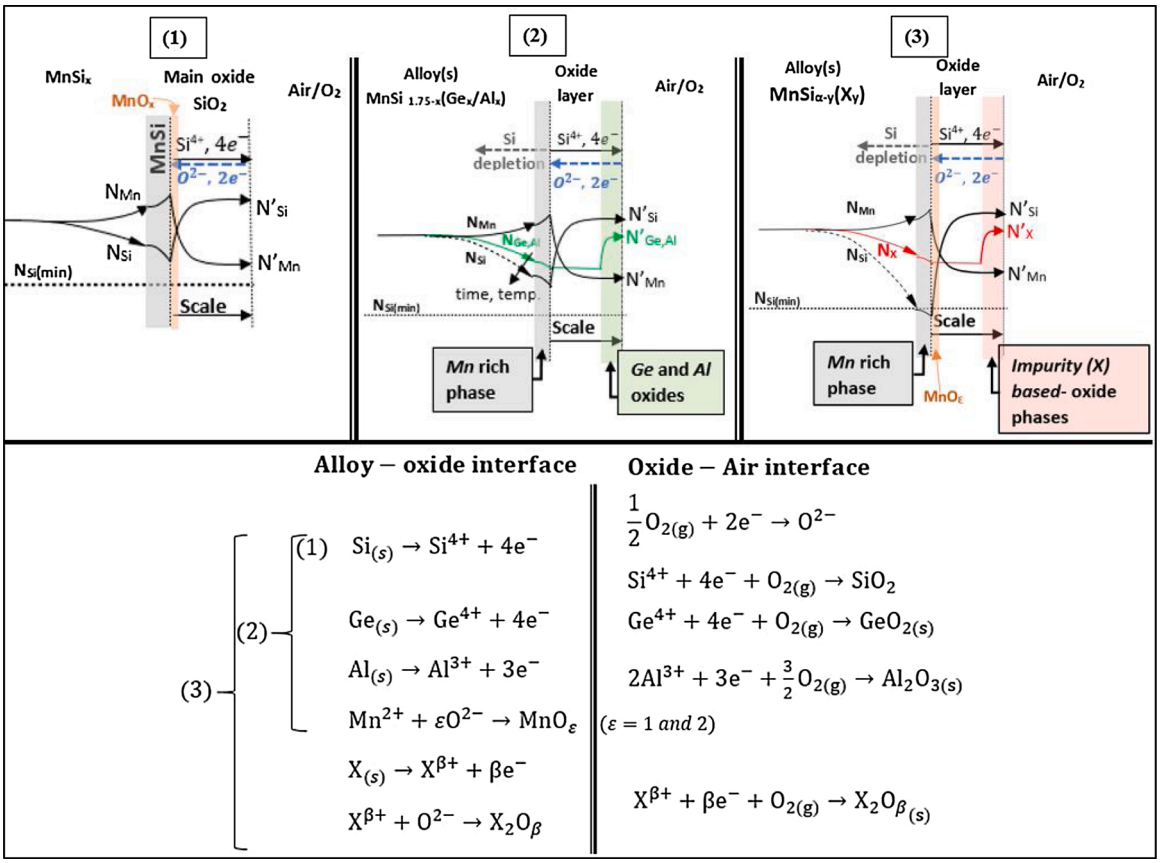

Fig. 16. Schematic overview of the HMS (pure or doped) oxidation profile showing "the main scenarios" of Si diffusion through the oxide scale and its inward depletion. The material transport is subdivided in three categories: (1) $N_{Si}>N_{Si(min)}$ – selective oxidation, usually for undoped HMS or doped HMS (for short retention time or below 500ºC), Mn oxide is little to none and SiO2 protective; (2) $N_{Si}>N_{Si(min)}$ – similar to (1) though at longer period or high temperature at low dopant concentration; (3) $N_{Si}<N_{Si(min)}$ (Nonprotective) all elements are involved starting from the most reactive to oxidation (formation of a conglomerate of oxides).

thermodynamic activity or higher affinity to oxidation relative to other elements. As schematically illustrated in Fig. 16 , initially, the oxidant (air) is adsorbed at the alloy surface; with temperature, high energy electrons on the silicon atom are knocked out and creates a Si^{2+} cation defect, as a result, the silica layer nucleates and grows continuously at a very slow rate ($0.23\mu g^2/mm^4h$ at 400 °C). The scale coexists with a silicon depleted layer, with which as silicon is consumed close to the oxide alloy interface, Ge relative activity increases inversely proportional to the Si diffusion rate, preferentially above 600 °C. As a result, a Ge based oxide nucleates a GeO_2 oxide. Similar mechanisms apply to the Al-doped compound which exhibited Al_2O_3 among oxides, though at a distinct rate. Moreover, it was noticed (by the XPS analysis) that at high temperature the stability of the Al-doped alloy is compromised as the level of Mn-oxide increase relative to the Ge doped or pure HMS. This reveals and confirms that Ge along with Si oxides is more protective than with alumina, where Fig. 4 (right panel) shows that with Ge-doping the oxide scale is almost solely SiO_2.

The thermal oxidation robustness of HMS is unquestionable below 600 °C and this study has proven the case. However, it was also revealed that the oxidation resistance of HMS does not rely only on the stoichiometry but also depends on the densification method, the dopant type, and the purity of the raw materials feedstock. This was seen when comparing the oxidation rate of as-cast, HP, and SPS material. With HP the specimen oxidised at a very high rate, especially at high temperature. The main cause is the weak mechanical strength between particles such that oxidation can occur easily along grain boundaries of non-completely sintered grains, as evident from Fig. 14(a) and Fig. A4, and also seen from physical images of the samples Fig. A2 thermally oxidized for 24 h, where the oxides increased the volume of the specimen till it disintegrated. In contrast, the SPS consolidated specimen Fig. 14(b) at 600 °C shows that the internal oxidation is greatly reduced, and all oxidation occurs at the surface following more standard scale growth diffusion kinetics. Hence, the mechanical integrity of the sample showed huge advantages in reducing the oxidation of the compounds, mainly because of reduced surface to volume ratio exposed to heat and oxidation agent(s).

The effect of dopants and impurities on the oxidation rate is also clearly seen and the mechanisms underlaying this is summarised in Fig. 16, dividing it roughly into three different groups: (1) Pure HMS oxidation for short and long retention time, or low dopant/impurity concentration for short retention time, (2) higher temperature or longer exposure at low dopant/impurity concentration, and (3) high dopant/impurity concentration leading to non-protective oxide scale growth.

Case (1) was seen mainly for undoped HMS samples, where the mechanism of oxidation is governed by "Si" selective oxidation to SiO_2 and further details were discussed in section 4.1 above.

Case (2) was observed for doped HMS alloys. With Ge and Al as dopants, transient GeO_2 and Al_2O_3 oxides grow at the same time as SiO_2

(though relatively faster). As shown in Fig. 16(2), overtime a continuous silica layer is formed with respective Ge- and Al-oxides at the SiO_2 - Air interface. At temperature below 400 °C (see Fig. 11), the depletion layer is very small after 200 h of oxidation time, revealing the SiO_2 passivity at this temperature and justifying the lack of Mn oxide with XPS characterisation. However, at 600 °C a wide silicon depleted layer is witnessed on the alloy side of the interface (see Fig. 12), and the alloy presented crucks at the alloy-oxide interface. With reduced Si molar fraction at the alloy side, the stresses were a result of compositional changes at the alloy-oxide interface and can also be linked to compressive stress between MnSi and SiO_2 phases. Over time, the alloy oxidation mechanisms could shift to as represented by Fig. 16(3). The latter would lead to the formation of Mn-based oxide(s) and compromise the SiO_2 protectiveness.

Case (3) was seen mainly on alloys with high dopant/impurity concentration. HMS sample synthesized from more impure silicon feedstock showed slow (cubic) oxidation at temperatures below 400 °C, at 450 °C temperature the compound oxidizes linearly, and finally, at high temperature, it oxidizes catastrophically (see Fig. 8(b)). This kinetics of oxidation is a result of nucleation of a conglomerate of oxides that form based on the impurities (Fe, Al, B, etc) and nucleate in parallel with silica, therefore compromising the protectiveness of silica. Though the mechanisms leading to catastrophic oxidation was out of the article's scope, it is represented in the same angle as the high temperature oxidation by scenario three (see equations of both oxide interfaces Fig. 16).

The three cases presented above are only valid for atmospheres where $O_2(g)$ is the dominant oxidation species. However, after long term oxidation tests in laboratory (humid) air Fig. 10(a), it was noticed that the effect of humidity should also be considered. In a water contained atmosphere, H_2O is adsorbed on SiO_2 and react to form silicon hydroxide ($Si(OH)_{4(s)}$ Eq. 5, also reported by Copland E. et al. [45] in the temperature range of 300 °C–600 °C. The nucleated hydroxide will reach an equilibrium concentration "K" (Eq. 6) where it slows down both Si^{2+} and O^{2-} diffusion (meanwhile the oxidation rate). The stability of $Si(OH)_4$ (also reported by [46]) is reached under certain H_2O partial pressure (pH_2O) in the atmosphere. Simultaneously due to varying pH_2O, some $Si(OH)_{4(s)}$ dissociates following Eq. 5 and H_2O vaporises, which is witnessed in the weight loss sections, see Fig. 10(a). Towards the night, the silica formation is again resumed under reduced pH_2O and the cycle continues.

$$SiO_{2(s)} + 2H_2O_{(g)} \leftrightarrow Si(OH)_{4(s)} \tag{5}$$

$$K = \frac{a_{Si(OH)_4}}{pH_2O \times a_{SiO_2}} \tag{6}$$

Where $a_{Si(OH)_4}$ – is the local (oxide-air interface) molar fraction of $Si(OH)_4$, a_{SiO_2} – is the local molar fraction of SiO_2. Further studies could extensively investigate the effect of H_2O on the stability of SiO_2, pertaining to oxidation of HMS.

5. Conclusion

High temperature oxidation of $MnSi_{1.75-\alpha}X_\alpha$ was investigated in this article. The alloys showed robustness to oxidation at temperatures below 500 °C forming a SiO_2 protective layer. However, the formation of SiO_2 layer mechanisms was studied and the level of protectiveness was discussed.

At temperature above 600 °C, the rate of outward diffusion of Si ions at the alloy-oxide interface is higher than that from the core. That affects much the oxidation kinetics, with the formation of third element-based oxides (Al_2O_3 and GeO_2) and Mn-oxides, which coexist with the main oxide (SiO_2) and reduce its protectiveness.

At temperature below 500 °C, the oxidation rate is reduced and with time (as seen after 200 h of isothermal exposure), a compact and continuous layer of SiO_2 is formed at the alloy edges with GeO_2 (for Ge doped HMS) at the oxide-gas interface. Moreover, all other oxides were found to be quantitatively minor to SiO_2 for alloys with pure Si-feedstock (purity >99.999 wt%).

XPS composition analysis revealed that with Ge doping the Mn-oxide was quantitatively reduced than with Al doping by a difference of almost 8% (considering 1at% doping on both sides). Therefore, $GeO_2 – SiO_2$ was a more protective combination than with Al_2O_3. Moreover, this study found that alloys with 0.5at% dopant concentration were more resistant to oxidation, and in case of excessive doping, both the kinetics and mechanisms of oxidation of HMS alloys are considerably affected.

The oxidation kinetics and mechanisms are also dependent on the mechanical integrity of the alloys. The samples densified by hot pressing had 3 times more weight gain than as-cast samples, while with SPS the oxidation resistance was much better than the others.

Finally, at worst scenario coupling excessive doping (or more impurities) with HP consolidation method, the alloys oxidized at the grain boundaries, and lead to catastrophic oxidation. Therefore revealing the important relationship between oxidation potential, impurities optimisation, and density of alloys.

Declaration of Competing Interest

The authors report no declarations of interest.

Data availability

Data used in this manuscript will be made available by the corresponding author upon reasonable request.

CRediT authorship contribution statement

Antoine de Padoue Shyikira: Conceptulization, Data curation, Formal analysis, Investigation, Methodology, Project administration, Validation, Writing - original draft, Writing - review & editing. **Naureen Akhtar:** Methodology, Investigation, Validation, Formal analysis, Writing - original draft. **Gunstein Skomedal:** Conceptualization, Methodology, Supervision, Writing - review & editing. **Tor Oskar Sætre:** Supervision. **Peter Hugh Middleton:** Supervision, Writing - review & editing.

Acknowledgments

The author would like to acknowledge all partners: Elkem ASA, Sintef, and the University of Oslo (UiO) in TESil project, for their help form material synthesis, pellet consolidation, and transport properties tests. Moreover, the authors would like to appreciate Prof. Spyros Diplas tremendous contribution to conducting the XPS tests. Finally, we acknowledge financial support from the Research Council of Norway (Project No 269326).

Appendix

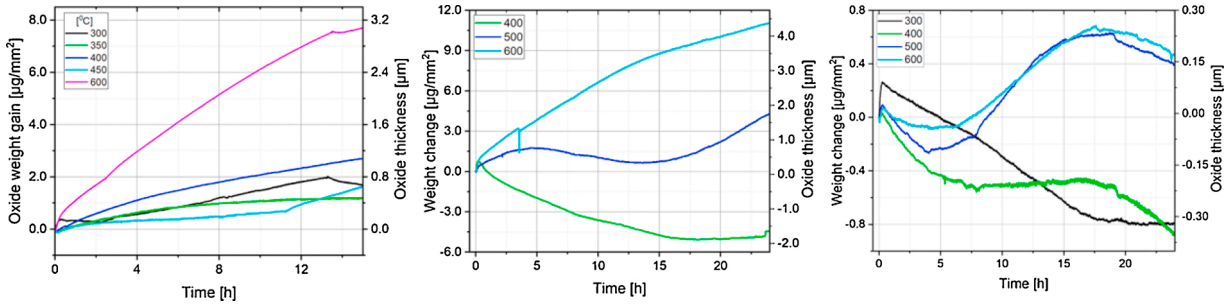

Fig. A1. Thermal gravimetric weight change of 0.5at% Ge HMS alloy in laboratory air, a) as-cast, b) milled and consolidated by HP, c) milled and consolidated by SPS.

Fig. A2. Isothermal oxidation of Siligrain based pure HMS, HP consolidated in laboratory air. Specimen at 450 °C and 600 °C considerably increased in volume and the reaction was driven with 4.82 kJ/mol activation energy.

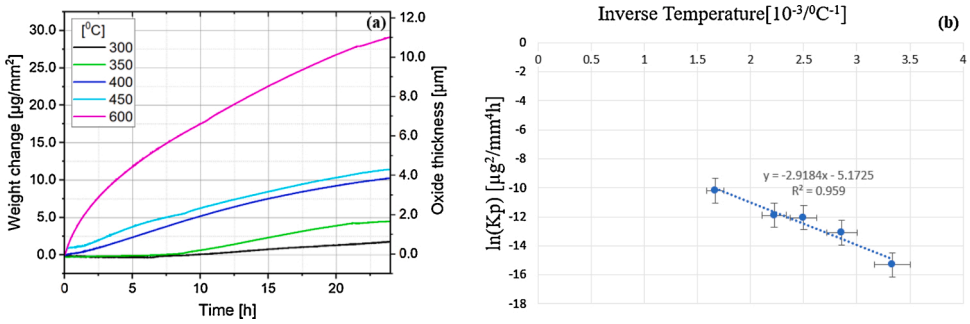

Fig. A3. (a)Weight gain over time of 1at% Ge doped HMS, densified by HP and heat treated in Dry Air at temperatures ranging from 300 °C to 600 °C, (b) An illustration of how the parabolic oxidation rate constant k_p was approximated by Arrhenius plot/model. The natural logarithm of k_p is plotted against reciprocal temperature.

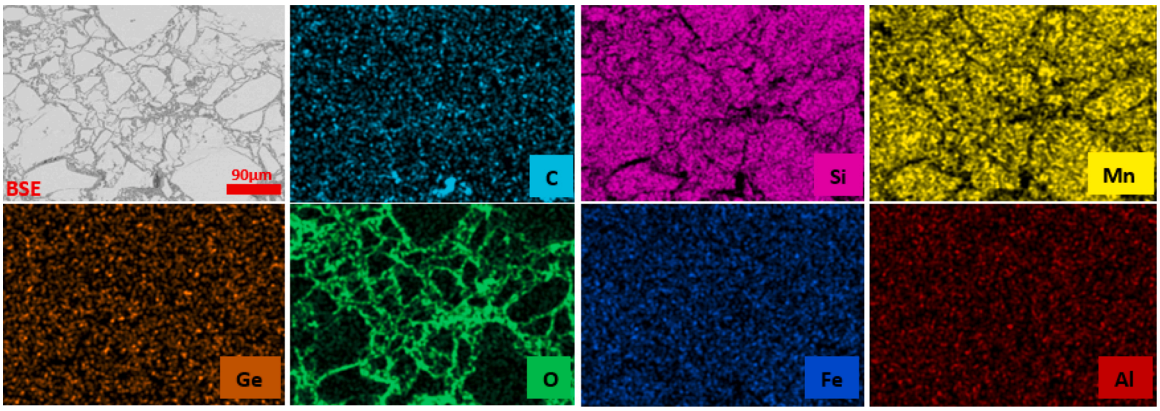

Fig. A4. Elemental mapping by SEM-EDS of the pure HMS synthesized based on siligrain (as a Si feedstock), oxidized at 450 °C for 15 h in Air.

References

[1] D.M. Rowe, CRC Handbook of Thermoelectrics, CRC Press, Cardif, Wales, 1995. Boca Raton.

[2] Z. Zamanipour, X. Shi, M. Mozafari, J.S. Krasinski, L. Tayebi, D. Vashaee, Synthesis, characterization, and thermoelectric properties of synthesis, characterization, and thermoelectric properties of nanostructured bulk p-type $MnSi_{1.73}$, $MnSi_{1.75}$, and $MnSi_{1.77}$, Ceram. Int. 39 (2021) 2353–2358, https://doi.org/10.1016/j.ceramint.2012.08.086, 2. 13.

[3] A. Nozari, P. Norouzzadef, F. Suarez, D. Vashaee, Thermoelectric silicides: a review, J. Appl. Phys. 56 (May) (2017) 1–27.

[4] D.Y.N. Truong, Thermoelectric Properties of Higher Manganese Silicides, University of Waterloo, Ontario, 2015.

[5] I. Aoyama, H. Kaibe, L. Rauscher, T. Kanda, M. Mukoujima, S. Sano, T. Tsuji, Manganese silicides (HMSs, $MnSi_{1.74}$) and characterization of thermoelectric generating module using p-type (Al, Ge and Mo)-doped HMSs and n-Type $Mg_2Si_{0.4}Sn_{0.6}$ legs, J. Appl. Phys. 44 (2005) 4275–4281, https://doi.org/10.1143/JJAP.44.4275.

[6] W. B. a. F. Gillen, Process of making Mn_4Si_7 thermoelectric element and product of said process, USA Patent (Oct (22)) (1968), 3407037.

[7] D.Y.N. Truong, H. Kleinke, F. Gascoin, Preparation of pure higher manganese silicides through wet ball milling and reactive sintering with enhanced thermoelectric properties, Intermetallics 55 (2015) 127–132, https://doi.org/10.1016/j.intermet.2015.07.002.

[8] G. Kima, H.J. Rima, K.H. Lee, J.W. Roh, W. Lee, Suppressed secondary phase generation in thermoelectric higher manganese silicide by fabrication process optimization, Ceram. Int. 45 (2019) 19538–19541, https://doi.org/10.1016/j.ceramint.2019.06.104.

[9] S. Perumal, S. Gorsse, U. Ail, M. Prakasam, P. Rajasekarb, A.M. Umarji, Enhanced thermoelectric figure of merit in nano-structured Si dispersed higher manganese silicide, Mater. Sci. Semicond. Process. 104 (2019), https://doi.org/10.1016/j.mssp.2019.104649.

[10] W. Luo, H. Li, F. Fu, W. Hao, X. Tang, Improved thermoelectric properties of Al-doped higher manganese silicide prepared by a rapid solidification method, J. Electron. Mater. 40 (5) (2011) 1233–1237.

[11] A.J. Zhou, T.J. Zhu, X.B. Zhao, S.H. Yang, T. Dasgupta, C. Stiewe, R. Hassdorf, E. Mueller, Improved thermoelectric performance of higher manganese silicides with Ge additions, J. Electron. Mater. 39 (9) (2010) 2002–2007.

[12] H. Lee, G. Kima, B. Lee, J. Kima, S.-M. Choi, K.H. Lee, W. Lee, Effect of Si content on the thermoelectric transport properties of Ge-doped higher manganese silicides, Scr. Mater. 135 (2017) 72–75, https://doi.org/10.1016/j.scriptamat.2017.03.011.

[13] P. Dharmaiah, C.-hee Lee, G. Song, S.-J. Hong, Mechanical and thermoelectric properties of environment friendly higher manganese silicide fabricated using water atomization and spark plasma sintering, Intermetallics 119 (2020), https://doi.org/10.1016/j.intermet.2020.106705.

[14] X. She, X. Su, H. Du, T. Liang, G. Zheng, Y. Yan, R. Akram, C. Uherb, X. Tang, High thermoelectric performance of higher manganese silicides propared by ultra-fast thermal explosion, J. Mater. Chem. C 3 (2015) 12116–12122, https://doi.org/10.1039/c5tc02837j.

[15] H. Nagai, M. Okabayashi, Deleterious effect of Ti addition on the oxidation resistance of Ni-20Cr alloy, Trans. Japan Inst. Met. 22 (10) (1981) 691–698.

[16] E. Anzini, N. Glaenzer, P.M. Mignanelli, M.C. Hardy, H.J. Stone, S. Pedrazzini, The effect of manganese and silicon additions on the corrosion resistance of a polycrystalline nickel-based superalloy, Corros. Sci. 176 (2020).

[17] H. Yu, S. Ukai, S. Hayashi, N.H. Oono, Effect of Cr and Y_2O_3 on the oxidation behavior of Co-based oxide dispersion strengthened superalloys at 900 °C, Corros. Sci. 127 (2017) 147–156.

[18] S. Okada, T. Shishido, M. Ogawa, F. Matsukawa, Y. Ishizawa, K. Nakajima, T. Fukuda, T. Lundstrom, MnSi and $MnSi_{2-x}$ single crystals growth by Ga flux method and properties, J. Cryst. Growth 229 (2001) 532–536.

[19] G. Skomedal, A. Burkhov, Ar Samunin, R. Haugsrud, P.H. Middleton, High temperature oxidation of Mg_2(Si-Sn), Corros. Sci. (2016).

[20] H. Ning, M.J. Reece, F. Smeacetto, M. Salvo, Oxidation protective glass-ceramic coating for higher manganese silicide thermoelectrics, J. Mater. Sci. 51 (2016) 9484–9489.

[21] R. Funahashi, Y. Matsumura, T. Barbier, T. Takeuchi, R.O. Suzuki, S. Katsuyama, A. Yamamoto, H. Takazawa, E. Combe, Durability of silicide-based thermoelectric modules at high temperatures in air, J. Electron. Mater. 44 (8) (2015) 2946–2952.

[22] M. Salvo, F. Smeacetto, F. D'Isanto, G. Viola, P. Demitri, F. Gucci, M.J. Reece, Glass-ceramic oxidation protection of higher manganese silicide thermoelectrics, J. Eur. Ceram. Soc. (2018), https://doi.org/10.1016/j.jeurceramsoc.2018.01.007.

[23] Xiao-jiang Liu, Yong-quan He, Guang-ming Cao, Tao Jia, Teng-zhi Wu, Zhen-yu Liu, Effect of Si content and temperature on oxidation resistance of Fe-Si alloys, J. Iron Steel Res. Int. 22 (3) (2015) 238–244.

[24] D.J. Young, High Temperature Oxidation and Corrosion of Metals, Elsevier, Amsterdam, 2016.

[25] Elkem, "Thermoelectric Silicides," Elkem, [Online]. Available: https://www.elkem.com/innovation/research-projects/tesil/.

[26] N.B. Pilling, R.E. Bedworth, Oxidation of metals at high temperature, J. Inst. Met. 29 (1923), p. 529.

[27] B.N. Popov, Corrosion Engineering, Elsevier, Columbia, 2015.

[28] G. Lablanche, U.F. Volkert, G. Eggeler, E.P. George, Oxidation behavior of the CrMnFeCoNi hing-entropy alloy, Oxid. Met. 85 (2016) 629–645.

[29] G. Xie, X. Liu, Q. Li, H. Lin, Y. Li, M. Nie, L. Qin, The evolution of a-MnO_2 from hollow cubes to hollow spheres and their electrochemical performance for supercapacitors, J. Mater. Sci. 52 (18) (2017) 10915–10926.

[30] Zhi-Qiang Zou, Gao-Ming Shi, Li-Min Sun, Xiao-Yong Liu, Manganese nanoclusters and MnSi~1.7 nanowires formed on Si(110): a comparative x-ray photoelectron spectroscopy study, J. Appl. Phys. 113 (2013) 1–5.

[31] M.C. Biesinger, B.P. Payne, A.P. Grosvenor, L.W.M. Lau, A.R. Gerson, R.St. C. Smart, Resolving surface chemical states in XPS analysis of first row transition metals, oxides and hydroxides: Cr, Mn, Fe, Co and Ni, Appl. Surf. Sci. 257 (2011) 2717–2730.

[32] H. Sun, X. Qin, F. Zaera, Chemical nature of the thin films that form on SiO_2/Si (100) surfaces upon manganese deposition, J. Phys. Chem. Lett. 2 (20) (2011) 2525–2530.

[33] A. Thogersen, J.H. Selj, E.S. Marstein, Oxidation effects on graded porous silicon anti-reflection coatings, J. Electrochem. Soc. 159 (5) (2011) 1–7.

[34] E.S. Ilton, J.E. Post, P.J. Heaney, F.T. Ling, S.N. Kerisit, XPS determination of Mn oxidation states in Mn (hydr)oxides, Appl. Surf. Sci. 366 (2016) 475–485.

[35] A. Barrera, F. Tzompantzi, J. Campa-Molina, J.E. Casillas, R. Pérez-Hernández, S. Ulloa-Godinez, C. Velásquez, J. Arenas-Alatorre, Photocatalytic activity of Ag/Al_2O_3–Gd_2O_3 photocatalysts prepared by the sol–gel method in the degradation of 4-chlorophenol, RSC Advance 8 (2018) 3108–3119.

[36] K. Prabhakaran, T. Ogino, Oxidation of Ge(100) and Ge(111) surfaces: an UPS and XPS study, Surf. Sci. 325 (3) (1995) 263–271.

[37] A.H. Alshehri, K. Mistry, V.H. Nguyen, K.H. Ibrahim, D. Muñoz-Rojas, M. Yavuz, K. P. Musselman, Quantum-tunneling metal-insulator-metal diodes made by rapid atmospheric pressure chemical vapor deposition, Adv. Funct. Mater. 29 (7) (2018).

[38] J.Y. Wang, X.M. Duan, Z.H. Yang, D.C. Jia, Y. Zhou, Ablation mechanism and properties of SiC/SiBCN ceramic composites under an oxyacetylene torch environment, Corros. Sci. 82 (2014) 101–107.

[39] L.Y. Xiang, L.F. Cheng, X.M. Fan, L. Shi, X.W. Yin, L.T. Zhang, Effect of interlayer on the ablation properties of laminated HfC-SiC ceramics undrer oxyacetylene torch, Corros. Sci. 93 (2015) 172–179.

[40] C. Wagner, Theoretical analysis of the diffusion processes determining the oxidation rate of alloys, J. Electrochem. Soc. 99 (1952) 369–380.

[41] R.A. Robie, S. Russell-Robinson, H.T. Evans, Flux growth of $MnSiO_3$ (rhodonite) crystals, J. Cryst. Growth 94 (1989) 981–982.

[42] Young-Min Kim, In-Ho Jung, Thermodynamic evaluation and optimization of the MnO-B_2O_3 and MnO-B_2O_3-SiO_2 systems and its application to oxidation of high-strength steels containing boron, Miner. Met. Mater. Soc. ASM Int. 46A (2015) 2736–2747.

[43] Y. Liu, S. Liu, X. Su, H. Peng, J. Wang, H. Tu, Calculation of selective oxidation in grain an grain boundary, J. Phase Equilibria Diffus. 34 (2) (2013) 82–88.

[44] N. Birks, G.H. Meier, F.S. Péttit, Introduction to The High-Temperature Oxidation of Metals, Cambridge University Press, New York, 2006.

[45] E. Copland, D. Muers, E.J. Opila, N.S. Jacobson, Thermodynamics of silicon-hydroxide formation in H2O containing atmospheres. High Temperature Corrosion and Materials Chemistry III, 1994.

[46] A. Hashimoto, The effect of H20 gas on volatilities of planet-forming major elements: I. Experimental determination of thermodynamic properties of Ca-, Al-, and Si-hydroxide gas molecules and its application to the solar nabula, Geochim. Cosmochim. Acta 56 (1992) 511–532.

Paper III

The effect of Mo and Ge reactive elements on high-temperature oxidation of higher manganese silicide

Authors: **Antoine de Padoue Shyikira**, Naureen Akhtar, Gunstein Skomedal, Peter Hugh Middleton

Corrosion Science 194 (2022) 109920

Contents lists available at ScienceDirect

Corrosion Science

journal homepage: www.elsevier.com/locate/corsci

The effect of Mo and Ge reactive elements on high-temperature oxidation of higher manganese silicide

Antoine de Padoue Shyikira [a,*], Naureen Akhtar [a], Gunstein Skomedal [a,b], Peter Hugh Middleton [a]

[a] University of Agder, Norway
[b] Elkem ASA-Kristiansand, Norway

ARTICLE INFO

Keywords:
Higher manganese silicides
High-temperature corrosion
Thermal oxidation
Silicide thermoelectric materials

ABSTRACT

Higher manganese silicide (HMS) alloys ($Mn_{x-\alpha}Mo_{\alpha}Si_{y-\beta}Ge_{\beta}$ (x = 0.99–1.011, α = 0.005–0.02, y = 1.75, β = 0.005–0.01)) were studied to elucidate the effect of Mo and Ge pertaining to oxidation. Oxidation experiments were conducted using thermogravimetry and characterized using x-ray photoelectron spectroscopy (XPS) and scanning electron microscopy (SEM). Isoconversion experiments below 450 °C, shows that doping (up to 2 at%) raises the oxidation potential of HMS. Isothermally, the oxidation rate reduces buy one order of magnitude by doping on Mn and/or Si sites from 0.5 to 2 at%, revealing that the dopants-based oxides do not lessen the robustness of SiO_2 oxide.

1. Introduction

Thermal oxidation robustness in thermoelectricity is an important facet to consider while studying the stability of thermoelectric materials and modules. D.P. Whittle and J. Stringer [1] defines two essential requirements for alloys to withstand thermal oxidation, first to grow an oxide that thickens at a slow rate, and second that the oxide adheres to the alloy surface at any condition (thermal or environmental). Similarly, higher manganese silicide (HMS) as a binary alloy oxidises selectively forming a stable and protective silicon dioxide (SiO_2). As discussed in our recent publication [2], oxidation stability concerns stem from the level of impurities/dopants and the synthesis route including densification. In this article, much focus is put on the effect of dopants, and doping sites in the HMS matrix.

The benefits of "Al" and "Ge" doping on HMS were observed in our recent article [2], and thoroughly reviewed by Y. Miyazaki [3]. The common interest with HMS doping as a semiconductor is improved electrical conductivity of the thermoelectric (TE) materials, through increased charge carrier concentration. Moreover, particularly with Ge doping on the Si-site, a considerable reduction of MnSi striation was reported [4,5], the latter being another factor that lowers the electrical conductivity of the materials due to lack of crystallographic relationship between HMS and MnSi polycrystalline phases [6]. A similar effect (reduced striation) was also reported in case of doping on the Mn-site with Cr and Co ([7,8] and [9], respectively).

The effect of doping on the oxidation of alloys has been investigated on several compounds or systems, mostly on alumina and chromia scale adhesion [1,10–12], though not much was done on HMS. The main outcome of the studies was that the reactive elements (RE) additives, improved the oxide scale adhesion, interfacial diffusion, mechanical and chemical potential in the alloys or oxide scales. However, D. Naumenko et.al. [11], showed that another important aspect to consider is the level of interactions between RE and other elemental constituents of the alloy, since these reactions may complicate the optimisation of RE-dopant type and content.

The current study is a continuation of [2], we empirically discuss the oxidation kinetics/mechanisms of HMS (and its alloys), and qualitatively present the effect of dopant on the oxidation of HMS. A deviation in the oxidation kinetics of the pure HMS due to dopants and a thorough discussion of the mechanism is reported in this article. Finally, the coexistence of resultant Mo- and Ge-oxide species with the protective SiO_2 is presented, and an outlook towards further improvement is provided.

* Corresponding author.
E-mail addresses: antoine.d.shyikira@uia.no, tonnydepadoue15@gmail.com (A. de Padoue Shyikira).

https://doi.org/10.1016/j.corsci.2021.109920
Received 6 September 2021; Received in revised form 26 October 2021; Accepted 26 October 2021
Available online 31 October 2021

Table 1
Elemental composition by EDS of alloys in Fig. 1.

Alloy	Spot	Si [at %]	Mn [at %]	Ge [at %]	Mo [at %]	Tentative phases
$Mn_{0.97}Mo_{0.02}Si_{1.75}$	1	62	38			$MnSi_{1.75}$
	2	64	36			$MnSi_{1.75}$
	3	52	47		1	MnSi
	4	51	48		1	MnSi
	5	65	12		23	Mo rich
	6	66	13		21	Mo rich
$Mn_{0.99}Mo_{0.02}Si_{1.73}Ge_{0.02}$	1	63	37			$MnSi_{1.75}$
	2	64	13		23	Mo rich
	3	50	50			MnSi
	4	54	19	22		Ge rich

2. Materials and methods

2.1. Powder and pellet production

HMS alloys $Mn_{x-\alpha}$ Mo_{α} $Si_{y-\beta}$ Ge_{β} (x = 0.99–1.011, α = 0.005 – 0.02, y = 1.75, β = 0.005 – 0.01) were synthesized (check Table 2), an overview of raw material type and composition can be found in Table 1 of reference [2]. The elemental powder of Mn and Si were pre-alloyed with Mo and Ge, respectively. The pre-alloyed mixtures (Mn-Mo and/or Si-Ge) were mixed in a lid covered graphite crucible and heated fast (heating rate 100 °C/min) up to 1400 °C backfilling with Argon. The process was held for 10 min and then further heated up to above silicon melting temperature (specifically at 1450 °C). This temperature was then held for around 30 min to ensure all material melted and then poured into a graphite mould with a thickness of approximately 5 mm. To produce micron-sized powder, a Herzog HSM 100 vibratory mill with Tungsten Carbide (WC) vessel was used milling casted material pieces in batches of ~200 g running at 1400 rpm for 30 s. In addition, A RETSCH® Planetary Ball Mill PM 100 was used to mill the ingots down to nanosized powder. 20 g ingot were loaded together with stainless steel balls into a WC milling jar in an inert atmosphere (Ar). The ratio of milling ball, sample, and free space is 1/3: 1/3: 1/3 in volume. The powder was milled at 300 rmp with 2 min milling time and 1 min break to release the local heat, alternatively. The particle size distribution of the micron-sized powder was measured with a Malvern Mastersizer 2000, the D50 is around 5 μm, and a relatively broad range of particle sizes between 1 and 20 μm.

To consolidate the powder into ingots, Spark Plasma Sintering (Dr Sinter, SPS-825) was used. The powder was enfolded in graphite paper, loaded into a crucible (in an inert environment), and then cold-pressed using a manual hydraulic press at ~0.5 MPa. The cold-pressed pellet was then loaded in the SPS machine, pressure and temperature increased to 90 MPa and 850 °C (at 100 K/min heating rate), respectively. This temperature and pressure were held for a dwell time of 2 min. Furthermore, the temperature was reduced to 800 °C and pressure to 30 MPa. From then on, the pressure was released, and the pellets cooled naturally to room temperature.

2.2. Oxidation and microstructure analysis

The oxidation experiments were conducted using a TGA/DSC 1 (Mettler Toledo) on both powder and bulk samples. For isoconversion experiments, the powder samples were oxidised from room temperature to 1100 °C, with a constant heating rate of 5 °C/min in synthetic/dry air (5.0) with 50 ml/min purging rate. Isothermal experiments were carried out on bulk specimens, at temperatures from 250 °C to 600 °C for 24 h. Moreover, long-term oxidation experiments were conducted using an electric kiln SQ11 (KITTEC®) for 200 h in ambient air at 300 °C and 400 °C.

The oxidation residue was studied using Powder diffraction x-ray spectroscopy (XRD) for powder samples and X-ray photoelectron spectroscopy (XPS) on bulk samples. The XRD powder diffraction spectroscopy was carried out using a D8 Advance XRD instrument (from BRUKER). The instrument was set at 40 kV and 40 mA with a Cu X-ray tube. A continuous diffraction pattern was collected in locked coupled scan mode with a step size of 0.02° in the 2θ range of 10–80°. Moreover, the phases were qualitatively identified using the Bruker software EVA using the ICDD PDF-2 database.

Table 2
List of samples, nominal composition, and maximum isoconversion weight gain.

Sample ID[a]	Nominal composition	Powder - Total Weight gain [%]
$MnSi_{1.75}$	$MnSi_{1.75}$	12.673
Mo0.5_α	$Mn_{1.005}Mo_{0.005}Si_{1.75}$	8.878
Mo2_β	$Mn_{0.97}Mo_{0.02}Si_{1.75}$	5.32
Ge0.5_α	$Mn_{1.01}Si_{1.745}Ge_{0.005}$	5.671
Ge1_β	$Mn_{0.99}Si_{1.74}Ge_{0.01}$	7.726
Mo0.5- Ge0.5_β	$Mn_{0.985}Mo_{0.005}Si_{1.745}Ge_{0.005}$	19.116
Mo0.5- Ge1_γ	$Mn_{0.995}Mo_{0.005}Si_{1.74}Ge_{0.01}$	5.543
Mo2- Ge0.5_γ	$Mn_{0.98}Mo_{0.02}Si_{1.745}Ge_{0.005}$	7.86
Mo2- Ge2_α	$Mn_{0.99}Mo_{0.02}Si_{1.73}Ge_{0.02}$	6.663
Mo0.5-a	$Mn_{1.0095}Mo_{0.005}Si_{1.75}$	7.762
Mo1-a	$Mn_{1.0090}Mo_{0.010}Si_{1.75}$	8.352
Mo1.5-a	$Mn_{1.0085}Mo_{0.015}Si_{1.75}$	8.658
Mo0.5-b	$Mn_{1.0105}Mo_{0.005}Si_{1.75}$	7.455
Mo1-b	$Mn_{1.0100}Mo_{0.010}Si_{1.75}$	8.038
Mo1.5-b	$Mn_{1.0095}Mo_{0.015}Si_{1.75}$	8.075
Mo0.5-c	$Mn_{1.0115}Mo_{0.005}Si_{1.75}$	8.649
Mo1-c	$Mn_{1.0110}Mo_{0.010}Si_{1.75}$	8.531
Mo1.5-c	$Mn_{1.0105}Mo_{0.015}Si_{1.75}$	8.221

[a]Greek letters and a to c denote distinct Mn concentration in HMS before doping.

The XPS surface analysis was conducted using a Kratos Axis Ultra^{DLD} spectrometer with Al Kα X-ray monochromatic source (hν=1486.6 eV, at 10 A and 15 kV). The survey and high-resolution spectra were collected using step sizes of 1 eV and 0.1 eV, respectively. Similarly, the pass-energies used were 160 eV (survey spectra) and 40 eV (high-resolution core-level spectra). The spectra analysis was conducted using CasaXPS software, while the binding energy axis was calibrated using adventitious carbon (C-C) C 1 s photoemission peak centred at 284.8 eV. Further details and analysis of the XPS data are detailed in [2]. On bulk specimen, the microstructure images were taken using SEM (JEOL 772), the microscope was operated at a working distance of 10 mm and accelerating voltage of 15 kV. Based on backscattered images, the oxide phase composition was detected using an energy dispersive X-ray spectrometer (EDS) detector and analysed through line scan, spot analysis, and phase mapping using TEAM™ software (EDAX®-AMETEK®).

3. Results

3.1. Microstructure of the alloys

Among the alloys in Table 2, Mo2_β and Mo2- Ge2_α were selected to investigate the phase composition of the respective compounds, the selection is based on that is doped on the Mn site only while the other on both Mn and Si sites. Fig. 1 shows bulk $Mn_{0.97}Mo_{0.02}Si_{1.75}$ and $Mn_{0.99}Mo_{0.02}Si_{1.73}Ge_{0.02}$ SEM - backscattered electron (BE) micrographs, and Table 1 contains the EDS elemental compositions of spots shown on (a) and (b), respectively. The micrographs show that both compounds are multiphase alloys. $Mn_{0.97}Mo_{0.02}Si_{1.75}$ is composed of a heterogeneous mixture of $MnSi_{1.75}$, MnSi, and a ternary Mn-Mo-Si phase. HMS is the majority phase and is composed of relatively bigger grains, while the other two phases are minor especially MnSi, which is mainly found at the $MnSi_{1.75}$ grain boundaries. As discussed in our recent publication on oxidation of HMS [2], increasing the dopant (Al or Ge on the Si site) concentration from 0.5 at% towards 2 at% substantially increased the amount of MnSi striation in the compound. However, as shown by Fig. 1 substituting Mn with Mo relatively reduced the concentration of the one-to-one Mn-Si phase in the bulk.

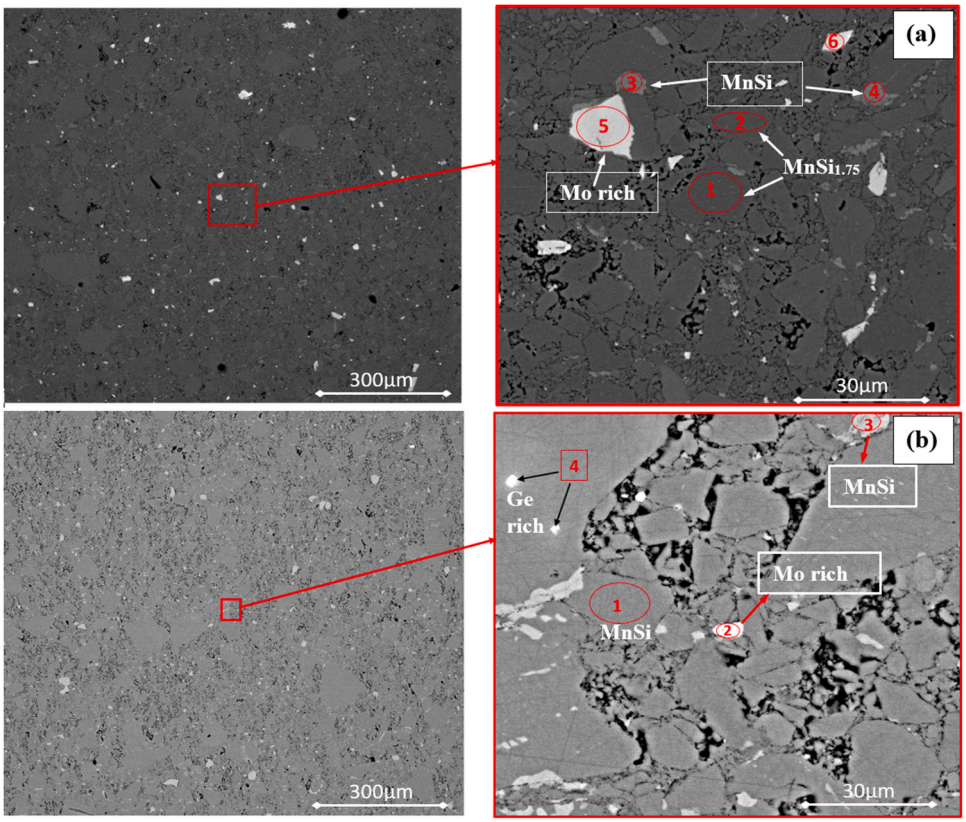

Fig. 1. As consolidated alloys' EDS spot analysis (see nominal composition in Table 1), (a) $Mn_{0.97}Mo_{0.02}Si_{1.75}$, (b) $Mn_{0.99}Mo_{0.02}Si_{1.73}Ge_{0.02}$.

Similarly, doping on both Mn and Si sites exhibited non-homogeneous microstructures, mostly composed of the $MnSi_{1.75}$, MnSi, and two ternary phases (Mn-Mo-Si and Mn-Si-Ge). As a general remark, it is evident that with doping on both sites the MnSi phase increases and the grains are bigger than doping on Mn Site only. There is no quaternary phase (Mn-Mo-Si-Ge) achieved, as a result of non-resolved "Ge" and "Mo" dopants as thoroughly described by J.S. Graff [13].

3.2. Isoconversion

The isoconversion was conducted on powder samples from 25 °C - 1100 °C with a 5 °C/min constant heating rate. Fig. 2 represents (a) three batches (α, β, and γ) of HMS with Ge and Mo dopants on the Si and Mn sites, respectively, and (b) batches (a, b and c) of HMS with Mo as dopant on the Mn site only. The zoomed images (upper right conners) show the oxidation at low temperatures (25 °C - 450 °C). All powders lost weight below 100 °C which is linked to humidity evaporation, while significant weight gain(oxidation) begins between 200 °C - 300 °C. The oxidation onset temperature varies with the dopant(s) concentration, where the higher the dopant concentration, the lower the onset temperature. In addition, the HMS alloys with low dopant concentration are more robust to oxidation relative to high doped compounds Fig. 3(a). However, at high-temperature oxidation (up to 1100 °C), the alloys are more robust with high dopant concentration Fig. 3(b).

Based on the XRD spectrum Fig. 4, silica (SiO_2) is the dominant and stable oxide phase among other present oxide phases. This is witnessed through Differential Scanning Calorimetry (DSC) Fig. 4(b), where the silica scale crystalizes at 420 °C, 540 °C, and 960 °C to form alpha quartz, beta quartz, and beta tridymite, respectively. The alloys' oxidation kinetics remain steady till 900 °C for most of the samples Fig. 2(a), except for those with higher Ge impurities which the weight gain rate was steeper at around 600 °C associated with germanium oxidation. Meanwhile, manganese- and molybdenum-based oxides were also present, which could be noticed by the endothermic reaction at 665 °C in Fig. 2(a) and (b).

3.3. Isothermal oxidation

The isothermal oxidation experiments were conducted to investigate the effect of doping HMS (on the Mn and/or Si sites) based on the thermal oxidation kinetics from 250 °C to 600 °C. Fig. 5 shows (a) the final relative weight gain of HMS alloys (with different dopant concentrations) after 24 h of isothermal oxidation in dry air. The magnified plot in the upper left corner shows that the weight gain of most of the alloys is below 1 $\mu g/mm^2$ up until 450 °C. Though the doping effect is minimal at low temperatures, the trend indicates that increasing Mo or Ge concentration translates into an increase in weight gain during oxidation. The doping effect was more pronounced on alloys with doping on both Mn and Si sites, where varying doping concentrations from 0.5 at% to 2 at% increased around ten times the weight gain, even at low temperatures (<450 °C).

Fig. 6 are maps of weight gain data per unit area of, three among studied compounds with different dopant concentrations, (a) $Mn_{1.005}Mo_{0.005}Si_{1.75}$, (b) $Mn_{0.985}Mo_{0.005}Si_{1.745}Ge_{0.005}$ and (c) $Mn_{0.99}Mo_{0.02}Si_{1.73}Ge_{0.02}$. The data were recorded every hour during isothermal treatment at respective temperatures (250 °C - 600 °C), and as the compound in (c) had the most weight gain, (a) and (b) data were mapped on (c) scale for comparison purpose. The dopant effect is shown by the trend of weight gain over time. With both Mo and Ge doping (0.5 at% each), the oxidation rate is reduced relative to the compound with Mo doping only, however with increased dopant concentration (2 at% on both Mo and Ge), the weight gain is substantially increased by one order of magnitude especially at higher temperature.

From 250 °C to around 450 °C, the oxidation kinetics fit well both linear and logarithmic oxidation laws (oxidation rates per model

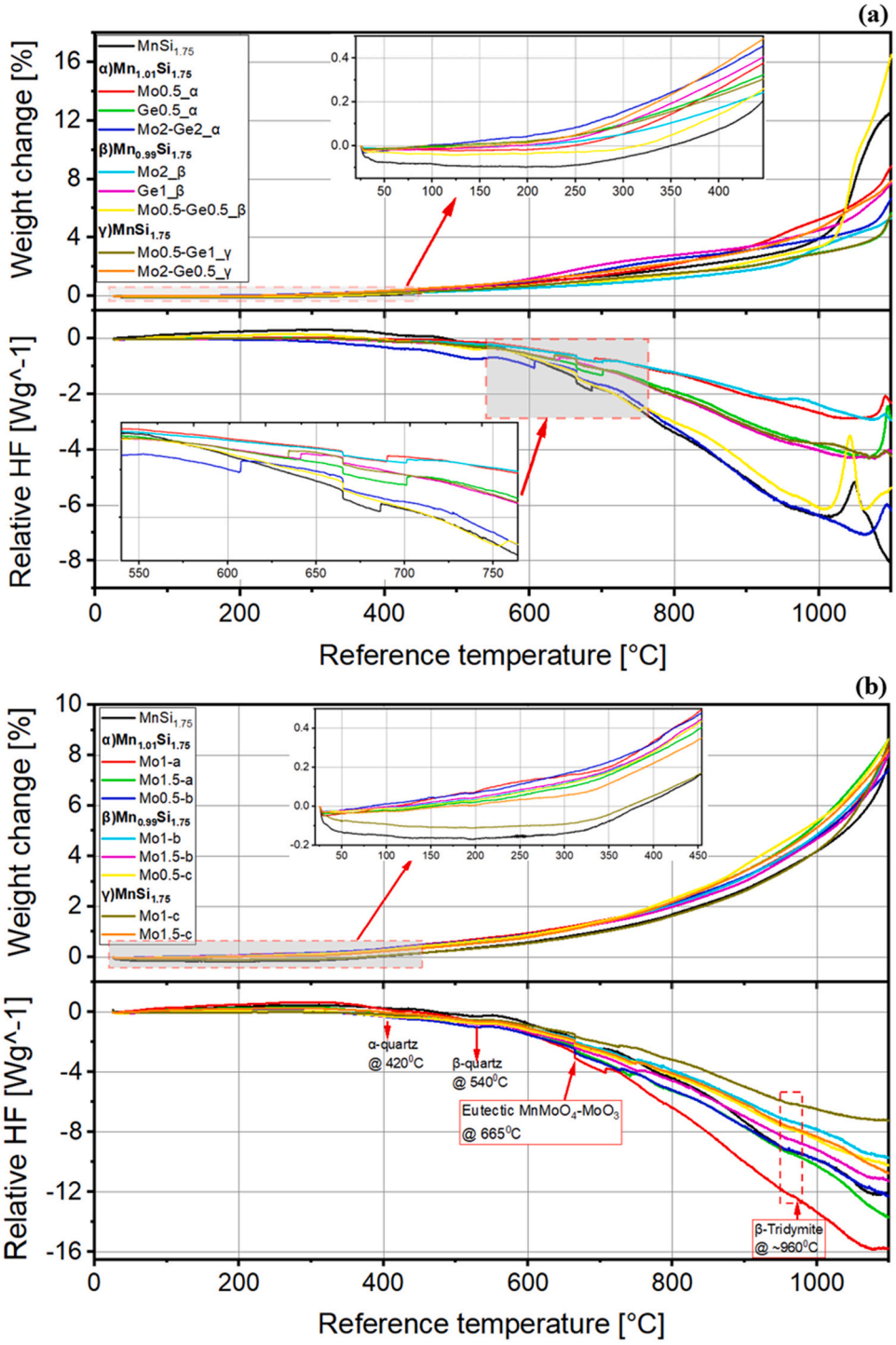

Fig. 2. TGA representation of HMS powder samples (a) Compounds with Ge and Mo dopants on the Si and Mn sites, respectively, (b) Only with Mo doping on the Mn site oxidized in Dry air from room temperature to 1100° C. Zoomed areas show oxidation at low temperatures 25 °C - 450 °C.

summarized in Table 3), however, as from the studies conducted on oxidation of Si [14,15], logarithmic law is considered the right model to represent the Si oxidation kinetics. Similarly, the logarithmic model was empirically found to better describe the HMS alloys oxidation in this study (mostly at 400 °C). That is simply because, Si is the major oxidation reactive element for all alloys and despite the well-known diffusion-controlled model (parabolic rate law), at low temperature, the oxidation reactions are much more reaction controlled than diffusion controlled.

On the other hand, Fig. 5(a) shows that at 600 °C for all alloys the weight gain course substantially deviated to a higher oxidation rate regime. The deviation is also shown for example on the TGA oxidation weight gain graph of Mo2-Ge2 Fig. 5(b), where the major factor is the weight gain at 600 °C where the oxidation followed a parabolic model. Therefore, in contrast to low temperature, HMS alloys above 500 °C oxidised parabolically. Table 3 tabulates the oxidation rates "kp" (approximated using Arrhenius model) of the studied alloys and addresses the composition effects on oxidation of the alloys (summarized in Table 3) as follows:

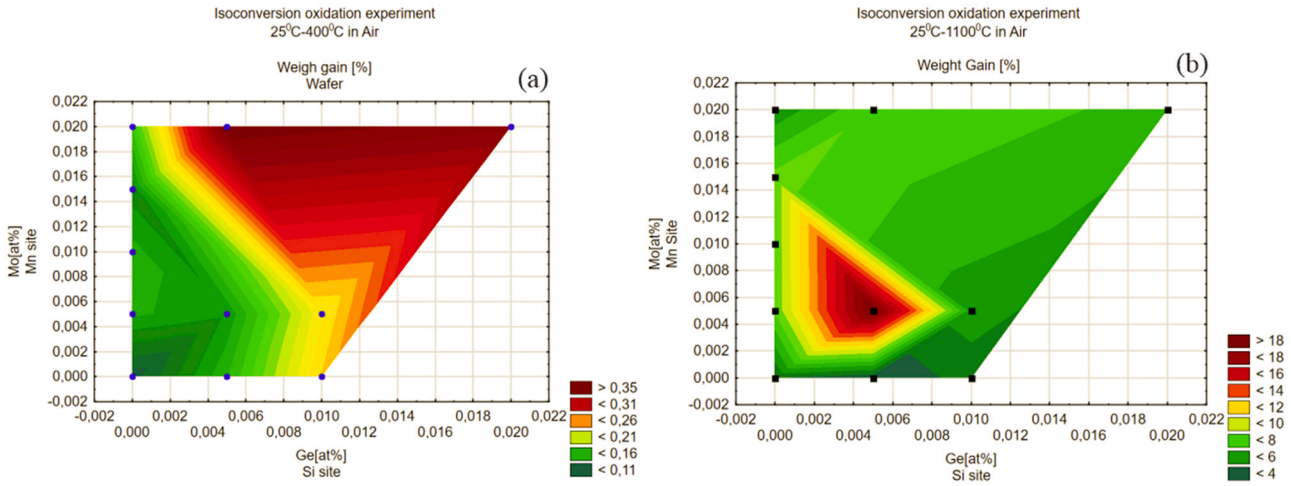

Fig. 3. Three-dimensional wafer map of the oxide weight gain after thermal oxidation in Dry air in the temperature range (a) 25 °C - 400 °C and (b) 25 °C - 1100 °C. Round and square spots represent the plotted data position.

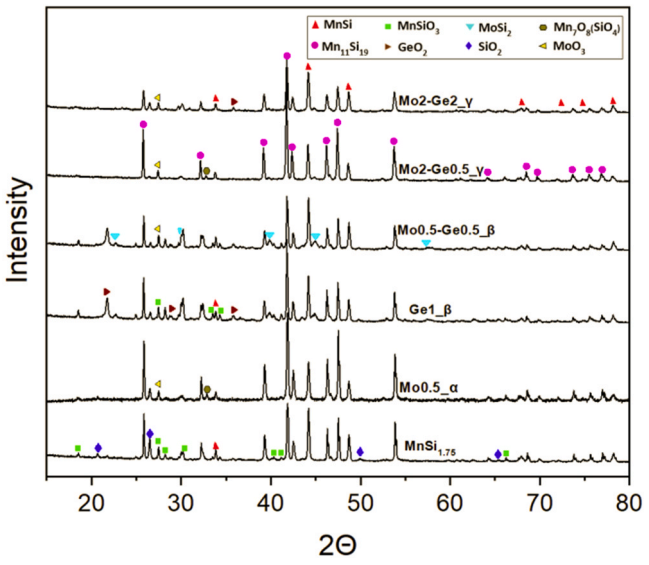

Fig. 4. X-ray powder diffraction spectrum showing the composition of the powder residue after oxidation at 1100 °C of the alloys marked by the samples ID as in Table 1.

a. For all alloys at low temperatures (250 °C – 350 °C), the thermogravimetric behaviour is similar, with oxidation rates of around 0.12 μg/mm^2. Moreover, the weight gain during oxidation follows the linear kinetics model or logarithmic model (especially for alloys with low dopant concentration). Empirically, the weight gain data following linear or logarithmic rate laws cannot be distinguished numerically (kp) or by looking at the TGA curves. However, as will be discussed in later sections, logarithmic rates have numerically lower kp values than linear rates. For example, in Table 3, $Mn_{1.005}Mo_{0.005}Si_{1.75}$ if both at 250 °C and 300 °C are fitted linearly, the growth rate at the higher temperature is lower than at lower temperature. Therefore, at 300 °C the oxidation kinetics follows logarithmic model.
b. Between 350 °C - 450 °C, most of the alloys followed logarithmic model, especially at 400 °C. Another common trend among all alloys is that the lower the dopant the more the alloys follow logarithmic law. The latter can be seen on alloys with Mo doping or Mo and Ge doped alloys, which means that it would take longer for compounds with higher Mo dopant to grow a protective scale than for those with less Mo concentration. However, at higher temperatures (≥ 450 °C), the alloys oxidise following parabolic law and logarithmic low. Table 3 shows that the alloys with low dopant 0.5–1 at% follow parabolic law, while from and above 2 at% dopant concentration the alloys still follow logarithmic law.

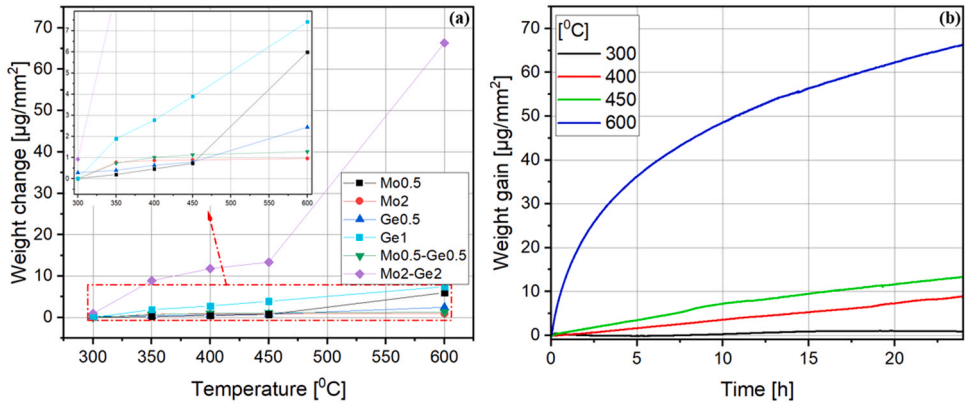

Fig. 5. Weight gain after isothermal TGA oxidation in synthetic air (5.0) for 24 h. (a) Comparison of different HMS alloys with different dopant concentrations (Mo dopant on the Mn site and Ge on the Si site) from the maximum weight gain at respective oxidation temperatures, (b) Isothermal TGA of Mo2-Ge2 at temperature from 300 °C to 600 °C.

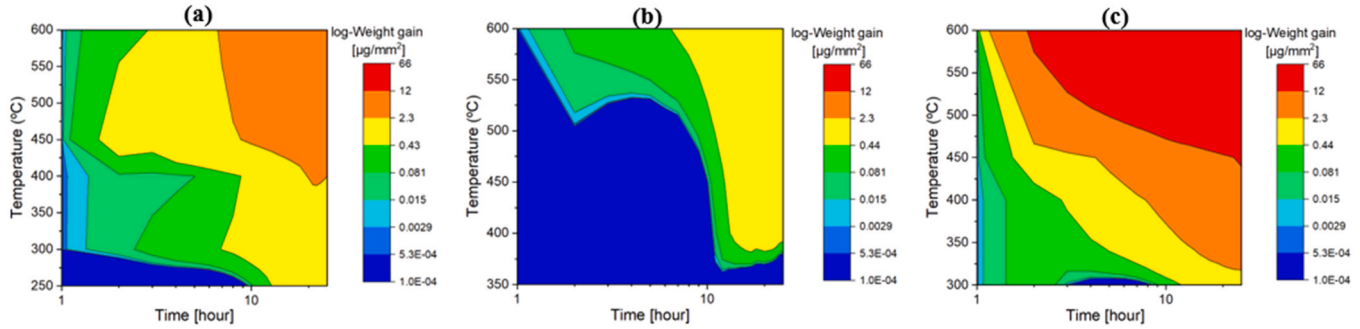

Fig. 6. Contour plot for the weight gain versus time at temperature from 250 °C - 600 °C. (a) $Mn_{1.005}Mo_{0.005}Si_{1.75}$, (b) $Mn_{0.985}Mo_{0.005}Si_{1.745}Ge_{0.005}$ and (c) $Mn_{0.99}Mo_{0.02}Si_{1.73}Ge_{0.02}$.

Table 3
Oxidation kinetics approximated by the Arrhenius model, the reaction rates are tabulated at specific temperatures and the model that the data fit symbolized by the superscript letter a to c.

Alloys	Weight gain - rate (kp) and law					
	250	300	350	400	450	600
$Mn_{1.005}Mo_{0.005}Si_{1.75}$	0.13[a]	0.08[b]	–	0.7[c]	0.9[c]	2.5[c]
$Mn_{1.005}Mo_{0.02}Si_{1.75}$	0.11[a]	–	0.12[a]	0.02[b]	0.46[b]	–
$MnSi_{1.74}Ge_{0.005}$	0.11[a]	–	0.114[a]	0.23[b]	2.91[c]	–
$MnSi_{1.74}Ge_{0.01}$ [2]	–	–	–	0.07[b]	0.02[c]	0.2[c]
$Mn_{0.985}Mo_{0.005}Si_{1.745}Ge_{0.005}$	–	–	0.16[a]	–	0.2[c]	0.22[c]
$Mn_{0.99}Mo_{0.02}Si_{1.73}Ge_{0.02}$	–	0.12[a]	1[a]	0.4[b]	0.6[b]	12[c]

[a] Linear law[µg/mm2],
[b] Logarithmic law[µg/mm2],
[c] Parabolic law [µg2/mm4].

c. Finally, around 600 °C, the growth rate follows parabolic law for all compounds.

3.4. Oxide scale micrographs and composition

3.4.1. XPS analysis

To acquire XPS data, samples were flooded with low-energy electrons to compensate for the charging effects. Fig. 7 shows the Mn 2p, Si 2p, and O 1 s high-resolution spectra core lines. For Mn 2p spectra, peaks at ~ 642 eV and ~ 654 eV were ascribed to the 3/2 and 1/2 spin-orbit splitting components, respectively, and are indicative of the Mn-oxide phases. However, the $Mn_{1.005}Mo_{0.02}Si_{1.75}$ (at 400 °C) showed the presence of another component at low binding energy as indicated by an arrow in Fig. 7. Compared to the Mn $2p_{3/2}$ (638.8 eV) for manganese silicide, this component appears at high binding energy. In case of a sample that consists of phases with different electrical properties, charge compensation may lead to differential charging. As a result, the relative position of the peaks coming from different phases may shift. To confirm if this chemical shift is due to differential charging, data was collected without and with flooded low energy electrons for charge compensation. After calibration of the binding energy axis using adventitious carbon (284.8 eV), the oxide component lines up. However, this is not the case for the silicide component.

Stable manganese oxide grows at different oxidation states (Mn^{2+}, Mn^{3+}, and Mn^{4+}), exhibiting many multiplet splitting [16]. It is, however, challenging to conduct a quantitative analysis due to the coinciding binging energies of the multiplet splitting structures [16,17]. However, manganese oxidation states can be identified from the Mn 2p peak features and the magnitude of the Mn3s peak splitting. The absence of the satellite feature on the higher binding energy side of the Mn $2p_{3/2}$ peak rules out the presence of MnO [16,18]. Mn 3 s peak splitting of ~5.5 eV (not shown here) evidence the presence of manganese as Mn^{3+}. The Si 2p XPS spectra for $Mn_{1.005}Mo_{0.02}Si_{1.75}$ (at 400 °C) Fig. 7, showed an intense peak (~103.7 eV) corresponding to Si^{4+} oxidation state and a small feature at the low binding energy core indicative of Si in the low-oxidation state(s) [19]. Similarly, the O 1 s spectra exhibited two features which components 1 and 2 are characteristic of Si-oxide and Mn-oxide, respectively [20]. The relative amount of Si-oxide to that of Mn-oxide increases with the oxidation temperature as evidenced in Fig. 7.

Furthermore, Fig. 8 shows that higher oxidation temperature promotes the formation of SiO_2 phase. Sample $Mn_{1.005}Mo_{0.02}Si_{1.75}$ (at 400 °C) showed the presence of Si_2O_3 and Si_2O phases apart from SiO_2. Nevertheless, the Si_2O phase is not present in sample $Mn_{0.99}Mo_{0.02}Si_{1.73}Ge_{0.02}$ (at 400 °C).(Fig. 9).

Analysis of Mo3d core level region evidenced the presence of two phases, MoO_3 and MoO_2 [21]. At higher oxidation temperatures, the only phase observed is MoO_3. Fig. 10 shows the presence of the GeO_2

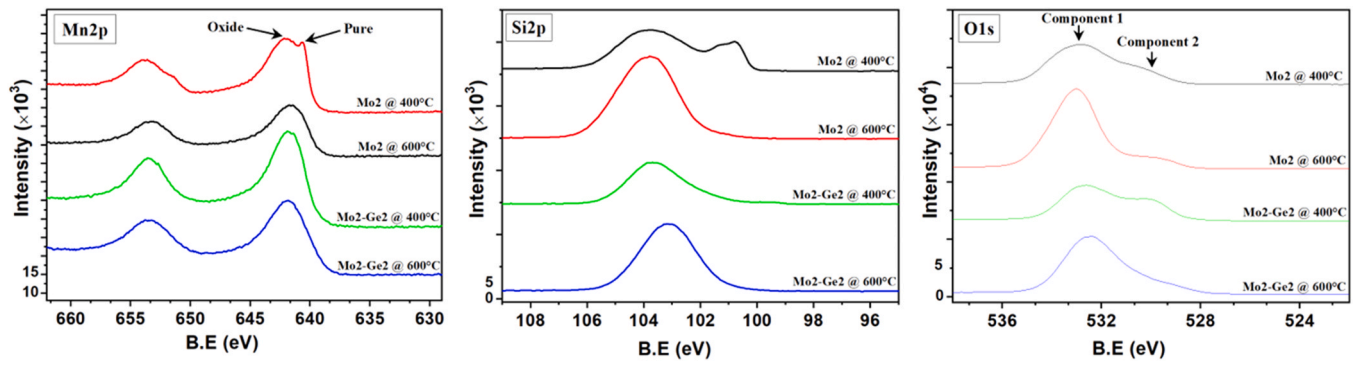

Fig. 7. X-ray photoemission spectra of the Mn 2p, Si 2p and O 1 s core-level regions.

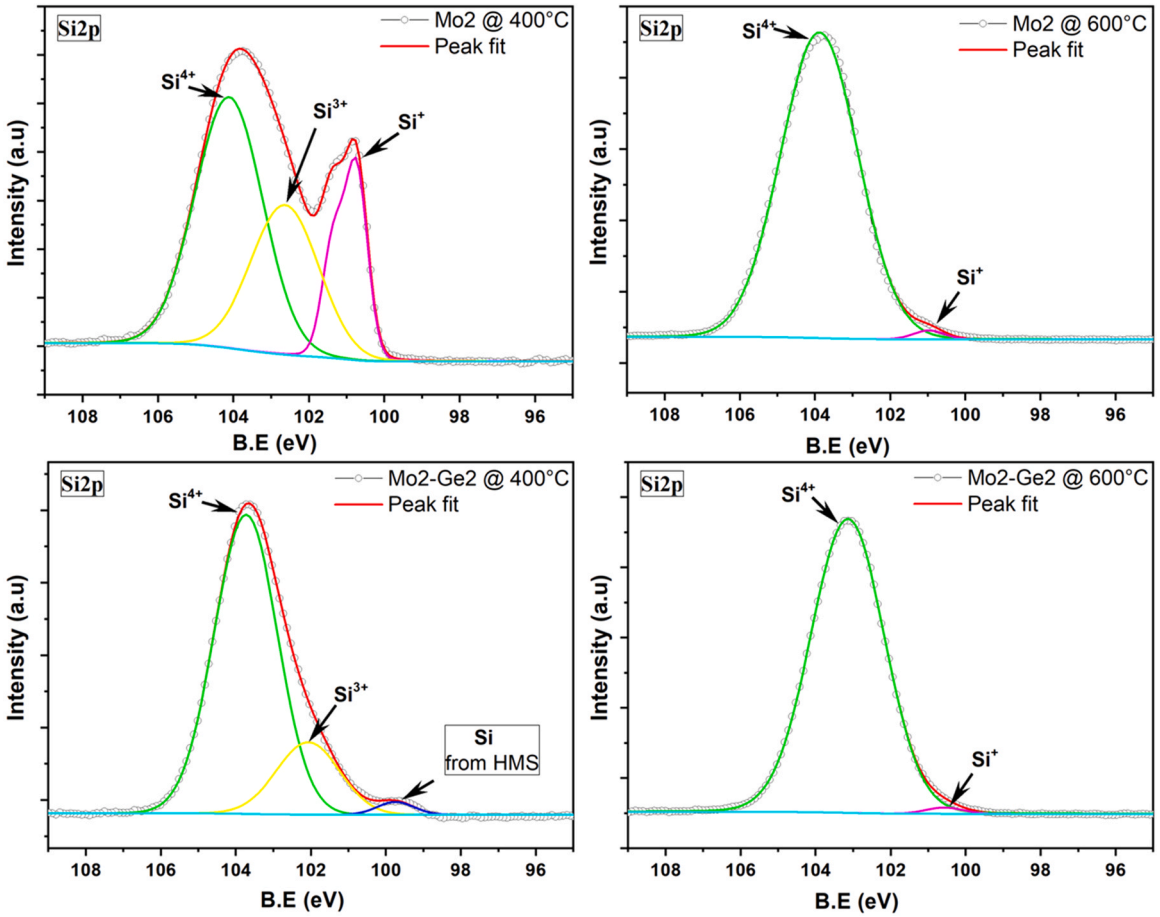

Fig. 8. X-ray photoemission spectra of the Si 2p core level region with peak fitting results.

phase in the Ge-doped samples [22]. However, at lower oxidation temperature (sample $Mn_{0.99}Mo_{0.02}Si_{1.73}Ge_{0.02}$ at 400 °C), another component at the lower binding energy side is present that is assigned to the elemental germanium.

3.4.2. SEM-EDS analysis

HMS alloys are robust to oxidation especially at low temperatures and short exposure to air, therefore, long-term exposure is key to enabling a microscopic visual analysis of the oxide scale. Figs. 11 and 12 present the SEM-EDS micrographs and phase maps of $Mn_{1.0095}Mo_{0.005}Si_{1.75}$ oxidation in air for 200 h at 300 °C and 400 °C, respectively. At 300 °C, a 150 nm non-uniform and coarse oxide layer can be seen. Much of the scale is SiO_2 as shown by the EDS phase maps, however, the lack of the other oxide species is attributed to the low detection level of the EDS detector. XPS as a more effective technique revealed the presence of Mn- oxides and Mo-based oxides (or Ge-based oxides for alloys with Ge dopant). Moreover, Fig. 11 shows that the oxide is thicker (around 250 nm) at the grain boundaries and thinner at the surface of the grains. This lack of scale uniformity at the alloy surface is due to the low phase homogeneity that leads to the presence of a conglomerate of oxides, especially at the grain boundaries. Fig. 12 on the other hand, shows that at 400 °C the oxide scale is more compact and thicker than at 300 °C. The oxide thickness is around 270 nm and is similarly composed mainly of SiO_2.

4. Discussion

4.1. The oxidation kinetic regimes

HMS alloys follow different oxidation models at respective temperatures as stated in the result section above, therefore it makes it difficult to experimentally approximate the energies of formation (for the alloys). Moreover, the alloys are robust to oxidation that in case of isothermal test carried out at short dwell time (24 h), it is difficult to accurately obtain reliable oxidation reaction rate using ideal cases Wagner theory since it does not consider some complicating factors including effects of impurities [23]. It is in that regard that, a new representation was adopted to discuss the mixed rate of oxidation per temperature as shown in Table 3. The technique used in this study employed the notion of Time-Temperature-Transform (TTT) diagram, to draw an oxidation map based on the thermogravimetric weight gain per unit area data of the actual alloys Fig. 6. The contour lines plots are not frequently used to interpret the oxidation kinetics of alloys. However, in this article, we adopted contour plots to recreate the oxidation weight gain profiles by projecting the elevations on the y-axis and distance on the x-axis (of the cartesian coordinate system) as in [24]. From the weight gain and oxidation rate profiles, the TTT diagram can be drawn in a simplified diagram, as in Fig. 13. The green and red curves are drawn based on TGA weight gain data of $Mn_{0.99}Mo_{0.02}Si_{1.73}Ge_{0.02}$, they represent the isothermal oxidation onset time and an approximate of the oxidation offset time, respectively. Further analysis and discussions are based on where you would land on the map if you projected data of a different alloy (among the studied compounds).

The TTT diagram, Table 3, and Table 4 combined reveal that the oxidation occurs through 4 different kinetic regimes.

1. Below 250 °C (represented by dashed area), the weight gain after 24 h was little to none, implying that the alloys were resistant to oxidation at low temperatures.

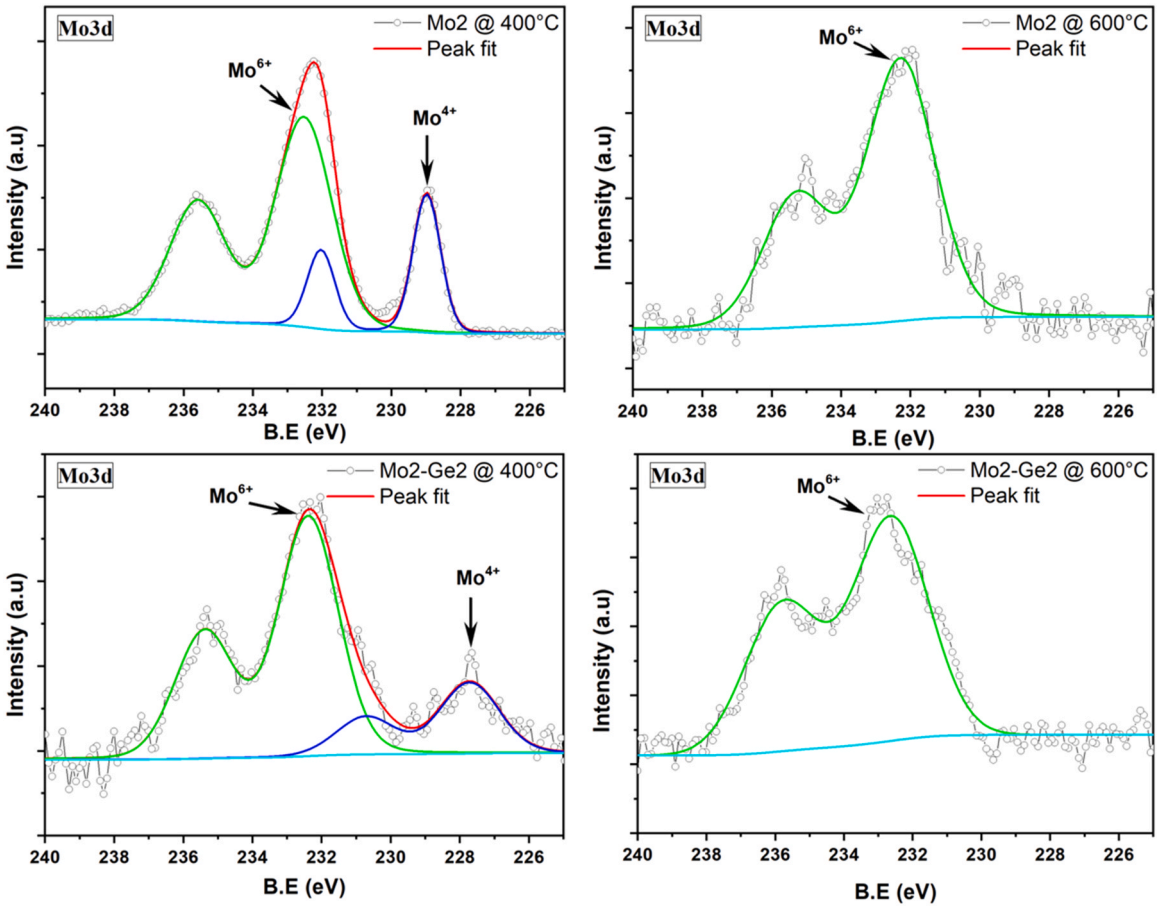

Fig. 9. X-ray photoemission spectra of the Mo 3d core level region with peak fitting results.

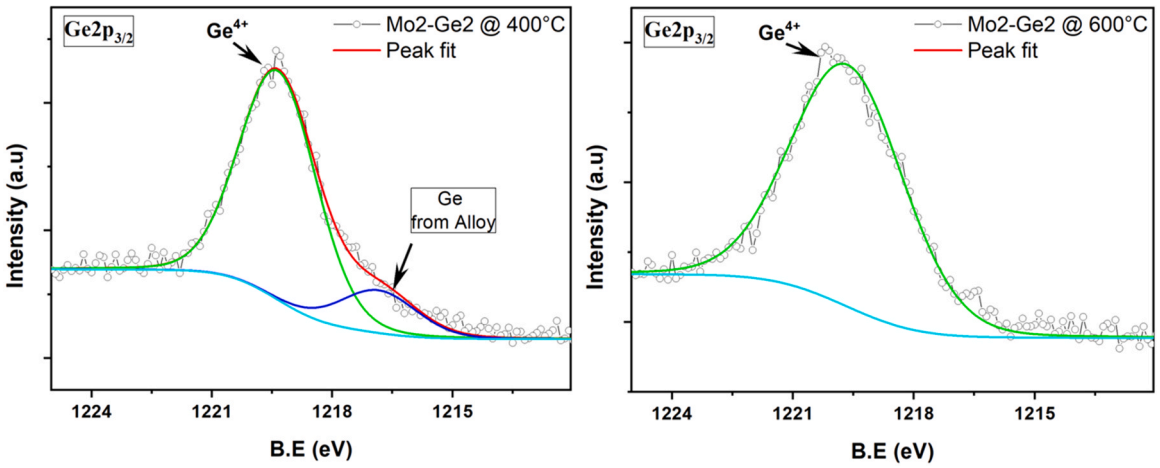

Fig. 10. X-ray photoemission spectra of the Ge 2p3/2 core level region with peak fitting results.

2. At temperature < 300 °C, the thermal gravimetric weight gain per unit area is low and fits the linear rate low (see the Byzantium colour area at the TTT diagram) as mentioned in Section 3.3. The linear rate law pertains to that, initially, the oxidant agent is adsorbed on the alloy surface at a constant rate(linear) until the whole surface is covered (monolayer) of adsorbate [25], therefore chemical reactions being the rate-determining process in this temperature range. By consulting Table 3, the linear regime extends up until 300 °C for alloys with high doping concentration and 350 °C for alloys with less doping. The same pattern is followed even at temperature > 400 °C, though, the gas adsorbate is quite fast and short (less than 1 h). The fast chemisorbed oxidant species at the oxide-gas interface, attract cations from the thin oxide scale to grow further the scale, though leaving hole defects in the old oxide phase. The latter creates cation defects gradient at the alloy-oxide phase that leads to consumption/transport of cations from the alloy across the alloy-oxide interface. At this point the scale is still too thin (hundreds of Angstroms ~1000) [26] and follows a logarithmic rate law (represented by the light and dark blue of the TTT diagram) for compounds with 2 at% dopant, while with less dopant the respective compounds fall

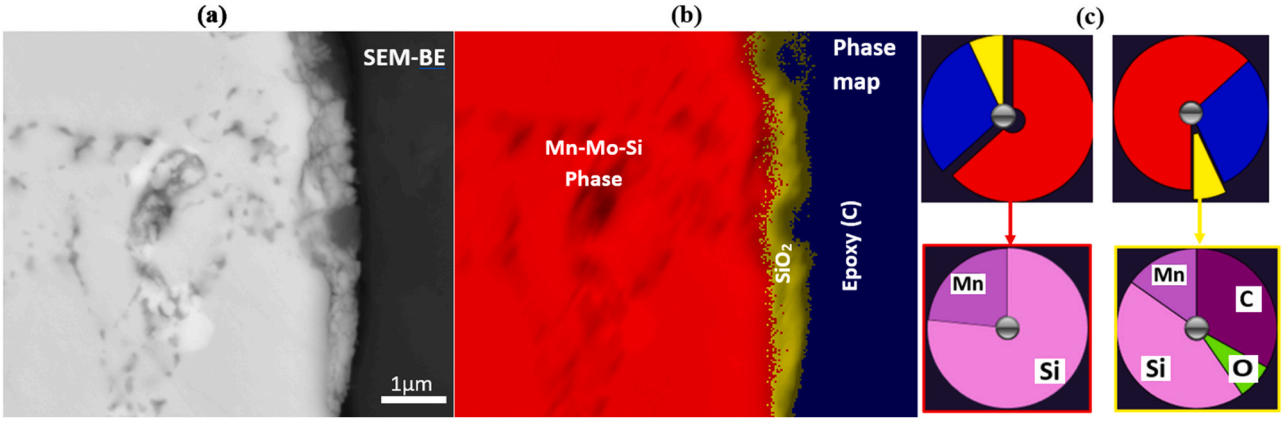

Fig. 11. SEM/EDS representation of $Mn_{1.0095}Mo_{0.005}Si_{1.75}$ oxidized at 300°C for 200 h in ambient conditions. (a) Backscattered electron (BE) image, (b) EDS Phase map image showing the cross-section of the interface between alloy and oxide scale layers, and (c) elemental composition illustrative of phases in (b), red – alloy phase and yellow – oxide phase. (For interpretation of the references to colour in this figure legend, the reader is referred to the web version of this article.)

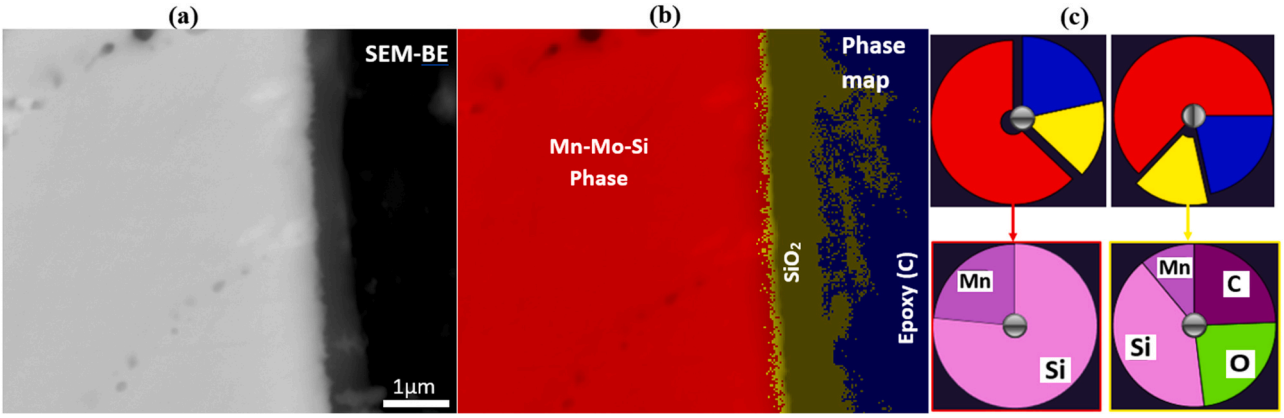

Fig. 12. SEM/EDS representation of $Mn_{1.0095}Mo_{0.005}Si_{1.75}$ oxidized at 400°C for 200 h in ambient conditions. (a) Backscattered electron (BE) image, (b) EDS Phase map image showing the cross-section of the interface between alloy and oxide scale layers, and (c) elemental composition illustrative of phases in (b), red – alloy phase and yellow – oxide phase. (For interpretation of the references to colour in this figure legend, the reader is referred to the web version of this article.)

in the parabolic regime in this temperature range (the latter will be discussed at point 4 below).

3. The logarithmic law extends to higher temperatures of 500 °C and 600 °C for the respective compounds, though for a very short duration. The logarithmic regime is described as a state at which the reactive species adsorbed at the alloy surface (linearly), creates a diffusion of anions towards the alloy core and cations in the opposite direction that creates an electric field across the oxide-alloy interface [26]. As it can be seen from Fig. 13, in the first 24 h of isothermal experiments, logarithmic law would be the main rate law for the studied alloys especially at temperatures from ~300–400 °C. However, considering the long-term experiments at 300 °C and 400 °C, it was empirically concluded that the logarithmic regime reduces over time, as a result of reduced ion diffusion at the alloy-oxide interface.
4. Finally, the parabolic regime (represented by dark yellow colour), is characteristic of a protective layer mainly composed of SiO_2. Empirically the compounds with less dopant, fall in the parabolic regime earlier than with high dopant concentration. This is simply because with fewer impurities the alloys would follow a model clause to that of pure HMS, with which the oxidation is selective with "Si" being the preferential element. The parabolic regime extends towards 600 °C, and as the colour gets lighter meaning that the scale is less protective at higher temperatures, though the study was conducted up to 600 °C. In the parabolic regime, interdiffusion across the oxide scale is the rate-determining process.

To summarize, the TTT diagram in Fig. 13 in this case used as an oxidation map, shows that the compounds studied were isothermally resistant to oxidation below 250 °C in dry air. However, above that temperature, they follow different oxidation models (linear, logarithmic, and parabolic), depending on the isothermal temperature and/or the composition (impurities concentration). The more impurities the alloys contained, the longer the alloy oxidised following linear law, and the lesser the impurities (for example, HMS in an extreme case), the early the alloy oxidized parabolically, where the oxide is mainly SiO_2. It is worth noting that non-protective oxide below the green curve connotes that there is no or non-substantial oxidation reaction in that temperature range. Nonetheless, non-protective oxide above the red curve conveys a threat to the stability of the alloys.

4.2. Mechanisms of oxidation

The individual constituents of the $Mn_{x-\alpha}$ Mo_{α} $Si_{y-\beta}$ Ge_{β} alloys have got a certain affinity to oxygen which tends to create a mixture of oxides, therefore the need to protect the alloy from all elements to be involved. Originally the alloys model was designed with oxidation resistance taken into capital consideration. As illustrated in [2], at the beginning Si is the preferential element involved in oxidation forming SiO_2 oxide, and HMS should theoretically be able to provide sufficient flux of Si until a compact SiO_2 layer is formed. In case, Si concentration reduces below the minimum concentration at the alloy-oxide interface, other reactive

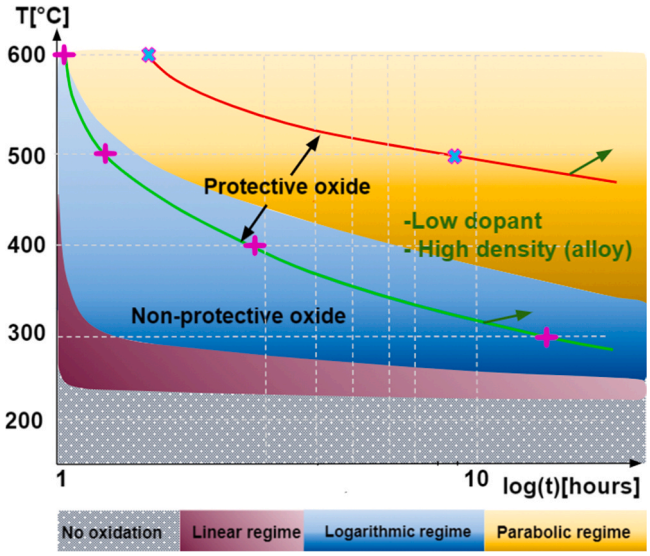

Fig. 13. The TTT diagram for isothermal oxidation of HMS with Mo and/or Ge as dopant(s). The green curve presents the process(oxidation) starts and the red curve - the process end. Green arrows point in the direct the curves are shifted towards relative to dopants concentration and density of the alloys. (For interpretation of the references to colour in this figure legend, the reader is referred to the web version of this article.)

Table 4
Classification scheme of the oxidation of the studies HMS alloys.

Class	Temperature range	Oxidation reaction	Rate governing factor	Oxide stability (Empirical)
1	< 250 °C	No signification reaction, hard to adhere to the alloy surface	The alloy robustness to oxidation	–
2	250–350 °C	Oxide scale is adherent to the alloy surface, significant weight gain starts after around 7 – 10 h of exposure, and fits a linear model	Chemical reaction (gas adsorption) at the alloy surface	1. Stable at low temperature 2. Stable over time[a]
3	400 °C < T < < 600 °C	Fast (1–2 h) gas adsorption (usually logarithmically), followed by a thickening of the oxide, mainly SiO_2 parabolic growth and protective.	Wagner diffusion-controlled or lattice diffusion of electrons/ions	1. Metastable for short[b] exposure 2. Stable over time
4	600 °C	Fast interdiffusion across the scale, and oxide volatility at higher temperatures (>700 °C)	Interdiffusion across the alloy-oxide interface, and oxide volatility	1. Stable for short exposure 2. Long-term should be investigated

[a] Long-term stand for 200 h;
[b] Short-term stand for 24 h

elements would be involved in oxidation. However, the coexisting Si, Mo, and Ge oxides mixture overlay in layers of the respective oxides, with the oxide with the higher solubility on the top (that being MoO_3, GeO_2, and SiO_2 at the alloy interface).

The above scenario is true for a homogeneous/single-phase alloy, but in case of multiphase or porous alloys, the oxidation mechanisms deviate from the ideal situation. The alloy studied being multiphase alloys, Fig. 14 is a schematic representation of the oxide growth mechanisms of $Mn_{x-\alpha}\,Mo_{\alpha}Si_{\,y-\beta}\,Ge_{\beta}$. The map is composed of 4 stages, starting from the original alloy composition (at the alloy surface – left on the figure) and progresses over time through stage 4, which is the final oxide layer studied using different surface characterization techniques (SEM-EDS and XPS) employed in this study.

Stage 2 of Fig. 14 shows the melt cast compound before oxidation, the composition of the alloys is as presented by the alloy's micrograph (Section 3.1) for further details. From the 3rd stage onward, it is evident that the alloys' oxidation mechanisms were a result of the alloy matrix structure and impurities' solubility. Therefore, the oxide growth on the alloy surface is governed by several oxidation processes. For HMS rich phase, the process follows the classic binary alloy oxidation theory, where Si is selectively reactive to oxidation and leaves a Si depleted phase with a composition close to MnSi at the alloy-oxide interface, where Wagner chemical diffusion (the theory of diffusion in solid oxides is also discussed by C.A.C. Sequeira [27]) is the rate defining factor.

On the other hand, based on the XRD results Fig. 4, two manganese silicates were detected as braunite (Mn_7SiO_{12}) and pyroxmangite ($MnSiO_3$). Moreover, Fig. 2(a) and (b) shows an endothermic reaction at 665 °C which is interpreted as the formation of a eutectic Mn-Mo oxide (33 wt% $MnMoO_4$ and 67 wt% MnO_3). The reaction occurrence is due to MnO_3, $MnMoO_4$, and Mn_2O_3 solid oxides mixture as by the Mn-Mo-O ternary phase diagram Fig. A1 [28] and discussed by K. Ivanov [29].

Above 1000 °C a sudden weight gain is noticed, early for less doped compounds (as Mo0.5-Ge0.5_β and $MnSi_{1.75}$). The exothermic reaction is represented by Eq. (1), and can also be seen in the $MnO\text{-}SiO_2\text{-}O_2$ computed phase diagram (using FactSage) in $p(O_2)$= 21% atm [30].

$$\frac{2}{3}Mn_7SiO_{12} + 4SiO_2 \rightarrow \frac{14}{3}MnSiO_3 + O_2 \quad (1)$$

$$Si + O_2 \rightarrow SiO_{2(S)} \quad (2)$$

Since none of the silicates was detected with XPS, the two would be attributed to being internal oxides or located at the alloy-oxide interface. It is difficult to know the exact mechanisms of formation of the two compounds, however, there are two possibilities. The first and most relevant is that the oxidant ions diffuse through the already formed oxide to react with the "Si" depleted layer, therefore the inner oxygen anions diffusion being the rate-determining factor. The second is that, though the presence of silica as protective oxide, the reaction of the dopants with oxygen may have compromised the level of protectiveness and lead to the formation of Mn-based oxides as shown in Fig. 14(3). Consequently, the coexisting Mn oxides and SiO_2 form a manganese silicate Mn_7SiO_{12} [31] as by Eq. (3), and the latter would transform into $MnSiO_3$ (check phase diagram, Figure) and release oxygen anion as shown by Eq. (1). Nevertheless, in both cases, the thicker SiO_2 gets the more the inner alloy surface will be attained.

$$2Mn_2O_3 + Mn_3O_4 + SiO_2 \rightarrow Mn_7SiO_{12} \quad (3)$$

As represented by Fig. 1, the alloys contain some Mo and Ge rich phases ($MoSi_2$ and possibly $GeSi_2$, respectively). Both phases contribute to the oxidation of the alloy, though following slightly different mechanisms to the classic binary alloy oxidation scheme they would follow if they were pure phases state. Unlike the case of oxidation of $MoSi_2$ [32] or $GeSi_2$ [33] compounds, at low temperature, the growth of MoO_2, MoO_3, and/or GeO_2 is much dominated by the growth of SiO_2 Fig. 14(3), that a continuous silica layer formation would leave them at the oxide/gas interface. Several studies [34,35] were conducted on the oxidation of Mo and showed that above 500 °C the Mo-oxide volatility increases, and becomes linear above 650 °C. Moreover, K. Ivanov [29], found that superficial Mo- oxides are not stable at temperatures above 600 °C.

To summarise, the alloys studied were multiphase alloys, which had a negative effect on the oxidation mechanisms of the alloys. As described

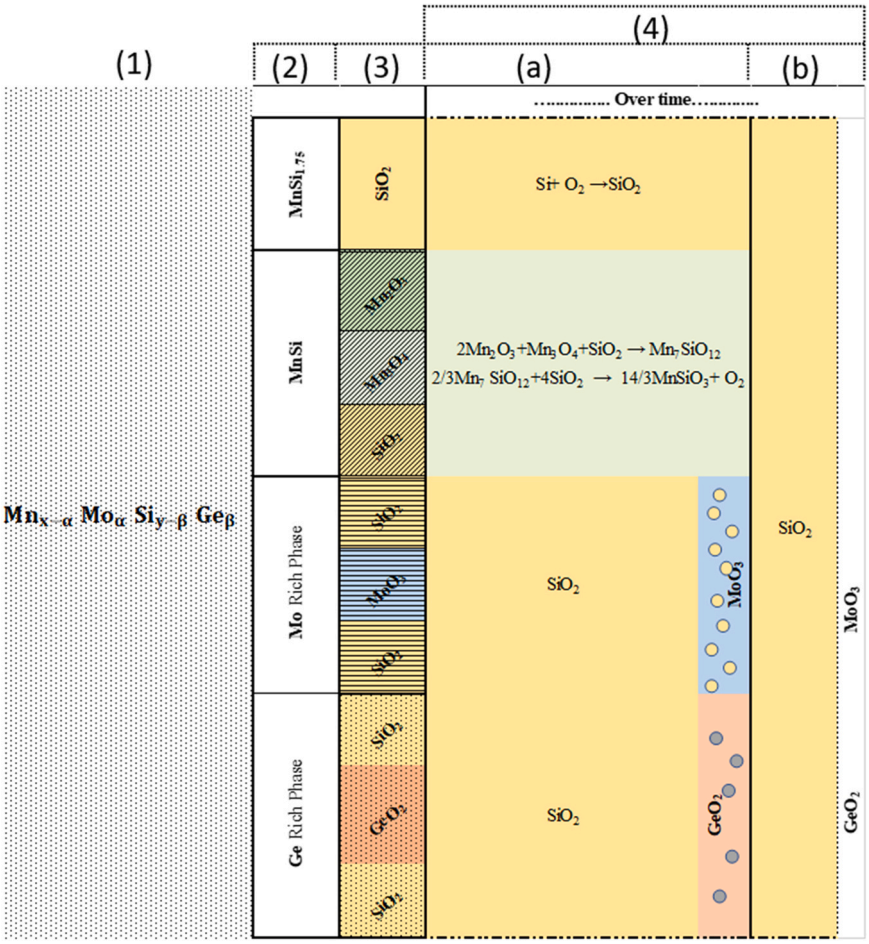

Fig. 14. Schematic representation of the evolution of the surface oxide layer of $Mn_{x-\alpha}\ Mo_{\alpha}\ Si_{y-\beta}\ Ge_{\beta}$ alloy in subsequent time steps from (1−4).

in a couple of paragraphs above, the overall performance of both short-term (24 h) and long-term (200 h) experiments showed that the compounds were resistant and resilient to oxidation. However, forasmuch as the dopants were involved in the early stage of the oxidation process, the thermoelectric performance (specifically the electrical conductivity) will much be affected because of reduced charge carrier concentration. It would highly be recommended to adapt/retune the synthesis method's parameters to achieve a more homogeneous compound, or possibly explore other possible synthesis methods rather than melt casting.

5. Conclusion

The oxidation of $Mn_{x-\alpha}\ Mo_{\alpha}\ Si_{y-\beta}\ Ge_{\beta}$ alloys are studied in the temperature range of 250–600 °C in synthetic air (5.0) for 24 h (for all alloys) and 200 h (for selected alloys). The study shows that the kinetic model of oxidation, varies from linear to parabolic at temperature around 300 °C and above. This is due to increased oxidation rate that originates from reaction to the oxidant agent of almost all elements that comprise the alloy. At low temperature (< 300 °C), chemical reactions at the alloy surface are the reaction rate-controlling factor in this temperature range. While at temperatures higher than 450 °C, diffusion through the oxide layer is the rate-determining factor, where SiO_2 is the main/dominant oxide phase. In addition, long-term experiments showed that the layer is protective with only 150 nm thick oxide at 300 °C and 250 nm thickness at 400 °C after 200 h. Therefore, revealing the potential of HMS alloys in the medium temperature range for thermoelectric application. Finally, based on the short-term (24 h) exposure experiments, all the alloys' constituents were involved in oxidation, which is unwanted. Though, this study did not determine how charge carrier density was affected by the alloy's oxidation, it is important to note that there is a level of materials consumption due to oxidation and take it into consideration during alloys' modelling stage. At temperatures lower than 400 °C, the alloys are resistant to oxidation even at longer thermal exposure, revealing the potential of HMS alloys in the medium temperature range for thermoelectric application.

CRediT authorship contribution statement

Antoine de Padoue Shyikira: Conceptualization, Methodology, Investigation, Validation, Formal analysis, Writing – original draft preparation, Writing – reviewing and Editing, Project administration. **Naureen Akhtar:** Methodology, Investigation, Validation, Formal analysis, Writing – original draft and Reviewing. **Gunstein Skomedal:** Grant writing and application, Conceptualization, Methodology, Supervision, Reviewing and Editing. **Peter Hugh Middleton:** Supervision, Reviewing and Editing.

Declaration of Competing Interest

The authors declare that they have no known competing financial interests or personal relationships that could have appeared to influence the work reported in this paper.

Data availability

Data used in this manuscript will be made available by the corresponding author upon reasonable request.

Acknowledgment

The authors would like to acknowledge the contribution of Elkem ASA, Sintef, and the University of Oslo (UiO) as partners in the TESil project. The contribution extends from material synthesis, pellet consolidation, and transport properties tests. Moreover, the authors would like to appreciate Ingvild Thue Jensen for her tremendous help in conducting the XPS tests. Finally, we acknowledge financial support from the Research Council of Norway (Project No 269326).

Appendix

See appendix Fig. A1 and Fig. A2.

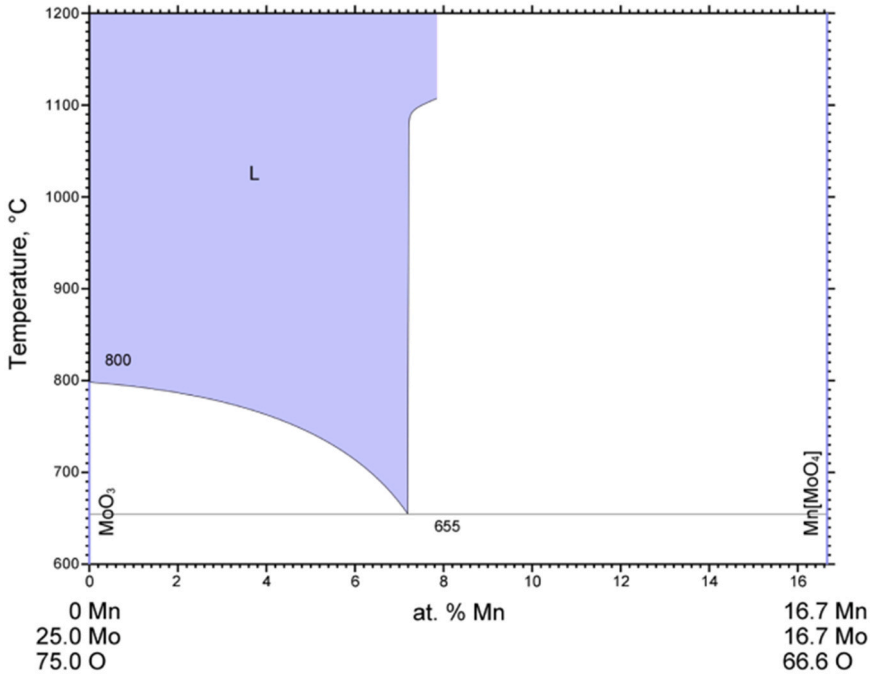

Fig. A-1. Mn-Mo-O Phase diagram [36].

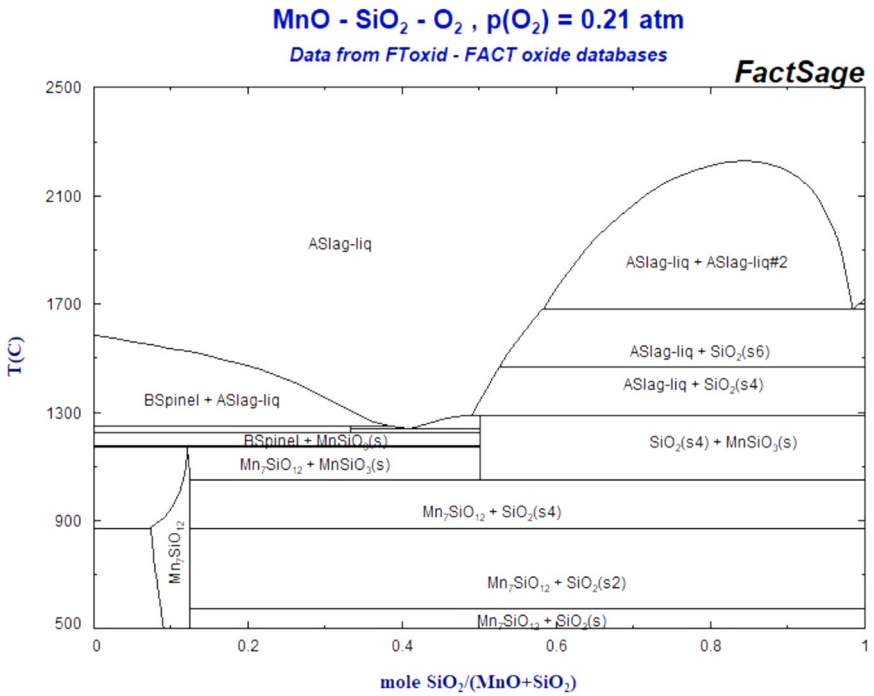

Fig. A-2. MnO-SiO_2-O_2 Phase diagram in P(O2) = 0.21 atm [30].

References

[1] D.P. Whittle, J. Stringer, Improvement in high temperature oxidation resistance by additions of reactive elements or oxide dispersions, Philos. Trans. R. Soc. Lond. 295 (1980) 309–329.

[2] Antoine de Padoue Shyikira, Naureen Akhtar, Gustein Skomedal, Tor Oskar Sætre, Peter Hugh Middleton, High temperature oxidation of higher manganese silicides (p), Corros. Sci. 185 (2021), 109327, https://doi.org/10.1016/j.corsci.2021.109327.

[3] Y. Miyazaki, 2.15. Higher manganese silicides, in Thermoelectric Energy Conversion, Woodhead Publishing, Sawston, 2021, pp. 374–387.

[4] I. Aoyama, M.I. Fedorov, V.K. Zaitsev, F. Solomkin, Yu, I.S. Eremin, A. Samunin, Yu, M. Mukoujima, S. Sano, T. Tsuji, Effect of Ge doping on micromorphology of MnSi in MnSi1.7 and on their thermoelectric transport properties, Jpn. J. Appl. Phys. 44 (12) (2005) 8562–8570.

[5] Yuzuru Miyazaki, Haruki Hamada, Hiroki Nagai, Kei Hayashi, Crystal structure and thermoelectric properties of lightly substituted higher manganese silicides, Materials 11 (6) (2018) 926.

[6] E.I. Suvorova, V.V. Klechkovskaya, Precipitates of MnSi cubic phases in tetragonal Mn4Si7 crystal, Crystallogr. Rep. 58 (6) (2013) 854–861.

[7] Quansheng Guo, Wenhao Zhang, Zihang Liu, Xiuwei Fu, Sylvain Le Tonquesse, Naoki Sato, Hyoung-Won Son, Kiyoshi Shimamura, David Berthebaud*, Takao Mori, Thermoelectric performance of Cr doped and Cr–Fe double-doped higher manganese silicides with adjusted carrier concentration and significant electron–phonon interaction, ACS Appl. Mater. Interfaces 13 (7) (2021) 8574–8583.

[8] Guo Liu, Qingmei Lu, Xin Zhang, Jiuxing Zhang, Yongjun Shi, In situ synthesis and thermoelectric properties of cr-doped higher manganese silicides, J. Electron. Mater. 41 (6) (2012) 1450–1455.

[9] H. Nagai, H. Hamada, K. Hayashi, Y. Miyazaki, Effects of cobalt substitution on crystal structure and thermoelectric properties of melt-grown higher manganese silicides, J. Electron. Mater. 48 (4) (2019) 1902–1908.

[10] P. Kofstad, Changes of Oxide Properties Through Doping, in High Temperature Corrosion, Elsevier Applied Science Publishers Ltd., London - Newyork, 1988, pp. 345–346.

[11] D. Naumenko, B.A. Pint, W.J. Quadakkers, Current thoughts on reactive element effects in alumina-forming systems: in memory of John Stringer (no), Oxid. Met. 86 (2016) 1–43, https://doi.org/10.1007/s11085-016-9625-0.

[12] P.Y. Hou, J. Stringer, The effect of reactive element additions on the selective oxidation, growth and adhesion of chromia scales, Mater. Sci. Eng. A 202 (1) (1995) 1–10.

[13] Joachim S. Graff, Raphael Schuler, Xin Song, Gustavo Castillo-Hernandez, Gunstein Skomedal, Erik Enebakk, Daniel Nilsen Wright, Marit Stange, Johannes de Boor, Ole Martin, Løvvik, Matthias Schrade, Fabrication of a silicide thermoelectric module employing fractional factorial design principles, J. Electron. Mater. 50 (2021) 4041–4049.

[14] Keunjoo Kim, Young Hee Lee, Myung Hwan An, Moon Suhk Suh, Chang Joo Youn, Kee Bang Lee, Hyung Jae Lee, Growth law of silicon oxides by dry oxidation, Semicond. Sci. Technol. 11 (7) (1996) 1059–1064.

[15] Zhijie Xu, Kevin M. Rosso, Stephen M. Bruemmer, A generalized mathematical framework for thermal oxidation kinetics, J. Chem. Phys. 135 (2) (2011), 024108.

[16] Zhi-Qiang Zou, Gao-Ming Shi, Li-Min Sun, Xiao-Yong Liu, Manganese nanoclusters and MnSi~1.7 nanowires formed on Si(110): a comparative x-ray photoelectron spectroscopy study, J. Appl. Phys. 113 (2013) 1–5.

[17] Mark C. Biesinger, Brad P. Payne, Andrew P. Grosvenor, Leo W.M. Lau, Andrea R. Gerson, Roger St.C. Smart, Resolving surface chemical states in XPS analysis of first row transition metals, oxides and hydroxides: Cr, Mn, Fe, Co and Ni, Appl. Surf. Sci. 257 (2011) 2717–2730.

[18] Huaxing Sun, Xiangdong Qin, Francisco Zaera, Chemical nature of the thin films that form on SiO2/Si(100) surfaces upon manganese deposition, J. Phys. Chem. Lett. 2 (20) (2011) 2525–2530.

[19] Annett Thogersen, Josephine H. Selj, Erik S. Marstein, Oxidation effects on graded porous silicon anti-reflection coatings, J. Electrochem. Soc. 159 (5) (2011) 1–7.

[20] Eugene S. Ilton, Jeffrey E. Post, Peter J. Heaney, Florence T. Ling, Sebastien N. Kerisit, XPS determination of Mn oxidation states in Mn (hydr)oxides, Appl. Surf. Sci. 366 (2016) 475–485.

[21] S. Al-Kandari, H. Al-Kandari, F. Al-Kharafi and A. Katrib, Surface electronic structure-catalytic activity correlation of partially reduced molybdenum oxide(s) for the isomerization of light alkenes and alkanes, Journal of Physics: Conference Series, vol. 100, 2008.

[22] Shingo Ogawa, Ryohei Asahara, Yuya Minoura, Hideki Sako, Naohiko Kawasaki, Ichiko Yamada, Takashi Miyamoto, Takuji Hosoi, Takayoshi Shimura, Heiji Watanabe, Insights into thermal diffusion of germanium and oxygen atoms in HfO2/GeO2/Ge gate stacks and their suppressed reaction with atomically thin AlOx interlayers, J. Appl. Phys. 118 (23) (2015), 235704.

[23] P. Kofstad, Comparison of Theory and Experiment. High Temperature Corrosion, Elsevier Applied Science Publishers Ltd., London - Newyork, 1988, p. 182.

[24] Britannica, T. Editors of Encyclopedia, Contour line, 26 10 2016. [Online]. Available: ⟨https://www.britannica.com/topic/contour-line⟩. [Accessed 06 04 2021].

[25] P. Kofstad, Phase Boundary Reactions. High Temperature Corrosion, Elsevier Applied Science Publishers Ltd., London - Newyork, 1988, pp. 261–262.

[26] Neil Birks, Gerald H. Meier, Fred S. Pettit, Mechanisms of oxidation. Introduction to the high temperature oxidation of metals, second edition.,, Cambridge University Press, Cambridge, 2006, pp. 39–74.

[27] Cesar A.C. Sequeira, Diffusion in Solid Oxides. High Temperature Corrosion Fundamentals and Engineering, Wiley, Hoboken - New Jersey, 2019, pp. 160–161.

[28] A. International, Manganese-Molybdenum-Oxygen Ternary Alloy Phase Diagram (based on 1973 Ziolkowski J.), ASM International, Ohio, 2011.

[29] K. Ivanov, P. Litcheva, P. Klissurski, T. Popov, Thermal stability of MnMoO4-MoO3 catalysts for methanol oxidation, J. Therm. Anal. 36 (1990) 1361–1368.

[30] FactSage, MnO-SiO2-O2 Phase diagram, ⟨https://www.crct.polymtl.ca/fact/phase_diagram.php?file=Mn-Si-O_MnO-SiO2_air.jpg&dir=FToxid⟩: FactSage.

[31] P. Palvadeau, P. Euzen, M. Queignec, J.P. Venien, Characterization of Mn7SiO12, a synthetic equivalent of “braunite” a natural mineral with various manganese sites, Mater. Res. Bull. 26 (9) (1991) 841–848.

[32] Neil Birks, Gerald H. Meier, Frederick S. Pettit, Oxidation of alloys. High Temperature Oxidation of Metals, Cambridge University Press, 2006, p. 132.

[33] H.K. Liou, P. Mei, U. Gennser, E.S. Yang, Effects of Ge concentration on SiGe oxidation behavior, Appl. Phys. Lett. 59 (1991) 1200–1202.

[34] E.A. Gulbransen, K.F. Andrew, F.A. Brassart, Oxidation of molybdenum 550C to 1700C, J. Electrochem. Soc. 110 (9) (1963) 952–959.

[35] M. Simnad, Aija Spilners, Kinetics and mechanism of the oxidation of molybdenum, J. Met. 7 (1955) 1011–1016.

[36] ASM International, Manganese-Molybdenum-Oxygen Ternary Alloy Phase Diagram, ASM International, Cleveland - Ohio, 2007.

Appendix D

Automated point contact measurement rig design

D.1 The rig design

A point contact measurement (PCM) apparatus is a kind of electrical characterization equipment that measures and maps the electrical characteristics of materials with the help of a three-dimensional (3D) platform with automatic movability. As shown in figure 5.4 (b), by passing a constant DC current through the test sample, the test rig uses four-point techniques to measure the voltage drop across a defined area of the test sample. Then the electrical characteristics of the test area – namely, electrical resistance, and electrical conductivity or resistivity are automatically computed using a micro-conductive probe (Quad00 [291]). Analog and digital power supplies are used to pass a current through the sample and to power the rig's stepper motors, respectively.

A digital multimeter (DMM 34470A – KEYSIGHT) with 4 wire measurement capabilities is used to measure the voltage drop across the sample. The voltmeter readings are mapped in real time and saved in a text file for later analysis. The rig's 3D linear motion, the motor's power supplies, and the voltmeter are controlled via a National Instrument (NI) LabVIEW program. The program allows the user to define a target area (or scan region) and is used for data logging as well as automatic results mapping. The PCM test rig is composed of three main parts: the 3D linear motion actuator elements, the electronic components, such as DC power suppliers and multi-meters, and a computer with LabView control program.

D.1.1 Linear motion control

The 3D motion is executed in three stages in the X, Y and Z directions (as shown in figure A.4) by three stepper motors in combination with aluminum plates, one for each of the three axes. The plates were designed using SOLIDWORKS® and machined from aluminum blocks using a computer numerical control (CNC). On all axes, the linear motion is actuated by a combination of step- per motors, coupled to a leadscrew and nut assemblies. Figure A.1 shows the x-axis configuration where the stepper motor is attached to the base by a bracket and the middle plate is assembled with the leadscrew, which connects to the motor by "flexible shaft coupling [292]". This assembly actuates the x-axis linear motion from the stepper motor's rotational motion sliding the middle plate using four carriages on the rail (or linear guide) attached to the base.

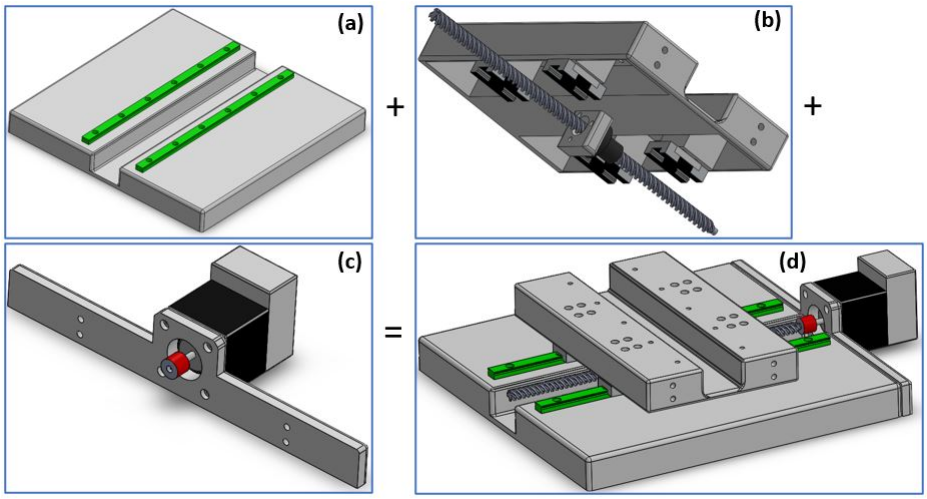

Figure A.1: (a) The base plate mounted with two linear guides, (b) the middle plate, the anti-backlash leadscrew and four carriages assembly, (c) a stepper motor and bracket assembly and (d) the full x-axis positioning stage.

Similarly, on the y-axis, the stepper motor is attached to the middle plate by a bracket and the linear motion is actuated by the sample plate (see figure A.2(b)) and y-axis leadscrew assembly. The y-axis components are assembled using the same process used for the x-axis above, except that there are only two carriages (or slides) since the sample plate is not as wide as the middle plate. The z-axis motion is executed in a similar fashion as on the x and y axes, though in a vertical direction. However, the probe arm is attached to the carriage by a bracket (see figure A.2 (a)), which is a slightly different design than the x and y positioning stages.

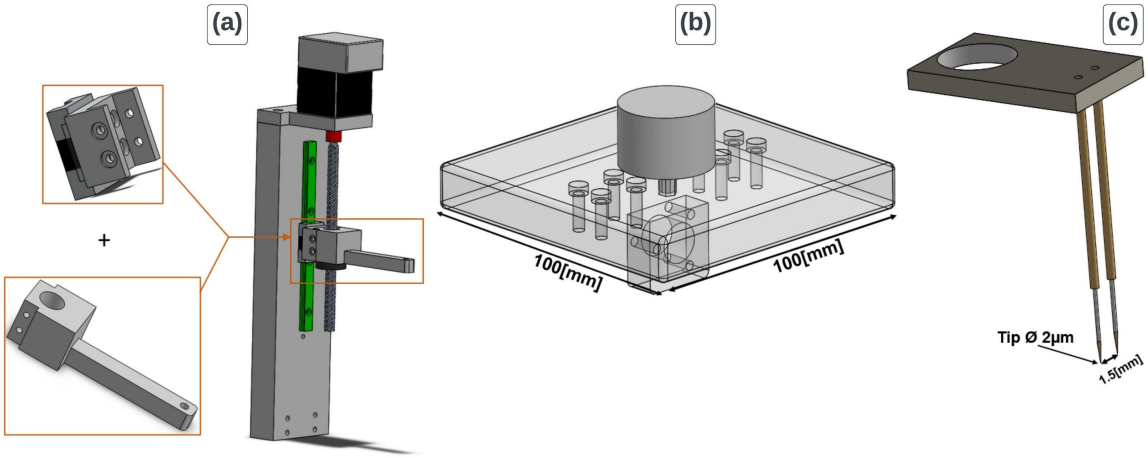

Figure A.2: (a) The full z-axis positioning stage. On the left-hand side, we see how the probe arm is connected to the carriage by a bracket. (b) A 100x100 [mm] sample plate. It has a hexagonal cylinder-shaped hole that holds the top sample holder used in case of small or special samples. (c) The probe mount model.

Figure A.4 shows the complete 3D model of the PCM test rig, which is 350x350x400 [mm] in size and weighs 5 kilograms. The number labels in red show the main parts of the rig. The motors and the motorized actuators were all purchased from RELIANCE PRECISION^{TM} [292] (See figure A.3 (b)-(d)). (1) corresponds to the stepper motors.

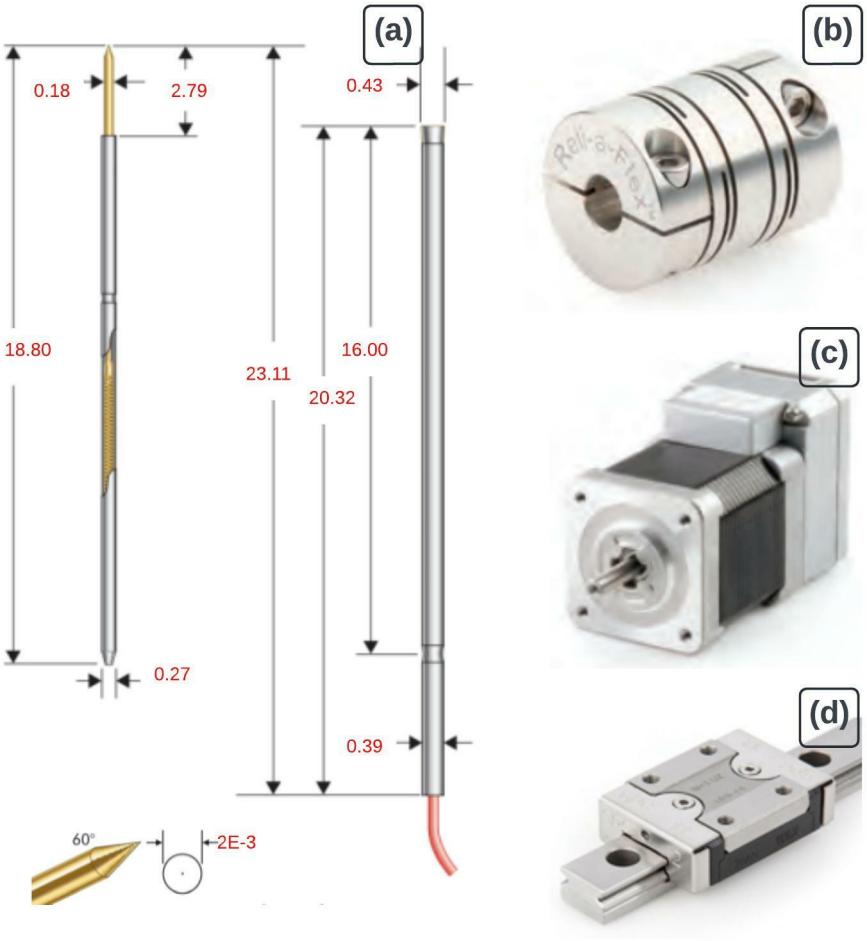

Figure A.3: (a) The QUAD-00 Spring Contact Probe and dimensions, (b) the flexible coupling, (c) the stepper motor, and (d) the miniature linear guide.

Each motor produces up to 18-watt output power and continuous torque of 0.36Nm and can reach up to 3000rpm maximum speed. (2) is the anti-backlash lead screw (1mm pitch) and nut assembly that converts the radial to linear motion. One revolution is equivalent to 1mm linear travel. (3) and (4) are the miniature linear guide combinations which consist of a stainless steel rail and a carriage(s) with re-circulation ball bearings. (5) is the flexible shaft coupling, which is adapted to couple the stepper motor shaft with the leadscrew to transfer kinetic motion, but at the same time to compensate for any misalignment (angular: $\pm$ 3°, axial:$\pm$ 0.5mm). (6), (7), (8) and (10) are the base, middle, sample, and z-axis mast plates, respectively; they are machined from aluminum blocks. (9) serves as the sample holder (maximum size 20x20 [mm]); however, in the case of wider samples of maximum 100x100 [mm], the samples are mounted on the sample plate. It is important to note that the sample holder slides in/out of the sample plate by a

hexagonal prism extension, figure A.2 (b). (11) is the probe arm that serves to both hold the probe(s) and linearly travel up and down, for point contact purpose.

Finaly, (12) is the QUAD-00 Spring Contact Probe figure A.3 [291] mounted as on figure A.2 (c). The probe is spring loaded with a working travel distance of 1.7 mm (to suppress the vertical contact shock) and have a rated current of 0.3 amperes.

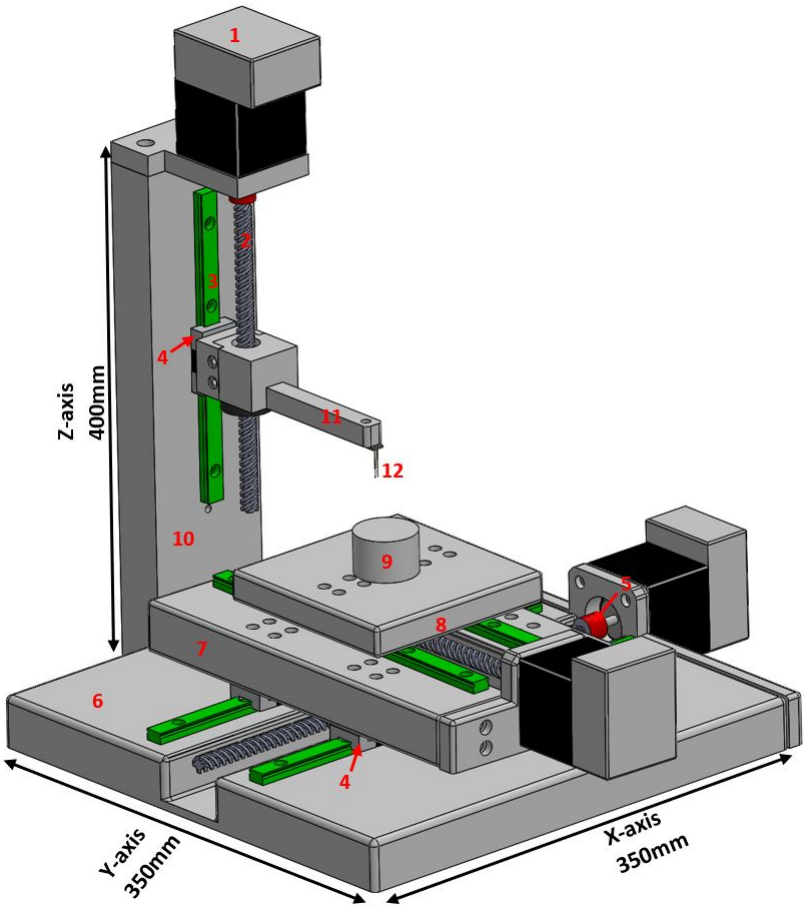

Figure A.4: The complete 3D model of the PCM test rig, with all components numbered.

D.1.2 Motion control program

The test rig built shown in figure A.4 operates along three axes, two horizontally interlaced (x & y) and one vertical platform (z). The main task is to scan a two-dimensional area of length "X" and width "Y" and at the same time perform point contact motions along the vertical axis "Z". Moreover, the system should be able to operate at a high resolution of up to 1 μm linear step size. This means a scan area of 20x20 [mm] with 1µm resolution on both the x- and y-axes would result in around 1 billion data points, which would without a doubt, take more than 24 hours.

Therefore, it is important to develop a fast and automated system both for control purposes and high-resolution linear displacement practicality. Figure A.6 is a control program flowchart that controls motors, linear actuators, electronic components, and data processing (record, processes, plotting and storage).

The control program was built using LabView software from National Instruments. Initially, the program starts by switching on all electronic components (motor's power supply, DC current supply, and the voltmeter). Then the user must choose between operating the rig automatically or manually using scroll bars. Manual operation was adopted, not only to allow manual operation of the rig but also to be able to set the "home position". After setting the home position, the desired scan area is inserted on all axes, as well as the respective step sizes (note that the step size on all axes may differ if desired).

At the start of the automatic area scan and point contact measurement, the y-axis motion is initiated to the starting position "$Y_i = 0$", then "$X_i = 0$" sequentially. The sequence continues with the initiation of the motion at the z-axis, where the probe will be carried toward the sample until full contact between the probe tip and the sample. At this point the control system locks the linear motion and proceeds to trigger the digital multi meter (DMM) to acquire, process, display and store data as shown in figure A.5 below. Then the z-axis travel upward to the initial position.

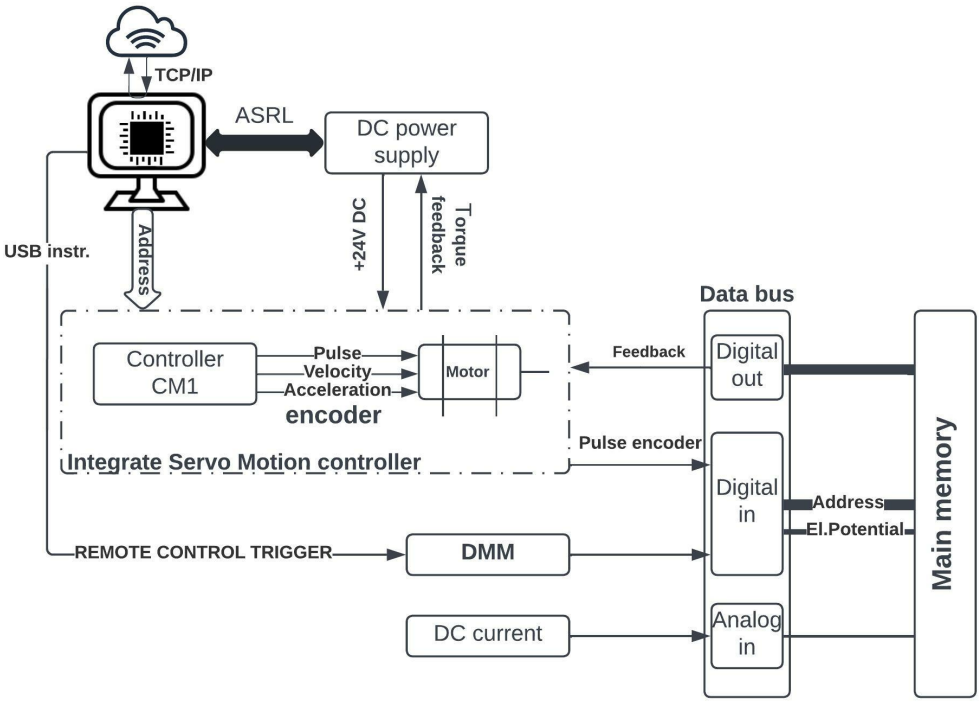

Figure A.5: Electronic signals/data flow and hardware connections.

After the probe is off the sample, the x-axis is updated to the next address or position (i.e. $X=X_i+X_{stepsize}$); subsequently the z- axis travels back to the sample and data are recorded as in step one. The same process will be repeated on the x-axis until the full length of "X" is finished. At that point the y-axis motor updates by one step to the next line scan and the x-axis travels back to the position parallel to its starting position and so forth until the width of the scan area "Y" is finished. When the scan area is finished and the last data point written into the data base, the program is terminated, and all electronic components stop automatically.

Through an internet connection, the test rig (figure A.8) can be safely operated remotely along with a camera that helps to visualize the test rig live and allows recording a video of the whole apparatus if needed. It is also important to note that the scan area and step size can be updated (made shorter or longer) mid-scan, and the apparatus can run for a long period without supervision. Lastly, since the database is updated at every data point, data can be retrieved anytime during the scan time without affecting the test.

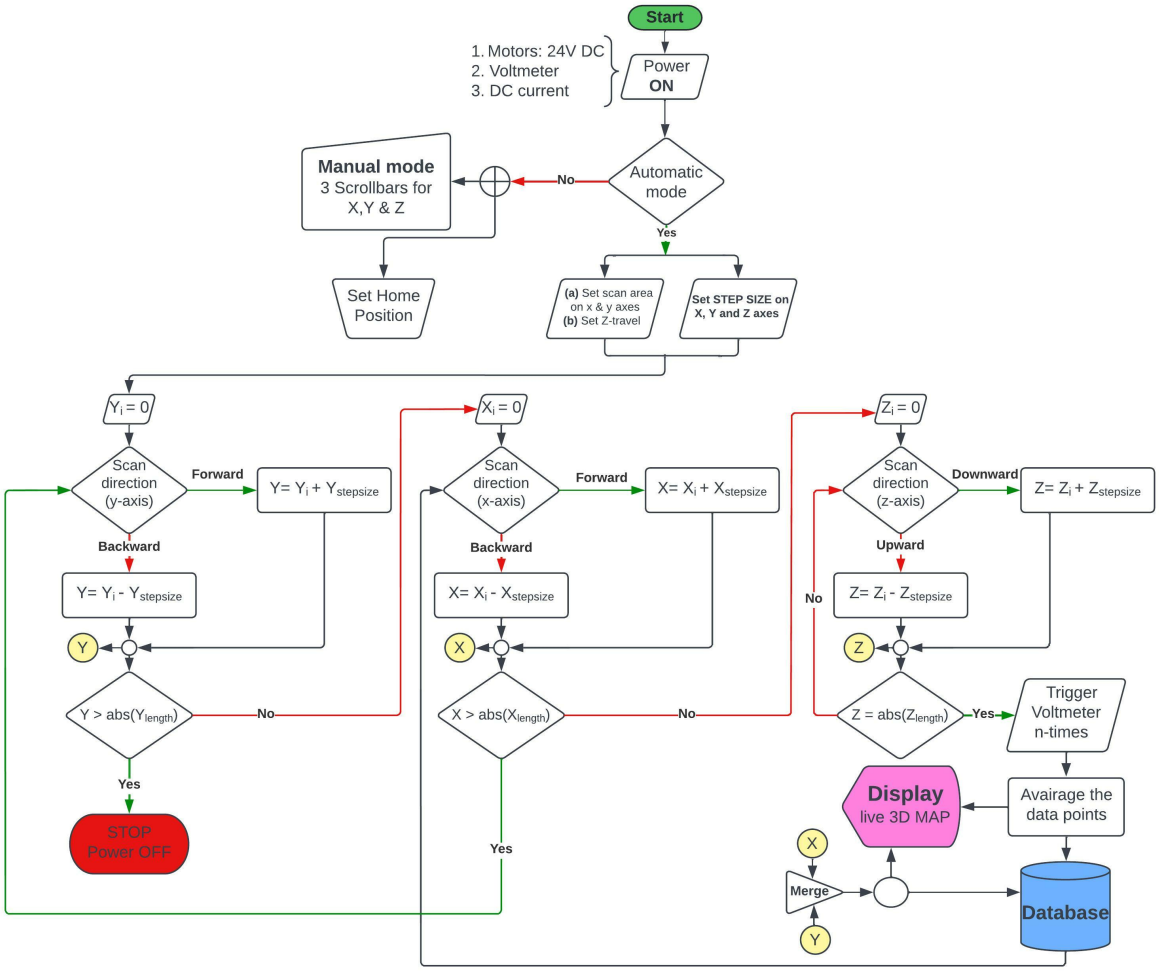

Figure A.6: Three-dimensional linear positioning, point contact data acquisition, and 3D map live display flow chart.

D.2 Sample preparation for PCM

Figure A.2 (b) shows that the sample holder platform can accommodate up to a 100x100 [mm] sample. Moreover, it has a 20x20 [mm] circular shaped sample holder, which can also be used to attach a sample.

However, for specific applications, special sample holders were designed. The first and more general approach was to design a sample holder system which allows the user to clamp the sample between two conductive electrodes and acquire the potential difference/voltage drop across a defined scan area. Figure A.7 shows the components of the whole system, and a video animation of the assembly process is available on [293].

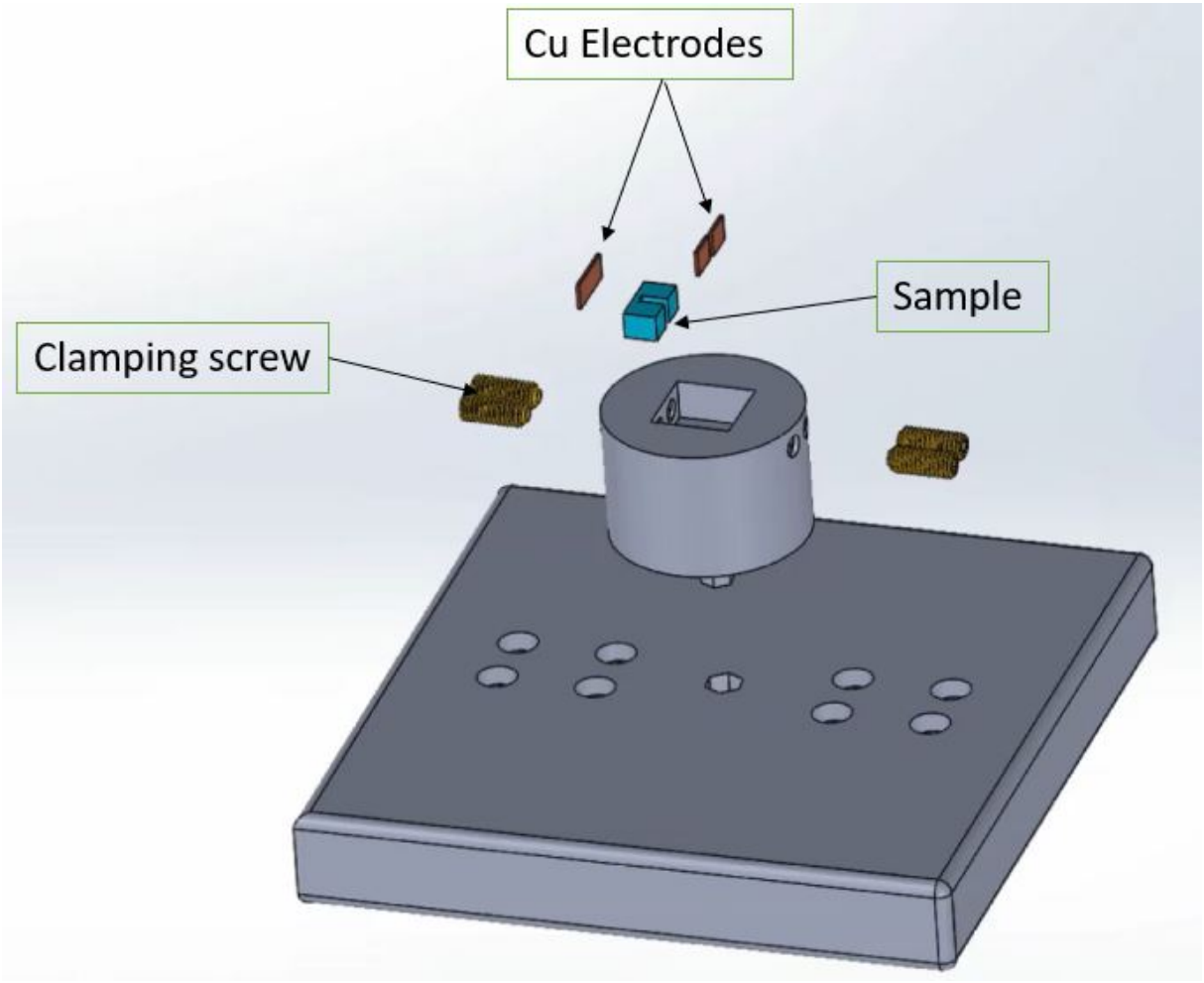

Figure A.7: Special sample holder for specific applications.

Another special case involves samples that require special care, such as samples whose electrical characteristics may be affected by the pressure applied by the probe(s). One example used in our research, was testing the contact resistance of the TEM–electrode interfaces; the samples had to be mounted before the test to avoid cracking the contact layer (bond). A detailed description of sample preparation was provided in the main text section 5.3.2.2.

Finally, the reliability and repeatability of PCM results are directly related to the sample's surface characteristics. It is therefore recommended that the sample surface should be polished to a mirror-like surface. Moreover, since most samples are in bulk state, the denser the samples are, the higher the result's repeatability and reliability.

Appendix E

The full compilation of all line scan recorded at the HMS–MGS unicouple.

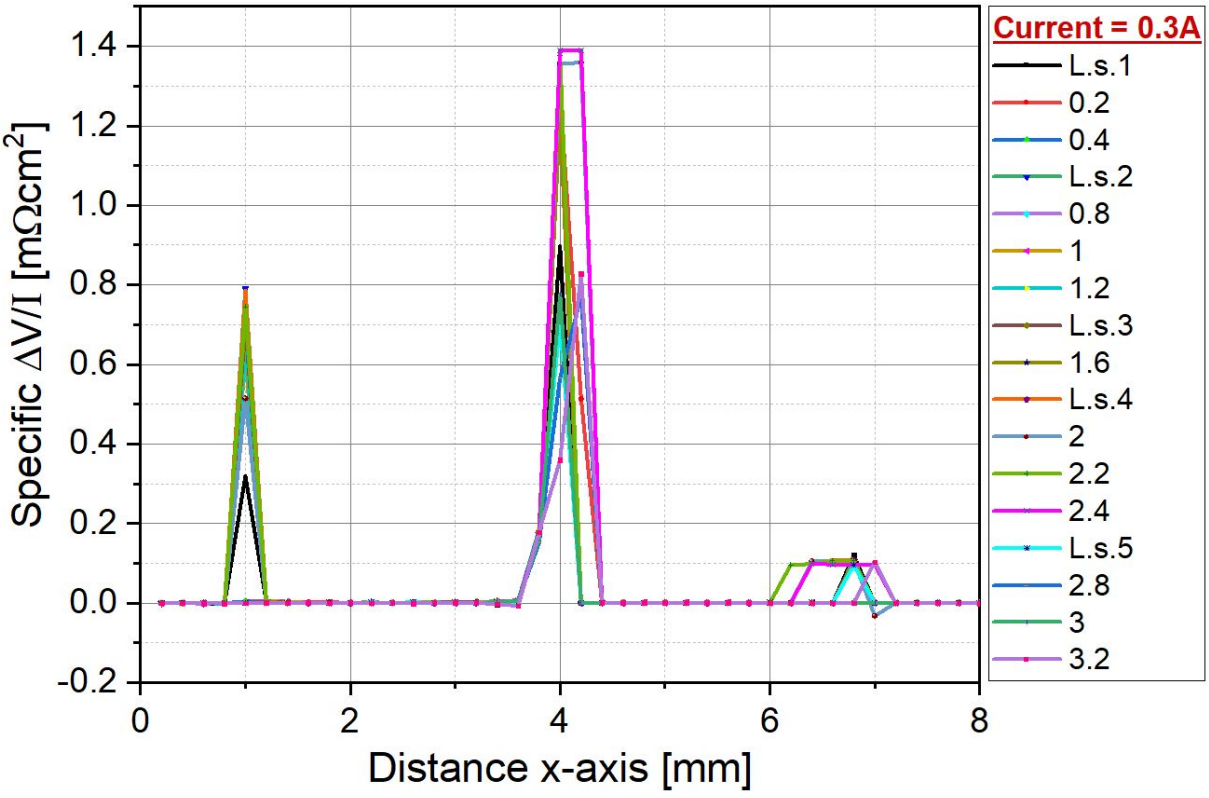

Figure A.8: All line scan "specific contact resistance spectrum" on the HMS–MGS unicouple recorded using the PCM test rig.